

Lanthanide-Loaded Nanoscaffolds for Multimodal Imaging and Therapy

Zhang, Wuyuan

DOI

[10.4233/uuid:5c69fe9c-a129-4934-a29c-e9397b62405f](https://doi.org/10.4233/uuid:5c69fe9c-a129-4934-a29c-e9397b62405f)

Publication date

2016

Document Version

Final published version

Citation (APA)

Zhang, W. (2016). *Lanthanide-Loaded Nanoscaffolds for Multimodal Imaging and Therapy*. [Dissertation (TU Delft), Delft University of Technology]. <https://doi.org/10.4233/uuid:5c69fe9c-a129-4934-a29c-e9397b62405f>

Important note

To cite this publication, please use the final published version (if applicable). Please check the document version above.

Copyright

Other than for strictly personal use, it is not permitted to download, forward or distribute the text or part of it, without the consent of the author(s) and/or copyright holder(s), unless the work is under an open content license such as Creative Commons.

Takedown policy

Please contact us and provide details if you believe this document breaches copyrights. We will remove access to the work immediately and investigate your claim.

**Lanthanide-Loaded
Nanoscaffolds for Multimodal Imaging
and Therapy**

WUYUAN ZHANG

Lanthanide-Loaded Nanoscaffolds for Multimodal Imaging and Therapy

Proefschrift

ter verkrijging van de graad van doctor
aan de Technische Universiteit Delft,
op gezag van de Rector Magnificus prof. ir. K.C.A.M. Luyben,
voorzitter van het College voor Promoties,
in het openbaar te verdedigen op
vrijdag 8 juli 2016 om 10:00 uur

door

Wuyuan Zhang

Master of Science in Applied Chemistry, Hainan University, China
geboren te Gansu Province, China

Dit proefschrift is goedgekeurd door de promotoren:

Prof. Dr. I.W.C.E. Arends

Copromotor: Dr. K. Djanashvili

Samenstelling promotiecommissie:

Rector Magnificus,	voorzitter
Prof. Dr. I.W.C.E. Arends	Technische Universiteit Delft, promotor
Dr. K. Djanashvili	Technische Universiteit Delft, co-promotor

Onafhankelijke leden:

Prof. Dr. J.R. van Ommen	Technische Universiteit Delft
Prof. Dr. H.T. Wolterbeek	Technische Universiteit Delft
Dr. J.A. Peters	Technische Universiteit Delft
Prof. Dr. M. Botta	Universita del Piemonte Orientale, Italy
Dr. C. Platas Iglesias	Universidade de Coruna, Spain
Prof. Dr. U. Hanefeld	Technische Universiteit Delft, reserve lid

The research described in this thesis was financed by China Scholarship Council (CSC) and supported by COST Action TD1004 “Bimodal PET-MRI molecular imaging technologies and applications for in vivo monitoring of disease and biological processes”.

ISBN: 978-94-028-0212-2

Copyright © 2016 Wuyuan Zhang

All rights reserved. No part of the material protected by this copyright notice may be reproduced or utilized in any form or by any other means, electronic or mechanical, including photocopying, recording or by any information storage and retrieval system, without written permission from the author.

Printed in the Netherlands by IPSKAMP

To my family

CONTENTS

CHAPTER 1

EXPLORING THE VERSATILE PROPERTIES OF METALS IN THE DESIGN OF MULTIMODAL IMAGING PROBES	1
INTRODUCTION	2
METALS IN IMAGING AND THERAPY	3
PHYSICO-CHEMICAL CONSIDERATIONS IN MRI	5
TYPES OF MRI CONTRAST AGENTS	9
<i>T₁-T₂ MRI dual probes</i>	13
MRI COMBINED WITH RADIONUCLEAR IMAGING MODALITIES	15
<i>T₁ MRI-PET and MRI-SPECT dual probes</i>	18
<i>T₂ MRI-PET and MRI-SPECT dual probes</i>	21
MRI COMBINED WITH OPTICAL IMAGING MODALITIES	24
<i>T₁ MRI-Optical dual probes</i>	24
<i>T₂ MRI-Optical dual probes</i>	26
CONCLUSIONS AND FUTURE PERSPECTIVES	27
OUTLINE OF THE THESIS	28
REFERENCES	32

CHAPTER 2

SELECTIVE DEPOSITION OF LN(III)-IONS INTO THE LARGE AND SMALL CAVITIES OF NANOZEOLITE-LTL FOR MAGNETIC RESONANCE AND OPTICAL IMAGING	41
INTRODUCTION	42
RESULTS AND DISCUSSION	44
<i>Loading of zeolite-LTL with lanthanide ions</i>	44
<i>Luminescence study</i>	46
<i>Relaxivity study and MRI performance</i>	48
<i>Fitting procedures of the obtained ¹H NMRD profiles</i>	50
CONCLUSIONS	57
EXPERIMENTAL SECTION	58
<i>Materials and methods</i>	58
<i>Zeolite loading (Ln-LTL-L)</i>	59
<i>Ion relocation</i>	59
<i>Extraction</i>	60
<i>Stability</i>	60

ACKNOWLEDGEMENTS	60
REFERENCES	61
CHAPTER 3	
PROTOTROPIC EXCHANGE GOVERNS T_1 AND T_2 RELAXIVITIES OF NANOZEOLITE Gd-LTL WITH HIGH pH RESPONSIVENESS	63
INTRODUCTION	64
RESULTS AND DISCUSSION	67
<i>Preparation of Ln^{3+}-loaded zeolite LTL</i>	67
<i>Dependence of the longitudinal relaxivity of Gd-LTL suspensions on the pH</i>	68
<i>^{17}O NMR measurements on Gd-LTL suspensions</i>	71
<i>Transverse electronic relaxation rates by EPR measurements on Gd-LTL suspensions</i>	73
<i>Transverse relaxivity of suspensions of the Gd^{3+}-loaded zeolite LTL nanoparticles</i>	74
<i>Magnetic field dependence of the relaxivities of Gd-LTL-L</i>	84
<i>Magnetic field dependence of the relaxivities of Gd-LTL-E</i>	85
<i>Relaxivities of Ho-LTL</i>	87
CONCLUSIONS	88
EXPERIMENTAL SECTION	89
<i>Ion exchange</i>	89
<i>Ion relocation</i>	89
<i>NMR relaxation and EPR measurements</i>	89
ACKNOWLEDGMENTS	90
REFERENCES	91
CHAPTER 4	
THE EFFECTS OF PEGYLATION ON STABILITY AND RELAXIVITY OF Gd-LOADED NANOZEOLITE LTL FOR MR IMAGING	95
INTRODUCTION	96
RESULTS AND DISCUSSIONS	98
<i>PEGylation of Gd-LTL</i>	98
<i>Evaluation of the effects of PEGylation on water access to Gd(III)-ions in the LTL channels</i>	104
<i>Stabilizing role of PEG chains</i>	106
<i>Cytotoxicity study</i>	108
CONCLUSIONS	110
EXPERIMENTAL SECTION	111
<i>Materials and methods</i>	111

<i>Synthesis of mPEG₂₀₀₀-COOH and mPEG₂₀₀₀-silane</i>	112
<i>Procedures for PEGylation</i>	112
<i>Stability assessment</i>	112
<i>Cytotoxicity test</i>	113
ACKNOWLEDGEMENTS	114
REFERENCES	115
CHAPTER 5	
RAPID RADIOLABELING OF Gd-LOADED ZEOLITE LTL FOR APPLICATION IN MR-PET DUAL IMAGING	119
INTRODUCTION	120
RESULTS AND DISCUSSION	122
<i>Ion-exchange efficiency</i>	122
<i>Co-loading of Cu²⁺ and Gd³⁺ into LTL, relaxivity study and surface functionalization</i>	123
<i>Radiolabeling of Gd-LTL using ⁶⁴Cu</i>	125
<i>Radiolabeling of Gd-LTL using ⁸⁹Zr</i>	126
<i>Stability of ⁶⁴Cu-LTL and ⁸⁹Zr-LTL under physiological conditions</i>	127
CONCLUSIONS	128
EXPERIMENTAL SECTION	129
<i>Production of ⁶⁴Cu and radiolabeling of zeolite LTL</i>	129
<i>Radiolabeling of zeolite LTL using ⁸⁹Zr</i>	129
<i>PET/CT phantoms and radioactivity measurements</i>	130
<i>Relaxation time measurements</i>	130
ACKNOWLEDGEMENTS	130
REFERENCES	131
CHAPTER 6	
MOLECULAR ARCHITECTURE CONTROL IN SYNTHESIS OF SPHERICAL LN-CONTAINING NANOPARTICLES	133
INTRODUCTION	134
RESULTS AND DISCUSSION	136
<i>Formation of the nanodroplets</i>	136
<i>Formation of the nanoparticles</i>	139
<i>Relaxivity measurements of Ln₂O₂SO₄ and Ln₂O₃ NPs</i>	145
CONCLUSIONS	147
EXPERIMENTAL SECTION	148

<i>Materials and methods</i>	148
<i>Preparation of Ln-containing nanodroplets by miniemulsion</i>	149
<i>Phase transformation</i>	149
<i>Characterization</i>	149
ACKNOWLEDGEMENTS	150
REFERENCES	151
CHAPTER 7	
NANOPARTICLES OF LANTHANIDE OXYSULFATE/OXYSULFIDE FOR IMPROVED CAPABILITIES IN O₂ STORAGE/RELEASE	153
INTRODUCTION	154
RESULTS AND DISCUSSION	156
CONCLUSIONS	162
EXPERIMENTAL	162
<i>Materials and methods</i>	162
<i>Preparation of nanosized Pr₂O₂SO₄ and characterization</i>	162
ACKNOWLEDGEMENTS	164
REFERENCES	165
SUMMARY	167
SAMENVATTING	171
LIST OF PUBLICATIONS	175
ACKNOWLEDGEMENTS	177
CURRICULUM VITAE	181

Exploring the Versatile Properties of Metals in the Design of Multimodal Imaging Probes

1

H																	He
Li	Be											B	C	N	O	F	Ne
Na	Mg											Al	Si	P	S	Cl	Ar
K	Ca	Sc	Ti	V	Cr	Mn	Fe	Co	Ni	Cu	Zn	Ga	Ge	As	Se	Br	Kr
Rb	Sr	Y	Zr	Nb	Mo	Tc	Ru	Rh	Pd	Ag	Cd	In	Sn	Sb	Te	I	Xe
Cs	Ba	*	Hf	Ta	W	Re	Os	Ir	Pt	Au	Hg	Tl	Pb	Bi	Po	At	Rn
Fr	Ra	**	Rf	Db	Sg	Bh	Hs	Mt	Ds	Rg	Uub	Uut	Uuq				
		*	La	Ce	Pr	Nd	Pm	Sm	Eu	Gd	Tb	Dy	Ho	Er	Tm	Yb	Lu
		**	Ac	Th	Pa	U	Np	Pu	Am	Cm	Bk	Cf	Es	Fm	Md	No	Lr

INTRODUCTION

The concept of multimodality is an emerging field in biomedical imaging nowadays. Several remarkable imaging techniques have been employed in this regard, including magnetic resonance imaging (MRI), optical imaging (OI), computed X-ray tomography (CT), positron emission tomography (PET), and single photon emission computed tomography (SPECT).¹ Each of these techniques has its own strengths or weaknesses in terms of sensitivity, resolution, penetration depth, and signal-to-noise ratio. However, so far there is no single technique that has all the advantages rolled into one, and therefore, the current research is focusing on technical integration of two or more imaging modalities with complementary features.²⁻⁴ The advantage of simultaneous imaging is obvious: multiple evaluations occur at once, excluding the interfering factors such as interim changes in alignment and condition of the patient as well as alteration of the disease state, which could be an issue in case of two separate examinations. A single probe combining multiple imaging modalities is promising to take full advantage of a hybrid scanner's simultaneous imaging capability.⁵ Moreover, such a single probe ensures the identical pharmaceutical dynamics in biodistribution and hence increases the reliability of the outcome of the diagnostic exam.⁶

MRI can be considered as the most powerful imaging technique, due to its non-invasive and non-ionizing nature combined with superb spatial and temporal resolution (10-100 μm) without limits in penetration depth.⁷ Using a strong magnetic field and radiofrequency pulses to influence the alignment of magnetic moments of water protons in the body, MRI generates high resolution 2- and 3D images of a wide range of tissues and can be applied for the clinical whole body imaging. The contrast in MRI is based on the differences in NMR signal intensity of water protons in various tissues, which on their turn depends on the tissue density, presence of metal ions, local concentration of water, its velocity, diffusion etc.⁸ Consequently, the low sensitivity is an inherent limitation of MRI due to the low energy difference between the excited and relaxed protons. A large amount of contrast agents (CAs) have been developed and used to enhance the contrast and specificity of MRI. Based on the mechanisms of proton relaxation, the MRI CAs can be classified as T_1 (longitudinal) and T_2 (transversal) agents, and chemical exchange saturation transfer (CEST) agents.⁹ In clinical practice, more than 35 % of MRI examinations involve the

administration of CAs, which have been under the continuous development for more than 30 years. Nowadays, chemists are exploring the concepts of highly sensitive and safe probes for higher magnetic fields, with targeted, responsive and therapeutic properties.¹⁰ Furthermore, the focus lies in development of multimodal probes, e.g. combining MRI with other more sensitive imaging modalities, such as PET, SPECT or OI.¹ The latter techniques have remarkable ability to quantitatively assess cellular and molecular processes by exploiting a wide range of radio-labeled and optically active small molecules, often conjugated with targeting vectors, e.g. peptides, antibodies etc.¹¹ The sensitivity of this type of detection (down to 10^{-15} M) is several orders of magnitudes higher than that of MRI (10^{-5} M), while the opposite is true for the resolution. In clinics, tumor diagnosis and treatment requires morphological and functional monitoring to assess tumor stages and therapy response. An example of an agent suitable for this assessment is [^{18}F]-2-fluoro-2-deoxy-D-glucose (FDG), which is often used to evaluate tumor metabolism,¹² but it does not provide anatomical information. Consequently, a high-resolution technique such as MRI is often consulted to obtain this.^{13,14}

While the first PET-MRI systems have already been installed,¹⁵ the research on dedicated multimodal probes is gaining substantial interest among chemists as well as radiologists.¹⁶ In this chapter, the state of the art of the rapidly developing field of multimodal imaging is described and different strategies to introduce an additional imaging reporter to an MRI-based probe are discussed. Multimodal agents have been the subject of many excellent reviews published recently,¹⁷⁻²⁵ this survey emphasizes the role of metal ions loaded into various chelates and nanoplatforms in the design of a single probe with MRI-based multimodal imaging and therapeutic potential.

METALS IN IMAGING AND THERAPY

Metal ions play a pivotal role in the development of multimodal probes, offering great advantages and opportunities compared to organic compounds. The versatility of physical properties of metals in nature, together with the big library of man-made isotopes can be exploited in the design of multimodal probes by using the same platforms that carry these ions. Thereby, the choice of the metal is determining the final application of the designed probes. Obviously, the design of such probes should rely on consideration of physical principles of imaging techniques and type of therapy involved.

Lanthanides are among the most important metals in medical imaging.²¹ The members of the series exhibit great similarity in their chemical properties, whereas their physical and radiochemical properties vary significantly. This phenomenon has been exploited intensively in research of MRI, optical, radionuclide based PET/SPECT and therapy.^{22,26,27} The physical properties of lanthanides are determined by the $4f$ -electrons, which are shielded by $5s$ - and $5p$ -electrons, and are therefore, not available for covalent binding with ligands. The lanthanides with unpaired f -electrons are paramagnetic, and hence can be used as MRI CAs due to their ability to alter relaxation times of the surrounding water molecules. The most common clinically applied CAs are stable chelates of Gd(III), which besides a high magnetic moment possesses a conveniently long electronic relaxation time.^{28,29} On the other hand, Dy(III) as well as Ho(III) exhibit the highest magnetic moment, and are therefore, more interesting for the application as T_2 susceptibility agents due to the ability to affect the transversal relaxation of water molecules in their proximity.³⁰ Nanoparticles (NPs) of these two lanthanides are promising for MRI at higher magnetic field strengths (> 1 T) because the magnetization caused by these materials does not show saturation in contrast to the clinically applied iron oxide NPs (*vide infra*).^{30,31}

Some of the lanthanides exhibit excellent optical properties based on sharp emission bands through the whole spectral region (< 10 nm).²⁶ Eu(III), Tb(III) and Nd(III) are the most common examples of Ln-ions applied in design of optical imaging probes throughout visible, NIR, and IR region. Once an f -electron is excited, the decay to the ground state will be slow, leading to conveniently long luminescence life-times (microseconds for IR-emitting Er and Nd, milliseconds for Eu and Tb). However, due to the shielding by s - and p -electrons, the molecular vibrations of f -orbitals are weak, and consequently, the emission by Ln-ions is not too strong. Therefore, organic “antennas” are typically applied as a part of chelate coordinating Ln-ion to activate f - f transitions and strengthen the luminescence signal by lanthanides.³²

Lanthanide ions cannot be used as free ions *in vivo* due to their toxicity,³³ and are therefore, often used as complexes.³⁴ The choice of chelates is driven by thermodynamic and kinetic stability considerations as well as the charge, bulk size, and spatial geometry of the complexes. The most common ligands are either linear or macrocyclic polyamino-carboxylate derivatives.³⁵

Recently, concerns have been raised about Gd(III)-based MRI CAs in connection to their *in vivo* toxicity after detection of several cases of nephrogenic systemic fibrosis (NSF) in patients with renal diseases.³⁶ This has been stimulating research on safer alternatives, such as manganese-complexes.³⁷ Mn(II) is necessary for metabolic functions in body and exhibits the right properties for MRI applications: high spin due to the 5 unpaired *4d*-electrons, high magnetic moment, slow electronic relaxation times, and fast exchange of coordinated water molecules. Thereby, development of Mn(II)-based contrast agents profits from the research on Gd(III) counterparts by using the knowledge in relaxation theory, coordination chemistry etc.

Some of the paramagnetic metals also have isotopes that are suitable for PET/SPECT and/or therapy, offering great interest in design of multifunctional probes relying only on a single metal. For example, ¹⁶⁶Ho ($t_{1/2}$ = 26.6 h, $E_{\max,\beta}$ = 1.84 MeV and $E_{\max,\gamma}$ = 80.6 keV) has emerged as a promising SPECT reporter³⁸ and effective radio-therapeutic for liver tumors.³⁹ Radionuclides ⁵⁹Fe ($t_{1/2}$ = 44.5 d)⁴⁰ and ⁵²Mn ($t_{1/2}$ = 5.6 d)⁴¹ can also be used for SPECT and PET, respectively. ¹⁵⁷Gd exhibits good ability for neutron capture therapy.⁴² These metals are already in use for MRI, which means that the existing preparation procedures can be readily applied to the radio-analogues to obtain multimodal probes for MRI-PET/SPECT or MRI-guided therapy.

PHYSICO-CHEMICAL CONSIDERATIONS IN MRI

MRI relies on the signals that originate from the large water content of the body tissues, and can therefore, be conducted without the application of CAs. However, to increase the contrast between the site of interest and the surroundings, administration of CAs is preferred aiming at its interaction with water protons to accelerate their relaxation rates. This can be sufficiently achieved by paramagnetic metal-ions due to their unpaired electrons, such as Gd³⁺, Fe³⁺, and Mn²⁺. The theory of water relaxation in the presence of paramagnetic CAs has been well developed over the past decades.^{29,43,44} A paramagnetic CA increases both longitudinal ($1/T_1$) and transverse ($1/T_2$) relaxation rates of water protons in the proximity of the metal ion. The observed relaxation rates ($1/T_{i,obs}$) are the contribution of paramagnetic ($1/T_{i,p}$) and diamagnetic ($1/T_{i,d}$) relaxation rates, as shown in Eq. 1.1. For the Gd-based CAs, the diamagnetic term corresponds to the relaxation rate of the water protons in the presence of a diamagnetic CA-analogues (e.g. La(III), Lu(III)),

while the paramagnetic term gives the relaxation rate enhancement induced by paramagnetic Gd(III)-ions which is proportional to its concentration in mmol/L ([Gd], Eq. 1.2). A plot of the observed relaxation rate versus the concentration gives a linear line and its slope is defined as relaxivity, r_1 ($\text{mM}^{-1}\text{s}^{-1}$).

$$\frac{1}{T_{i,obs}} = \frac{1}{T_{i,d}} + \frac{1}{T_{i,p}} \quad \text{where } i = 1, 2 \quad 1.1$$

$$\frac{1}{T_{i,obs}} = \frac{1}{T_{i,d}} + r_i[\text{Gd}] \quad \text{where } i = 1, 2 \quad 1.2$$

The number of water molecules in the first coordination sphere of Gd(III)-complexes (q) is one of the most important factors influencing the overall longitudinal relaxivity, as it is in a linear correlation with the longitudinal relaxivity (Eq. 1.3, where τ_M is the time that water molecules spend in coordination with Gd(III) and T_{1M} is their longitudinal relaxation time).⁴⁵⁻⁴⁷ In Gd(III) aqua-ion, q is equal to 8, which leads to a relaxation enhancement proportionally higher to that of a Gd(III)-complex with $q = 1$. Gd(III)-ions at the surface of Gd-based NPs are able to coordinate up to 7 water molecules, which results in much higher relaxivities for particles with high surface-to-volume ratio compared to Gd(III)-chelates.⁴⁸ In a common MRI CA, typically 8 coordination sites of Gd(III)-ion are occupied by pendant arms of an organic ligand, leaving one position open for coordination with water molecule ($q = 1$). Logically, much of the research efforts have been devoted into development of chelates with the ability to coordinate more than 1 water molecule, which, however, in some cases has led to a decreased thermodynamic stability.⁴⁹

$$r_1 = \frac{q}{1000 \times 55.6} \frac{1}{T_{1M} + \tau_M} \quad 1.3$$

The residence time (τ_M) represents the efficiency of chemical exchange of coordinated water molecule with the bulk water (Figure 1.1). The exchange rate can be influenced by the ligand used, and the pH. When polyaminocarboxylate complexes are used to coordinate Gd(III), the exchange rate is three orders of magnitude slower in comparison to the Gd(III) aqua-ion. Around neutral pH, the exchange rate is generally equal to that of the entire water molecules, while at increased acidity or basicity of the solution, the exchange rates become faster due to acid/basic-accelerated pathways.⁵⁰ When Gd(III)-ions are encapsulated in porous nanoplateforms, e.g. mesoporous silica or zeolite, the overall relaxation rates can be

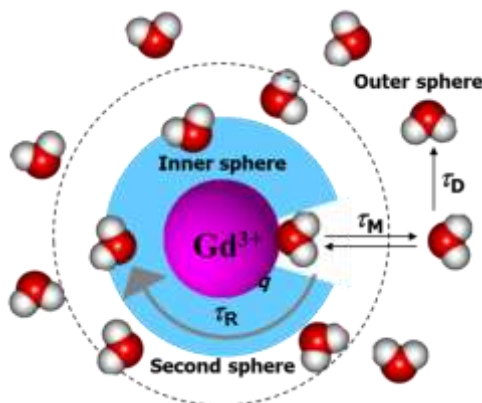


Figure 1.1. Schematic representation of inner-, second- and outer-sphere water interactions with a typical T_1 contrast agent.

enhanced by alterations of water diffusion through the pore compartment of these platforms.⁵¹ In a 3-dimensional framework of zeolites Y and A, the two-step mechanism of water exchange is mainly accounted for the overall high relaxivity: the exchange between Gd-bound water and bulk water within the interior of zeolite, and between the bulk water inside and outside of zeolite. While in the 1-dimensional channel of zeolite LTL, proton exchange becomes dominant (see chapter 3). The proton exchange rate of the second step is three orders of magnitude faster than water exchange, leading to significantly enhanced longitudinal relaxivities.⁵²

The origin of the paramagnetic relaxation rates is mainly considered as the contributions from the inner- and outer-sphere mechanisms. The inner sphere contribution ($R_{i,IS}$) is due to the processes governed by the above-mentioned parameters (q , τ_M , τ_R , T_{1e} , and T_{2e}), while the outer-sphere contribution ($R_{i,OS}$) is from effects that water molecules experience diffusing (τ_D) along the paramagnetic ions or through the magnetic field gradients induced by the Gd(III) in rotating complex without being bound (Figure 1.1). The second-sphere mechanism represents the contribution from water molecules bound to the functional groups of the ligand via hydrogen bonding. This term can be misleading because some of the water molecules in the second coordination-sphere frequently can also be the ones involved in outer-sphere relaxation. Both inner- and outer-sphere mechanisms are very important factors to take into account when designing efficient MRI CAs. The total

relaxation rate and relaxivity enhancement is given by Eqs. 1.4-1.8, where r_{GdH} is the distance between the Gd(III) electron spin and the water protons, γ_S and γ_I are the electron and proton gyromagnetic ratios, τ_{di} is given by $\tau_{\text{di}}^{-1} = \tau_{\text{m}}^{-1} + \tau_{\text{R}}^{-1} + T_{\text{ie}}^{-1}$, T_{ie} are the electronic relaxation rates ($i = 1, 2$), ω_S is the Larmor frequency, Δ^2 is the trace of the square of the zero field splitting (ZFS) tensor, and τ_v is the correlation time for the modulation of ZFS.

$$\left(\frac{1}{T_{i,p}}\right) = \left(\frac{1}{T_{i,p}}\right)^{IS} + \left(\frac{1}{T_{i,p}}\right)^{OS} = R_i^{IS} + R_i^{OS} \quad 1.4$$

$$r_i = r_i^{IS} + r_i^{OS} \quad 1.5$$

$$\frac{1}{T_{1m}} = \frac{2}{15} \left(\frac{\mu_0}{4\pi}\right)^2 \frac{\hbar^2 \gamma_S^2 \gamma_I^2}{r_{\text{GdH}}^6} S(S+1) \left(\frac{3\tau_{d1}}{1+\omega_I^2 \tau_{d1}^2} + \frac{7\tau_{d2}}{1+\omega_S^2 \tau_{d2}^2}\right) \quad 1.6$$

$$\frac{1}{T_{1e}} = \frac{1}{25} \Delta^2 \tau_v [4S(S+1) - 3] \left(\frac{1}{1+\omega_S^2 \tau_v^2} + \frac{4}{1+4\omega_S^2 \tau_v^2}\right) \quad 1.7$$

$$\frac{1}{T_{2e}} = \Delta^2 \tau_v \left(\frac{5.26}{1+0.372\omega_S^2 \tau_v^2} + \frac{7.18}{1+1.24\omega_S \tau_v}\right) \quad 1.8$$

The rotational correlation time (τ_R) determines the effective correlation time of proton relaxation (τ_C), expressed by Eq. 1.9, which indicates that τ_R is a limiting factor for small and fast tumbling Gd-complexes.

$$\frac{1}{\tau_{iC}} = \frac{1}{\tau_m} + \frac{1}{\tau_R} + \frac{1}{T_{ie}} \quad 1.9$$

Simulations show that the relaxivity of small Gd-complexes becomes significantly higher when τ_R increases already by one order of magnitude.⁴³ Therefore, a broad variety of approaches, mainly on increasing the molecular weight of the complexes, have been used to slow down the rotation and reach higher relaxivities.

If the transverse relaxation time (T_2) of a CA is much shorter than its longitudinal relaxation time (T_1), it is usually considered as a T_2 CA. Typically long repetition and echo times are needed to acquire a T_2 -weighted MR image. Both inner- and outer-sphere mechanisms are important in enhancing T_2 relaxation rates, whereas the latter mechanism (diffusion of water molecules) is the dominating factor in case of magnetic NPs. External factors such as magnetic field inhomogeneity can decrease the T_2 relaxation time. This leads to another important term T_2^* , which is the sum of T_2 relaxation and the contribution

of all magnetic field inhomogeneities in the field.⁵³ The T_2^* is of great use in clinical MRI as it is dependent on the specific properties of the tissues.

TYPES OF MRI CONTRAST AGENTS

The vast majority of clinically applied MRI CAs are small Gd(III)-chelates for T_1 -weighted imaging, mainly used for detection of lesions in the blood brain barrier, changes in vascularity, flow dynamics, and perfusion. The most commonly used ligands are based on a macrocycle 1,4,7,10-tetraazacyclododecane (cyclen), and some linear polyamino-carboxylates. Some of the most important derivatives of DOTA and DTPA are depicted in Figures 1.2 and 1.3. These hepta- or octadentate ligands possess a number of properties that are advantageous for their *in vivo* applicability: i) strong complexation of Gd(III) leads to high thermodynamic and kinetic stabilities of the complexes, and thus reduces toxicity of the free Gd(III)-ion, ii) relaxivity properties of the CAs can be well predicted and optimized to some extent by modulating the parameters such as q , τ_m , τ_R etc. (see examples in Table 1.1), iii) the ligands can be used as platforms, in which functional and specific groups can be incorporated to either improve the overall performance of the CAs or make them more specific. Examples of the latter efforts include strategies to functionalize the CAs with targeting vectors to improve local delivery to the site of interest, binding with macromolecules *in vivo*, or providing the probe with a responsive mechanism to the endogenous triggers, such as temperature, pH or a particular enzyme activity.^{22,54}

In the past decades, the nanochemistry has grown tremendously and many novel nanomaterials have been explored in the field of MRI CAs. Methodologies have been developed to control the synthesis of nanoparticulate CAs (e.g. dimension, composition, crystalline phase and morphology) and their surface engineering has been explored significantly. These parameters are closely related to the *in vivo* behavior of NPs. Up to day, a number of nanosystems have been playing important roles in development of T_1 and/or T_2 CAs, such as Ln_2O_3 ,⁵⁵ upconversion NPs,⁵⁶ liposomes and micelles,⁵⁷ graphene oxides,⁵⁸ and clinically applied SPIO and USPIO NPs²⁰ (see Figure 1.4). Gd(III) oxides have been studied for the use of multimodal imaging probes, drug carriers and therapeutic agents.⁵⁵ Compared to the solid NPs, the porous systems such as mesoporous silica NPs (MSN),⁵⁹ zeolites,⁵¹ and carbon nanotubes⁶⁰ exhibit unique features due to their inert chemical properties and peculiar porous structures.

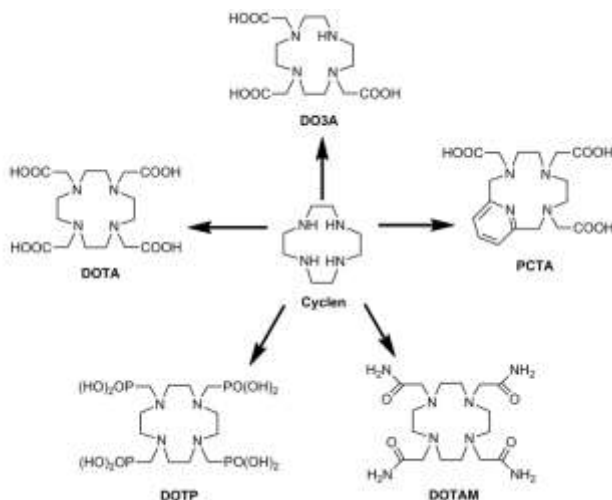


Figure 1.2. General synthetic scheme of ligands based on cyclen for chelating Gd as MRI T_1 CAs.

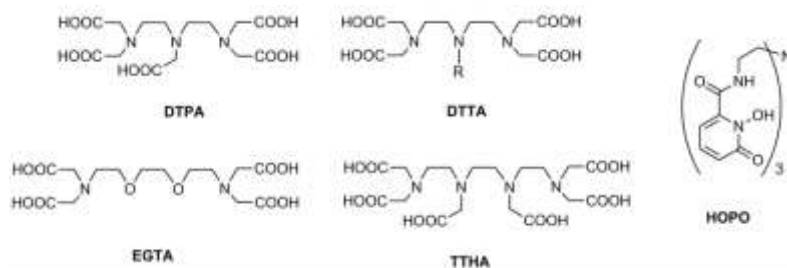


Figure 1.3. Selected examples of linear polyaminocarboxylic complexes for Gd-based MRI T_1 CAs.

From Eq. 1.2 it is clear that the relaxivity is linearly proportional to the concentration of a CA, thus a high payload is particularly important to reach a high local concentration at sites of interest and thus in enhancing the sensitivity. A recent example shows that, more than 4000 Gd(III)-ions per particle can be achieved by a simple ionic exchange between Na^+ and Gd(III)^- ions in zeolite LTL (20×40 nm), see Chapter 3.⁵² Particle size is an important parameter to consider not only from the biodistribution point of view, but also in order to control the relaxivity.⁶¹ Smaller sizes are preferred for the NPs, which enhance the r_1 relaxivity through the water exchange process, as the inner-sphere contribution increases with increasing surface-to-volume ratio.^{62,63} On the other hand, NPs that influence r_2 ,

Table 1.1. Examples of MRI CAs and their relaxivity properties measured at 1.0 T and 37 °C, unless stated otherwise.

Type	Name	Charge (mV)/size (nm)	Relaxivity ($s^{-1}mM^{-1}$)		Ref.
			r_1	r_2	
T_1					
Small chelates	Gd-DOTA, Dotarem®	-1	3.4	4.3	35
	Gd-DTPA, Magnevist®	-2	3.4	3.8	35
	Gd-DTPA-BMA, Omniscan®	0	3.9	4.3	35
	Gd-HPDO3A, Prohance®	0	3.7	4.8	35
	Mn-DPDP, Teslascan®	-4	2.3	4.0	35
Polymeric	Gd-DTPA-17, Vistarem®	-1	11.9	16.5	35
	Gd-HPDO3A, Gadomelitol®	0	42	50 ^a	35
	Gd-DTPA-PEG	-2	6.0	-	35
Nanoparticles	Gd-ultrasmall NPs	2.4 nm	4.3	27.1 ^b	50
	Gd-LTL nanozeolite	20×40 nm	30.4	-	64
	Mn-EDTA-PP liposomes		37.4	53.2 ^a	
T_2					
Small chelates	Dy-DTPA	-2	-	^a	35
	Dy-DTPA-BMA	0	3.4	3.8 ^{a,b}	35
Nanoparticles	Ferumoxtran-10 AMI-227, Sinerem®	15-40 nm	22.7	53.1 ^a	35
	Fe ₂ O ₃ , FeO, SPIO, Feridex®	80 nm	40.0	160.0	35
	Dy-ultrasmall NPs	2.9 nm	0.2	40.3 ^b	62
	Ho-ultrasmall NPs	2.4 nm	0.1	31.2 ^b	62

^a measured at 0.47 T. ^b measured at 1.5 T. ^c T_2^* is enhanced as well. “-“ = not reported.

operate via the generation of magnetic field gradients that affect water molecules diffusing along the particles.

This effect can be achieved more effectively with bigger sizes since the r_2 is proportional to the overall magnetic moment of NPs. This phenomenon has been generally observed for iron oxide NPs⁶⁵ as well as for Ln₂O₃ NPs,^{31,66} and ferrites (iron oxide NPs doped with Mn(II), Co(II), Zn(II), Ni(II) and their mixtures.^{67,68} However, magnetization saturation at increasing magnetic field is a common feature of iron oxides based T_2 CAs. In contrast, magnetization and thus r_2 values of Ln-based NPs increase with increased magnetic fields, which render these materials promising for the emerging high magnetic field MRI.⁶⁶

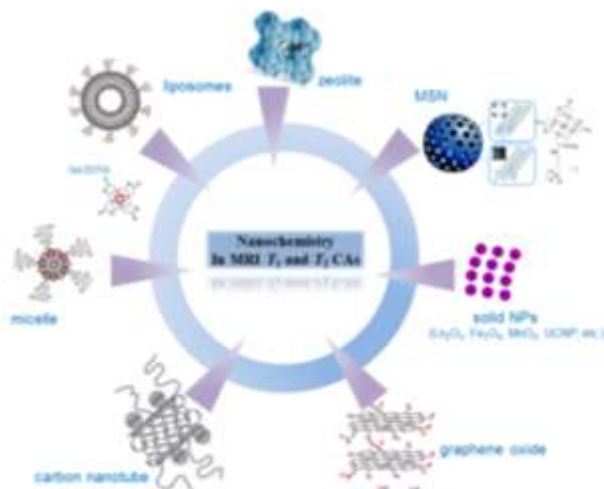


Figure 1.4. Nanoparticles and nanocarriers used for the design of efficient MRI T_1 , T_2 CAs.

Apart from the influence on relaxivity, the size of the NPs is also closely related to the *in vivo* behavior and possible toxicity of the CAs. Particles below 5 nm can be efficiently cleared by renal excretion.⁶⁹ On the other hand, the bigger particles are typically cleared by mononuclear phagocyte system.^{70,71} The particles between 10 and 100 nm in general are small enough to go through small capillaries and they have relatively longer blood half-life time. The size of NPs is crucial in cancer imaging due to enhanced permeability and retention (EPR) effect, typical for the leaky vasculature in the fast and uncontrolled growing tumors. This phenomenon is particularly interesting for MRI-guided therapy as it allows delivering imaging and therapeutic components simultaneously to the diseased site and monitoring the treatment. Shape of NPs is another morphological property that determines their circulation behavior. Spherical NPs tend to remain longer in the blood flow in comparison to their asymmetrical counterparts, such as rods or discs,^{72,73} while the angular particles can even damage cell membranes.⁷⁴ Finally, the *in vivo* performance as well as toxicity of NPs is determined by the surface chemistry such as charge, coating and the presence of certain functionalities.⁷⁵ Positively charged NPs are known to be internalized by cells due to the electrostatic interaction with the negatively charged cell membranes, while negatively charged NPs are usually cleared by the liver.

In the case of Mn-based T_1 CAs, Mn(II) has been complexed with EDTA,⁷⁶ stabilized by dendrimers,⁷⁷ amphiphilic dextran micelles,⁷⁸ and mesoporous silica spheres.⁷⁹ In all these systems, parameters such as water exchange rate and hydration number are near optimal for an efficient MRI T_1 CA compared to Gd-based compounds. Multifunctional properties can be realized in the same nanosystems, which have become the main strategy to provide the resultant imaging probes with identical biodistribution. The NP itself can provide the magnetic function, while an extra modality (e.g. fluorescence, radiotracers, or therapeutic) are often introduced by the surface engineering of the particles.⁸⁰ Porous nanoplatforms open many pathways to achieve the multifunction by using pore-loading⁶⁴ as well as functionalization of internal and external surfaces.⁸¹

T_1 - T_2 MRI dual probes

Two different proton relaxation mechanisms that form the basis of MR imaging can already be exploited for multimodal imaging as such. Longitudinal (T_1) and transverse (T_2) relaxations create bright and dark contrast, respectively. Combination of the ability to affect both processes by a single CA molecule or a nanosystem creates the opportunity for T_1 - T_2 dual imaging, sometimes indicated as “fault-free MRI”.⁸² This approach becomes particularly interesting when there is a need to verify the uncertainties in case of negative contrast, magnetic susceptibility artefacts, or concerns about signal-to-noise ratio in a dark image.⁸² The effort led to CAs with the value of r_2/r_1 ratio between 1 and 10, as required for optimal performance of T_1 CAs, and simultaneous ability to affect T_2 - or T_2^* -weighted contrast. More importantly, the T_1 - T_2 properties of the probes can be tuned through a synthetic design, e.g. control over particle size, shape and composition of dual systems based exclusively on Gd or Mn, and/or their combination with Fe.^{67,83-85}

Despite of the fact that Gd-based complexes are the main class as T_1 CAs, recently a few examples of only Gd-containing nanosystems have been demonstrated as T_1 - T_2 dual probes. In our recent work we presented a Gd-loaded zeolite LTL with a large payload of Gd-ions per particle (see Chapter 3). The r_1 relaxivity was found to be independent of τ_R , while another key parameter τ_{zeo} , the proton exchange between the interior of LTL and bulk, is three orders of magnitude faster than the corresponding water exchange, which suggests a fast prototropic exchange mechanism in this nanosystem.⁵² Interestingly, the

high T_2 relaxivity could also be ascribed to the prototropic exchange mechanism, rendering it a T_1 - T_2 dual responsive probe.

One of the strategies to enhance both types of relaxivities while retaining the convenient r_2/r_1 ratio is to assemble a nanosystems by conjugation of Gd(III)-complexes to a carrier. Recently, Roullin *et al.* have demonstrated this approach by encapsulation of the hydrophilic Gd(III)-DOTA into a hydrogel consisting of biocompatible chitosan and hyaluronic acid.⁸⁶ The r_1 - and r_2 -relaxivities measured with this nanosystem at 1.5 T (25 °C) were 72.3 and 177.5 s⁻¹ mM⁻¹, respectively, which is extremely high, compared to Gd(III)-DOTA (Table 1.1). The relaxation properties could be well-tuned by adjusting the Gd-complexes, the hydrogel matrix composition, and gelation process.⁸⁷ Silica NPs are also used to incorporate the Gd-complexes, e.g. *via* a simple and versatile sol-gel method.⁸⁸ In general, porous structures often allow for fast water exchange, and thus increased r_1 . The r_2/r_1 ratio can be optimized by choosing the appropriate particle size that mainly influences the r_2 value.

Gd-based ultrasmall NPs represent another alternative to affect both types of relaxation mechanisms. Ultrasmall Gd₂O₃ NPs (1-3 nm) synthesized via a polyol method are generally considered as T_1 CAs. When these ultrasmall NPs are surface coated with MnO, the T_1 relaxivity is basically the same as that of pure Gd₂O₃, whereas T_2 relaxivity nearly doubles due to the presence of MnO, making it interesting for T_1 - T_2 dual imaging.⁸⁹ Doping of the ultrasmall Gd₂O₃ with Eu(III) and subsequent coating with biocompatible and colloiddally stable lactobionic acid has resulted in T_1 and T_2 relaxivities of 11.9 and 38.7 s⁻¹ mM⁻¹ at 1.5 T, respectively.⁸³ Ultrasmall Fe₃O₄ NPs are also proved suitable for both T_1 - and T_2 -weighted MRI. Gao *et al* experimentally demonstrated that for iron oxides NPs, the main contribution of the T_1 contrast enhancement is from the water exchange on the iron-rich Fe₃O₄(111) surface, whereas the T_2 relaxation is dominated by the intrinsic superparamagnetism of the NPs.⁹⁰ Combination between Gd and Fe in a core-shell structure can maximally utilize the advantages of each metal and lead to promising T_1 - T_2 probes, which represent an important strategy. Luo *et al.* reported Fe₃O₄/SiO₂/Gd₂O(CO₃)₂ NPs for T_1 - T_2 dual imaging in which the SiO₂-layer between the Fe₃O₄ core and the Gd₂O(CO₃)₂ shell can modulate r_1 and r_2 relaxivities.⁸⁴ The r_2 relaxivity of the Fe₃O₄ core appeared to be enhanced in the presence of Gd(III) most probably due to dipole-dipole coupling of the

neighboring Gd(III)-Fe(II)/Fe(III) ions interacting with each other and generating increased transverse electronic relaxation.⁹¹

It has been shown that the saturation of magnetization of MnFe₂O₄ NPs is decreasing with decreased particle size. Conjugation of Gd(III)-DTPA at the surface of medium-size NPs results in both enhanced T_1 and T_2 .⁹² Cheng *et al.* bridged Au and iron oxide via Pt into a dumbbell structure, and the surface of Au is covalently immobilized with Gd-DOTA.⁹³ This design resulted in dual T_1 and T_2 -weighted functions for MRI with favorable biodistribution. As T_1 relaxation is mainly accelerated by Gd while T_2 enhancement originates from Fe, manipulating the spatial arrangement of each component in order to adjust the magnetic coupling was shown to be the key strategy to synergistically enhance both T_1 and T_2 contrast effects.

MRI COMBINED WITH RADIONUCLEAR IMAGING MODALITIES

Despite the excellent spatial resolution, the inability of MRI to quantitatively assess the events at tissue and cellular level forms a major disadvantage in diagnosis. To overcome this limitation, a feasible solution is to combine MRI CAs with radionuclide reporters that allows localization and quantification of the whole probe.¹⁶ There are many examples in the literature reporting on the combinations between Gd (T_1) and/or Fe(T_2) CAs with other metal-ions (Figure 1.5). This strategy opens possibility to assess many physiological parameters, such as pH, metabolic rates, and receptor densities. Several radioisotopes have emerged currently as interesting for design of dual probes for MRI-radionuclide imaging (Table 1.2), which is determined by the choice of the isotopes applied. For instance, representative metallic isotopes including ⁶⁴Cu, ⁶⁸Ga, ⁸⁹Zr, ⁴⁴Sc, ⁸⁶Y with relatively long half-life time have been widely used in PET, while ⁶⁷Ga, ^{99m}Tc, ¹¹¹In, ¹⁷⁷Lu, and ¹⁶⁶Ho are typical isotopes for SPECT. For therapeutic applications, isotopes that emit particles, such as ⁴⁷Sc, ^{114m}In, ¹⁶⁶Ho, ¹⁷⁷Lu, ⁹⁰Y, ^{212/213}Bi, ²¹²Pb, ²²⁵Ac, and ^{186/188}Re are widely investigated.

PET and SPECT are non-invasive nuclear imaging techniques based on a tomographic reconstruction method to produce a 3-dimensional image of functional processes in the body, and the use of radiotracers is the prerequisite. For PET, the emitted photons of a positron-emitting radionuclide come across electrons in the body and then annihilate. The annihilation generates two 511 keV γ -rays emitted simultaneously in opposite directions. The acquisition of the annihilation by surrounding detectors permits the translation of

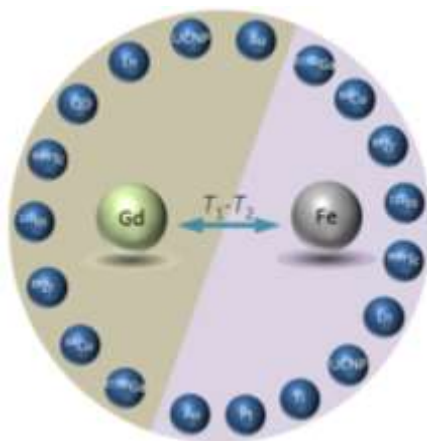


Figure 1.5. Combination between Gd (T_1) or Fe (T_2) and various metals for dual/multimodal imaging reported in the literatures. Ln = lanthanides, UCNP = upconversion nanoparticle, and QD = quantum dots.

spatial distribution of the radioactivity into an image. The technique SPECT utilizes single photons with energies in the range of 30 to 250 keV. The single photon emitted from a radioisotope, travels through tissues and is then detected by a sensitive gamma-radiation detector. Although the sensitivity is 1-3 orders of magnitude lower than in PET, SPECT has remarkable sensitivity and demonstrates very promising in imaging biological processes in *vivo* and staging of cancer.⁹⁴

So far, radiotracers used in PET imaging are typically isotopes with short half-lives such as ^{11}C ($t_{1/2} = 20.3$ min), ^{13}N ($t_{1/2} = 9.9$ min), ^{15}O ($t_{1/2} = 122.2$ sec) and ^{18}F ($t_{1/2} = 109.7$ min), which are used extensively for radiolabeling of molecules and drugs, due to their endogenic nature and low atomic mass, leading to a less possible interference with the biological activity. For example, FDG-glucose (2- ^{18}F fluoro-2-deoxy-D-glucose) is routinely used in PET clinics to assess the metabolic state tumors. However, the short half-life time can also be a disadvantage because the chemical procedures of the preparation of the imaging probes including synthesis, purification, and characterization, in general take longer time. Therefore, optimizing and developing efficient methodologies for the chemical synthesis are of vital importance. Radioisotopes of metals with longer half-life times are easier to handle and therefore are often interesting alternatives. Selected examples are

Table 1.2. Selected metallic radionuclides, useful for nuclear imaging and their properties.

Isotope	$t_{1/2}$ (h)	Decay mode	E (keV)	Production method	Application
^{60}Cu	0.4	β^+ (93%) EC (7%)	β^+ , 3920, 3000 2000	cyclotron, $^{60}\text{Ni}(p,n)^{60}\text{Cu}$	PET
^{61}Cu	3.3	β^+ (62%) EC (38%)	β^+ , 1220, 1150 940, 560	cyclotron, $^{61}\text{Ni}(p,n)^{61}\text{Cu}$	PET
^{62}Cu	0.16	β^+ (98%) EC (2%)	β^+ , 2910	$^{62}\text{Zn}/^{62}\text{Cu}$ generator	PET
^{64}Cu	12.7	β^+ (19%) EC (41%) β^- (40%)	β^+ , 656	cyclotron, $^{64}\text{Ni}(p,n)^{64}\text{Cu}$	PET
^{67}Cu	62.01	β^- (100%)	β^- , 577, 484, 395 γ , 91, 93, 185	accelerator, $^{67}\text{Zn}(n,p)$	SPECT/ Therapy
^{66}Ga	9.5	β^+ (56%) EC (44%)	β^+ , 4150, 935	cyclotron, $^{63}\text{Cu}(\alpha, n\gamma)^{66}\text{Ga}$	PET
^{67}Ga	78.26	EC (100%)	γ , 91, 93, 185, 296, 388	cyclotron	SPECT
^{68}Ga	1.1	β^+ (90%) EC (10%)	β^+ , 1880	$^{68}\text{Ge}/^{68}\text{Ga}$ generator	PET
^{44}Sc	3.9	β^+ (94%) EC (6%)	β^+ , 1474 γ , 1157	$^{44}\text{Ti}/^{44}\text{Sc}$ generator	PET
^{47}Sc	80.2	β^- (100%)	β^- , 441, 600 γ , 159	$^{47}\text{Ti}(n,p)^{47}\text{Sc}$	SPECT
^{111}In	67.9	EC (100%)	γ , 245, 172	cyclotron, $^{111}\text{Cd}(p,n)^{111m}\text{gIn}$	SPECT
^{114}In	73 s	β^- (100%)	β^- , 1989	^{114m}In daughter	SPECT/ Therapy
^{177}Lu	159.4	β^- (100%)	β^- , 4177, 385, 4980 γ , 112, 208	$^{176}\text{Lu}(n,\gamma)^{177}\text{Lu}$	SPECT/ Therapy
^{86}Y	14.7	β^+ (33%) EC (66%)	β^+ , 1221	cyclotron, $^{86}\text{Sr}(p,n)^{86}\text{Y}$	PET
^{89}Zr	78.5	β^+ (22.7%) EC (77%)	β^+ , 897	cyclotron, $^{89}\text{Y}(p,n)^{89}\text{Zr}$	PET
^{166}Ho	26.8	β^- (100%)	γ , 1855	$^{165}\text{Ho}(n,\gamma)^{166}\text{Ho}$	SPECT/ Therapy
^{52}Fe	8.3	β^+ (55%) EC (45%)	β^+ , 803 γ , 1825	$^{52}\text{Fe}/^{52m}\text{Mn}$ generator	PET/Therapy
^{99m}Tc	6	γ (91.5%)	γ , 140	Cyclotron, $^{100}\text{Mo}(p,2n)^{99m}\text{Tc}$ or $^{99}\text{Mo}/^{99m}\text{Tc}$ generator	SPECT
^{201}Tl	72.9	EC (100%)	γ , 346, 451, 481	Cyclotron, $^{203}\text{Tl}(p,3n)^{201}\text{Pb} \rightarrow ^{201}\text{Tl}$ or $\text{Hg}(p,n/p,2n/p,4n)^{201}\text{Tl}$	SPECT

shown in Table 1.2. The production and transportation of the metal radionuclides are practical concerns related to their application. Cyclotrons and generators are two main systems for the production of the radionuclides.⁹⁵ The cyclotron is usually used for long-lived nuclides such as ^{64}Cu , ^{89}Zr , ^{86}Y , ^{55}Co , ^{52}Mn , etc., allowing the transportation of these

nuclei over a long distance from the cyclotron facility. For comparison, there are many short-lived metallic radionuclides available from corresponding generators, such as $^{62}\text{Cu}/^{62}\text{Zn}$, $^{68}\text{Ga}/^{68}\text{Ge}$ generators. A generator system consists of a long-lived parent radionuclide that decays and continuously produces a short-lived daughter radionuclide. Such a generator is very important in clinical practice because it enables production of radionuclides at the sites that are far away from a cyclotron.

T₁ MRI-PET and MRI-SPECT dual probes

The development of MRI-PET/SPECT multimodal probes has become a fast growing area in medical imaging and diagnosis. The strategy typically starts radiolabeling the existing MRI T_1 and T_2 CAs (e.g. Gd-chelates, iron oxides NPs) that already possess magnetic imaging functionality. One of the most prominent examples on the advantage of combination of both imaging modalities in one probe was presented by Caravan *et al.* by conjugation of Gd(III)-DOTA to fibrin-binding peptides for MRI visualization and by partly replacing Gd(III) with ^{64}Cu (II) for PET observation.^{96,97} The amount of Cu used for the complexation with DOTA was much less than that of Gd due to the large differences in the sensitivity of PET compared to MRI. The *in vivo* evaluation of the mixture demonstrated high affinity of this probe to thrombi with possibilities not only to locate but also to quantify this tissue. The approach of using ‘lanthanide cocktails’ in combination with the same chelate is of course a straight-forward strategy to adapt the existing MRI probes to the nuclear imaging.⁹⁸ However, some researchers emphasize the importance of identical thermodynamic and kinetic stability aspects of the probes and put efforts in designing probes containing two different chelates in the same molecule. A representative example of heterometallic complexes is reported by Kumal *et al.* who combined DOTA and NOTA rings in one dendritic structure (Figure 1.6).⁹⁹ The specific coordination ability of the DOTA and NOTA (1,4,7-triazacyclononane-1,4,7-triacetic acid) moieties offer specific chelation of Gd(III) and $^{68/67}\text{Ga}$ (III) for MRI and PET/SPECT, respectively. The researchers demonstrate specific delivery of the designed dual probe to the tumor site through a targeting peptide, c(RGDyK). To overcome the steric hindrance from the dendritic structure that can reduce the targeting capability of the final probe, a PEG₁₂ linker was thus introduced between the complex and the peptide. The high r_1 -relaxivity ($15.99\text{ s}^{-1}\text{mM}^{-1}$ at 20 MHz) was originated from six peripheral Gd(III)-DOTA units, while the central

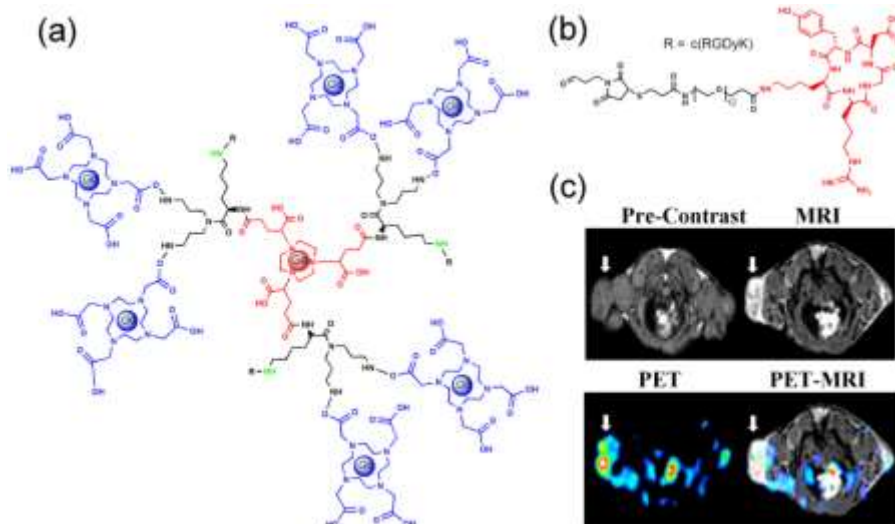


Figure 1.6. Schematic representation of a dual-modality molecular probe design: a) structure targeting of ligand of heterocomplex, the coordinating bonds between Gd(III) and DOTA, Ga(III) and NOTA were omitted for simplicity; b) the targeting peptide c(RGDyK); c) Representative PET, MR and PET-MR images of U87MG tumor xenograft in SCID mice at 1 h post injection of the dual probe. The white arrow indicates the tumor site.

Ga(III)-NOTA complex provided a PET/SPECT signal. The probe exhibited a single pharmacokinetic behavior *in vivo* and thus is an excellent example of visualization of tumor by both MRI and PET/SPECT via a single dose injection. DOTA and NOTA and their derivatives are majorly considered as the matrix of dual probes to complex Gd(III) and Ga(III) due to the specific coordination.^{19,100}

Development of responsive probes based on the relaxivity change in MRI is an important direction in the MRI-PET research. Botta *et al.* reported another variation on the combination of Gd(III)-DOTA and Ga(III)-AAZTA units in one molecule and introduced sulfonamide bridge to conjugate the heterodimer.¹⁰¹ As a result, the r_1 by Gd(III)-ion complexed to the DOTA-chelate became pH-dependent by virtue of change in the hydration state. The reversible on/off complexation of the sulfonamide nitrogen makes it a smart probe for pH-readout by MRI assisted by PET, which actually uses $^{68}\text{Ga(III)}$ for quantification. It is worth noting that the above-mentioned synthetic strategies would

permit the formation of a large series of heterodimetallic complexes for different biomedical applications by simply changing the coordinated metal ions.

Laprise-Pelletier and coworkers recently reported an MRI-PET dual probe based on mesoporous silica NPs grafted with DTPA for chelation of Gd(III) and $^{64}\text{Cu(II)}$.¹⁰² The obtained nanosystem benefited from the enhanced r_1 -relaxivity ($33.8 \text{ s}^{-1}\text{mM}^{-1}$) due to the multiple paramagnetic units conjugated to one nanocarrier, while the PET signal was delivered by the radioactive $^{64}\text{Cu(II)}$ present in a trace dose.

In our current research we are exploring the ability of Gd-loaded zeolite LTL to accommodate ^{64}Cu as well as ^{89}Zr in the same nanostructure, which can be done efficiently with a very high labelling yield (88.4% of ^{64}Cu and 74% of ^{89}Zr in 60 min). In addition, the observed high r_1 and r_2 were not affected by the co-loading of the isotopes, see Chapter 5.

The strategies mentioned for design of MRI-PET dual probes can of course be readily extended to MRI-SPECT simply by exchanging the radioisotope.^{101,103} For example, the chemically homogeneous probe combined Gd(III)-DOTA and $^{68}\text{Ga(III)-NOTA}$ can be directly translated into $^{67}\text{Ga(III)-NOTA}$ for MRI-SPECT applications.⁹⁹ The same is true for radiolabeling of chelates conjugated to the surface of NPs. *Kryza et al.* have demonstrated this using ultrasmall Gd_2O_3 NPs (2 nm) in combination with DTPA, tethered at their surface and used to coordinate ^{111}In .¹⁰⁴ The long-lived ^{111}In ($t_{1/2} = 67.9 \text{ h}$) is often the radioisotope of choice for the accurate assessment of biodistribution and clearance of injected agents. The derivatives of DTPA that are generally suitable for complexation of many trivalent metal-ions can have additional complexation abilities. An example is the DTPA-*bis*-(histidylamide) that was used to incorporate Gd in the DTPA core and $^{99\text{m}}\text{Tc}$ coordinated to the histidylamide side arms.⁹⁸ A high r_1 of this dual probe was obtained ($7.8 \text{ mM}^{-1} \text{ s}^{-1}$ at 128 MHz) as a result of reduced tumbling rate (τ_R) through DTPA-histidine conjugation.

Recently there has been an increasing interest of developing iron oxides with high T_1 effects for positive contrast at clinical magnetic field strengths. Rosales *et al.* used USPIO NPs functionalized dipicolylamine-alendronate (DPA-ale) and PEG-biphosphonates radiolabeled with $^{99\text{m}}\text{Tc}$.¹⁰⁵ These radiolabeled iron oxide NPs ($5.5 \pm 0.7 \text{ nm}$) showed a very high r_1 value ($9.5 \text{ mM}^{-1} \text{ s}^{-1}$ at 3 T), and additionally, promising SPECT properties due to the $^{99\text{m}}\text{Tc-DPA-ale}$ complex stably bound onto the particle surface.

T₂ MRI-PET and MRI-SPECT dual probes

High acceleration of T_2 relaxation rate can be achieved by susceptibility of the solid particles. The induced magnetic moment of these particles reduces the phase coherence of water molecules diffusing along the particle surface. This effect depends on the total number of paramagnetic ions per particle, e.g. $\text{Fe}_2\text{O}_3/\text{Fe}_3\text{O}_4$, Ln_2O_3 . Therefore, the r_2 increases with the increase of particle size. Majority of the reported T_2 MRI-PET probes are based on surface radiolabeling of solid particles possessing high T_2 relaxivities. The strategies include coating of the surface of various types of NPs with a silica layer, peptides, polymers, macrocyclic ligands, etc. High radiolabeling yield with metal radionuclides can then be achieved depending on the amount and properties of the chelates present on the surface of NPs. In a very recent work, Herranz *et al.* developed a one-step modular approach for multi-functionalization of different hydrophobic NPs.⁶ Bovine serum albumin (BSA) was used as a modular platform for the attachment of various functionalities in a parallel process onto the surface of the NP core for dual imaging purposes. Rosales *et al.* reported a strategy to prepare a MRI-PET probe by exploiting *bis*-dithiocarbamate (CS_2)-bisphosphonate (BP) to functionalize the dextran-coated SPIO NPs.¹⁰⁶ The BP-group was used to accomplish the attachment of the organic functionality to the surface of particles, while the CS_2 -group was responsible for the stable complexation of ^{64}Cu . The resultant probe had both PET signal and T_2 MRI enhancement ($r_2 = 34 \text{ s}^{-1} \text{ mM}^{-1}$) in addition to very good stability and no indications of any decomposition *in vivo*. Using a similar ligand, the strategy was also extended to other radioisotopes and radiolabeling of ferrites MnFe_2O_4 NPs, the 100% labelling yield could be easily achieved in a short time. The *in vivo* study demonstrated the potential of the radiolabeled NPs for dual MRI-PET imaging.¹⁰⁷ This strategy proved to be versatile to radiolabel many other metallic NPs, such as Ln_2O_3 , TiO_2 , CaCO_3 , Al_2O_3 , etc.¹⁰⁷

Besides acting as a platform for conjugation with radio-metal complexing chelates, NPs and, silica-based NPs in particular, can be exploited for encapsulation of optically active motifs. This approach was investigated by Kim *et al.* on magnetic silica particles that contained CoFe_2O_4 core for T_2 MRI and $^{68}\text{Ga(III)}$ -NOTA grafted on the surface.¹⁰⁸ The MRI-PET active particles were additionally used for cell tracking by near-infrared due to fluorescent dye encapsulated in the silica layer simultaneously (MRI-PET-OI triple

modality). Not surprisingly but importantly, the use of $^{68}\text{Ga(III)-NOTA}$ is extended to functionalize iron oxides NPs for MRI-PET dual imaging.¹⁰⁸⁻¹¹⁰

While the above-mentioned strategies are mainly based on the particular coordination chemistry and selection of the best chelate for sufficient *in vivo* stability, in a very recent report, Liu *et al.* demonstrated a novel efficient strategy for the synthesis of chelate-free ^{64}Cu labelled MoS_2 nanosheets for PET-MRI.¹¹¹ The iron oxides NPs were modified with meso-2,3-dimercaptosuccinic acid (DMSA) and self-assembled on the surface of atomically thin MoS_2 nanosheets, likely via sulfur chemistry occurring on the defect sites of MoS_2 . $^{64}\text{Cu(II)}$ -ions have high affinity to sulfur atoms and could anchor on the MoS_2 defect sites in the nanosheets.

Aime *et al.* reported a dual MRI-SPECT probe for the pH-mapping by using Gd(III) - and $^{166}\text{Ho(III)-DOTA-sulfonamide}$ derivatives exhibiting pH dependent relaxivities as a consequence of a change in hydration number.³⁸ Another interesting property of Ho is the highest magnetic moment, which can be used for T_2 MRI, and in this way a single metal itself, provides the bases for dual imaging. In our work we have investigated Ho-containing NPs ($\text{Ho}_2(\text{CO}_3)_3$, Ho_2O_3 , and $\text{Ho}_2\text{O}_2\text{SO}_4$) of different sizes and demonstrated linear increase of the r_2 relaxivities with increased magnetic field and particle size.³¹ Therefore, we have developed synthetic procedures for size-controlled synthesis of spherical Ln-NPs, including microwave-assistance and miniemulsion mediation (Chapter 6). A proper functionalization of the surface of Ho NPs with PEG and targeting vectors is under current research to endow the particles with the ability for local delivery for therapy monitored by MRI-SPECT.

Several excellent examples are based on the surface radiolabeling of USPIOs for MRI-SPECT. The ^{111}In labeled antimesothelin antibody mAbMB can be conjugated to surface of iron oxide NPs.¹¹² Such a design ensures the magnetic properties for T_2 MRI as well as the ability to localize the probe via SPECT, more specifically, in mesothelin-expressing tumors. The radiometal $^{99\text{m}}\text{Tc}$ has also been explored to radiolabel the USPIOs with a high labelling efficiency to detect and quantify the particles *in vivo*.¹¹³ In a recent example, Wang *et al.* deposited iron oxides on the surface of carbon nanotubes (CNTs), resulting in a very efficient T_2^* MRI probe.¹¹⁴ The NPs were then successfully radiolabeled with $^{99\text{m}}\text{Tc}$ through a functionalized BP, enabling the SPECT/CT imaging and γ -scintigraphy to quantitatively analyze the biodistribution of the hybrid materials in mice. The information the MRI properties of some selected probes are shown in Table 1.3.

Table 1.3. Selected examples of MRI-based dual probes.^a

Metals used	Strategy/Carrier	Dual(multi) modality	r_2 ($s^{-1} mM^{-1}$) ^a	r_1 ($s^{-1} mM^{-1}$) ^a	Ref.
Fe- ⁶⁸ Ga	Surface coating	MRI (T_2)-PET	203.4	3.2	6
Gd	Zeolite LTL	MRI T_1 - T_2	98.0	32	115
Gd	Hydrogel	MRI T_1 - T_2	177.5	72.3	86
Gd	Hydrogel	MRI T_1 - T_2	47.6-109.5	41.5-98.0	87
Gd-Eu	NPs	MRI T_1 - T_2	38.7	11.9	83
Gd-Mn	NPs	MRI T_1 - T_2	26.6	12.8	83
Fe-Gd	Core-shell	MRI T_1 - T_2	269.4	32.9	84
Fe-Gd	Nanoclusters	MRI T_1 - T_2	181.5	64.7	116
Fe-Gd	NPs	MRI T_1 - T_2	123-136	1.7-4.1	93
Fe	NPs	MRI T_1 - T_2	39.5	19.7	117
Fe-Mn	NPs	MRI T_1 - T_2	53.9-67.2	19.3-21.5	118
Fe-Eu	NPs	MRI T_1 - T_2	97.5	36.8	68
Gd- ⁶⁴ Cu	MSN	MRI (T_1)-PET	62.9	33.8	102
Gd- ⁶⁸ Ga	Complex	MRI (T_1)-PET	-	16.0	101
Gd- ⁶⁸ Ga	Complex	MRI (T_1)-PET	7.1	-	119
Fe- ⁶⁸ Ga	Ferrites-silica	MRI (T_2)-PET	297.0	-	108
Fe- ⁸⁹ Zr	Surface coating	MRI (T_2)-PET	203.4	3.2	6
Fe- ⁶⁴ Cu	NPs	MRI (T_2)-PET	34.0	-	106
Fe- ⁶⁴ Cu	NPs	MRI (T_2)-PET	92.6	-	111
Gd- ⁶⁸ Cu-Eu	NPs	MRI (T_1)-PET-OI	83.7	33.3	120
Gd- ^{67/68} Ga	Dendritic structure	MRI (T_1)-SPECT	-	16.0	99
Fe- ^{99m} Tc	NPs	MRI (T_1)-SPECT	28.2	9.5	121
Gd- ^{99m} Tc	Complexes	MRI (T_1)-SPECT	-	7.8-8.5	98
Fe- ^{99m} Tc	Ferrites	MRI (T_2)-SPECT	121.9	4.9	107
Fe- ^{99m} Tc	CNTs	MRI (T_2)-SPECT	325.0	-	114
Fe- ¹¹¹ In	NPs	MRI (T_2)-SPECT	469.6	0.6	112
Gd-UP	NPs/nanorods	MRI (T_1)-OI	-	4.6-6.0	122
Gd-UP	NPs	MRI(T_1)-OI	-	2.1	123
Gd-QD	NPs	MRI (T_1)-OI	26.5-36.1	11.5-15.8	124
Mn-QD	NPs	MRI (T_1)-OI	-	3.0	125
Gd-Eu	NPs	MRI (T_1)-OI	34.3	-	126
Gd-UP	Core/shell NPs	MRI (T_1)-OI	-	12.3	127
Gd-QD	NPs	MRI (T_1)-OI	-	8.5	128
Gd-Eu	NPs	MRI (T_1)-OI	7.8	6.1	129
Gd-Ag	NPs	MRI (T_1)-OI	-	29.0	130
Gd-Eu	NPs	MRI (T_1)-OI	4.8	2.6	131
Gd-Eu	Zeolite LTL	MRI (T_1)-OI	93.0	27	64
Gd-Eu	Nanorods	MRI (T_1)-OI	-	1.4	132
Gd-UP ^b	NPs	MRI (T_1)-OI	8.8	4.5	133

Gd-Tb	NPs	MRI (T_1)-OI	-	15.5	134
Fe-UP	NPs	MRI (T_2)-OI	28.7	-	135
Tb	Self-assembly	MRI (T_2)-OI	15		136
Dy-UP	NPs	MRI (T_2)-OI	438.0	0.3	137
Up-Up (Gd)	NPs	MRI-OI		2.9	138
Co-UP	NPs	MRI (T_2)-OI	1544.2	-	139
Gd-UP-Zn	Core-Shell	MRI (T_2)-OI-CT	19.3	0.8	140
Fe-Mo- ⁶⁴ Cu	Nanosheets	MRI (T_2)-OI-PAI	92.6	-	111

^a The conditions at which the relaxivities reported in this table are obtained can be found in the corresponding references; QD = quantum dots; “-” = not reported.

MRI COMBINED WITH OPTICAL IMAGING MODALITIES

MRI-OI has become one of the most well developed dual imaging modalities.^{18,141,142} In the past decade, there has been a significant development of MRI-OI dual probes in biomedical research and especially preclinical practice. Due to its high sensitivity the OI has been introduced as a second modality to compensate the low sensitivity of MRI, which on its turn simultaneously helped to overcome the low resolution of a single optical modality. A large amount of MRI-OI dual probes has been reported in the research on molecular imaging of biological events. Most of these probes are based on the conjugation between fluorescent organic dyes and MRI active CAs.²⁵ However, the excitation of Stokes-shifted fluorophores is usually in the UV or visible range, which have a limited light penetration depth and evoke strong imaging background creating artifacts.¹⁴³ Therefore, lanthanides are often used as alternatives due to their long excitation times and small linewidths (< 10 nm), which also enables the time-resolved imaging.^{18,21,27,141} Many promising studies have demonstrated the combination between various lanthanides with already existing Gd- or Fe-based MRI-probes for MRI-OI, which leads to higher quantum yields and reduced artifacts.

T₁ MRI-Optical dual probes

The metallic probes based on Gd(III) and Eu(III) represent a classical combination for MRI-Optical dual imaging. In very recent examples, the 2D ultrathin GdVO₄ nanosheet codoped with Eu(III) was synthesized by a facile solvothermal reaction, simultaneously providing the probe with fluorescent and paramagnetic properties.^{120,144} The hexagonal crystal Eu-doped GdPO₄ nanorods not only exhibited a higher enhancement of *in vivo* T_1 -weighted MR imaging, but also showed better luminescence imaging of living cells under

the fluorescence microscope.^{129,132} Gd(III) and Eu(III)-ions can be co-doped into zeolites and mesoporous silica NPs (MSNs).^{145,146} The resulting MSN with magnetism and fluorescence in the nanostructure could be used to T_1 MRI-optical dual imaging. Recently, we have demonstrated selective loading of Gd(III) and Eu(III)-ions into LTL into the well-defined framework of zeolite LTL with big and small cavities.⁶⁴ When Eu(III) ions were loaded into the small cavities, the luminescence quenching could be significantly reduced due to the limited access of water molecules (see Chapter 2). On the contrary, loading of Gd(III) into the big cages results in a very high r_1 relaxivity ($37.8 \text{ s}^{-1}\text{mM}^{-1}$ at 1.5 T) based on coordination of 6 water molecules ($q = 6$) and their efficient exchange with the bulk water via a prototropic mechanism.⁴⁶

A silica layer is used to encapsulate the CuInS₂/ZnS NPs in order to reduce the cytotoxicity, meanwhile, the Gd(III)-DTPA can be covalently grafted onto this silica layer.¹²⁸ The resultant nanocomposites have a good quantum yield (up to 7.8 %) and high r_1 value ($8.5 \text{ s}^{-1}\text{mM}^{-1}$ at 3 T), showing potential for biological *in vitro* and *in vivo* studies. Mesoporous Gd₂O₃ doped with Eu(III)-ions by facile wet-chemical route,¹⁴⁷ sub-10 nm monoclinic Gd₂O₃ co-doped with Eu(III) by laser ablation in liquids (LAL) technique,¹²⁶ and monoclinic/cubic Gd₂O₃ co-doped with Eu(III) by glycine-nitrate process¹³¹ are also representative endeavours of the combination between Gd and Eu for potential dual MRI-optical probes.

Variation of the concentration of the optical reporters within a dual probe can lead to optimization of fluorescence signal without compromise on magnetic properties. An example is doping of Gd₂O₃:Tb NPs with a fine-tuned fluorescence due to optimally chosen concentration of Tb.¹³⁴ In recent years, the upconversion nanoparticles (UCNPs) have been studied extensively as promising agents for optical imaging.^{23,148} Two strategies are dominating in the preparation of MRI-OI UCNP probes: 1) Gd(III)-based host lattice (e.g. NaGdF₄), doped with guest lanthanides such as Yb(III), Er(III), and/or Tm(III) to achieve efficient optical and MR imaging capability and 2) core/shell structures, fabricated with the optical core and Gd(III) as a shell-component for MRI. Thermolysis, hydrothermal and Ostwald-ripening are the most widely used methodologies to synthesize nicely shaped and monodispersed UCNPs for both strategies.

In any case, the presence of Ln-ions as guests in an appropriate inorganic host lattice is the key approach for fabrication of UCNPs. The dopants of long-lived lanthanides (e.g.

Eu(III) or Tb(III) are optically active centers in these unique structures, which produce emission when excited. UCNPs therefore convert two or more low-energy excitation photons (usually NIR) into shorter wavelength emissions (visible or UV).^{149,150} Thus, the selection of lanthanide dopants results in various optical properties, while incorporation of Gd(III)-ions into the host provides the multimodality to the UCNPs for MRI-OI. Many examples of this concept have been reported and demonstrated by both *in vitro* and *in vivo* studies, e.g. NaGdF₄:Tm/Er/Yb NPs, core/shell structures of NaGdF₄ layer on NaYF₄:Er/Yb cores, or NaGdF₄:Yb/Er. The performance in these probes could further be improved by attaching targeting groups.¹⁵¹⁻¹⁵³

Gd(III) is not the only metal-ion that can be co-doped to UCNPs for MRI purposes. Zhang and coworkers have demonstrated that sub-10 nm NaMnF₃:Yb/Er,Tm NPs have intense pure upconversion and showed very high r_1 up to 12.7 s⁻¹mM⁻¹ at 7 T, which is much higher than these of single Gd(III)- or Mn(II)-containing NPs due to careful optimization of paramagnetic centers.¹⁵⁴ Concerning optimal quantum yields for optical imaging, quantum dots (QDs) are among the most efficient materials. Interestingly, co-doped ZnSe QDs have shown a correlation between optical intensity with the concentration of added Mn(II), with quantum yield as high as 37% at 3.2% of Mn(II).¹²⁵ Together with the high r_1 relaxivity (11.5-15.8 s⁻¹mM⁻¹ at 1.5 T), this probe was reported as promising for T_1 MRI-OI. Some selected examples for MRI-OI purposes are included in Table 1.3.

T₂ MRI-Optical dual probes

Based on the core-shell strategy, the UCNPs are also combined with superparamagnetic iron oxides for T_2 MRI-OI dual function. Li *et al.* reported a step-wise synthesis of core-shell Fe₃O₄@NaLuF₄:Yb,Er/Tm nanostructure.¹⁵⁵ Due to the Fe₃O₄ cores, it exhibits superparamagnetic property with saturation magnetization of 15 emu g⁻¹, and T_2 -enhanced MR effect with an r_2 value of 21.63 s⁻¹mM⁻¹ at 0.5 T. However, one shortcoming of these particles is their relatively large diameter of about 330 nm. Another approach was implemented by Liu *et al.* for a multifunctional NaYF₄:Yb/Er@Fe₃O₄@Au core-shell prepared by a step-wise synthetic method, whereby the optical and magnetic properties are combined in the same particle.¹⁵⁶ The presence of Au on the surface of these UCNPs, provides this MRI-OI dual probe with an additional functionality for photothermal therapy.

Recently, the Co(II) co-doped NaYF₄:Yb/Tm NPs were reported to have a remarkable capability for high-performance in T_2 -MRI-optical dual imaging.¹³⁹ The probe exhibited extremely high r_2 value of 1544.2 s⁻¹mM⁻¹ at 0.5 T, even though the reasons for this high value were not explained by the authors. As a result, a minimum dosage of CA could be applied for contrast enhancement (1.6 µg mL⁻¹), cytotoxicity at this concentration could be considered negligible.

Assembly of Ln-chelates by means of nanoaggregates is an interesting approach to create combined T_2 MRI-optical contrast by a single metal-ion Tb(III) complexed with DOTA-chelate, which was then assembled into monodispersed micelles.¹³⁶ The r_2 values up to 15 s⁻¹ mM⁻¹ could be achieved at high magnetic fields (11.7 T, 37 °C). The water molecules coordinating to the Tb(III)-ion were in competition with the pendant arms of the ligand upon micelle formation, giving rise a very high quantum yield of 7.3% in water.

CONCLUSIONS AND FUTURE PERSPECTIVES

The development of multimodal imaging/therapeutic probes is a clear goal in modern diagnostics that will most probably keep the researchers at work for the next decades. The fast growing technology in the multimodal imaging and therapy opens new areas of research, allowing profound understanding of molecular events, detection and monitoring of diseases, and optimization of the follow-up therapy. The advantage of combination of complimentary imaging techniques such as high-resolution MRI with high-sensitivity nuclear or optical techniques is extensively demonstrated in the literature by many different approaches. The success rate in the development of novel multimodal probes in translational medicine will depend on the simplicity of the designed materials in combination with high biological safety and imaging/therapeutic performance.

Gd-based T_1 MRI probes have been studied extensively over the last 30 years. The theory of relaxivity and the importance of water-exchange phenomena are now understood and applied in the design of new CAs with better characteristics. However, it has been recognized that the strategies to enhance the T_1 relaxivity through alterations in coordination chemistry or water exchange and residence time are limited as in many cases they lead to a decreased stability of the paramagnetic complexes. From this point of view, nanosystems are promising to become efficient diagnostic probes with many possibilities to be combined with other imaging modalities of validation and quantification of the images

as well as co-delivery of drugs. Nanosystems have already been applied in T_2 MRI due to their ability to shorten transversal relaxation times in the liver, spleen, and bone marrow simply based on the passive uptake by reticuloendothelial system. Such an uptake mainly concerned SPIO and USPIO NPs, while bigger NPs (< 100 nm) are known to be accumulating in the tumors based on the EPR effect, typical for the leaky cancerous vasculature. Nowadays, a certain part of the scientific community is convinced of the uselessness of targeting vectors conjugated to NPs, as the targeting purpose can also be achieved by giving the main role to the EPR effect. Nevertheless, there is a tremendous amount of research studies demonstrating various targeting moieties, chosen to recognize specific receptors and ensure high accumulation at the target site in combination with different NPs. All these research efforts are currently being translated into multimodal probes that profit from the strength of each imaging technique. Additionally, design of the agents that can simultaneously deliver drugs to the diseased site and release it upon activation of either endogenous or exogenous trigger mechanisms is certainly a promising research direction.

Metals are invaluable for the above-mentioned strategies. The immense variety in physical properties of metals, including the existence of radioisotopes, can be exploited in nanochemistry and will lead to creation of novel multimodal probes even by a simple exchange of the functional metals within the existing probe.

OUTLINE OF THE THESIS

This thesis describes the development of multimodal probes for MRI-based medical imaging and therapy. MRI has a superb resolution among the imaging modalities, however, the low sensitivity is an inherent limitation. Several strategies, including exploitation of targeting vectors to deliver high-payloads of an MRI contrast agent to the site of interest have been addressed by the researchers in the recent years. *Chapter 1* focuses on the combination between MR and radionuclides and other imaging reporters in one nanocarrier, which acts as a multimodal imaging probe. As a result, the probes will be suitable for simultaneous imaging by MRI and other imaging techniques, such as PET, SPECT, and optical imaging that are well-known for their high sensitivity.

The following three chapters focus on the application of nanozeolite LTL as a platform for loading with metal-ions with various imaging abilities and describe physico-chemical

properties of these multimodal imaging probes. Recently, zeolite LTL has been a subject of several biological studies due to its biocompatibility and well-defined crystallinity. The interconnecting channels form cavities of various dimensions and the surface of these systems can be utilized for asymmetric functionalization. *Chapter 2* presents a novel strategy to selectively load Gd(III)- and Eu(III)-ions into the large and small cavities of nanozeolite LTL, respectively. This smart exploitation of the framework structure yields the highest relaxivity density ($13.7 \text{ s}^{-1}\text{Lg}^{-1}$ at 1.5 T and 25 °C) reported so far for aluminosilicates, and enhanced luminescence, rendering these materials promising candidates for the design of dual MRI-optical imaging probes.

In *Chapter 3*, the mechanisms governing the relaxivity of Gd-loaded nanozeolite LTL are further investigated. The ^1H and ^{17}O NMR studies reveal exceptionally high transversal (r_2) and longitudinal (r_1) relaxivities with the r_2/r_1 ratio between 2 and 5, convenient for MRI T_1 - T_2 dual probe. The prototropic exchange mechanism appeared to be governing the relaxivities, which furthermore turned out to be strongly pH dependent within the range of pH 4-9. The latter property can be seen as very interesting for the application of the designed materials for imaging of tumors, as the pH of cancerous tissue is known to be lower compared to the healthy one.

Surface chemistry of nanoprobe is an important aspect as it not only influences the imaging properties but also determines the biodistribution and *in vivo* behavior of the particles. For instance, of the common strategies to prolong the circulation time of the intravenously injected nanoprobe is conjugation of polyethylene glycol (PEG) chains on their surface. *Chapter 4* demonstrates how functionalization of the surface of Gd-loaded LTL zeolite affects the relaxivity and stability of the system. The conjugation was achieved by converting PEG molecules into PEG-silane, which was then successfully attached to the surface of the LTL particle. Increased PEG loading appeared to decrease the relaxivity, which could be explained by the limitations resulted from PEG layer on water exchange between the interior water molecules of LTL and that of bulk. The high pH responsiveness of Gd-loaded LTL was not affected after PEGylation. Additionally, the presence of PEG layer neutralizes the surface charge of Gd-loaded LTL, leading to interesting properties such as significantly reduced leakage of Gd-ions under physiological media, enhanced

interaction between LTL and cells, and stabilized longitudinal relaxivity at higher temperature as discussed in details.

Radiolabeling of MRI contrast agents has become a key strategy to multimodal imaging. A trace amount of radionuclides added to a CA allows the use of the extremely sensitive PET/SPECT technique to detect and quantify the MRI CAs. This strategy leads to multifunctional MRI-PET/SPECT probes and opens the possibility to assess many physiological parameters, such as pH, metabolic rates and receptor densities. As a preliminary study, *Chapter 5* presents chelate-free radiolabeling of LTL nanoparticles with two PET tracers ^{64}Cu and ^{89}Zr . The successful radiolabeling of LTL with ^{64}Cu is achieved by simple ionic exchange with Na^+ , whereas using ^{89}Zr results in coordination between ^{89}Zr and O of the LTL framework. The labeling mechanism determines the stability of the samples in terms of radionuclide leakage in physiological media. The Gd-loaded LTL radiolabeled by ^{64}Cu or ^{89}Zr has potential for MRI-PET dual imaging.

The size and morphology of the NPs are another two important aspects that determine the biodistribution, circulation, excretion, and cytotoxicity. Lanthanide based nanoparticles are under intensive scrutiny by the researchers in the field of bioimaging due to their versatile physical properties, which depend on the type of lanthanide as well as the size of the NPs, for example, the r_2 value is linearly dependent on the size. Among various procedures for the preparation of Ln-based NPs reported in the literature, a gap exists in the range between 5 and 40 nm. *Chapter 6* reports on a facile miniemulsion technique to synthesize the spherical Ln-containing NPs intended to fill this discontinuity. The choice of the surfactant determines the final elemental composition of the particles, leading to either lanthanide oxides or oxysulfates when using Brij® 35 or sodium dodecyl sulfate, respectively. Holmium and gadolinium NPs were prepared and their applicability as MRI CAs is demonstrated. The miniemulsion method can be predictably expanded to other lanthanides, as these elements are chemically equivalent, whereas the great variety of physical and radiochemical properties can be exploited in other imaging techniques and even be interesting for other research field, e.g. catalysis.

The latter potential is demonstrated in *Chapter 7*, which focuses on the investigation of redox properties of Ln-oxysulfate nanoparticles. The lanthanide oxysulfates are known for their large-volume oxygen storage/release capability, which could further be increased by application of this material in nanoparticulate dimensions. The nanosized $\text{Pr}_2\text{O}_2\text{SO}_4$

particles synthesized by the miniemulsion method using sodium dodecyl sulfate as a surfactant, doped with Ni have shown higher activity in oxygen storage/release, in comparison with bulk materials.

References

- (1) Waerzeggers, Y.; Monfared, P.; Ullrich, R.; Viel, T.; Jacobs, A. H.; World Scientific Publishing Co. Pte. Ltd.: 2012, p 319-382.
- (2) Santos Ribeiro, A.; Rota Kops, E.; Herzog, H.; Almeida, P.; *Nucl. Instrum. Methods Phys. Res., Sect. A* **2014**, *734*, 166-170.
- (3) Mansi, L.; *J. Nucl. Med.* **2014**, *55*, 529-530.
- (4) Hu, Z.; Yang, W.; Liu, H.; Wang, K.; Bao, C.; Song, T.; Wang, J.; Tian, J.; *Mol. Pharmaceutics* **2014**, *11*, 3798-3809.
- (5) Locatelli, E.; Gil, L.; Israel, L. L.; Passoni, L.; Naddaka, M.; Pucci, A.; Reese, T.; Gomez-Vallejo, V.; Milani, P.; Matteoli, M.; Llop, J.; Lellouche, J. P.; Franchini, M. C.; *Int. J. Nanomed.* **2012**, *7*, 6021-6033.
- (6) Groult, H.; Ruiz-Cabello, J.; Pellico, J.; Lechuga-Vieco, A. V.; Bhavesh, R.; Zamai, M.; Almarza, E.; Martin-Padura, I.; Cantelar, E.; Martinez-Alcazar, M. P.; Herranz, F.; *Bioconjugate Chem.* **2015**, *26*, 153-160.
- (7) Weissleder, R.; Pittet, M. J.; *Nature* **2008**, *452*, 580-589.
- (8) Schroeder, L.; Faber, C.; *Methods Mol. Biol. (NY, U. S.)* **2011**, *771*, 45-67.
- (9) Terreno, E.; Castelli, D. D.; Viale, A.; Aime, S.; *Chem. Rev.* **2010**, *110*, 3019-3042.
- (10) Pierre, V. C.; Allen, M. J.; Caravan, P.; *JBIC, J. Biol. Inorg. Chem.* **2014**, *19*, 127-131.
- (11) Lee, S. Y.; Jeon, S. I.; Jung, S.; Chung, I. J.; Ahn, C.-H.; *Adv. Drug Del. Rev.* **2014**, *76*, 60-78.
- (12) Lin, M.; Wong, C.; Lin, P.; Shon, I. H.; Cuganesan, R.; Som, S.; *Hematol. Oncol.* **2011**, *29*, 67-74.
- (13) Nappi, C.; Altiero, M.; Imbriaco, M.; Nicolai, E.; Giudice, C. A.; Aiello, M.; Diomiaiuti, C. T.; Pisani, A.; Spinelli, L.; Cuocolo, A.; *Eur. J. Nucl. Med. Mol. Imaging* **2015**, *42*, 1025-1031.
- (14) Einspieler, I.; Thuermel, K.; Pyka, T.; Eiber, M.; Wolfram, S.; Moog, P.; Reeps, C.; Essler, M.; *Eur. J. Nucl. Med. Mol. Imaging* **2015**, *42*, 1012-1024.
- (15) Carpenter, T. A.; Ansorge, R.; *eMagRes* **2014**, *3*, 75-86.
- (16) de Rosales, R. T. M.; *J. Labelled Compd. Radiopharm.* **2014**, *57*, 298-303.
- (17) Huang, W.-Y.; Davis, J. J.; *Dalton Trans.* **2011**, *40*, 6087-6103.
- (18) Verwilt, P.; Park, S.; Yoon, B.; Kim, J. S.; *Chem. Soc. Rev.* **2015**, *44*, 1791-1806.
- (19) Price, E. W.; Orvig, C.; *Chem. Soc. Rev.* **2014**, *43*, 260-290.
- (20) Gallo, J.; Long, N. J.; Aboagye, E. O.; *Chem. Soc. Rev.* **2013**, *42*, 7816-7833.
- (21) Amoroso, A. J.; Pope, S. J. A.; *Chem. Soc. Rev.* **2015**, *44*, 4723-4742.
- (22) Heffern, M. C.; Matosziuk, L. M.; Meade, T. J.; *Chem. Rev.* **2013**, *114*, 4496-4539.

- (23) Chen, G.; Qiu, H.; Prasad, P. N.; Chen, X.; *Chem. Rev.* **2014**, *114*, 5161-5214.
- (24) Ramogida, C. F.; Orvig, C.; *Chem. Commun.* **2013**, *49*, 4720-4739.
- (25) Jennings, L. E.; Long, N. J.; *Chem. Commun.* **2009**, 3511-3524.
- (26) Eliseeva, S. V.; Bunzli, J.-C. G.; *Chem. Soc. Rev.* **2010**, *39*, 189-227.
- (27) Bünzli, J.-C. G.; *Chem. Rev.* **2010**, *110*, 2729-2755.
- (28) Kotek, J.; Kubiček, V.; Hermann, P.; Lukeš, I. In *The Chemistry of Contrast Agents in Medical Magnetic Resonance Imaging*; John Wiley & Sons, Ltd: 2013, p 83-155.
- (29) Fries, P. H.; Belorizky, E. In *The Chemistry of Contrast Agents in Medical Magnetic Resonance Imaging*; John Wiley & Sons, Ltd: 2013, p 277-309.
- (30) Norek, M.; Peters, J. A.; *Prog. Nucl. Magn. Reson. Spectrosc.* **2011**, *59*, 64-82.
- (31) Mayer, F.; Peters, J. A.; Djanashvili, K.; *Chem. Eur. J.* **2012**, *18*, 8004-8007.
- (32) Parker, D.; Dickins, R. S.; Puschmann, H.; Crossland, C.; Howard, J. A. K.; *Chem. Rev.* **2002**, *102*, 1977-2010.
- (33) Bulman, R. A.; *Met. Ions Biol. Syst.* **2003**, *40*, 683-706.
- (34) Brücher, E. o.; Tircsó, G.; Baranyai, Z.; Kovács, Z.; Sherry, A. D. In *The Chemistry of Contrast Agents in Medical Magnetic Resonance Imaging*; John Wiley & Sons, Ltd: 2013, p 157-208.
- (35) Geraldès, C. F. G. C.; Laurent, S.; *Contrast Media & Molecular Imaging* **2009**, *4*, 1-23.
- (36) Kanal, E.; Tweedle, M. F.; *Radiology* **2015**, *275*, 630-634.
- (37) Kueny-Stotz, M.; Garofalo, A.; Felder-Flesch, D.; *Eur. J. Inorg. Chem.* **2012**, *2012*, 1987-2005.
- (38) Gianolio, E.; Maciocco, L.; Imperio, D.; Giovenzana, G. B.; Simonelli, F.; Abbas, K.; Bisi, G.; Aime, S.; *Chem. Commun.* **2011**, *47*, 1539-1541.
- (39) Nijsen, J. F. W.; Zonnenberg, B. A.; Woittiez, J. R. W.; Rook, D. W.; Swildens-van Woudenberg, I. A.; van Rijk, P. P.; van het Schip, A. D.; *Eur. J. Nucl. Med.* **1999**, *26*, 699-704.
- (40) Hoffman, D.; Sun, M.; Yang, L.; McDonagh, P. R.; Corwin, F.; Sundaresan, G.; Wang, L.; Vijayaragavan, V.; Thadigiri, C.; Lamichhane, N.; Zweit, J.; *Am. J. Nucl. Med. Mol. Imaging* **2014**, *4*, 548-560.
- (41) Topping, G. J.; Schaffer, P.; Hoehr, C.; Ruth, T. J.; Sossi, V.; *Med. Phys.* **2013**, *40*, 042502/042501-042502/042508.
- (42) Mi, P.; Dewi, N.; Yanagie, H.; Kokuryo, D.; Suzuki, M.; Sakurai, Y.; Li, Y.; Aoki, I.; Ono, K.; Takahashi, H.; Cabral, H.; Nishiyama, N.; Kataoka, K.; *ACS Nano* **2015**.
- (43) Caravan, P.; Ellison, J. J.; McMurry, T. J.; Lauffer, R. B.; *Chem. Rev.* **1999**, *99*, 2293-2352.
- (44) Helm, L.; *Prog. Nucl. Magn. Reson. Spectrosc.* **2006**, *49*, 45-64.
- (45) Swift, T. J.; Connick, R. E.; *J. Chem. Phys.* **1962**, *37*, 307-320.

- (46) Leigh Jr, J. S.; *J. Magn. Reson. (1969)* **1971**, *4*, 308-311.
- (47) McLaughlin, A. C.; Leigh Jr, J. S.; *J. Magn. Reson. (1969)* **1973**, *9*, 296-304.
- (48) Bridot, J.-L.; Faure, A.-C.; Laurent, S.; Rivière, C.; Billotey, C.; Hiba, B.; Janier, M.; Jossierand, V.; Coll, J.-L.; Vander Elst, L.; Muller, R.; Roux, S.; Perriat, P.; Tillement, O.; *J. Am. Chem. Soc.* **2007**, *129*, 5076-5084.
- (49) Botta, M.; Tei, L.; *Eur. J. Inorg. Chem.* **2012**, *2012*, 1945-1960.
- (50) Aime, S.; Barge, A.; Bruce, J. I.; Botta, M.; Howard, J. A. K.; Moloney, J. M.; Parker, D.; de Sousa, A. S.; Woods, M.; *J. Am. Chem. Soc.* **1999**, *121*, 5762-5771.
- (51) Peters, J. A.; Djanashvili, K.; *Eur. J. Inorg. Chem.* **2012**, *2012*, 1961-1974.
- (52) Zhang, W.; Peters, J. A.; Mayer, F.; Helm, L.; Djanashvili, K.; *J. Phys. Chem. C* **2015**, *119*, 5080-5089.
- (53) Weishaupt, D.; Köchli, V. D.; Marincek, B. *How does MRI work? An Introduction to the Physics and Function of Magnetic Resonance Imaging*; 1st English Edn. ed.; Springer, 2003.
- (54) Davies, G.-L.; Kramberger, I.; Davis, J. J.; *Chem. Commun.* **2013**, *49*, 9704-9721.
- (55) Kim, T. J.; Chae, K. S.; Chang, Y.; Lee, G. H.; *Curr. Top. Med. Chem.* **2013**, *13*, 422-433.
- (56) Hu, F.; Zhao, Y. S.; *Nanoscale* **2012**, *4*, 6235-6243.
- (57) Langereis, S.; Geelen, T.; Gruell, H.; Strijkers, G. J.; Nicolay, K.; *NMR Biomed.* **2013**, *26*, 728-744.
- (58) Shi, S.; Chen, F.; Ehlerding, E. B.; Cai, W.; *Bioconjugate Chem.* **2014**, *25*, 1609-1619.
- (59) Davis, J. J.; Huang, W.-Y.; Davies, G.-L.; *J. Mater. Chem.* **2012**, *22*, 22848-22850.
- (60) Wang, J. T.-W.; Cabana, L.; Bourgognon, M.; Kafa, H.; Protti, A.; Venner, K.; Shah, A. M.; Sosabowski, J. K.; Mather, S. J.; Roig, A.; Ke, X.; Van Tendeloo, G.; de Rosales, R. T. M.; Tobias, G.; Al-Jamal, K. T.; *Adv. Funct. Mater.* **2014**, *24*, 1880-1894.
- (61) Chen, G.; Yang, C.; Prasad, P. N.; *Acc. Chem. Res.* **2013**, *46*, 1474-1486.
- (62) Kattel, K.; Park, J. Y.; Xu, W.; Kim, H. G.; Lee, E. J.; Bony, B. A.; Heo, W. C.; Lee, J. J.; Jin, S.; Baeck, J. S.; Chang, Y.; Kim, T. J.; Bae, J. E.; Chae, K. S.; Lee, G. H.; *ACS Appl. Mater. Inter.* **2011**, *3*, 3325-3334.
- (63) Faucher, L.; Tremblay, M.; Lagueux, J.; Gossuin, Y.; Fortin, M.-A.; *ACS Appl. Mater. Inter.* **2012**, *4*, 4506-4515.
- (64) Mayer, F.; Zhang, W.; Brichart, T.; Tillement, O.; Bonnet, C. S.; Tóth, É.; Peters, J. A.; Djanashvili, K.; *Chem. Eur. J.* **2014**, *20*, 3358-3364.
- (65) Jun, Y.-w.; Huh, Y.-M.; Choi, J.-s.; Lee, J.-H.; Song, H.-T.; KimKim; Yoon, S.; Kim, K.-S.; Shin, J.-S.; Suh, J.-S.; Cheon, J.; *J. Am. Chem. Soc.* **2005**, *127*, 5732-5733.
- (66) Norek, M.; Kampert, E.; Zeitler, U.; Peters, J. A.; *J. Am. Chem. Soc.* **2008**, *130*, 5335-5340.

- (67) Huang, G.; Li, H.; Chen, J.; Zhao, Z.; Yang, L.; Chi, X.; Chen, Z.; Wang, X.; Gao, J.; *Nanoscale* **2014**, *6*, 10404-10412.
- (68) Yang, L.; Zhou, Z.; Liu, H.; Wu, C.; Zhang, H.; Huang, G.; Ai, H.; Gao, J.; *Nanoscale* **2015**, *7*, 6843-6850.
- (69) Soo Choi, H.; Liu, W.; Misra, P.; Tanaka, E.; Zimmer, J. P.; Itty Ipe, B.; Bawendi, M. G.; Frangioni, J. V.; *Nat Biotech* **2007**, *25*, 1165-1170.
- (70) Xie, J.; Chen, K.; Lee, H.-Y.; Xu, C.; Hsu, A. R.; Peng, S.; Chen, X.; Sun, S.; *J. Am. Chem. Soc.* **2008**, *130*, 7542-7543.
- (71) Huang, J.; Bu, L.; Xie, J.; Chen, K.; Cheng, Z.; Li, X.; Chen, X.; *ACS Nano* **2010**, *4*, 7151-7160.
- (72) Toy, R.; Peiris, P. M.; Ghaghada, K. B.; Karathanasis, E.; *Nanomedicine* **2013**, *9*, 121-134.
- (73) Doshi, N.; Prabhakarandian, B.; Rea-Ramsey, A.; Pant, K.; Sundaram, S.; Mitragotri, S.; *J. Controlled Release* **2010**, *146*, 196-200.
- (74) Kihara, T.; Zhang, Y.; Hu, Y.; Mao, Q.; Tang, Y.; Miyake, J.; *J. Biosci. Bioeng.* **2011**, *111*, 725-730.
- (75) Soenen, S. J.; Parak, W. J.; Rejman, J.; Manshian, B.; *Chem. Rev.* **2015**, *115*, 2109-2135.
- (76) Troughton, J. S.; Greenfield, M. T.; Greenwood, J. M.; Dumas, S.; Wiethoff, A. J.; Wang, J.; Spiller, M.; McMurry, T. J.; Caravan, P.; *Inorg. Chem.* **2004**, *43*, 6313-6323.
- (77) Caravan, P.; Gale, E. M.; Loving, G. S.; Mukherjee, S.; Zhu, J.; The General Hospital Corporation, USA . 2014, p 122pp.
- (78) Wu, C.; Li, D.; Yang, L.; Lin, B.; Zhang, H.; Xu, Y.; Cheng, Z.; Xia, C.; Gong, Q.; Song, B.; Ai, H.; *J. Mater. Chem. B* **2015**, *8*, 1639-1645.
- (79) Niu, D.; Luo, X.; Li, Y.; Liu, X.; Wang, X.; Shi, J.; *ACS Appl. Mater. Inter.* **2013**, *5*, 9942-9948.
- (80) Erathodiyil, N.; Ying, J. Y.; *Acc. Chem. Res.* **2011**, *44*, 925-935.
- (81) Tsotsalas, M.; Busby, M.; Gianolio, E.; Aime, S.; De Cola, L.; *Chem. Mater.* **2008**, *20*, 5888-5893.
- (82) Shin, T.-H.; Choi, J.-s.; Yun, S.; Kim, I.-S.; Song, H.-T.; Kim, Y.; Park, K. I.; Cheon, J.; *ACS Nano* **2014**, *8*, 3393-3401.
- (83) Xu, W.; Park, J. Y.; Kattel, K.; Bony, B. A.; Heo, W. C.; Jin, S.; Park, J. W.; Chang, Y.; Do, J. Y.; Chae, K. S.; Kim, T. J.; Park, J. A.; Kwak, Y. W.; Lee, G. H.; *New J. Chem.* **2012**, *36*, 2361-2367.
- (84) Yang, M.; Gao, L.; Liu, K.; Luo, C.; Wang, Y.; Yu, L.; Peng, H.; Zhang, W.; *Talanta* **2015**, *131*, 661-665.

- (85) Im, G. H.; Kim, S. M.; Lee, D.-G.; Lee, W. J.; Lee, J. H.; Lee, I. S.; *Biomaterials* **2013**, *34*, 2069-2076.
- (86) Courant, T.; Roullin, V. G.; Cadiou, C.; Callewaert, M.; Andry, M. C.; Portefaix, C.; Hoeffel, C.; de Goltstein, M. C.; Port, M.; Laurent, S.; Elst, L. V.; Muller, R.; Molinari, M.; Chuburu, F.; *Angew. Chem. Int. Ed.* **2012**, *51*, 9119-9122.
- (87) Callewaert, M.; Roullin, V. G.; Cadiou, C.; Millart, E.; Van Gulik, L.; Andry, M. C.; Portefaix, C.; Hoeffel, C.; Laurent, S.; Elst, L. V.; Muller, R.; Molinari, M.; Chuburu, F.; *J. Mater. Chem. B* **2014**, *2*, 6397-6405.
- (88) Wartenberg, N.; Fries, P.; Raccurt, O.; Guillermo, A.; Imbert, D.; Mazzanti, M.; *Chem. Eur. J.* **2013**, *19*, 6980-6983.
- (89) Sook Choi, E.; Young Park, J.; Ju Baek, M.; Xu, W.; Kattel, K.; Hyun Kim, J.; Jun Lee, J.; Chang, Y.; Jeong Kim, T.; Eun Bae, J.; Seok Chae, K.; Jin Suh, K.; Ho Lee, G.; *Eur. J. Inorg. Chem.* **2010**, *2010*, 4555-4560.
- (90) Zhou, Z.; Zhao, Z.; Zhang, H.; Wang, Z.; Chen, X.; Wang, R.; Chen, Z.; Gao, J.; *ACS Nano* **2014**, *8*, 7976-7985.
- (91) Huang, C.-C.; Tsai, C.-Y.; Sheu, H.-S.; Chuang, K.-Y.; Su, C.-H.; Jeng, U. S.; Cheng, F.-Y.; Su, C.-H.; Lei, H.-Y.; Yeh, C.-S.; *ACS Nano* **2011**, *5*, 3905-3916.
- (92) Wang, Z.; Liu, J.; Li, T.; Liu, J.; Wang, B.; *J. Mater. Chem. B* **2014**, *2*, 4748-4753.
- (93) Cheng, K.; Yang, M.; Zhang, R.; Qin, C.; Su, X.; Cheng, Z.; *ACS Nano* **2014**, *8*, 9884-9896.
- (94) Misri, R.; Saatchi, K.; Haefeli, U. O.; *Nanomedicine (London, U. K.)* **2012**, *7*, 719-733.
- (95) McQuade, P.; McCarthy, D. W.; Welch, M. J.; Springer-Verlag London Ltd.: 2003, p 251-264.
- (96) Uppal, R.; Ciesiensi, K. L.; Chonde, D. B.; Loving, G. S.; Caravan, P.; *J. Am. Chem. Soc.* **2012**, *134*, 10799-10802.
- (97) Uppal, R.; Catana, C.; Ay, I.; Benner, T.; Sorensen, A. G.; Caravan, P.; *Radiology* **2011**, *258*, 812-820.
- (98) Park, J.-A.; Kim, J. Y.; Kim, H.-K.; Lee, W.; Lim, S. M.; Chang, Y.; Kim, T.-J.; Kim, K. M.; *ACS Med. Chem. Lett.* **2012**, *3*, 299-302.
- (99) Kumar, A.; Zhang, S.; Hao, G.; Hassan, G.; Ramezani, S.; Sagiyama, K.; Lo, S.-T.; Takahashi, M.; Sherry, A. D.; Öz, O. K.; Kovacs, Z.; Sun, X.; *Bioconjugate Chem.* **2015**, *26*, 549-558.
- (100) Stasiuk, G. J.; Long, N. J.; *Chem. Commun.* **2013**, *49*, 2732-2746.
- (101) Vologdin, N.; Rolla, G. A.; Botta, M.; Tei, L.; *Org. Biomol. Chem.* **2013**, *11*, 1683-1690.

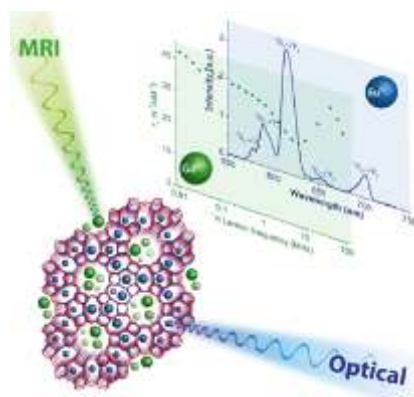
- (102) Laprise-Pelletier, M.; Bridot, J. L.; Guillet-Nicolas, R.; Lagueux, J.; Kleitz, F.; Fortin, M. A.; CRC Press: 2013; Vol. 3, p 20-23.
- (103) Suchy, M.; Bartha, R.; Hudson, R. H. E.; *RSC Adv.* **2013**, *3*, 3249-3259.
- (104) Kryza, D.; Taleb, J.; Janier, M.; Marmuse, L.; Miladi, I.; Bonazza, P.; Louis, C.; Perriat, P.; Roux, S.; Tillement, O.; Billotey, C.; *Bioconjugate Chem.* **2011**, *22*, 1145-1152.
- (105) Sandiford, L.; Phinikaridou, A.; Protti, A.; Meszaros, L. K.; Cui, X.; Yan, Y.; Frodsham, G.; Williamson, P. A.; Gaddum, N.; Botnar, R. M.; Blower, P. J.; Green, M. A.; de Rosales, R. T. M.; *ACS Nano* **2013**, *7*, 500-512.
- (106) Torres Martin de Rosales, R.; Tavaré, R.; Paul, R. L.; Jauregui-Osoro, M.; Protti, A.; Glaria, A.; Varma, G.; Szanda, I.; Blower, P. J.; *Angew. Chem. Int. Ed.* **2011**, *50*, 5509-5513.
- (107) Cui, X.; Belo, S.; Kruger, D.; Yan, Y.; de Rosales, R. T. M.; Jauregui-Osoro, M.; Ye, H.; Su, S.; Mathe, D.; Kovacs, N.; Horvath, I.; Semjani, M.; Sunassee, K.; Szigeti, K.; Green, M. A.; Blower, P. J.; *Biomaterials* **2014**, *35*, 5840-5846.
- (108) Kim, J. S.; Kim, Y.-H.; Kim, J. H.; Kang, K. W.; Tae, E. L.; Youn, H.; Kim, D.; Kim, S.-K.; Kwon, J.-T.; Cho, M.-H.; Lee, Y.-S.; Jeong, J. M.; Chung, J.-K.; Lee, D. S.; *Nanomedicine (London, U. K.)* **2012**, *7*, 219-229.
- (109) Kim, S.-m.; Chae, M. K.; Yim, M. S.; Jeong, I. H.; Cho, J.; Lee, C.; Ryu, E. K.; *Biomaterials* **2013**, *34*, 8114-8121.
- (110) Madru, R.; Tran, T. A.; Axelsson, J.; Ingvar, C.; Bibic, A.; Staahlberg, F.; Knutsson, L.; Strand, S.-E.; *Am. J. Nucl. Med. Mol. Imaging* **2014**, *4*, 60-69.
- (111) Liu, T.; Shi, S.; Liang, C.; Shen, S.; Cheng, L.; Wang, C.; Song, X.; Goel, S.; Barnhart, T. E.; Cai, W.; Liu, Z.; *ACS Nano* **2015**, *9*, 950-960.
- (112) Misri, R.; Meier, D.; Yung, A. C.; Kozlowski, P.; Hafeli, U. O.; *Nanomedicine (New York, NY, U. S.)* **2012**, *8*, 1007-1016.
- (113) Tsai, C.-S.; Liu, W.-C.; Chen, H.-Y.; Hsu, W.-C.; *Appl. Mech. Mater.* **2014**, *459*, 51-59.
- (114) Wang, J. T.-W.; Cabana, L.; Bourgognon, M.; Kafa, H.; Protti, A.; Venner, K.; Shah, A. M.; Sosabowski, J. K.; Mather, S. J.; Roig, A.; Ke, X.; Van Tendeloo, G.; de Rosales, R. T. M.; Tobias, G.; Al-Jamal, K. T.; *Adv. Funct. Mater.* **2014**, *24*, 1880-1894.
- (115) Zhang, W.; Peters, J. A.; Mayer, F.; Helm, L.; Djanashvili, K.; *J. Phys. Chem. C* **2014**, *119*, 5080-5089.
- (116) Wang, X.; Zhou, Z.; Wang, Z.; Xue, Y.; Zeng, Y.; Gao, J.; Zhu, L.; Zhang, X.; Liu, G.; Chen, X.; *Nanoscale* **2013**, *5*, 8098-8104.
- (117) Hu, F.; Jia, Q.; Li, Y.; Gao, M.; *Nanotechnology* **2011**, *22*, 245604.
- (118) Wang, L.; Wu, Q.; Tang, S.; Zeng, J.; Qiao, R.; Zhao, P.; Zhang, Y.; Hu, F.; Gao, M.; *RSC Adv.* **2013**, *3*, 23454-23460.

- (119) Notni, J.; Hermann, P.; Dregely, I.; Wester, H.-J.; *Chem. Eur. J.* **2013**, *19*, 12602-12606.
- (120) Hu, H.; Li, D.; Liu, S.; Wang, M.; Moats, R.; Conti, P. S.; Li, Z.; *Biomaterials* **2014**, *35*, 8649-8658.
- (121) Sandiford, L.; Phinikaridou, A.; Protti, A.; Meszaros, L. K.; Cui, X.; Yan, Y.; Frodsham, G.; Williamson, P. A.; Gaddum, N.; Botnar, R. M.; Blower, P. J.; Green, M. A.; de Rosales, R. T. M.; *ACS Nano* **2012**, *7*, 500-512.
- (122) Tian, Y.; Yang, H.-Y.; Yu, S.; Li, X.; *ChemPlusChem* **2014**, *79*, 1584-1589.
- (123) Sun, L.; Ge, X.; Liu, J.; Qiu, Y.; Wei, Z.; Tian, B.; Shi, L.; *Nanoscale* **2014**, *6*, 13242-13252.
- (124) Guo, W.; Yang, W.; Wang, Y.; Sun, X.; Liu, Z.; Zhang, B.; Chang, J.; Chen, X.; *Nano Res.* **2014**, *7*, 1581-1591.
- (125) Sharma, V. K.; Gokyar, S.; Kelestemur, Y.; Erdem, T.; Unal, E.; Demir, H. V.; *Small* **2014**, *10*, 4961-4966.
- (126) Liu, J.; Tian, X.; Luo, N.; Yang, C.; Xiao, J.; Shao, Y.; Chen, X.; Yang, G.; Chen, D.; Li, L.; *Langmuir* **2014**, *30*, 13005-13013.
- (127) Liu, J.; Bu, J.; Bu, W.; Zhang, S.; Pan, L.; Fan, W.; Chen, F.; Zhou, L.; Peng, W.; Zhao, K.; Du, J.; Shi, J.; *Angew. Chem., Int. Ed.* **2014**, *53*, 4551-4555.
- (128) Lin, B.; Yao, X.; Zhu, Y.; Shen, J.; Yang, X.; Li, C.; *RSC Adv.* **2014**, *4*, 20641-20648.
- (129) Li, Y.; Chen, T.; Tan, W.; Talham, D. R.; *Langmuir* **2014**, *30*, 5873-5879.
- (130) Li, J.; You, J.; Dai, Y.; Shi, M.; Han, C.; Xu, K.; *Anal. Chem.* **2014**, *86*, 11306-11311.
- (131) Goglio, G.; Kaur, G.; Pinho, S. L. C.; Penin, N.; Blandino, A.; Geraldies, C. F. G. C.; Garcia, A.; Delville, M.-H.; *Eur. J. Inorg. Chem.* **2014**, *2015*, 1243-1253.
- (132) Du, Q.; Huang, Z.; Wu, Z.; Meng, X.; Yin, G.; Gao, F.; Wang, L.; *Dalton Trans.* **2015**, *44*, 3934-3940.
- (133) Zhang, L. e.; Zeng, L.; Pan, Y.; Luo, S.; Ren, W.; Gong, A.; Ma, X.; Liang, H.; Lu, G.; Wu, A.; *Biomaterials* **2015**, *44*, 82-90.
- (134) Chen, F.; Chen, M.; Yang, C.; Liu, J.; Luo, N.; Yang, G.; Chen, D.; Li, L.; *Phys. Chem. Chem. Phys.* **2015**, *17*, 1189-1196.
- (135) Liu, B.; Li, C.; Ma, P. a.; Chen, Y.; Zhang, Y.; Hou, Z.; Huang, S.; Lin, J.; *Nanoscale* **2015**, *7*, 1839-1848.
- (136) Harris, M.; Carron, S.; Vander Elst, L.; Laurent, S.; Muller, R. N.; Parac-Vogt, T. N.; *Chem. Commun.* **2015**, *51*, 2984-2986.
- (137) Zhang, Y.; Das, G. K.; Vijayaragavan, V.; Xu, Q. C.; Padmanabhan, P.; Bhakoo, K. K.; Tamil Selvan, S.; Tan, T. T. Y.; *Nanoscale* **2014**, *6*, 12609-12617.

- (138) Yang, C.; Liu, Q.; He, D.; Na, N.; Zhao, Y.; Ouyang, J.; *Analyst (Cambridge, U. K.)* **2014**, *139*, 6414-6420.
- (139) Xia, A.; Zhang, X.; Zhang, J.; Deng, Y.; Chen, Q.; Wu, S.; Huang, X.; Shen, J.; *Biomaterials* **2014**, *35*, 9167-9176.
- (140) Lv, R.; Yang, P.; He, F.; Gai, S.; Li, C.; Dai, Y.; Yang, G.; Lin, J.; *ACS Nano* **2015**, *9*, 1630-1647.
- (141) Chan, W. T. K.; Wong, W.-T.; *Polyhedron* **2014**, *33*, 150-158.
- (142) Pan, D.; Caruthers, S. D.; Chen, J.; Winter, P. M.; SenPan, A.; Schmieder, A. H.; Wickline, S. A.; Lanza, G. M.; *Future Med. Chem.* **2010**, *2*, 471-490.
- (143) Xu, C. T.; Axelsson, J.; Andersson-Engels, S.; *Appl. Phys. Lett.* **2009**, *94*, 251107.
- (144) Kim, T.; Lee, N.; Park, Y. I.; Kim, J.; Kim, J.; Lee, E. Y.; Yi, M.; Kim, B.-G.; Hyeon, T.; Yu, T.; Na, H. B.; *RSC Adv.* **2014**, *4*, 45687-45695.
- (145) Chan, M.-H.; Lin, H.-M.; *Biomaterials* **2015**, *36*, 149-158.
- (146) Tse, N. M. K.; Kennedy, D. F.; Kirby, N.; Moffat, B. A.; Muir, B. W.; Caruso, R. A.; Drummond, C. J.; *Adv. Healthc. Mater.* **2013**, *2*, 836-845.
- (147) Zhou, C.; Wu, H.; Huang, C.; Wang, M.; Jia, N.; *Part. Part. Syst. Charact.* **2014**, *31*, 675-684.
- (148) Park, Y. I.; Lee, K. T.; Suh, Y. D.; Hyeon, T.; *Chem. Soc. Rev.* **2015**, *44*, 1302-1317.
- (149) DaCosta, M. V.; Doughan, S.; Han, Y.; Krull, U. J.; *Anal. Chim. Acta* **2014**, *832*, 1-33.
- (150) Chen, J.; Zhao, J. X.; *Sensors* **2012**, *12*, 2414-2435.
- (151) Zhang, L. e.; Zeng, L.; Pan, Y.; Luo, S.; Ren, W.; Gong, A.; Ma, X.; Liang, H.; Lu, G.; Wu, A.; *Biomaterials* **2015**, *36*, 82-90.
- (152) Li, L.-L.; Zhang, R.; Yin, L.; Zheng, K.; Qin, W.; Selvin, P. R.; Lu, Y.; *Angew. Chem., Int. Ed.* **2012**, *51*, 6121-6125, S6121/6121-S6121/6117.
- (153) Ni, D.; Zhang, J.; Bu, W.; Xing, H.; Han, F.; Xiao, Q.; Yao, Z.; Chen, F.; He, Q.; Liu, J.; Zhang, S.; Fan, W.; Zhou, L.; Peng, W.; Shi, J.; *ACS Nano* **2014**, *8*, 1231-1242.
- (154) Zhang, Y.; Lin, J. D.; Vijayaragavan, V.; Bhakoo, K. K.; Tan, T. T. Y.; *Chem. Commun.* **2012**, *48*, 10322-10324.
- (155) Zhu, X.; Zhou, J.; Chen, M.; Shi, M.; Feng, W.; Li, F.; *Biomaterials* **2012**, *33*, 4618-4627.
- (156) Cheng, L.; Yang, K.; Li, Y.; Chen, J.; Wang, C.; Shao, M.; Lee, S.-T.; Liu, Z.; *Angew. Chem. Int. Ed.* **2011**, *50*, 7385-7390.

Selective Deposition of Ln(III)- Ions into the Large and Small Cavities of Nanozeolite-LTL for Magnetic Resonance and Optical Imaging

2



The contents of this chapter have been published in:

F. Mayer, W. Zhang, T. Brichart, O. Tillement, C. S. Bonnet, É. Tóth, J. A. Peters, K. Djanashvili, *Chem. Eur. J.*, **2014**, *20*, 3358-3364.

INTRODUCTION

The aluminosilicate frameworks of all zeolites are anionic, due to the presence of tetrahedrally coordinated Al.¹⁻³ The negative charges are usually compensated by loosely bound cations, which are accessible for the surrounding solution due to the porous nature of the zeolites. As a result, a fraction of those ions can be easily exchanged by any cation of choice that fits into the pores. In fact, zeolites in which alkali-ions were exchanged with rare earth ions have been successfully exploited as cracking catalysts in petrochemical processes.⁴ The fact that rare earth elements and especially the elements of the lanthanide series are also widely applied in medical imaging, drew the attention of researchers from this field towards zeolites as carriers for paramagnetic Gd³⁺ ions applied for contrast enhancement in magnetic resonance imaging (MRI).⁵⁻⁹ Ln³⁺-loaded zeolite nanoparticles are a versatile tool to overcome sensitivity issues by delivering a high payload of active material with each single particle.¹⁰ Another advantage of the zeolites is that the compartmentalization of their interior can be used to trap ions in different framework environments.¹¹ This accurate control over the ion locations leads to increased performances of the single components in the zeolite and offers the possibility to combine different imaging modalities in a single probe.¹²

Zeolite LTL is an interesting candidate for the design of bimodal imaging probes because it is composed of both, large channels that are well accessible for water and smaller cavities that are isolated from the bulk.¹¹ The framework is built up from so-called cancrinite cages (Figure 2.1A), which are connected via their upper and lower 6-membered rings to form columns (Figure 2.1B (I)), interlinked to neighboring columns via oxygen bridges (II). This peculiar arrangement creates large channel-like cavities (III), which are separated from each other by elliptical 8-membered ring channels (IV), parallel to the original columns along the *c*-axis of the crystal. The diameter of the narrowest point of the 12-membered ring ‘superchannels’ (III) is 7.1 Å, whereas at the widest point the channel has a free diameter of 12.6 Å (Figure 2.1C). Ion-exchange in aqueous zeolite LTL dispersions exclusively takes place in these large channels, as all other cavities are not accessible from the bulk solution.¹³ Nevertheless, loading of the other sites can be realized by thermal treatment of the Ln³⁺-exchanged zeolites. The relocation of the large Ln³⁺ into the smaller cavities requires high temperatures, but has to be done carefully in order not to

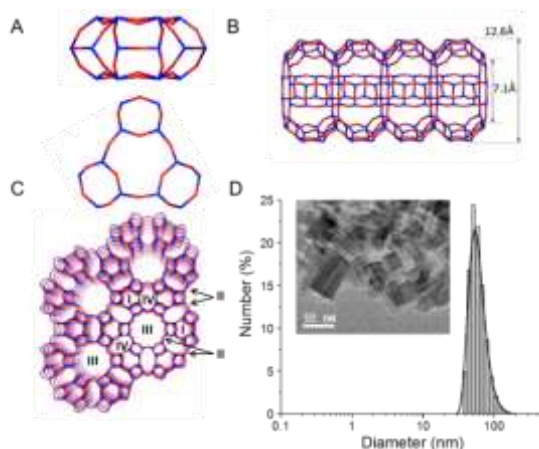


Figure 2.1. Framework and particle size of zeolite LTL: A) concantrite cages (top = view along (100), bottom = view along (001)); B) detail of the zeolite framework viewed along (001); C) a side view along (100) of the largest channel and its dimensions; D) Hydro-dynamic radius determined by DLS, insert represents a TEM image of zeolite LTL crystals.

destroy the zeolite framework.¹¹ Ln-ions once moved into small cages, are locked there and cannot be exchanged or extracted anymore. In contrast, ions in the largest channels are prone to exchange and can be extracted by saturated NH₄Cl solutions for more than 90% within 24 h.

In this study, Eu³⁺ was chosen as an optical reporter because of its sharp emission bands in the visible region (570 -720 nm).¹⁴ One of the limiting factors of lanthanides in medical imaging is the strong quenching effect of water molecules that are directly coordinated to the luminescent ion. Therefore, it was envisioned that the deposition of Eu³⁺ in the small cages of the zeolite framework, which are hardly accessible for water molecules would lead to a dramatic increase of the luminescence intensities and lifetimes. On the other hand, Gd³⁺ was chosen as an MRI reporter since high r_1 relaxivities (increase of the longitudinal water proton relaxation rate in s⁻¹mM⁻¹) can be achieved with it.^{15,16} As r_1 is directly proportional to the number of water molecules coordinated to the Gd-center (q), loading of Gd³⁺ into the big pores of the zeolite-LTL pre-loaded with Eu³⁺ into the small cages offers an elegant approach for the exploitation of the unique physical properties of each of these lanthanides in combination with the zeolite LTL framework for the design of a bimodal optical/MRI probe.

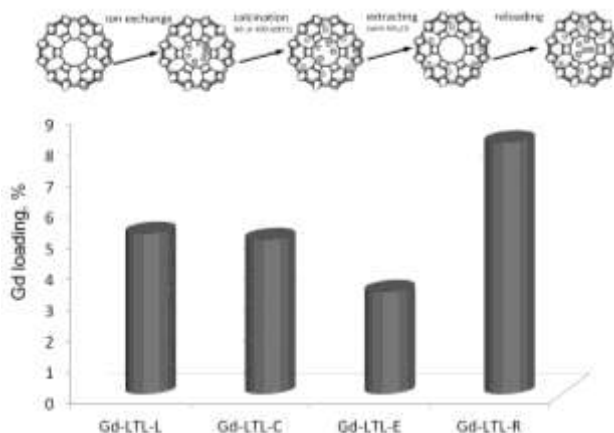


Figure 2.2. Gd-content (determined by BMS) in nanozeolite LTL after successive treatments: loading of Gd^{3+} into LTL (Gd-LTL-L), calcination at 400-600 °C for 6 h (Gd-LTL-C), extraction with saturated NH_4Cl (Gd-LTL-E), and reloading with Gd^{3+} (Gd-LTL-R). The same technique can be used for any other lanthanide (Ln).

RESULTS AND DISCUSSION

Loading of zeolite-LTL with lanthanide ions

For the ion exchange it turned out to be sufficient to stir Na-LTL crystals in an aqueous LnCl_3 solution for 24 h. In this way, loadings up to 5.2 wt-% of Ln^{3+} into the zeolite (Figure 2.2, Ln-LTL-L) could be achieved. Since only 3.6 alkali ions per unit cell are located in the large channels,¹¹ the theoretical maximum exchange capacity for Gd^{3+} ions is 6.4 wt-%. In this context, the achieved 5.2 wt-% loading (corresponding to 0.97 Gd^{3+} ions per unit cell) is close to complete substitution of the exchangeable alkali ions. The loading did not change substantially upon calcination of the material (Figure 2.2, Ln-LTL-C), which is not surprising as no ions are extracted during this step and only intra-zeolitic ion-migration takes place. To prove this relocation, three different samples were subjected to extensive ion extraction in saturated NH_4Cl solution. The first sample was Gd-loaded (Gd-LTL-L), and the next two were calcined during 6 h at 400 or 600 °C (Gd-LTL-C). Before extraction, all three samples had the same Gd^{3+} content of ~5.2 wt-%. After extracting with NH_4Cl for 72 h the determined Gd^{3+} loading was 0.48%, 2.29% and 3.30% (Figure 2.2, Gd-LTL-E)

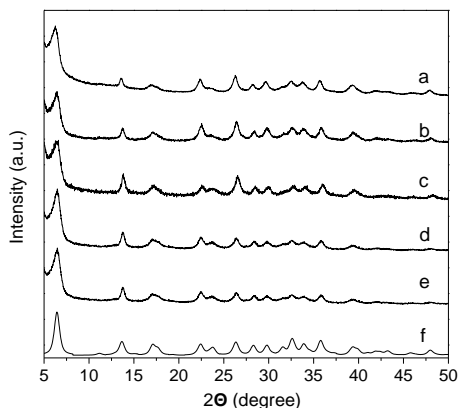


Figure 2.3. XRD patterns of the zeolite framework after different steps of the loading procedure: a) initial material (K-LTL), b) after loading with Ln^{3+} -ions (Ln-LTL-L), c) calcination at 600 °C (Ln-LTL-C), d) extraction of the Ln-ions remaining in the supercage (Ln-LTL-E), and e) reloading of the LTL with Ln-ions (Ln-LTL-R). The last diffractogram (f) represents the powder pattern as it was calculated from the database of zeolite structures for the Linde Type L framework with a wavelength of 1.78897 Å (Co K α) and $U = 0.5$ for the peak width adjustment.³

for the three samples respectively, showing that only after calcination a considerable amount of Gd^{3+} is retained during the extraction step. The influence of the temperature on the migration of the ions is illustrated by the fact that after an increase of the temperature from 400 to 600 °C, the amount of the migrated ions increased from 2.3 to 3.3 wt-%. A subsequent reloading (analogous to the first loading step) yielded materials in which the Gd^{3+} -loading was increased by 4.8% (Gd-LTL-R), which is comparable to the first loading step, indicating that in all cases the large cavities are available for reloading. After each step, X-ray diffraction (XRD) patterns were recorded, to demonstrate the integrity of the zeolite structure (Figure 2.3).

The amount of Gd^{3+} present in the zeolite framework after each step was determined by bulk magnetic susceptibility (BMS)¹⁷ measurements on aqueous suspensions. Via the mass of the dispersed zeolite the loading was calculated. The loading-relocation-extraction procedure is not limited to Gd^{3+} but was also successfully applied to introduce Eu^{3+} to the different framework environments. The harsh conditions needed to extract Ln^{3+} -ions from the framework indicate the strength of the ion absorption in zeolite. Under all

Table 2.1. Stability study in terms of Gd-leaching of Gd-LTL in water and phosphate solution.

	Water				NaH ₂ PO ₄ 45 mg/L, pH 7
	pH 4	pH 5	pH 6	pH 8	
Initial Gd ³⁺ [μ M]	685.8	597.3	508.8	465.5	591.0
Free Gd ³⁺ [μ M]	5.7	2.1	2.9	3.3	0.4
Leaching [%]	0.84	0.36	0.57	0.73	0.08

conditions needed for the here presented investigations, no leaching of Gd³⁺ ions could be detected. Additionally, the leaching was investigated within the pH range from 4 to 8, as well as in the presence of phosphate ions (Table 2.1). Only the value obtained for the sample incubated for 24 h, at pH 4 in HCl solution was above the detection limit of 4 μ M of the colorimetric assay. Clearly, the feasibility of these materials for medical or biological applications will require a more detailed leaching study under physiological conditions, as well as the decoration of the surface with organic moieties along with a thorough toxicology study.

Luminescence study

Dispersions of Ln-LTL-L, Ln-LTL-C and Ln-LTL-E (Ln = Eu and Gd) in water were investigated with respect to their photo-physical properties. The luminescence intensities for both, Gd³⁺ and Eu³⁺-loaded samples, increased upon calcination and even further after the extraction step (Figure 2.4). This effect is accompanied by an increase in the luminescence decay lifetime. Both phenomena can be explained by the decrease of the amount of water molecules in the first coordination sphere of the lanthanide ions leading to a reduction of possible non-radiative decay pathways.¹⁸

To get an insight into the different coordination behavior, the luminescence lifetimes were used to determine the number of water molecules in the first coordination sphere of Eu³⁺ ions in different locations in the framework of LTL (Figure 2.5). From the fitting of the decay curves, the average q -values were evaluated to be 6.2, 0.9 and 0.8 for Eu-LTL-L, Eu-LTL-C and Eu-LTL-E, respectively. To exclude contributions from the fast decaying ions in the large channels, the obtained curves for LTL-C and LTL-E samples were only fitted for lifetimes > 1ms. Thus, the q -values reported for those samples only represent the Eu³⁺-ions in the small cages.

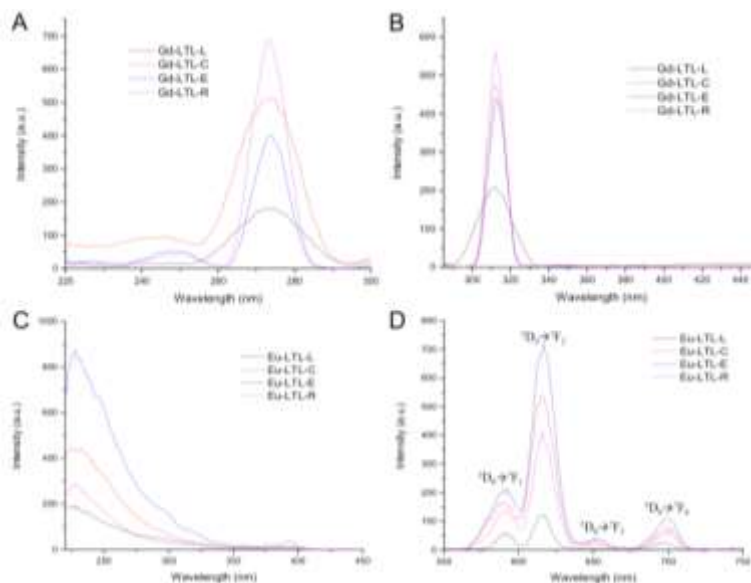


Figure 2.4. Excitation (A/C) and emission (B/D) spectra of Gd- and Eu-loaded samples obtained in time-resolved mode with a delay of 0.1 ms and an averaging time of 0.1 s. Due to the large difference in luminescence intensity in the emission spectra slits had to be open for Gd-loaded samples (inducing the difference in peak width). The result of this change is that intensities of Gd-loaded samples cannot be compared precisely. For the Eu-loaded samples, slits of all 4 samples were not changed, resulting in the following relation in fluorescence intensities: $\text{Eu-LTL-L} < \text{Eu-LTL-R} < \text{Eu-LTL-C} < \text{Eu-LTL-E}$.

To reproduce the complete decay curves, a bi-exponential fit with one decay constant fixed to the value obtained for Eu-LTL-L (0.158 ms) resulted in functions that fit the whole curve with adjusted R^2 values > 0.99 and a second decay constant that was identical with the one, that was obtained from the mono-exponential fit > 1 ms. Going from Eu-LTL-C to Eu-LTL-E, the ratios of the pre-exponential factor changed in favor of the longer decaying function, showing that the amount of Eu^{3+} -ions in the big cage was reduced during the washing procedure.

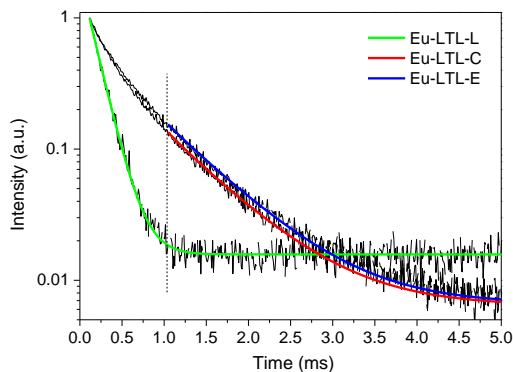


Figure 2.5. Normalized luminescence decay profiles of Eu-LTL-L, Eu-LTL-C, and Eu-LTL-E dispersions. The smooth lines represent the fits that were used to calculate q -values, using the data above 1 ms for Eu-LTL-C and Eu-LTL-E.

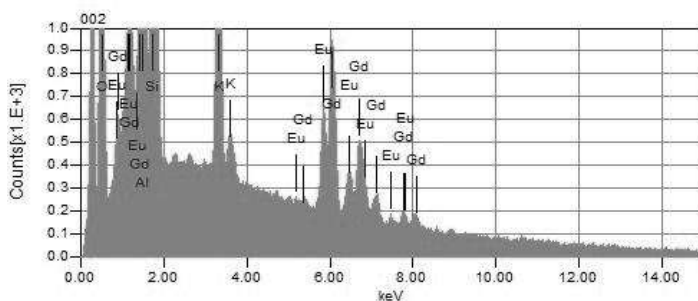


Figure 2.6. EDX spectrum of the Eu-LTL-R(Gd) sample with Gd^{3+} in the big and Eu^{3+} in the small cages. The mass ratio of Si to Al and Gd to Eu is 2.9 and 1.8, respectively. The Si to Al ratio is in a good agreement with theoretical ratio (Si/Al 3.0) of the pure LTL. The Gd/Eu ratio is very close to the one determined by the BMS method (Gd/Eu 1.4).

Relaxivity study and MRI performance

As it has been discussed, to optimally exploit the imaging performance of Gd^{3+} and Eu^{3+} in zeolite-LTL, Gd^{3+} should be deposited in the big cages whereas Eu^{3+} should be localized in the small cages. The ion-exchange started by replacing Na^+ with Eu^{3+} , while Gd^{3+} was used in the final reloading step (Eu-LTL-R(Gd)). The Energy-dispersive X-ray (EDX) spectroscopy was used to confirm the coexistence of Gd^{3+} and Eu^{3+} ions in the framework of zeolite LTL (Figure 2.6).

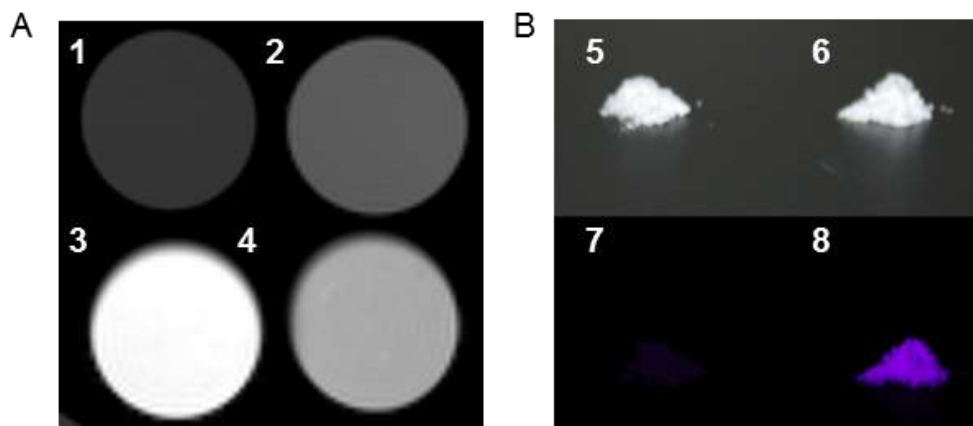


Figure 2.7. Dual-imaging performance of Gd- and Eu-loaded LTL-zeolite. A) T_1 -weighted MR images (7 T, 25 °C) of phantoms formed by four pellets containing 1% aqueous xanthan (1), Milli-Q water (2), Gd-LTL-L (3) and Gd-LTL-E (4) suspended in 1% xanthan at Gd concentration of 0.5 mM; B) Photographic images of solid powders of Eu-LTL-L (5, 7) and Eu-LTL-E (6, 8) under daylight (upper panel) and UV-light of 258 nm (lower panel).

The location of Eu^{3+} in the small cage is advantageous to reduce the luminescence quenching by water, whereas Gd^{3+} profits from the high q -values in the large channels. These effects are illustrated in Figure 2.7. However, coordinated water is not the only parameter influencing r_1 . Other parameters governing the relaxivity were evaluated using proton nuclear magnetic relaxation dispersion (^1H NMRD) of aqueous dispersions of Gd-LTL samples stabilized with 1% xanthan gum. The ^1H NMRD profiles were recorded at different temperatures from 25 to 50 °C (Figure 2.8). The increase of r_1 at high magnetic field (>10 MHz) is an indication of a relatively long rotational correlation time (τ_R), and the maximum of relaxivity reached between 40 and 60 MHz is for the typically immobilized Gd^{3+} in the framework (Figure 2.8A). For the three samples studied, the r_1 is Gd-LTL-E < Gd-LTL-C < Gd-LTL-L (Figure 2.8B), which is due to the migration of the Gd^{3+} between the big and small cages under different conditions, and is in a good agreement with the luminescence study.

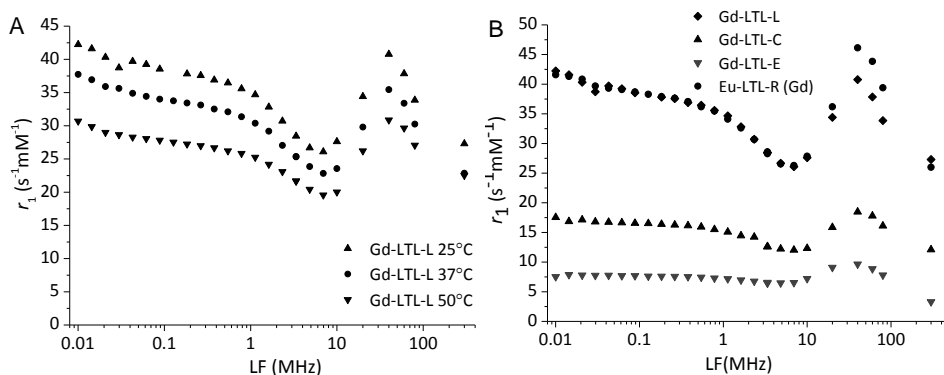


Figure 2.8. 1H NMRD profiles of the Gd-LTL-L samples from 25 to 50 °C (A) and comparison of Gd-LTL-L, Gd-LTL-C, Gd-LTL-E and Eu-LTL-R (Gd) at 25°C (B). The curve from 0.01 to 1 MHz is not constant for the loaded and reloaded samples, which is attributed to the contribution of the silica surface.

Fitting procedures of the obtained 1H NMRD profiles

The relaxivities of Gd-LTL-L appear to be substantially higher than those of the previously studied Gd^{3+} -loaded NaY zeolite with similar Gd^{3+} contents (Figure 2.9A). The trend of r_1 to decline with the Larmor frequency (LF) up to 1 MHz rather than being constant, as usually observed, can be explained by a contribution of the zeolite to the relaxivity due to the long correlation time modulation of the dipole-dipole relaxation of the protons of relatively immobile water molecules adsorbed on the surface of the zeolite particles.¹⁹ Similar phenomena have previously been observed in the NMRD profiles of Gd-chelates grafted to hydroxyapatite and TiO_2 particles.²⁰⁻²² By contrast, the low field parts of the NMRD profiles for the Gd-LTL-E are perfectly horizontal (Figure 2.9A). Most likely, the strong adsorption of water to the surface of loaded zeolite particles involves silanol groups, which are removed during calcination. For the fittings only the results at 25 °C were used because at higher temperatures a slight decrease of r_1 was observed over time. A more detailed study revealed that this effect can be attributed to the presence of xanthan (see Chapter 4). Prior to the fitting procedures, the obtained NMRD profiles had to be corrected for the contribution of the zeolite framework. Therefore, a fraction of the NMRD profile of pure silica as it was published by Gillis et al.²³ was subtracted from the obtained data in a

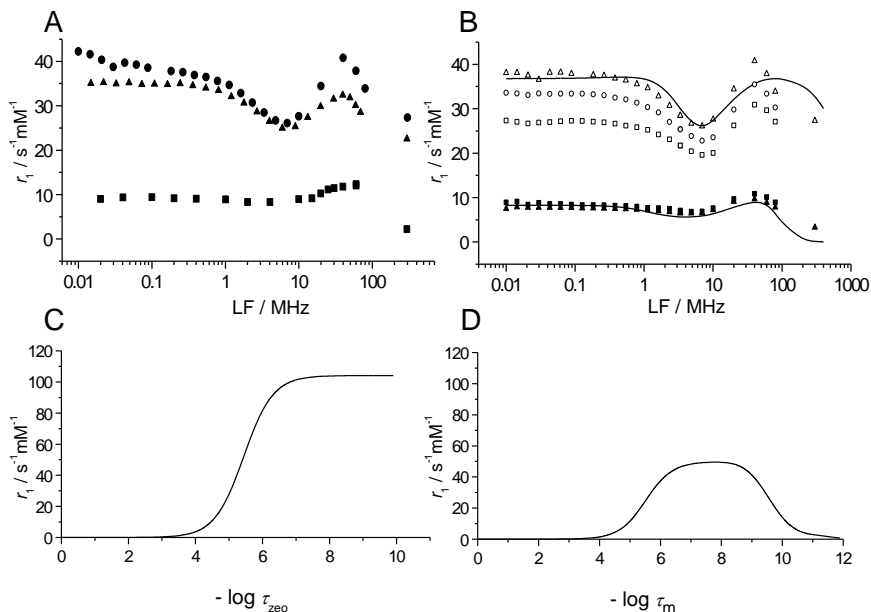


Figure 2.9. A) ^1H NMRD profiles of Gd-LTL-L (circles, 5.18 % loading, 25 °C), Gd-Al-TUD1 (triangles, 3.8% loading, 25 °C)¹³ and Gd-NaY (squares, 5% loading, 25 °C).²³ B) ^1H NMRD profiles of the Gd-LTL-L (open symbols) and Gd-LTL-E (filled symbols) at 25 °C (triangles), 37 °C (circles), and 50 °C (squares) after correction for the silica contribution. The curves were calculated with best-fit values, tabulated in Table 2.2. Simulation of r_1 as a function of C) $\tau_{\text{zео}}$ (fixed $\tau_{\text{m}} = 6.5 \times 10^{-10}$ s) and D) τ_{m} (fixed $\tau_{\text{zео}} = 6.6 \times 10^{-8}$ s) using Eqs. 2.1-2.5, assuming $\tau_{\text{R}} > 10^{-8}$ s, $\tau_{\text{zео}} = 1.4 \times 10^{-11}$ s, $\Delta^2 = 2.1 \times 10^{19} \text{ s}^{-2}$, $w = 15$,³⁰ and $q = 6$.

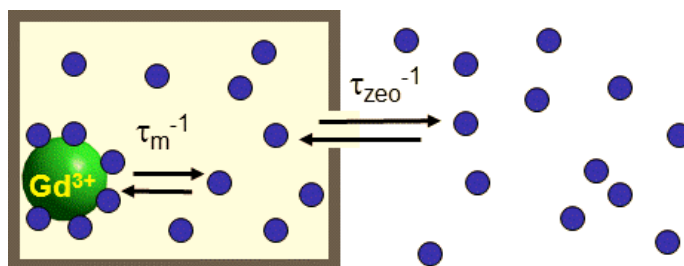


Figure 2.10. Schematic representation of the two-step mechanism to account for an aqueous suspension of Gd^{3+} -loaded zeolite nanoparticles.

way, that the first part of the resulting profile (up to 1 MHz) was constant. The profiles as obtained and after the correction are as shown in Figures 2.8A and 2.9A, respectively.

In zeolitic systems studied until now, the diffusion of water from the interior of the zeolite to the bulk limits the relaxivity, and this requires additional parameters to be taken into account for the analysis of NMRD. Therefore, we have previously developed a two-step model (Figure 2.10).²⁴

First, the relaxivity of the water inside the zeolite nanoparticles (T_{1zeo}) is derived by considering the exchange between water molecules in the first coordination sphere of Gd^{3+} and free water molecules inside the zeolite (Equation 2.1). Here, w is the number of free water molecules (not bound to Gd^{3+}) inside the zeolite per Gd^{3+} ion and T_{1m} is the longitudinal relaxation time of inner sphere water protons, which is given by the Solomon-Bloembergen-Morgan Equation (Equation 2.2).^{25,26}

$$x = \frac{1}{T_{1,zeo}} = \frac{\frac{q}{w}}{\tau_m + T_{1m} \left(1 + \frac{q}{w}\right)} \quad 2.1$$

$$\frac{1}{T_{1m}} = \frac{2}{15} \left(\frac{\mu_0}{4\pi}\right)^2 \frac{\hbar^2 \gamma_S^2 \gamma_I^2}{r_{GdH}^6} S(S+1) \left(\frac{3\tau_{d1}}{1 + \omega_I^2 \tau_{d1}^2} + \frac{7\tau_{d2}}{1 + \omega_S^2 \tau_{d2}^2} \right) \quad 2.2$$

Here, r_{GdH} is the effective distance between the Gd^{3+} electron spin and the water protons, γ_S and γ_I are the electron and proton gyromagnetic ratios, respectively, and τ_{di} is given by $\tau_{di}^{-1} = \tau_m^{-1} + \tau_R^{-1} + T_{ie}^{-1}$ ($i = 1, 2$). The electronic relaxation rates (T_{ie}) are approximated by Equations 2.3 and 2.4, where ω_S is the Larmor frequency, Δ^2 is the trace of the square of the zero field splitting (ZFS) tensor, and τ_v is the correlation time for the modulation of ZFS.

$$\frac{1}{T_{1e}} = 1/25 \Delta^2 \tau_v [4S(S+1) - 3] \left(\frac{1}{1 + \omega_S^2 \tau_v^2} + \frac{4}{1 + 4\omega_S^2 \tau_v^2} \right) \quad 2.3$$

$$\frac{1}{T_{2e}} = \Delta^2 \tau_v \left(\frac{5.26}{1 + 0.372 \omega_S^2 \tau_v^2} + \frac{7.18}{1 + 1.24 \omega_S \tau_v} \right) \quad 2.4$$

In the second step, the exchange of water between the inside of the zeolite and the bulk by the diffusion through the zeolite channels is considered. This enables the propagation of the relaxation enhancement from the interior of the material to the bulk water outside. If the chemical exchange between protons in two magnetically distinct environments (inside and

outside the zeolite) is taking place under highly dilute conditions of the paramagnetic entities, Equation 2.5 can be derived for the overall longitudinal relaxivity:

$$r_1 = \frac{w+q}{55500} \left(\frac{1}{T_{1,zeo} + \tau_{zeo}} \right) \quad 2.5$$

Here, τ_{zeo} is the residence lifetime of water protons inside the zeolite. The contribution of water molecules diffusing along the paramagnetic center without being bound to it (the outer sphere contribution) can be neglected for both the exterior and the interior of the investigated materials because the contribution of this mechanism to the overall relaxivity has been shown to be small for zeolite-immobilized Gd^{3+} , particularly at Larmor frequencies higher than 0.1 MHz. This model has been validated for several zeolitic systems.^{15,23} For the fitting procedure of the obtained NMRD data, the following limitations and constraints were applied. The distance r_{GdH} was fixed at 3.1 Å, E_v at 1 kJ mol⁻¹, q at the values obtained from the luminescence decay experiments ($q = 1$ and 6 for the extracted and loaded sample, respectively), and w at the values calculated from the known total amount of water in the zeolites and from the Gd-loading.³⁰ Furthermore, the correlation times τ_m and τ_{zeo} were limited by the boundaries discussed in the manuscript. Attempts to fit the data with correlation times outside these boundaries led to unsatisfactory fits and/or to unrealistic values for the variable parameters, such as negative activation energies. It may be expected that τ_{zeo} is the same for calcined and uncalcined Gd-LTL and it should be smaller than 10⁻⁷ s. As Figure 2.9C shows that under these conditions τ_{zeo} has almost no influence on r_1 , its value was fixed at 10⁻⁸ s. Finally, we have included some values of transverse electronic rates ($1/T_{2e}$) in the fittings as obtained from EPR peak-to-peak line widths (Figure 2.11) with Equation 2.6, where μ_B is the Bohr magneton, g_L the electron Landé factor, h the Planck constant, and ΔH_{pp} the peak-to-peak line width.

$$\frac{1}{T_{2e}} = \frac{g_L \mu_B \pi \sqrt{3}}{h} \Delta H_{pp} \quad 2.6$$

Although the number of variables was still substantial, the obtained best fit values turned out to be reasonable. They are compiled in Table 2.2 and NMRD profiles calculated with these values are represented as curves in Figure 2.9B. For comparison, some previously determined data on Gd^{3+} -loaded zeolite NaY and mesoporous material AITUD-1 are

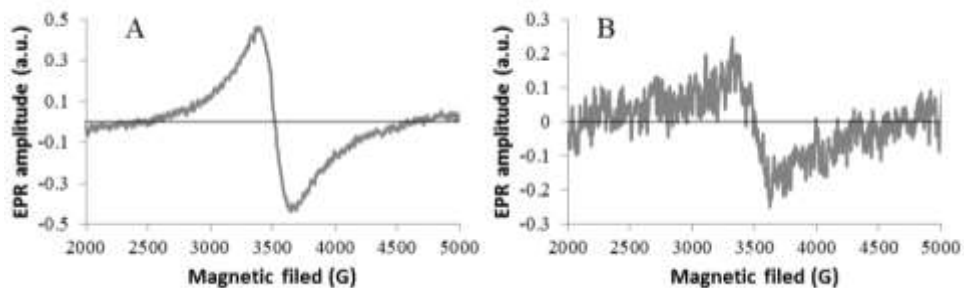


Figure 2.11. EPR spectra of (A) Gd-LTL-L and (B) Gd-LTL-E in aqueous solution containing 1 wt-% xanthan gum. Concentrations were 0.94 mM and 0.83 mM for Gd-LTL-L and Gd-LTL-E, respectively. The g -factors are 1.982 (LTL-L) and 1.988 (LTL-E) and the linewidth (ΔH_{pp}) is 250.3 and 285.4 G.

included in Table 2.2. The best-fit values of the parameters governing the transversal electronic relaxation rates, τ_v and Δ^2 , are in the range usually observed for Gd^{3+} complexes.^{9,23,24,27} The values of $1/T_{2e}$, measured by EPR at 0.34 T (9.77G), are in a good agreement with the best-fit values (see Table 2.2). The values for τ_m are very small compared to that of Gd-NaY with a comparable loading. In Gd-NaY systems, the water exchange process in the zeolite supercages speeds up substantially upon increasing the Gd^{3+} loading, which is a consequence of the increase of the Gd^{3+} concentration inside the zeolite cavities, which makes the probability of a water molecule being located in the inner coordination sphere of the Gd^{3+} ion higher. In the presently studied Gd-LTL-L system, the residence time of water inside the zeolite (τ_{zco}) is so short that in this case the process of exchange is probably not limited to the water inside the zeolite nanoparticles. For the Gd-LTL-E sample, however, the value for τ_m is rather large, which may be rationalized by the locked location of the Gd^{3+} ions after calcination. Assuming that the exchange follows a dissociative mechanism, the encapsulation may lead to a relatively high steric strain on the remaining bound water molecule and, consequently, lead to a relatively large free enthalpy gap between the ground state and the eight-coordinate transition state and thus to a relatively slow water exchange rate. Therefore, for the fitting of the obtained 1H NMRD data as discussed above, after subtracting the contribution of silica surface, the resulting profiles are represented in Figure 2.9B. Equation 2.5 shows that r_1 is proportional to q ,

Table 2.2. Preparation and studies on the properties of double loaded zeolite LTL.

	Ln-LTL-L	Ln-LTL-C ^a	Ln-LTL-E	Ln-LTL-R	Gd-AITUDI ²³	Gd-NaY ²⁴
Loading (wt%) ^b	5.2 (5.2/0)	5.0 (1.7/3.3)	3.3 (0.0/3.3)	7.9 (4.6/3.3)	3.8	5.0
Si/Al ratio	3	3	3	3	3.5	1.6
q^c	6.1	6.1/0.9	0.9	6.1/0.9	3.6	7
w^{30}	15	32	-	-	94	13
r_1 ($\text{mM}^{-1}\text{s}^{-1}$) ^d	37.8	17.8	8.9	43.8 ^e	30.0	12.0
r_1' ($\text{g}^{-1}\text{Ls}^{-1}$) ^d	12.5	5.7	1.9	13.7 ^e	7.3	3.8
τ_m (ns)	0.19	-	1660	-	0.27	625
τ_{zeo} (μs)	0.01	-	0.01	-	<10	33
τ_v (ps)	26.0	-	9.2	-	48	22
Δ^2 (10^{19} s^2)	3.8	-	2.9	-	1.2	5.1
$\ln 1/T_{2e}(\text{s}^{-1})^f$	22.1	22.2	-	-	22.30	22.64
$\ln 1/T_{2e}(\text{s}^{-1})^g$	22.4	21.6	-	-	22.10	22.63
$I_{@615\text{nm}}$ (p.d.u.)	120	538	718	415	-	-

^a6h at 600 °C; ^bdetermined by BMS for Gd-LTL and by EDX (Figure 2.6) for Gd/Eu-LTL (ratio large/small cavity in brackets); ^cdetermined by luminescence decay of Eu-LTL; ^d60 MHz, 25 °C; ^eEu in the small, Gd in the big cavities; ^fdetermined from EPR line widths at 0.34 T; ^gcalculated with best fit parameters.

which explains the substantial decrease in r_1 upon calcination of Gd-LTL-L. During the calcination, a loss of five water molecules in the first coordination sphere of the Ln^{3+} ion occurs. In contrast, r_2 is not depending on q and is similar for Gd-LTL-L and Gd-LTL-E with 93 and 72 $\text{s}^{-1} \text{mM}^{-1}$ (5.2 wt.% Gd-loading, 7 T, 25 °C), respectively. This leads to r_2/r_1 ratios of 3.4 for the loaded *vs* 22.0 for the extracted material, with the former value being between 1 and 10 as required for optimal performance as positive CAs.¹³

¹H NMRD profiles are influenced by a large number of parameters, which makes the quantitative evaluation of these data a difficult task. Therefore, several constraints were introduced as shown in the fitting procedures. The values of q were fixed at 6 and 1 for Gd-LTL-L and Gd-LTL-E, respectively, which are the values determined by the luminescence decay of the corresponding Eu^{3+} -loaded samples. As we have demonstrated that for zeolites, r_1 is independent of τ_R implying that $\tau_R \geq 10^{-8}$ s, τ_R was fixed to 10^{-8} s.²⁴ Further constraints could be derived from the peculiar temperature dependence of the relaxivities (Figure 2.9B), which appear to be opposite for Gd-LTL-L and Gd-LTL-E: for the former, r_1

decreases with temperature, whereas it increases for the latter. The parameters mainly determining the temperature dependence of r_1 are the residence time of the water molecules in the first coordination sphere of Gd^{3+} (τ_m) and that of the water molecules inside the zeolite (τ_{zeo}). Obviously, both residence times decrease with increasing temperature meaning that the exchange rates speed up. Two characteristic simulations of the dependence of r_1 on τ_{zeo} and τ_m are displayed in Figure 2.9C and D. An inspection of these curves shows that the temperature dependencies can only be explained if $\tau_m < 10^{-9}$ s for Gd-LTL-L and $> 10^{-7}$ s for Gd-LTL-E. Furthermore, the decrease of r_1 with temperature for Gd-LTL-L requires that the temperature effect due to τ_{zeo} is small, thus either $\tau_{zeo} > 10^{-4}$ or $< 10^{-8}$ s. The former possibility can be excluded, since that cannot explain the high relaxivities observed for Gd-LTL-L. Based on these considerations τ_{zeo} was fixed at 10^{-8} s and τ_m was constrained to $< 10^{-9}$ s for Gd-LTL-L and to $> 10^{-7}$ s for Gd-LTL-E, as these have been shown in the fitting procedures. Finally, further constraints were imposed by performing the fittings of the NMRD profiles simultaneously with EPR line widths using a set of Equations derived previously. A two-step model was applied taking into account (i) the exchange of Gd^{3+} -coordinated water molecules with “free” water molecules inside the zeolite particles and (ii) the exchange of “free” water molecules between the outside and inside of the zeolite particles.²⁴ The details are shown in the fitting section and Table 2.2.

As it has shown that reasonable fits were obtained, particularly considering the crudeness of the model applied. The best-fit-values of the variable parameters are compiled in Table 2.2 and NMRD profiles calculated with these values are represented as curves in Figure 2.9B. The best-fit values of the parameters governing the transversal electronic relaxation rate ($1/T_{2e}$) τ_v and A^2 , are in the range usually observed for Gd^{3+} complexes resulting in values of $1/T_{2e}$ that are in good agreement with the values measured by EPR at 0.34 T (Table 2.2 and Figure 2.11). Interestingly, in comparison with reported Gd-NaY, the τ_m of the presented Gd-LTL-L sample is extremely low.²⁴ The very high water exchange rate between the interior and exterior of Gd-LTL compared to that of Gd-NaY (2 orders of magnitude higher) is surprising since both zeolites have 12-membered ring entrance windows with minimum diameters of 7.1 and 7.4 Å, respectively. Most likely the linear channels are the reason for this fast diffusion within the material. This is corroborated by intra-crystalline self-diffusivity measurements by Caro *et al.*, who demonstrated the water mobility in zeolites NaX and NaY with 3-dimensional channel structures to be beneath that

in zeolite ZSM-5 with a linear channel structure.²⁸ The exchange rate of Gd-LTL is about as fast as for mesoporous materials,^{23,27} which have channels with diameters of 1-20 nm. Accordingly, both materials have comparable ¹H NMRD profiles with high relaxivities in comparison to the Gd-NaY zeolites (Figure 2.9A). However, the here presented Gd-LTL material is favorable for application as MRI contrast agent in contrast to Gd-AITUD-1, which showed significant leaching of Gd³⁺. It should be noted that relaxivities expressed in s⁻¹ mM⁻¹ do not give a good impression of the efficacy of these materials as MRI contrast agents, due to the difference in loading. Therefore, it is more useful to express them in s⁻¹ Lg⁻¹ for solid material. Reloaded Eu-LTL-R (Gd in the big cage) has a relaxivity density of 13.7 s⁻¹Lg⁻¹ at 60 MHz and 25 °C, which is about a factor of two higher than the values for the best zeolitic systems reported up to now (Table 2.2). This unmatched relaxivity density is also significantly higher than the one of clinically applied Gd-DOTA (6.6 s⁻¹Lg⁻¹ @ 20 MHz and 25 °C).

CONCLUSIONS

In this work we present a novel strategy to selectively deposit different ions into distinct framework locations of zeolite-LTL and we demonstrate that the carefully ion-exchanged Gd/Eu containing nanocrystals acquire exceptional magnetic properties in combination with enhanced luminescence. This smart exploitation of the framework structure yields the highest relaxivity density (13.7 s⁻¹Lg⁻¹ at 60 MHz and 25 °C) reported so far for aluminosilicates. The high MRI performance can be explained by the fastest water exchange that was found in zeolitic systems up to now, while the enhanced luminescence could be achieved by the efficient isolation of the Eu³⁺ ions from water molecules in the first coordination sphere. Based on these findings, nanozeolite-LTL is an interesting candidate for the development of high performance dual imaging probes, with the potential to be extended for radioisotopes for imaging and/or therapy. However, before the first *in vivo* studies can be started, more biological tests will be necessary, including cell toxicity and uptake studies. The functionalization of the surface with organic groups will also be investigated to further improve the stability and biocompatibility of this promising system.

EXPERIMENTAL SECTION

Materials and methods

All chemicals in this study were used as obtained. The K-LTL nanocrystals were purchased from NanoScape (Planegg, GE). GdCl₃ and EuCl₃ were obtained as hexahydrates from Strem Chemicals, Newburyport, USA. NaCl, NH₄Cl were purchased from Sigma Aldrich, St. Louis, MO 63103, U.S.A. In all reactions MilliQ water (>18.2 MΩ) was used. X-Ray diffraction patterns of the zeolites before and after loading and after each step of the preparation were measured using a Bruker AXS/D8 Advance diffractometer equipped with a Lynxeye detector and Co K_α radiation ($\lambda = 1.78897 \text{ \AA}$, 35 kV, 40 mA). The measurement range was from 5 to 70 °2 θ with a step size of 0.02° in continuous mode and an acquisition time of 0.5s per step. The scans were repeated until a good signal to noise ratio was achieved. Gd concentrations were determined by the BMS method. All measurements were done on a Varian Unity Inova 300 NMR spectrometer with *t*-butanol as internal standard. The sample was prepared by dispersing a defined amount of the Gd containing zeolite in a 10 vol% aqueous *t*-butanol solution containing 1 wt% xanthan. The induced shift was measured against an aqueous *t*-butanol solution in a standard inner tube that was added to the sample tube. The concentration was calculated from the shift following the procedure described in literature ¹H NMRD profiles were recorded on a Stellar SMARtracer Fast Field Cycling NMR relaxometer (0.01-10 MHz) and a Bruker WP80 NMR electromagnet adapted to variable field measurements and controlled by a SMARtracer PC-NMR console. The temperature was monitored by a VTC91 temperature control unit and maintained by a gas flow. The temperature was determined by previous calibration with a Pt resistance temperature probe. The longitudinal relaxation rates ($1/T_1$) were determined in water. The samples were prepared by dispersing defined amounts of zeolite (see Table S2) in 1 wt-% xanthan solution. Luminescence excitation and emission spectra and luminescence lifetimes were determined using a Varian Cary Eclipse spectrophotometer using a pulsed Xenon light source. The samples were prepared from dried zeolite materials by dispersion in distilled water and multiple sonications. The EPR spectra were recorded on a Bruker ESP300 Spectrometer, operating at 9.43 GHz, 0.34 T, X-band), at 298 K with typical parameters: MW power 4mW, modulation amplitude 1.0 mT and time constant 0.03 s. EDX spectra were recorded on a JEOL-JMS 6010 Scanning Electron Microscope with an acceleration

voltage 20kV. The spot analysis of larger agglomerates of particles was used to determine the Gd and Eu content of the samples. Therefore, the samples were put on conductive tape, that was fixed on an Aluminum holder. Dynamic light scattering (DLS) was done on a Zetasizer Nano ZS from Malvern Instruments Ltd (Malvern, UK). The machine is equipped with a 4.0 mW, 633 nm He-Ne Laser and the 173° back-scatter mode was used to analyze the obtained particles. The multiple-peak fitting procedure implemented in the Software for Zetasizer (Version 6.12) was used to evaluate the autocorrelation function. Diameters are given as number weighted mean values of the obtained particle size distributions. Dispersions were prepared from commercial dry material by suspending it in MilliQ water using a ¼' ultrasonic probe for 2 min.

Zeolite loading (Ln-LTL-L)

K-LTL zeolite was first ion exchanged with NaCl. This was done in order to obtain Na-LTL, which is supposed to be more active in the ion exchange with Ln³⁺ ions. For this purpose, 1 g of K-LTL was stirred in 20 mL NaCl solution (1 M) for 20 h. After finishing the exchange, the sample was centrifuged and the solid was washed with 20 mL of water (3x) and then re-dispersed in 15 mL of the corresponding Ln-containing solution (80 mM) at pH 5.5 and stirred for 24 h. After this procedure, the dispersion was dialyzed against 1 L of water (3x). The obtained solution was freeze dried and the resulting powder was collected as Ln-LTL-L sample.

Ion relocation

The ion relocation was done in a standard calcination oven. The Ln-LTL-L samples were put in porcelain crucibles and heated to 100 °C at a rate of 1 °C/min in order to allow the water in the zeolite to escape slowly without damaging the structure. Then the samples were heated to the desired temperature (400 or 600 °C) at a rate of 10 °C/min. After reaching the temperature, it was kept constant for 6 h. Then the oven was turned off and left to cool to room temperature. The calcined zeolites were stored in ambient atmosphere for rehydration and they were named Ln-LTL-C.

Extraction

1.4 g of the Ln-LTL-C samples was dispersed in 15 mL of saturated aqueous NH_4Cl solution. After stirring for 72 h the dispersion was centrifuged and the solid was washed with 20 mL of water (3x). The re-dispersed sample was then freeze dried to obtain the final Ln-LTL-E product. An in detail investigation indicated that the extraction was already finished after 24 h. Already after this shorter period more than 90% of the Ln ions were extracted and no change in the following 48 h could be found. This material could be reloaded with another or the same lanthanide according to the above described loading procedure. The NaCl exchange step was not repeated in the second round of loading, because it can be expected that there are only loosely bound NH_4^+ ions present in the channels. The obtained reloaded material was named Ln-LTL-R.

Stability

To investigate the extent of leaching of Gd^{3+} -ions from the framework, a defined amount of Gd-LTL-L were dispersed in 5 mL aqueous medium and sonicated for 10 min in an ultrasonic bath. The dispersions were divided into 4 portions and kept in a thermo-shaker at 37 °C for 24 h. After the incubation time, the zeolite dispersion was centrifuged at 13.2k rpm and the supernatant was tested for free Gd^{3+} -ions in a colorimetric assay.²⁹ Briefly, 100 μL of the supernatant was thoroughly mixed with 1 mL of a freshly prepared acetate buffered xylenol orange solution. Then the absorption spectrum was measured in the spectral range from 350 to 600 nm. The ratio of the absorptions at 573 nm and 433 nm was calculated and used to determine the Gd^{3+} concentration via a calibration curve, measured in the same way with Gd^{3+} stock solutions of known concentrations. The detectable concentrations of Gd^{3+} were in a range of 4 to 50 μM with an error of $\pm 2.5 \mu\text{M}$. All experiments were repeated in triplicate. The initial Gd^{3+} -concentration in the Gd-LTL-L dispersions was calculated from the amount of zeolite that was subjected to extraction and the concentration of free Gd^{3+} that was found in the supernatant after the extraction.

ACKNOWLEDGEMENTS

Thanks are due to Prof. W.R. Hagen (TU Delft) for the EPR measurements, Ben Norder (TU Delft) for the XRD measurements, F. Szeremeta and S. Môme (CNRS, Orléans, FR) for the MR images, and Dr. H.S. Figueiredo and Prof. I. Correia Neves (Braga, PT) for exploratory experiments.

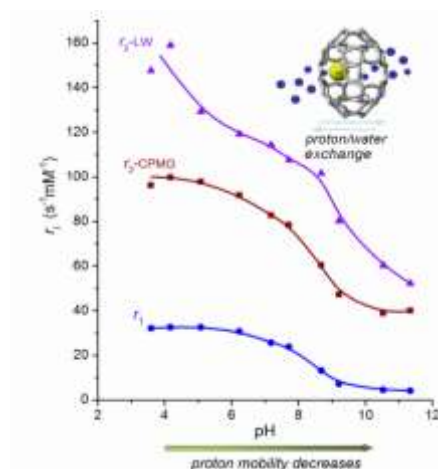
References

- (1) Čejka, J.; Bekkum, H. v.; Corma, A.; Schüth, F. In *Introduction to Zeolite Science and Practice*, Elsevier, Amsterdam (The Netherlands), **2007**.
- (2) van Bekkum, H.; Kouwenhoven, H. W. In *Zeolite Manual for the Organic Chemist*, mijnbestseller.nl, **2012**.
- (3) XRD profiles of Linde Type L framework are available at <http://www.iza-online.org/>, **2014**.
- (4) Scherzer, J. *Catal. Rev.* **1989**, *31*, 215-354.
- (5) Balkus, K. J.; Sherry, D. A.; Young, S. W. The University of Texas System, USA, US5122363, **1992**.
- (6) Rubin, D. L.; Falk, K. L.; Sperling, M. J.; Ross, M.; Saini, S.; Rothman, B.; Shellock, F.; Zerhouni, E.; Stark, D.; Outwater, E. K.; Schmiedl, U.; Kirby, L. C.; Chezmar, J.; Coates, T.; Chang, M.; Silverman, J. M.; Rofsky, N.; Burnett, K.; Engel, J.; Young, S. W. *J. Magn. Reson. Imaging* **1997**, *7*, 865-872.
- (7) Young, S. W.; Qing, F.; Rubin, D.; Balkus, K. J.; Engel, J. S.; Lang, J.; Dow, W. C.; Mutch, J. D.; Miller, R. A. *J. Magn. Reson. Imaging* **1995**, *5*, 499-508.
- (8) Csajbók, É.; Bányai, I.; Vander Elst, L.; Muller, R. N.; Zhou, W.; Peters, J. A. *Chem. Eur. J.* **2005**, *11*, 4799-4807.
- (9) Peters, J. A.; Djanashvili, K. *Eur. J. Inorg. Chem.* **2012**, *2012*, 1961-1974.
- (10) Aime, S.; Cabella, C.; Colombatto, S.; Geninatti Crich, S.; Gianolio, E.; Maggioni, F. *J. Magn. Reson. Imaging* **2002**, *16*, 394-406.
- (11) Newell, P. A.; Rees, L. V. C. *Zeolites* **1983**, *3*, 22-27.
- (12) Frullano, L.; Meade, T. *J. Biol. Inorg. Chem.* **2007**, *12*, 939-949.
- (13) Barrer, R. M.; Villiger, H. Z. *Kristallgr.* **1969**, *128*, 352.
- (14) Bünzli, J.-C. G. *Chem. Rev.* **2010**, *110*, 2729-2755.
- (15) Tóth, É.; Helm, L.; Merbach, A. In *The Chemistry of Contrast Agents in Medical Magnetic Resonance Imaging*; John Wiley & Sons, Ltd: 2013, p 25-81.
- (16) Caravan, P.; Ellison, J. J.; McMurry, T. J.; Lauffer, R. B. *Chem. Rev.* **1999**, *99*, 2293-2352.
- (17) Corsi, D. M.; Platas-Iglesias, C.; Bekkum, H. v.; Peters, J. A. *Magn. Reson. Chem.* **2001**, *39*, 723-726.
- (18) Horrocks, W. D.; Sudnick, D. R. *J. Am. Chem. Soc.* **1979**, *101*, 334-340.
- (19) Gillis, P.; Peto, S.; Muller, R. N. *Magn. Reson. Imaging* **1991**, *9*, 703-708.
- (20) Kubiček, V.; Rudovský, J.; Kotek, J.; Hermann, P.; Vander Elst, L.; Muller, R. N.; Kolar, Z. I.; Wolterbeek, H. T.; Peters, J. A.; Lukeš, I. *J. Am. Chem. Soc.* **2005**, *127*, 16477-16485.

- (21) Rehor, I.; Kubicek, V.; Kotek, J.; Hermann, P.; Lukes, I.; Szakova, J.; Vander Elst, L.; Muller, R. N.; Peters, J. A. *J. Mater. Chem.* **2009**, *19*, 1494-1500.
- (22) Vitha, T.; Kubíček, V.; Hermann, P.; Elst, L. V.; Muller, R. N.; Kolar, Z. I.; Wolterbeek, H. T.; Breeman, W. A. P.; Lukeš, I.; Peters, J. A. *J. Med. Chem.* **2008**, *51*, 677-683.
- (23) Norek, M.; Neves, I. C.; Peters, J. A. *Inorg. Chem.* **2007**, *46*, 6190-6196.
- (24) Platas-Iglesias, C.; Vander Elst, L.; Zhou, W.; Muller, R. N.; Geraldes, C. F. G. C.; Maschmeyer, T.; Peters, J. A. *Chem. Eur. J.* **2002**, *8*, 5121-5131.
- (25) Bloembergen, N.; Morgan, L. O. *J. Chem. Phys.* **1961**, *34*, 842-850.
- (26) Solomon, I. *Phys. Rev.* **1955**, *99*, 559-565.
- (27) Tse, N. M. K.; Kennedy, D. F.; Kirby, N.; Moffat, B. A.; Muir, B. W.; Caruso, R. A.; Drummond, C. J. *Adv. Healthcare Mater.* **2013**, *2*, 836-845.
- (28) Caro, J.; Höcevar, S.; Kärger, J.; Riekert, L. *Zeolites* **1986**, *6*, 213-216.
- (29) Barge, A.; Cravotto, G.; Gianolio, E.; Fedeli, F. *Contrast Media Mol. Imaging* **2006**, *1*, 184-188.
- (30) The w -value was calculated from the molecular formula of the zeolite $K_6Na_3(H_2O)_{21}Al_9Si_{27}O_{72}$ in combination with the loading. In detail, an average of one Gd^{3+} ion per unit cell was loaded into the framework. 21 water molecules are present per unit cell of which 15 are free and 6 are coordinated to the Gd-center ($q = 6$).

Prototropic Exchange Governs T_1 and T_2 Relaxivities of Nanozeolite Gd-LTL with High pH Responsiveness

3



INTRODUCTION

Magnetic resonance imaging (MRI) has found widespread applications in biomedical diagnostics. The contrast in resulting images originates from differences in water content in soft tissues and from variations in the longitudinal (T_1) and transverse (T_2) relaxation times of water protons. Contrast agents (CAs) improve the contrast by taking advantage of paramagnetic metal ions to reduce the relaxation times.¹⁻⁴ The efficacy of a CA is usually expressed as its relaxivity (r_i , $i = 1,2$), which is the relaxation rate enhancement expressed in $s^{-1} \text{ mM}^{-1}$ paramagnetic metal ion). CAs with small r_2/r_1 ratios give rise to bright spots in T_1 -weighted images and are called positive or T_1 CAs. Presently, most clinically applied T_1 CAs are low-molecular Gd-chelates, like Gd-DTPA and Gd-DOTA. T_2 or negative CAs decrease T_2 of water protons significantly more than their T_1 ($r_2 \gg r_1$) and afford dark spots in T_2 - or T_2^* -weighted images. Iron oxide-based nanoparticles are the main representatives of this class.

MRI is superior compared to other imaging techniques with respect to resolution and penetration depth, but the low sensitivity of the presently applied clinical MRI CAs is a serious shortcoming, particularly because CAs distribute rather unselectively over the body. Nanoparticles may be employed to overcome this by delivering a high payload of Gd^{3+} at points of interest such as, for example, tumors or arterial plaques. The resulting high local concentration of paramagnetic substance dramatically boosts the contrast in the area of interest. The local accumulation may be further enhanced by attachment of targeting vectors to the nanoparticles and/or by exploiting the enhanced permeability and retention effect, the propensity of nanoparticles to accumulate in tumors through the leaky neovasculature. The diagnostic value may be increased if the CAs are responsive to specific physiological parameters of the tissues in which the CAs are localized, such as pH, temperature, redox potential, and concentration of endogenous ions.

Much effort is focused on designing multimodal imaging probes. Those CAs can be used in more than one imaging technique either separately or simultaneously (for instance in PET-MRI) to compensate the weaknesses of one modality with the strength of the other.⁵ Furthermore, there is an increasing interest in the development of agents that can be applied for both diagnosis and therapy (theranostics).⁶ Nanoparticulate, water permeable silicas and

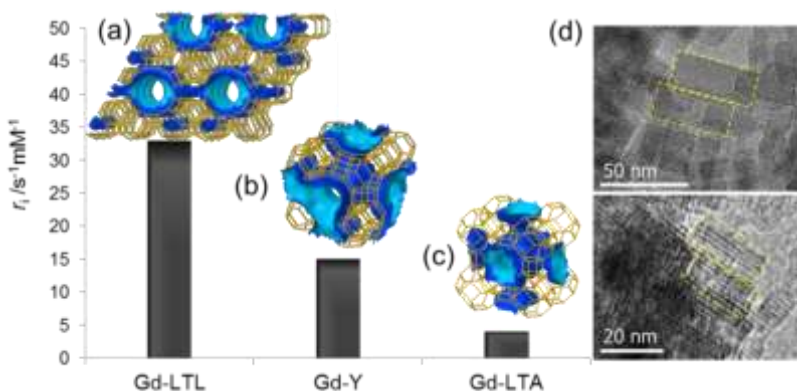


Figure 3.1. Illustration of 3D structures of zeolites with the water-accessible pores (blue). The zeolite Na-LTL (a) clearly shows parallel 1D-channels with a diameter of 7.1 Å at the narrowest point; zeolites Na-Y (b) and Na-LTA (c) show 3D-intercrossing channel systems with the size of entrance windows 7.4 and 4.1 Å, respectively. The columns represent the resultant longitudinal relaxivities of the zeolites with Gd³⁺-loadings of 1.6%, 1.3% and 1.5% for Gd-LTL,¹⁴ Gd-Y¹⁰ and Gd-LTA,¹¹ respectively (25 °C, 300MHz). d) TEM image of zeolite Na-LTL crystals.

zeolites are particularly attractive in this respect because they are suitable for the attachment of paramagnetic metal ions (for MRI), radioactive metal ions (for SPECT, PET, and radiotherapy), fluorescent materials, and for the confinement of therapeutic agents.⁷

Zeolites are aluminosilicates that in contrast to common silica are crystalline structures with well-defined pores and cavities. The AlO₄-tetrahedra provide a negative charge to the framework, which is counterbalanced by non-framework cations, usually alkali ions, which can easily be exchanged with other cations. In this way, Gd³⁺-exchanged zeolite Na-Y has been prepared and used as an oral T_1 MRI CA for imaging of the gastrointestinal tract,^{8,9} and later has been proposed as intravenous CA.¹⁰ The efficacy of these CAs is very high but still limited by the rather slow water exchange between the interior of zeolites and the bulk.¹¹ This was confirmed by comparison with the results of experiments with Gd³⁺-loaded Na-LTA nanozeolites, which have supercages of about the same size as Na-Y but the access to these cages is through an 8-membered ring with diameter of only 4.1 Å as compared to the 12-membered entrance ring of Na-Y with diameter 7.4 Å for zeolite Na-Y (Figure 3.1b,c).¹¹ Upon calcination, the Gd³⁺ ions in Gd-Y and Gd-LTA zeolites move irreversibly from the large cages to the smaller surrounding sodalite cages or their

hexagonal entrance windows and then become less accessible for water, resulting in a decrease in relaxivity. Partial destruction of walls between cavities by treatment with $(\text{NH}_4)_2\text{SiF}_6$ or diluted HCl resulted in an increase of r_1 due to the increase of the amount of non-coordinated water inside the zeolite. Zeolites with higher Si/Al ratios had higher relaxivities by virtue of an increased water exchange rate between the interior and the exterior of the zeolite.¹²

Dual MRI/optical probes have been constructed from zeolite LTL (Linde Type L).¹³⁻¹⁵ This zeolite has a framework with a pore system that is based upon so-called cancrinite cages, which are connected via their upper and lower six-membered rings to form columns (Figure 3.1a), interlinked to neighboring columns through oxygen bridges. This peculiar arrangement creates large undulating channels, which are separated from each other by elliptical 8-membered ring channels, parallel to the original columns along the c-axis of the crystal. The large 12-membered ring channels have free diameters between 7.1 Å at the most narrow and 12.6 Å at the widest point. Ion exchange exclusively takes place in the latter channels. A dual probe has been synthesized by ion exchange of the K^+ counter ions of the zeolite channels with a cationic dye for optical imaging and by functionalization of the Si–OH groups on the external surface with Gd^{3+} - or Eu^{3+} -DOTA chelates for MRI.¹³

Recently, we have prepared a different type of dual probe based on zeolite LTL. This probe had Gd^{3+} and Eu^{3+} both at the inside of the zeolite, but at different locations: Eu^{3+} was selectively deposited in the narrow and Gd^{3+} in wide channels of the LTL framework.¹⁴ The Gd^{3+} -ions have 6 water molecules in their first coordination sphere, whereas the confinement in the narrow channels leaves only space for coordination of a single water molecule to Eu^{3+} . This design is advantageous for the performance in MRI as well as in optical imaging, due to the fact that coordinated water is very desirable for increased relaxivity, whereas it is efficiently quenching luminescence. Consequently, Gd^{3+} is an efficient MRI probe and Eu^{3+} an efficient luminescent probe in this material. Surprisingly, the longitudinal relaxivity of this Gd^{3+} exchanged zeolite LTL is much higher than that of the previously investigated zeolite Gd-Y with similar Gd^{3+} -loadings.¹⁰ Even though the access of the channels in both zeolitic systems is through 12-membered ring entrance windows with a diameter of about 7.1 Å, the water exchange between the interior and the exterior was not limiting the longitudinal relaxivity of Gd-LTL,¹⁴ in contrast to the situation observed for Gd-Y¹⁰⁻¹² and also to that in a recently reported study on Gd^{3+} -loaded

mesoporous materials with pore sizes that were even an order of magnitude larger than that of the zeolites.¹⁶ To better understand this phenomenon, we have now performed more detailed relaxation studies to elucidate the origin of the unexpected high relaxivity of Gd-LTL. At the same time we have performed transverse relaxivity studies to investigate whether these materials have potential as T_2 CA as well. Generally, for Gd^{3+} -containing nanoparticles, the transverse relaxivity at higher magnetic fields steeply increases, whereas the longitudinal relaxivity decreases with increasing field strength.¹¹ Therefore, these materials might be promising as T_1 MRI CA at low field, and as T_2 CA at higher fields.

RESULTS AND DISCUSSION

Preparation of Ln^{3+} -loaded zeolite LTL

Cylindrical nanoparticles of zeolite LTL (radius 10 nm, height 40 nm, Figure 3.1d) were loaded with Ln^{3+} ($Ln = La, Gd, Ho$) by ion-exchange with the appropriate $LnCl_3$ in an aqueous suspension at room temperature.¹⁴ The extent of loading could easily be controlled by variation of the amount of $LnCl_3$ in suspension. The maximum loading reached for Gd^{3+} was 5.2 wt%, which is in good agreement with the amount of alkali ions (3) located in the easily accessible sites of the zeolite prior to exchange. A part of the loaded zeolites obtained was calcined at 600 °C, which leads to migration of Ln^{3+} -ions from the large channels to locked sites in the hexagonal prism, the cancrinite cage, and in between cancrinite cages.²⁰ The Ln^{3+} -ions that did not migrate during the calcination were extracted with a saturated aqueous NH_4Cl solution to obtain samples Ln -LTL-E.²⁰ In this way, loadings up to 3.3 wt% Gd^{3+} located exclusively in the locked sites were achieved, which suggests that the alkali ions in the “locked” sites can only be partially exchanged for Gd^{3+} -ions. Previously, we have shown by XRD that the integrity of the zeolite framework remains intact after exchange, calcination, and extraction.¹⁴

The Gd^{3+} ions in Gd-LTL-E have only one water molecule in their first coordination sphere, whereas those of Gd-LTL-L have six. Consequently, the paramagnetic NMR effects in aqueous suspensions of Gd-LTL-E are generally smaller and the data are less accurate than those of Gd-LTL-L. However, the trends in these data are similar to those shown by Gd-LTL-L.

Dependence of the longitudinal relaxivity of Gd-LTL suspensions on the pH

Previously, we have fitted the inner-sphere longitudinal relaxivity of Gd-LTL-L with 5.2 % loading using a two-step mechanism,¹⁴ in which first only the relaxivity inside the zeolite cavity is considered and treated as a concentrated solution of Gd³⁺-ions.¹⁰ In the second step, the propagation of the relaxation enhancement from the interior water of zeolite to the bulk water outside was taken into account (Figure 2.10, in Chapter 2). It appeared that for zeolite LTL, the residence time of protons inside the zeolite, τ_{zeo} , was so short ($\tau_{\text{zeo}} \leq 10^{-8}$ s) that this parameter was not limiting the longitudinal relaxivity. As stated in the introduction, the short τ_{zeo} is unexpected in view of other results obtained with zeolitic and mesoporous systems.^{10-12,16} A possible reason for this phenomenon may be that the relaxivity of the Gd-LTL system is not governed by exchange of water molecules in the first coordination sphere of Gd³⁺ but by prototropic exchange, which is surprising because normally proton exchange is much slower than whole water exchange at physiological pH.²¹⁻²³

Aime et al. have shown that the exchange of whole water for some highly kinetically stable cationic Gd³⁺-complexes of tetraamide DOTA derivatives in homogeneous solutions is so slow ($\tau_{\text{m}} = 8-17$ μs) that it is possible to evaluate the contribution of the prototropic exchange, which appeared to be acid and base catalyzed.²³ The latter was reflected in an increase of the relaxivity below pH 2 and above pH 8 for these compounds. Since we suspected that catalysis of prototropic exchange might be involved in the observed fast proton exchange observed in the presently studied suspensions of Gd-LTL as well, we have investigated the relaxivity of Gd-LTL as a function of the pH. A substantial dispersion of the relaxivity centered at a pH value around 7 was observed. At higher pH the relaxivities, r_1 as well as r_2 , decreased significantly, while no increase of the relaxivity occurred upon further increase of the pH. All pH effects were completely reversible and xylenol orange tests²⁴ showed that leaching of Gd³⁺-ions out of the zeolite particles did not occur in the pH range investigated. The reversible pH dependence of r_1 that we observed for Gd-LTL (3.5 wt % Gd loading) suggests that prototropic exchange dominates here at pH < 7 (Figure 3.2). It should be noted that the relaxivity of previously investigated zeolite systems did not show any pH dependence.¹⁰⁻¹²

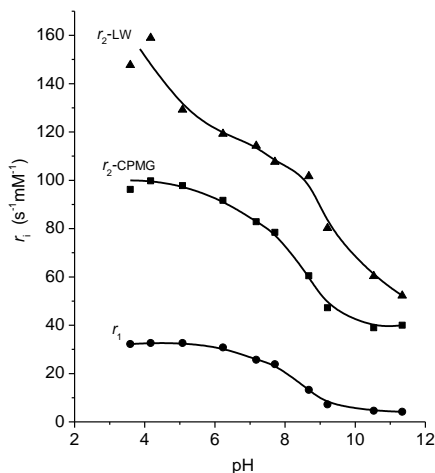


Figure 3.2. The relaxivity of aqueous samples of Gd-loaded LTL-L (3.5 wt % Gd) as a function of pH at 7.5 T and 25 °C in the presence of 0.5 wt% xanthan as dispersant; ● r_1 ; ■ r_2^{CPMG} as measured with $\tau_{\text{CP}} = 0.5$ ms; ▲ r_2^{LW} the curves are guides to the eye.

For the interior of the zeolite, r_1 and r_2 will be governed by the exchange of protons between the Gd-bound water and the water in the pores. It may be expected that the residence time of a water molecule in the first coordination sphere of Gd^{3+} for Gd-LTL-L is of about the same magnitude as that on the Gd-aquo ion ($\tau_{\text{m},0} = 1.2$ ns, the label O indicates that it concerns the parameter for whole water, the corresponding parameters for protons are not labeled)²⁵ and of that observed for Gd-Y ($\tau_{\text{m},0} = 10$ ns for 3.6 % Gd^{3+} -loading).¹⁰ The overall relaxivity of the Gd-LTL zeolites at $\text{pH} > 8$ seems to be limited by the slow exchange of (whole) water between the interior and the bulk water outside the zeolite. A changeover from relatively slow water exchange between cavities and bulk to fast prototropic exchange may explain the large increase in relaxivities observed upon decreasing the pH below 8 (Figure 3.2). Since this effect seems to be unique for Gd-LTL, it most likely can be explained by the structure of this zeolite. It has been demonstrated that the peculiar partition of the non-framework cations in zeolite LTL allows for variable amounts of water molecules to form 1D clusters exclusively in the main channel system.^{26,27} The presence of such confined water clusters has been confirmed by high-resolution synchrotron X-ray powder diffraction in a gallosilicate with LTL topology (see Figure 3.3).²⁷

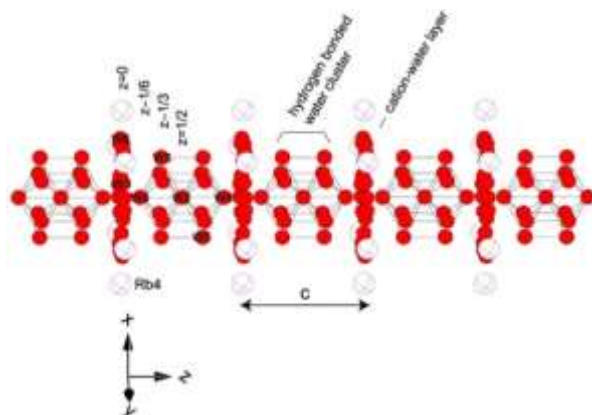


Figure 3.3. Non-framework contents inside the 12-ring channel of hydrated Rb-GaSi-LTL, illustrating the alternation of hydrogen bonded (with bars) water clusters and cation-water layers along the c -axis. Oxygen atoms from water molecules are depicted by filled circles, and rubidium cations at site D (Rb4) are depicted by open circles. The Rb4 and water sites are not fully occupied. The arrow indicates the c -axis length. Reprinted with permission from Lee, Y.; Kim, S. J.; Ahn, D.-C.; Shin, N.-S. *Chem. Mater.* **2007**, *19*, 2277. Copyright 2007, American Chemical Society.

Probably, a reaction path of very fast hops of water protons from the first coordination sphere of the Gd^{3+} -ion across clusters of hydronium ions (connected by hydrogen bonds) to the bulk water outside the zeolite is dominating the propagation of the relaxivity to the bulk water outside the zeolite (see Figure 3.4). Such a proton hopping mechanism, also known as the Grotthuss mechanism,²⁸ has been put forward as an explanation for the exceptionally high water proton mobility in zeolites²⁹⁻³³ and a similar mechanism has been proposed for the high methanol proton mobility in zeolite ZSM-5.³⁴ The protonated clusters may be associated with the Brønsted acidic silanol groups,³⁴ framework oxygen atoms, and Gd^{3+} -bound water molecules.

Above pH above 7, the water structuring inside the zeolite may be disrupted by ionization of the silanol groups, ionization of the Gd^{3+} -bound water molecules ($\text{p}K_{\text{a}} \approx 8$)³⁵ and by the low concentration of hydronium ions. As a result, the propagation of the relaxivity is then dominated by the much slower whole water exchange between zeolite interior and the bulk. The ionization of a Gd^{3+} -bound water molecule gives rise to an additional drop in relaxivity due to the accompanied decrease in q (the number of Gd^{3+} -coordinated water molecules) by 0.5 due to the loss of a Gd -coordinated water proton.

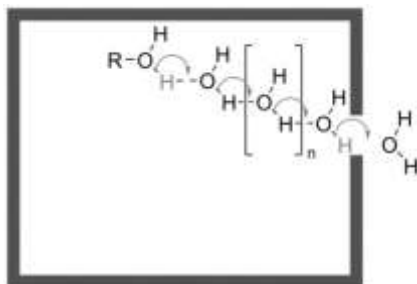


Figure 3.4. Schematic representation of the Grotthuss proton hopping mechanism proposed for the fast proton exchange observed for Gd-LTL below pH 7; R = H⁺, Gd³⁺.

By virtue of the large jump in relaxivity of Gd-LTL-L between pH 5 and 7.5 ($\Delta r_1 \approx 9 \text{ mM}^{-1} \text{ s}^{-1}$, $\Delta r_2 \approx 15 \text{ mM}^{-1} \text{ s}^{-1}$, at 7.5 T, see Figure 3.2), this material has great potential as pH responsive contrast agent with desirable r_2/r_1 ratio (3-4), particularly if one considers that each nanoparticle of 3.5 wt% Gd-loaded LTL-L contains about 2700 Gd³⁺-ions.

¹⁷O NMR measurements on Gd-LTL suspensions

Dominance of the prototropic exchange for the Gd-LTL system at pH < 6.5 should lead to exchange rates of water that differ from the proton exchange rate governing the longitudinal relaxivity. To verify this, information on the (whole) water exchange rates can be obtained from ¹⁷O NMR chemical shift and relaxation time measurements.¹ In the present case, the ¹⁷O NMR measurements could only be performed over a small temperature range (15 - 41 °C) to avoid irreversible changes in the relaxation rates caused by the xanthan dispersant blocking the pores of the zeolite.¹⁴ Longitudinal and transverse relaxation rates and chemical shifts were measured at 7.5 T for a sample of Gd-LTL-L with 5.2 wt % Gd³⁺-loading. The exchange rate of water will be limited by the relatively slow exchange between water in the pores and the external bulk water. Therefore, the 2-step model mentioned before should be considered for the interpretation of the data (Figure 2.10 in Chapter 2).¹⁰ The observed ¹⁷O NMR relaxation rates ($T_{1p,O}^{-1}$, $T_{2p,O}^{-1}$) and angular frequencies ($\Delta\omega_{p,O}$) of the suspensions, after correction for diamagnetic contributions by subtraction of data of a corresponding La-LTL-L sample (see Table 3.1), can be written as in Equations 3.1-3.3, where $T_{1zeo,O}^{-1}$ and $T_{2zeo,O}^{-1}$ are the longitudinal and the transverse

relaxation rates of water inside the zeolite pores, $\Delta\omega_{zeo,O}$ is the angular frequency,³⁶⁻³⁹ $\tau_{zeo,O}$ is the residence time of a (whole) water molecule in the interior of the zeolite, and $P_{zeo,O}$ is molar fraction of interior free water molecules per Gd^{3+} ion. Outer sphere contributions can be neglected in Equations 3.1-3.3.¹⁰

$$T_{2p,O}^{-1} = P_{zeo,O} \frac{(\tau_{zeo,O}^{-1} + T_{2zeo,O}^{-1})/T_{2zeo,O} + \Delta\omega_{zeo,O}^2}{(\tau_{zeo,O}^{-1} + T_{2zeo,O}^{-1})^2 + \Delta\omega_{zeo,O}^2} \quad 3.1$$

$$T_{1p,O}^{-1} = P_{zeo,O} \frac{1}{\tau_{zeo,O} + T_{1zeo,O}} \quad 3.2$$

$$\Delta\omega_{p,O} = P_{zeo,O} \frac{\Delta\omega_{zeo,O}}{(\tau_{zeo,O} T_{2zeo,O}^{-1} + 1)^2 + \Delta\omega_{zeo,O}^2 \tau_{zeo,O}^2} \quad 3.3$$

Since the contribution of $\Delta\omega_{zeo,O}$ in Equation 3.1 is relatively small, this Equation can be approximated by simplified Equation 3.4.

$$T_{2p,O}^{-1} = P_{zeo,O} \frac{1}{\tau_{zeo,O} + T_{2zeo,O}} \quad 3.4$$

In the fast exchange limit, $T_{2zeo,O}$ is the principal term in the denominator of Equation 3.4, while in the slow-exchange limit at $\tau_{zeo,O}$ is the principal term. Since $\tau_{zeo,O}$ decreases, while $T_{2zeo,O}$ increases with increasing temperature, $T_{2p,O}^{-1}$ decreases with temperature in the fast exchange limit, whereas the opposite holds for the slow exchange limit. The experimental values for $T_{2p,O}^{-1}$ decrease with temperature in the present case (see Table 3.1), it can be concluded that the fast exchange regime holds here. This is not unexpected because the local concentration of Gd^{3+} inside the zeolite is very high. For the fast exchange limit Equations 3.1-3.3 can be simplified to Equations 3.5 and 3.6.⁴⁰ Here, w is the number of free water molecules inside the zeolite per Gd^{3+} -ion, q is the number of water molecules coordinated to Gd^{3+} , P_m is the molal fraction of Gd^{3+} in the system ($P_{zeo,O} = wP_m/q$), and $\Delta\omega_{m,O}$ is the angular frequency of a Gd^{3+} bound water molecule ($\Delta\omega_{zeo,O} = q\Delta\omega_{m,O}/w$).

$$T_{2p,O}^{-1} - T_{1p,O}^{-1} = P_{zeo,O} \Delta\omega_{zeo,O}^2 \tau_{zeo,O} = qP_m \Delta\omega_{m,O}^2 \tau_{zeo,O} / (w + q) \quad 3.5$$

$$\Delta\omega_{p,O} = P_{zeo,O} \Delta\omega_{zeo,O} = P_m \Delta\omega_{m,O} \quad 3.6$$

Table 3.1. ^{17}O NMR measurements of Gd-LTL-L and Gd-LTL-E samples. ^a

T (K)	$\Delta\omega_{p,O}$ (10^6 rad s^{-1}) ^b	$1/T_{2p,O}$ (s^{-1}) ^b	$1/T_{1p,O}$ (s^{-1}) ^b	$\tau_{zeo,O}$ (μs)
<i>Gd-LTL-L</i>				
288.15	-0.461	108	12.1	1.9
293.15	-0.589	104	8.0	1.1
298.45	-0.452	109	9.9	2.0
303.15	-0.460	86	9.7	1.5
308.65	-0.421	71	7.8	1.5
314.35	-0.371	62	5.9	1.7
<i>Gd-LTL-E</i>				
298.15	-1.007	1	0.03	0.1

^aThe Gd^{3+} concentration of Gd-LTL-L sample is 2.248 mM, measured by bulk magnetic susceptibility (ref. 19). ^bAll data are with respect to the corresponding diamagnetic La-LTL-L sample. Chemical shifts were corrected for the BMS contribution as described in ref. 19.

The values of $\tau_{zeo,O}$ in Gd-LTL-L were evaluated by solving Equations 3.5 and 3.6 using the experimental values of $T_{1p,O}$, $T_{2p,O}$, $\Delta\omega_{p,O}$ and the previously determined values of q and w (6 and 15, respectively).¹⁴ The values of $\tau_{zeo,O}$ obtained varied from 4-7 μs for the temperature range investigated (see Table 3.1). Although the accuracy of these numbers is low due to the small magnitudes of the experimental data, they show that the exchange rate of (whole) water between the interior of the zeolite and that of bulk ($\tau_{zeo,O} \approx 7 \mu\text{s}$ at 298 K) is 3 orders of magnitude larger than the corresponding exchange rates of protons as evaluated from the ^1H NMRD profile ($\tau_{zeo} \approx 10$ ns),¹⁴ which confirms that prototropic exchange is dominating the relaxivity of Gd-LTL. The value for $\tau_{zeo,O}$ is of the same order of magnitude as that determined for previously studied zeolitic Gd-Y and Gd-A systems ($\tau_{zeo} \approx 30 \mu\text{s}$),¹² where prototropic exchange is unimportant.

Transverse electronic relaxation rates by EPR measurements on Gd-LTL suspensions

To investigate possible clustering of Gd^{3+} in the interior of the zeolite, X-band EPR spectra of the various Gd-LTL-L zeolite nanoparticles were studied in aqueous suspensions at 298 K (Figure 3.5). They display a single, approximately Lorentzian resonance at a field corresponding to a Landé g -factor, $g_L \approx 2$, probably resulting from rotational averaging of the various anisotropic magnetic interactions present (g tensor, hyperfine tensor and zero-field splitting tensor).

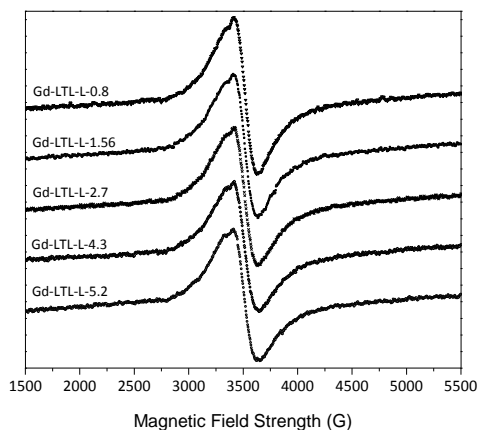


Figure 3.5. EPR spectra (0.34T, 9.43 GHz) of aqueous Gd-LTL-L suspensions. The samples are coded according to their Gd³⁺-loading (in wt%).

The transverse electronic relaxation rates, $1/T_{2e}$, were calculated from the peak-to-peak EPR line widths of the derivative of the absorption mode, ΔH_{pp} , with Equation 3.7, in which μ_B is the Bohr magneton and h the Planck constant.⁴¹

$$T_{2e}^{-1} = \frac{g_L \mu_B \pi \sqrt{3}}{h} \Delta H_{pp} \quad 3.7$$

The values of $1/T_{2e}$ are almost independent of the Gd³⁺-loading up to about 4 wt%, the sample at 5.2 wt% loading had a significantly higher electronic relaxation rate (Figure 3.6). Gd³⁺-loaded Na-Y zeolite also showed an increasing trend of $1/T_{2e}$, but with a steeper slope at low Gd³⁺-loadings.¹⁰ This phenomenon may probably be ascribed to dipolar and/or weak antiferromagnetic interactions between Gd³⁺-ions, when they are in close proximity of each other, for example due to formation of Gd-O-Gd type of aggregates at higher loadings.^{10,42} Apparently, the linear pore system in LTL results in a better distribution of the Gd³⁺-ions than in the tetragonal pores of Y, which leads to an onset of dimerization only when the maximal loading is almost reached.

Transverse relaxivity of suspensions of the Gd³⁺-loaded zeolite LTL nanoparticles

Samples of 2.5 mg of the Gd-LTL-L in 1 mL of water were stabilized by addition of 1% xanthan gum. The pH of the samples obtained was 5.0-5.8. The transverse relaxation times

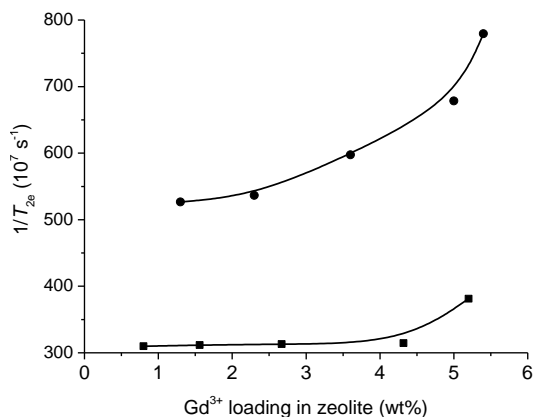


Figure 3.6. Transverse electronic relaxation rates ($1/T_{2e}$) of Gd³⁺-loaded zeolite LTL (Gd-LTL-L, ■) as obtained from EPR measurements (X band, 0.34 T, 9.43 GHz, 25 °C) on aqueous suspensions containing 0.5 wt% xanthan as emulsifier, compared to similar data for Gd-Y (●). The curves are guides to the eye.

(T_2) of these suspensions were determined by the Carr-Purcell-Meiboom-Gill (CPMG) pulse sequence (T_2^{CPMG})¹⁸ and through the line width ($1/T_2^{\text{LW}} = R_2^{\text{LW}} = \pi\Delta\nu_{1/2}$, where $\Delta\nu_{1/2}$ is the line width) at 7.5 T and 25 °C (see Table 3.2). The decay of the spin-echo signals of Gd-LTL-L in the CPMG experiment was always mono-exponential with a relaxation rate $R_2^{\text{CPMG}} (= 1/T_2^{\text{CPMG}})$ that was almost independent of the interval applied between successive 180° pulses ($0.2 \leq \tau_{\text{CP}} \leq 5$ ms). For comparison, the longitudinal relaxation rates of these samples were included in Table 3.2. The transverse relaxivities showed similar trends as a function of pH as the longitudinal relaxivities. Curves of r_2^{CPMG} and r_2^{LW} as a function of pH are included in Figure 3.2.

Table 3.2. Longitudinal and transverse relaxation of Gd-LTL-L.

Gd-loading (wt%)	Conc. (mM)	R_1 (s ⁻¹)	R_2^{CPMG} (s ⁻¹)	R_2^{LW} (s ⁻¹)	r_1 (s ⁻¹ mM ⁻¹)	r_2^{CPMG} (s ⁻¹ mM ⁻¹)	r_2^{LW} (s ⁻¹ mM ⁻¹)	Zeta mV	Gd-ions per particle
0.80	0.127	4.3	20	65	31	140	184	-35.5	530
1.56	0.248	8.3	32	81	32	122	159	-35.4	1100
2.70	0.425	13.1	41	90	30	92	114	-34.4	2000
4.30	0.687	18.0	60	109	26	85	98	-33.3	3300
5.20	0.798	21.0	68	128	26	84	108	-23.8	4100

The observed relaxation rates ($R_{2,obs}$) are the sum of diamagnetic ($R_{2,dia}$) and paramagnetic contributions ($R_{2,para}$) (Equation 3.8). To allow comparison of the efficacy of the relaxation enhancing compounds, the paramagnetic relaxation rate enhancement is expressed as the relaxivity, (r_2 , see Equation 3.9, where C is the concentration in mM Ln^{3+}).

$$R_{2,obs} = R_{2,dia} + R_{2,para} = R_{2,dia} + R_{2,1S} + R_{2,OS} \quad 3.8$$

$$r_2 = R_{2,para}/C = (R_{2,obs} - R_{2,dia})/C \quad 3.9$$

The diamagnetic contributions were estimated from the relaxation rates for similar suspensions of zeolite LTL loaded with the diamagnetic La^{3+} ions (see Table 3.3). These relaxation rates were almost identical to those of unloaded zeolite LTL and were, within the accuracy of the measurements, equal to the intercept of curves of R_2 versus amount of loading. Therefore, the observed relaxation rates were corrected for diamagnetic contributions by subtracting the relaxation rates of the corresponding La-LTL data.

The relaxivities evaluated after subtracting the diamagnetic contribution appear to be dependent on the loading of the Gd-LTL-L nanoparticles, the transverse relaxivities show a significant decrease with increasing loading (Figure 3.7, Table 3.2). In this respect, these materials differ from homogeneous solutions of Gd^{3+} -chelates, which have relaxivities that are independent of the Gd^{3+} -concentration in diluted aqueous solutions up to concentrations of at least 0.1 M. The transverse relaxivities obtained for Gd-LTL by CPMG experiments are somewhat lower than those obtained from the line widths. This may be explained by an exchange contribution to the line width that reduces the rate of spin-echo decay in the CPMG experiment (see below) and partly to inhomogeneities of the magnetic field due to imperfect shimming.

Table 3.3. Longitudinal and transverse relaxation rates of La-loaded zeolite LTL samples.

Sample name	La^{3+} loading (wt%)	R_1 (s^{-1})	R_2^{CPMG} (s^{-1})	R_2^{LW} (s^{-1})
La-LTL-L	5.2	0.33	1.9	46
La-LTL-C	5.2	0.34	1.6	47
La-LTL-E	3.3	0.36	1.5	45
LTL	-	0.35	1.4	41

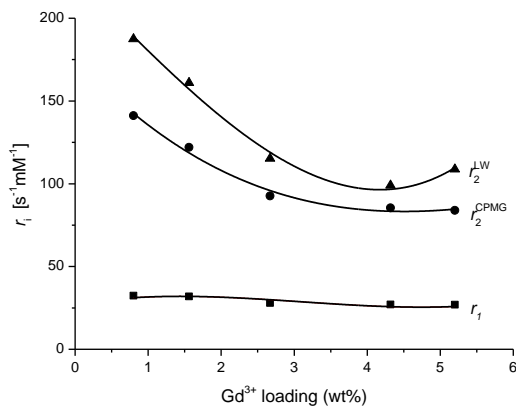


Figure 3.7. Relaxivities of Gd^{3+} -loaded zeolite LTL-L nanoparticles as a function of the Gd^{3+} content in aqueous suspension containing 2.5 mg Gd-LTL-L/mL and 0.5 wt% xanthan gum at 7.5 T and 25 °C. The curves are guides to the eye.

The paramagnetic relaxation rates ($R_{2,para}$) originate from a contribution due to exchange of bulk water molecules with water bound in the first coordination sphere of the paramagnetic metal ion (the inner sphere contribution, $R_{2,IS}$) and from effects that water molecules experience when they diffuse along the paramagnetic ions or through the magnetic field gradients induced by the Gd^{3+} -loaded zeolite particles without being bound (the outer-sphere contribution, $R_{2,OS}$).

The outer-sphere contribution to the relaxation rate can be evaluated by measuring the relaxation rates after addition of a compound that does not coordinate with the Ln^{3+} ion.⁴³⁻⁴⁵ However, the presently studied suspension is rather complex and addition of most compounds results in precipitation. As a compromise, we followed a modified procedure of Gossuin et al.⁴⁴ by measuring transverse relaxation rates of the methyl protons of methanol for samples of Gd-LTL-L in mixtures of methanol and water. ¹⁷O NMR measurements on solutions of $DyCl_3$ in water methanol mixtures have demonstrated that Ln^{3+} ions coordinate preferentially water molecules, for example the first coordination sphere of Dy^{3+} in a 1:1 mixture of methanol and water contains only 12 mol % methanol.⁴⁶ Therefore, in a first approximation the coordination of Gd^{3+} by methanol can be neglected, particularly since any coordination would have relatively small effects on the relaxation rates of the methyl protons because they are at large distance of the Gd^{3+} -ion as compared to water protons of coordinated water molecules. Figure 3.8 displays the observed transverse relaxivities versus

the reciprocal of the total concentration of OH protons (from water and methanol) for Gd-LTL-L samples with 1.6 and 5.2 wt% Gd³⁺-loading, Figure 3.9 shows a similar graph for Gd-LTL-E. If exclusively outer-sphere interaction would occur, the relaxation rate is only dependent on the concentration of Gd³⁺ and a horizontal line would be expected, whereas for inner-sphere interaction the relaxation rate would be proportional to the total number of protons participating in the exchange, hence to $1/C_{\text{OH}}$.⁴⁴ In Figure 3.8, it can be seen that the curve for the CH protons is nearly horizontal at low methanol concentrations (low $1/C_{\text{OH}}$); at higher methanol concentrations and higher Gd³⁺-loading the deviations become larger due to increasing inner-sphere complexation of methanol. Extrapolation of the curves for the CH protons to $1/C_{\text{OH}} = 0.09$ (corresponding to pure water) affords, after subtraction of the diamagnetic contribution, estimates of the outer-sphere contribution to the transverse relaxation. However, several complications may occur in the present case, such as the preferential absorption of methanol in hydrophobic pores of zeolite LTL nanoparticles, which will bring a relatively large amount of methanol in close proximity of the Gd³⁺ ions in the pores and thus will result in over-estimated values of $R_{2,\text{OS}}^{\text{CPMG}}$. Such an effect has also been observed in a study on esterification reactions catalyzed with zeolites.⁴⁷ Figures 3.8 and 3.9, however, clearly show that the inner-sphere contribution is dominating the relaxation of the OH protons whereas it is of minor importance in the CH relaxation. This contrasts with the relaxation behavior of solid particles, such as Ln-oxides and carbonates, where the relaxivity is almost exclusively determined by the outer-sphere mechanism.^{7,14,48,49}

Since no good theoretical models exist for the calculation of outer-sphere relaxivities in porous systems like zeolites, estimations were made using two extreme hypothetical models for this system. In the first model, the particles were considered to be impenetrable solid spheres, whereas in the second model a homogeneous aqueous solution of Gd³⁺ was used to model porous particles with unlimited access of water. The outer-sphere transverse relaxivity originates from water molecules experiencing the magnetic field gradients while diffusing along the Gd-LTL particles and from water molecules that diffuse through the large pores. The effect on the outside of the zeolite may be estimated by assuming the particles to be non-porous spheres with the same volume as the cylindrical LTL nanoparticles.

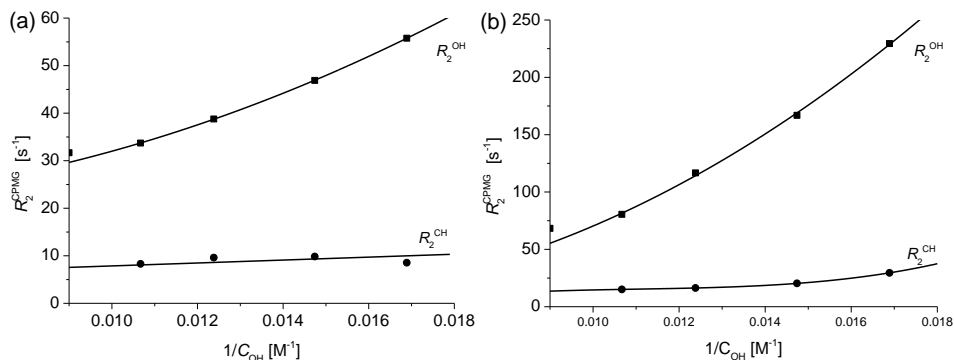


Figure 3.8. Transverse relaxation rates R_2^{CPMG} as a function of $1/C_{\text{OH}}$ for suspensions of Gd-LTL-L in various mixtures of methanol-water. (a) 1.6 wt % Gd³⁺ loading, (b) 5.2 wt % Gd³⁺-loading. The curves were obtained by fitting the experimental data with second order polynomial functions.

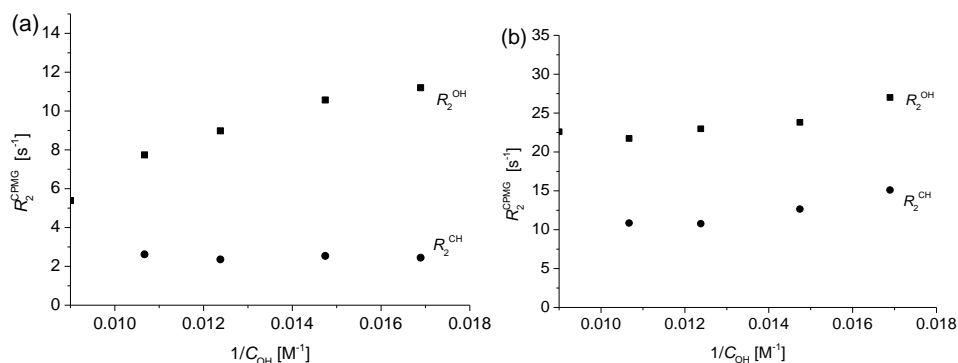


Figure 3.9. Transverse relaxation rates R_2^{CPMG} as a function of $1/C_{\text{OH}}$ for suspensions of Gd-LTL-E in various mixtures of methanol-water. (a) 1.6 wt % Gd³⁺ loading (before calcination), (b) 5.2 wt % Gd³⁺-loading (before calcination).

Since the Gd³⁺ content is lower than that of the previously studied solid Gd-carbonate particles for which the transverse relaxivity was in the motional averaging regime,¹⁴ this regime will hold in the present case as well. Then, $r_{2,\text{ext}}^{\text{OS}}$ is given by Equations 3.10-3.14,⁴⁸ where ν is the volume fraction occupied by the particles, τ_D the diffusion correlation time, $\Delta\omega$ the difference in resonance frequencies (in rad s⁻¹) of water protons at the surface and those in the bulk, R_p the radius of a particle, D the diffusion coefficient of water, μ_0 the permeability of a vacuum, γ_H the proton magnetogyric ratio, M_p the magnetization of a

particle, μ_C the Curie moment, μ_{eff} the effective magnetic moment of Gd^{3+} , B the magnetic field strength, k_B the Boltzmann constant, and T the temperature. The contributions of the external water to r_2^{OS} ($r_{2,\text{ext}}^{\text{OS}}$) were calculated to be only 0.3 and 0.9 $\text{s}^{-1} \text{mM}^{-1}$ for the Gd-LTL-L samples loaded with 1.6 and 5.2 wt% Gd^{3+} , respectively.

$$r_{2,\text{ext}}^{\text{OS}} = \frac{16}{45} \nu \tau_D (\Delta\omega)^2 \quad 3.10$$

$$\tau_D = \frac{R_p^2}{D} \quad 3.11$$

$$\Delta\omega = \frac{\mu_0 \gamma_H M_p}{3} \quad 3.12$$

$$M_p = \frac{n \mu_C}{V_p} \quad 3.13$$

$$\mu_C = \frac{\mu_{\text{eff}}^2 B}{3k_B T} \quad 3.14$$

Alternatively, we can get an impression of the importance of the outer sphere contribution by considering a homogeneous solution with the same Gd^{3+} concentration. For such a solution Equation 3.15 has been derived.⁵⁰

$$r_2^{\text{OS}} = \frac{16\pi N_A [M]}{405 \cdot 1000} \frac{\gamma_H^2 \mu_{\text{eff}}^2}{dD} [4J(0) + 13J(\omega_S) + 3J(\omega_I)] \quad 3.15$$

Where N_A is the Avogadro constant, $[M]$ the concentration of Gd^{3+} , d the distance of closest approach of water protons and Gd^{3+} and J the spectral density functions given by

$$J(\omega) = \text{Re}\left(\frac{1+z/4}{1+z+4z^2/9+z^3/9}\right) \text{ with } z = \sqrt{i\omega\tau_D + \tau_D/T_{ke}}; \tau_D = d^2/D; k = 1,2 \quad 3.16$$

Using the parameters obtained from the fitting of the ^1H NMRD profile of Gd-LTL,¹⁴ the value of r_2^{OS} would be 2.7 $\text{s}^{-1} \text{mM}^{-1}$ if it was a homogeneous solution. However in a suspension of Gd-LTL, only a part of the water protons will enter the zeolite and can approach the Gd^{3+} ions closely enough to experience the effect. These calculations confirm the minor importance of the outer-sphere contribution to the overall reactivity for the Gd-LTL zeolites. Therefore r_2^{OS} was not included in any further calculations.

Previously, we have derived that for the two-step mechanism the transverse relaxation rate of inner-sphere water protons can be expressed as in Equations 3.17-3.18.¹¹

$$r_2 = \frac{1}{1000} \frac{(q+x) T_{2zeo}^{-1} (T_{2zeo}^{-1} + \tau_{zeo}^{-1}) + \Delta\omega_{zeo}^2}{55.5 \tau_{2zeo} (T_{2zeo}^{-1} + \tau_{zeo}^{-1})^2 + \Delta\omega_{zeo}^2} \quad 3.17$$

$$T_{2zeo}^{-1} = \frac{q}{(w+q)T_{2m}} \quad 3.18$$

Here, $\Delta\omega_{zeo}$ is the frequency difference between the water protons in the bulk and in the interior of the zeolite cavities; T_{2zeo} , the transverse relaxation time of water protons in the interior of the zeolite, and τ_{zeo} is the average residence time of a water molecule in the zeolite pore system (It should be noted that all parameters here concern water protons). The transverse relaxation time of Gd-bound water protons, T_{2m} , is of predominant dipolar nature and can be given by:^{51,52}

$$T_{2m}^{-1} = \frac{1}{15} \left(\frac{\mu_0}{4\pi} \right)^2 \gamma_H^2 \mu_{eff}^2 \frac{q}{r^6} \left(4\tau_{d1} + \frac{3\tau_{d1}}{1+\omega_I^2\tau_{d1}^2} + \frac{13\tau_{d2}}{1+\omega_S^2\tau_{d2}^2} \right) \quad 3.19$$

Here r is the distance between Gd^{3+} and the bound water protons, ω_I and ω_S are the angular precession frequencies of proton and electron, respectively, and τ_{di} ($I = 1,2$) the correlation times modulating the dipolar interaction ($\tau_{di}^{-1} = \tau_r^{-1} + \tau_m^{-1} + T_{ie}^{-1}$). The electronic longitudinal and transverse relaxation rates (T_{ie} , $I = 1,2$) are given by Equations 3.20 and 3.21, respectively,⁵³ where Δ^2 is the mean squared fluctuation of the zero field splitting (ZFS) and τ_v is the correlation time for the modulation of the ZFS.

$$T_{1e}^{-1} = \frac{1}{25} \Delta^2 \tau_v [4S(S+1) - 3] \left(\frac{1}{1+\omega_S^2\tau_v^2} + \frac{4}{1+4\omega_S^2\tau_v^2} \right) \quad 3.20$$

$$T_{2e}^{-1} = \Delta^2 \tau_v \left(\frac{5.26}{1+0.372\omega_S^2\tau_v^2} + \frac{7.18}{1+1.24\omega_S\tau_v} \right) \quad 3.21$$

For homogeneous solutions of Gd^{3+} chelates, the bound shift is exclusively of a Fermi contact character and it is estimated to be 23 ppm.^{54,55} In the present case, the Gd^{3+} -bound water are located in the 1-dimensional pores of the cylindrical nanoparticles that contain about 4000 Gd^{3+} per particle (5.2 wt % Gd loading, Table 3.2). Because of the magnetization, the particles may orient along the magnetic field to some extent and therefore, it cannot be excluded that $\Delta\omega_{zeo}$ has a bulk magnetic susceptibility shift (BMS) contribution as well. Both, the contact and the BMS contributions are linearly proportional to the magnetic field strength B , and therefore it is convenient to convert $\Delta\omega_{zeo}$ into the

corresponding chemical shift difference, $\Delta\delta_{zeo}$ (in ppm) using Equation 3.22, where LF is the Larmor frequency.

$$\Delta\delta_{zeo} = \frac{10^6 \Delta\omega_{zeo}}{2\pi LF} \quad 3.22$$

The observed decrease in relaxivity upon raising Gd^{3+} -loading (Figure 3.7) could be due to blocking of the diffusion of water protons through the zeolite, for example because of formation of Gd-hydroxide oligomers. However, this explanation can be rejected because the EPR measurements (see above) indicated that this occurred only in the sample with 5.2 wt% loading, whereas the most significant decrease in relaxivity took place between 1 and 4 wt% Gd^{3+} . Furthermore, zeolite LTL exchanged with a mixture of Gd^{3+} and La^{3+} ions in such a way that the resulting samples containing 0.8 wt% Gd^{3+} and various amounts of La^{3+} , showed both r_1 and r_2 values that were almost identical to those of zeolites exclusively loaded with Gd^{3+} -ions and having the same total Ln^{3+} content (Figure 3.10).

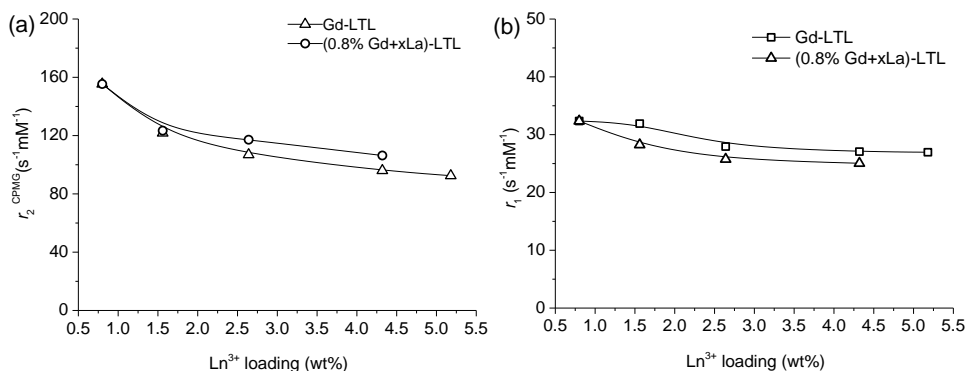


Figure 3.10. (a) r_2^{CPMG} of Gd-LTL and Gd-La-LTL. The Gd-La-LTL samples had loadings consisting of 0.8 wt% Gd^{3+} and an amount of La^{3+} to give the total Ln^{3+} -loading as indicated on the horizontal axis. (b) The corresponding r_1 relaxivities. All the measurements were performed at 25°C and 7.5 T.

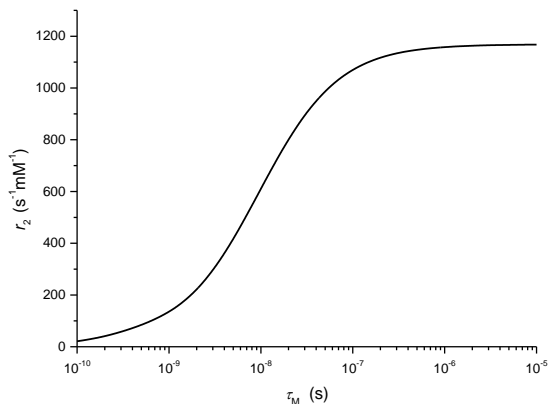


Figure 3.11. Simulation of r_2^{IS} as a function of τ_M using Equations 3.15-3.21, $LF = 300$ MHz and $|\Delta\delta| = 0.0$.

Simulations using Equations 3.17-3.22 show that the increase of electronic relaxation upon increase of the Gd^{3+} -loading, observed by EPR would result in a minor decrease in relaxivity, whereas τ_i is so large and τ_{zeo} so small, that they do not limit the relaxivity. Therefore, changes of these parameters can also be excluded as reason for the decrease in relaxivity with the Gd^{3+} -loading of Gd-LTL-L. However, simulations of r_2 as a function of τ_m or $|\Delta\delta_{\text{zeo}}|$, at $LF = 300$ MHz using Equations 3.17-3.22, while keeping all other variables at the values evaluated previously from the ^1H NMRD showed that these parameters had large effects on r_2 (Figure 3.11). Previously, an increase in τ_m from 4 to 769 ns has been observed for Gd-Y upon increase of the Gd^{3+} -loading from 1.3 to 5.5 wt%,¹⁰ which was ascribed to the increase of the local Gd^{3+} concentration in the zeolite pores making the probability of a water molecule being located in the inner coordination sphere of the Gd^{3+} ion higher. The simulation (Figure 3.11) shows that such an increase in τ_m would result in an increase in r_2 in the present case, whereas actually a decrease has been observed. Therefore, a decrease of $|\Delta\delta_{\text{zeo}}|$ remains as the most likely origin of the observed drop of r_2 with increasing loading. The increase of the Gd^{3+} -loading results in larger magnetization of the particles, which may lead to more alignment in the magnetic fields resulting in an increase of the BMS. Since the BMS and Fermi contact shifts have opposite signs, this probably results in a smaller overall $|\Delta\delta_{\text{zeo}}|$ at higher loadings.

Magnetic field dependence of the relaxivities of Gd-LTL-L

The magnetic field dependence of the transverse and the longitudinal relaxivities was evaluated for Gd-LTL-L with 3.1 wt% Gd³⁺-loading. The results (Figure 3.12) demonstrate that the ratio $r_2/r_1 \leq 10$ between $LF = 30$ and about 300 MHz for Gd-LTL-L sample. Therefore, it has potential for application as a dual T_1/T_2 MRI contrast agent for the presently applied clinical magnetic field strengths.

For Gd-LTL-L at 400 and 600 MHz, r_2^{LW} was significantly larger than r_2^{CPMG} , which suggests that chemical exchange is influencing the spin-echo decay. The obtained values of r_2^{LW} for Gd-LTL-L were fitted simultaneously with the previously reported longitudinal ¹H NMRD and the EPR data using Equations 3.17-3.22 for r_2^{LW} .¹⁴ Because many parameters are governing these data, several constraints were introduced. The value of q was fixed at 6, which was determined by the luminescence decay of the corresponding Eu³⁺-loaded samples.¹⁴ Since we have demonstrated that r_1 for zeolites is independent of τ_r implying that $\tau_r \geq 10$ ns,¹⁰ τ_r was fixed to 10 ns. Furthermore, we have previously shown that the NMRD data of Gd-LTL-L can only be explained with $\tau_{\text{zeo}} \leq 10$ ns and therefore, τ_{zeo} was fixed at 10 ns.¹⁴ A good fit was obtained for values of the variable parameters listed in Table 3.4 and the curve of r_2^{LW} as a function of LF , calculated with these parameters, is displayed in Figure 3.12. The obtained best-fit parameters agree well with those previously reported.¹⁴

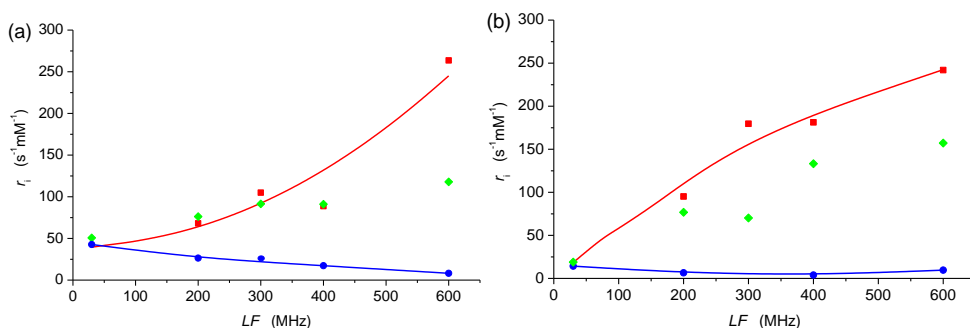


Figure 3.12. Magnetic field dependence of relaxivities of (a) Gd-LTL-L and (b) Gd-LTL-E at 25 °C, both with ~3 wt % Gd³⁺ loading; ●, r_1 ; ◆, r_2^{CPMG} ; ■, r_2^{LW} . The red curves are representing fits of r_2^{LW} with Equations 3.10-3.20; the blue curves are guides to the eye.

Magnetic field dependence of the relaxivities of Gd-LTL-E

The magnetic field dependence of the transverse and the longitudinal relaxivities was evaluated for a Gd-LTL-E samples with 3.3 wt% Gd³⁺-loading. Also this material has $r_2/r_1 \leq 10$ between $LF = 30$ and about 300 MHz (Figure 3.12) and has thus potential for application as a dual T_1/T_2 MRI contrast agent for the presently applied clinical magnetic field strengths. The value of r_2^{LW} was always significantly larger than that of r_2^{CPMG} . From a more detailed study of Gd-LTL-E at $LF = 300$ MHz, it appeared that in this case the spin-echo decay was dependent on τ_{CP} (Figure 3.13), which suggests that chemical exchange is influencing the spin-echo decay. The dependence of R_2^{CPMG} on τ_{CP} can be modeled with the Carver-Richards Equation.⁸⁻¹⁰ According to this model, a plot of R_2^{CPMG} versus $\log(1/\tau_{\text{CP}})$ has a sigmoidal shape with an inflection point at $1/\tau_{\text{CP}} \approx 1/\tau_{\text{m}}$, where τ_{m} is the lifetime of each of the exchanging sites and at the slow 180° pulse rate limit ($1/\tau_{\text{CP}} \rightarrow 0$) the curve approaches the value of R_2^{LW} .^{56,57}

In the present case, the full dispersion appears to be very distorted and there is a large gap between the slow pulse rate limiting value of R_2^{CPMG} and the value R_2^{LW} , which was determined to be 145 s⁻¹. The obtained values of r_2^{LW} for Gd-LTL-E were fitted simultaneously with the previously reported longitudinal ¹H NMRD and the EPR data using Equations 3.17-3.21 of the main text.¹⁴ The value of q was fixed at 1, which is the value determined by the luminescence decay of the corresponding Eu³⁺-loaded sample.¹⁴

Table 3.4. Best-fit-parameters governing the transverse relaxivity of 3.1 wt % Gd-LTL-L and of 3.3% wt Gd- LTL-E at 25 °C obtained from simultaneous fitting of r_2^{LW} , ¹H NMRD and EPR data.

	Gd-LTL-L	Gd-LTL-E
τ_{v} (ps)	29 ± 2	4.5 ± 1.3
Δ^2 (10 ¹⁹ s ²)	3.2 ± 1.8	6.9 ± 1.8
τ_{m} (ns)	0.19± 0.03	1600± 500
τ_{r} (ns) ^a	10	10
τ_{zeo} (ns) ^a	10	10
q ^a	6	1
$ \Delta\delta_{\text{zeo}} $ (ppm)	0.00± 0.00	0.00± 0.00

^a Fixed during the fittings.

The values of τ_r and τ_{zeo} were fixed at 10 ns. A good fitting was obtained for values of the variable parameters listed in Table 3.4, in which the values obtained for Gd-LTL-L were included for comparison. The curves of r_2^{LW} as a function of LF calculated with these parameters are displayed in Figure 3.12. The obtained best-fit parameters agree well with those previously reported.¹⁴ Surprisingly, the transverse relaxation rates of Gd-LTL-E were of the same magnitude as those of Gd-LTL-L, even though here $q = 1$ as compared to $q = 6$ for Gd-LTL-L. This can be ascribed to the large value of τ_m for Gd-LTL-E relative to that for Gd-LTL-L. This relatively large τ_m also explains why r_2^{CPMG} for Gd-LTL-E is dependent on τ_{CP} as opposed to r_2^{CPMG} for Gd-LTL-L (see above). The value of τ_m for Gd-LTL-E is close to the residence time for undissociated water as estimated from the ^{17}O NMR measurements (see Table 3.1) and on previous studies on other zeolites.^{58,59} However, an attempt to fit the present datasets with the value of τ_{zeo} fixed at 1-10 μs led to unreasonable values for the remaining variable parameters. This and the pH dependence of the relaxivity (Figure 3.2) suggest that for Gd-LTL-E prototropic exchange is also dominating over water exchange.

The negligible $|\Delta\delta_{zeo}|$ values obtained show that the Fermi contact shift inside zeolite Gd-LTL is completely compensated by the BMS with opposite sign, which suggests that the particles are aligned in the magnetic field. If the particles were randomly rotating, the BMS would average out and a relatively large overall shift determined by the Fermi contact interaction would result.

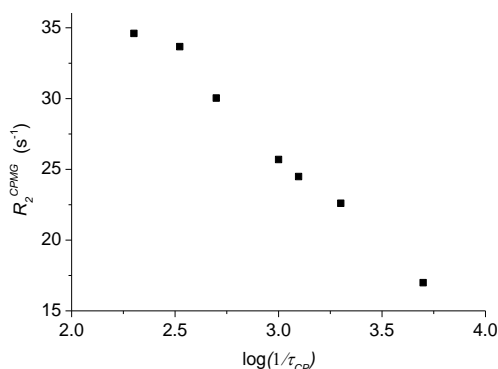


Figure 3.13. The dependence of the transverse relaxation rate R_2^{CPMG} on the rate of the refocusing pulse ($1/\tau_{cp}$). Sample of 5 mg Gd-LTL-E with 3.3 wt % Gd^{3+} -loading suspended in water with 0.5 % xanthan at 300 MHz and 25 °C.

Table 3.5. Comparison of relaxivities of Gd^{3+} and Ho^{3+} -loaded LTL samples in aqueous suspensions containing 1% xanthan at 25 °C and 7.5 T.

sample	Ln^{3+} -loading	r_1 ($\text{s}^{-1}\text{mM}^{-1}$)	r_2^{CPMG} ($\text{s}^{-1}\text{mM}^{-1}$)	r_2^{LW} ($\text{s}^{-1}\text{mM}^{-1}$)
Ho-LTL-L	5.1 wt% Ho^{3+}	0.6	17	208
Ho-LTL-C ^a	5.1 wt% Ho^{3+}	0.3	25	487
Gd-LTL-L	5.2 wt% Gd^{3+}	26	83	103
Gd-LTL-C ^a	5.2 wt% Gd^{3+}	10	29	207

^a Calcined, not extracted.

Relaxivities of Ho-LTL

For comparison two Ho^{3+} -loaded samples were included in this study. The relaxivities measured are compared with those of analogue Gd^{3+} -loaded LTL samples in Table 3.2. Ho^{3+} has electronic relaxation rates that are 4-5 orders of magnitudes lower than those of Gd^{3+} .⁶⁰ Consequently, the longitudinal relaxivities of these materials are substantially smaller than that of the comparable Gd^{3+} -loaded samples (see Table 3.5). Surprisingly, the Ho^{3+} -loaded samples show a large gap between r_2^{CPMG} and r_2^{LW} and a strong τ_{CP} -dependence (Figure 3.14). This demonstrates that here r_2^{LW} has a relatively large exchange contribution. This can be rationalized by a large value for $|\Delta\delta_{\text{m}}|$, which is determined by the Fermi contact and the BMS contribution and that both are proportional to μ_{eff}^2 and thus are a factor 1.8 larger for Ho as compared to Gd.⁶¹

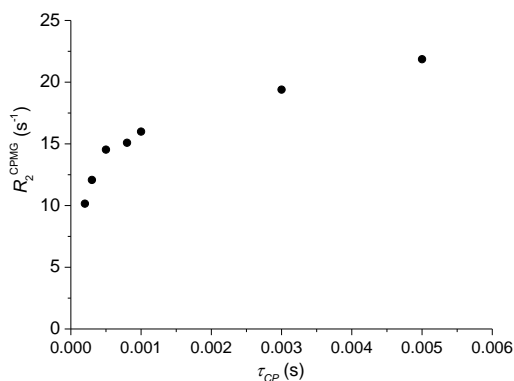


Figure 3.14. The dependence of the transverse relaxation rate R_2^{CPMG} on the refocusing pulse (τ_{CP}). Sample of 5 mg Gd-LTL-L with 5.2 wt % Ho^{3+} -loading suspended in water with 0.5 % xanthan at 300 MHz and 25 °C.

CONCLUSIONS

With the here presented study we show that the up to now unexplained high relaxivity of Gd-loaded zeolite LTL particles most likely originates from a prototropic exchange of water protons rather than water diffusion in the large channels. As a result of this prototropic mechanism, the relaxivities are highly pH dependent leading to a strong decrease of r_1 from 32.5 to 8 s⁻¹mM⁻¹ and r_2 from 98 to 50 s⁻¹mM⁻¹ when going from pH 5 to 9 (3.5 wt % Gd-LTL-L). At higher pH, when the concentration of hydronium ions becomes low, the exchange mechanism changes from prototropic to water diffusion, which significantly limits the relaxivity. In the physiological pH range, nanoparticulates LTL-L with up to 5.2 wt% Gd³⁺ have very high longitudinal and transverse relaxivities.

The strong pH response ($\Delta r_1 \approx 9$ s⁻¹ mM⁻¹ and $\Delta r_2 \approx 15$ s⁻¹ mM⁻¹ upon decrease from pH 7.5 to 5.0 for 3.5 wt % Gd-LTL-L) is among the strongest responses reported so far.⁶² Since the extracellular pH of tumors is 0.5 to 0.6 pH units lower than that of healthy tissue, the presence of these nanoparticles will result in bright spots near these tumors in T_1 weighted images and dark spots in T_2 weighted images. This opens the way to an increase of the contrast by subtracting the T_2 weighted from the T_1 weighted image and to reduce artifacts by the recently published “AND logic gate” algorithm.⁶³ Furthermore, the effect is multiplied by the presence of a large amount of Gd³⁺ in each particle. The zeolites can easily be loaded with additional radioactive cations, which enables application in ratiometric pH determination and pH mapping.

The ratio r_2/r_1 increases strongly with the magnetic field strength. At 7.5 T and 25°C it is 3-4 and therefore, this material is applicable for both T_1 and T_2 weighted images. Possible alignment of the nanoparticles in the magnetic field contributes to the efficacy as T_2 CA. Previously, we have already demonstrated that a fluorescent-MRI probe can be prepared by selectively locking Eu³⁺ in the small cavities, and depositing Gd³⁺ in the wide channels. As a result of its higher effective magnetic moment Ho-LTL has significantly higher transverse relaxivities than corresponding Gd-LTL materials and therefore, this material exclusively is an effective T_2 CA.

EXPERIMENTAL SECTION

Ion exchange

The nanozeolite LTL was purchased from NanoScape AG, Munich, Germany. The Gd-LTL-L and Gd-LTL-E (L=loaded, E=extracted) materials and aqueous suspensions thereof were prepared according to procedures described previously.¹⁴ Briefly, zeolite K-LTL (0.5 g) was first ion-exchanged with Na^+ for 24 h using 10 mL of NaCl (1 M) and then washed with 25 mL of water (3 \times). The obtained Na-LTL was re-suspended in 10 mL of the Ln^{3+} -containing solution, which has a defined mass ratio of Ln^{3+} and zeolite LTL. After the ion-exchange step between Na^+ and Ln^{3+} overnight, the suspension was dialyzed against 1 L of water (3 \times) at 45 $^\circ\text{C}$ to remove the loosely bound Gd^{3+} -ions. The obtained suspension was freeze-dried and the resulting powder was collected (Ln-LTL-L).

Ion relocation

The ion relocation was achieved in a standard calcination oven. The Ln-LTL-L samples were heated to 100 $^\circ\text{C}$ at a rate of 1 $^\circ\text{C min}^{-1}$ and then calcined at 600 $^\circ\text{C}$ for 6h with a heating rate of 10 $^\circ\text{C min}^{-1}$ to afford sample Ln-LTL-C. The Ln-LTL-C samples (0.5 g) were suspended in saturated aqueous NH_4Cl solution (10 mL). After stirring for 24 h the suspension was centrifuged and the solid was washed with water (3 \times). The samples were then freeze-dried to obtain the Ln-LTL-E products.

NMR relaxation and EPR measurements

^1H NMR spectra were measured on a Varian Inova-Unity 300, a Bruker Minispec 30, and Bruker Avance 200, 400, and 600 spectrometers. ^{17}O NMR spectra were measured at the Varian Inova-Unity 300 spectrometer. For all line width measurements, the magnetic field was carefully shimmed. Peak positions and line widths were determined by fitting Lorentzian functions to the experimental spectra. The EPR spectra were recorded on a Bruker ESP300E spectrometer, operating at 9.43 GHz (0.34 T, X-band) at 298 K. Typical parameters used were microwave power 4 mW, modulation amplitude 1.0 mT, and time constant 0.03s. For the longitudinal and transverse relaxivities as a function of pH, 5.0 mg of the Gd-LTL-L/E was suspended in 1.0 mL water by sonication and stabilized by 1.0 g of 1% xanthan gum solution. The pH of this sample was carefully adjusted by using 0.1 M

HCl or NaOH. The Gd-LTL samples for ^{17}O NMR measurements were prepared by suspending 15.0 mg of the Gd-LTL particles in 1.0 mL water to which 20 μL of ^{17}O -enriched water (10% ^{17}O , Cambridge Isotope Laboratories Inc.) was added, and the suspension was stabilized by 1.0 g of 1% xanthan gum solution. Longitudinal relaxation times were measured with the inversion recovery method.¹⁷ ^1H transverse relaxation time was measured with the CPMG pulse sequence in which the length of the spin echo train was varied.¹⁸ An echo time of 0.5 ms was applied, unless stated otherwise. The transverse relaxation times of H_2^{17}O were measured with a CPMG pulse sequence with two spin echoes of which interval between the echoes was varied. The Gd^{3+} concentration of all LTL samples was measured by using the bulk magnetic susceptibility (BMS) method.¹⁹

ACKNOWLEDGMENTS

Thanks are due to Prof. W.R. Hagen (TU Delft) for the EPR measurements.

References

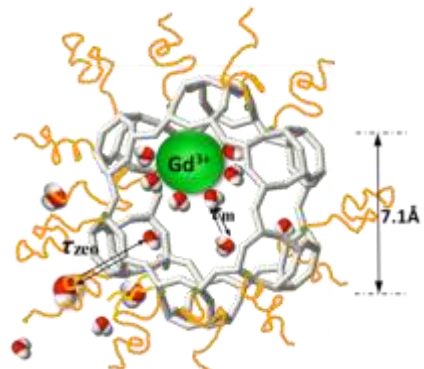
- (1) Merbach, A. E.; Helm, L.; Tóth, É. *The chemistry of contrast agents in medical magnetic resonance imaging*; Second ed.; John Wiley & Sons, Ltd: Chichester (UK), 2013.
- (2) Caravan, P.; Ellison, J. J.; McMurry, T. J.; Lauffer, R. B. *Chem. Rev.* **1999**, *99*, 2293-2352.
- (3) Caravan, P. *Chem. Soc. Rev.* **2006**, *35*, 512-523.
- (4) Dastrù, W.; Longo, D.; Aime, S. *Drug Discovery Today: Technol.* **2011**, *8*, e109-e115.
- (5) Wehrl, H. F.; Wiehr, S.; Divine, M. R.; Maier, F. C.; Rolle, A.-M.; Pichler, B. J.; Gatidis, S.; Gullberg, G. T.; Schwenck, J.; Thaïss, W. M. *J. Nucl. Med.* **2014**, *55*(Supplement 2), S11-S18.
- (6) Kelkar, S. S.; Reineke, T. M. *Bioconjugate Chem.* **2011**, *22*, 1879-1903.
- (7) Peters, J. A.; Djanashvili, K. *Eur. J. Inorg. Chem.* **2012**, *2012*, 1961-1974.
- (8) Balkus, K. J., Jr.; Sherry, A. D.; Young, S. W.; Eur. Patent 0,560,910, June 25, 1992.
- (9) Young, S. W.; Qing, F.; Rubin, D.; Balkus, K. J., Jr.; Engel, J. S.; Lang, J.; Dow, W. C.; Mutch, J. D.; Miller, R. A. *J. Magn. Reson. Imaging* **1995**, *5*, 499-508.
- (10) Platas-Iglesias, C.; Vander Elst, L.; Zhou, W.; Muller, R. N.; Geraldes, C. F. G. C.; Maschmeyer, T.; Peters, J. A. *Chem. Eur. J.* **2002**, *8*, 5121-5131.
- (11) Csajbók, É.; Banyái, I.; Vander Elst, L.; Muller, R. N.; Zhou, W.; Peters, J. A. *Chem. Eur. J.* **2005**, *11*, 4799-4807.
- (12) Norek, M.; Neves, I. C.; Peters, J. A. *Inorg. Chem.* **2007**, *46*, 6190-6196.
- (13) Tsotsalas, M.; Busby, M.; Gianolio, E.; Aime, S.; De Cola, L. *Chem. Mater.* **2008**, *20*, 5888-5893.
- (14) Mayer, F.; Zhang, W.; Brichtart, T.; Tillement, O.; Bonnet, C. S.; Tóth, É.; Peters, J. A.; Djanashvili, K. *Chem. Eur. J.* **2014**, *20*, 3358-3364.
- (15) IZA Structure commission home page. <http://www.iza-structure.org/> (accessed Nov. 21, 2014).
- (16) Skår, H.; Liang, Y.; Erichsen, E. S.; Anwander, R.; Seland, J. G. *Micropor. Mesopor. Mater.* **2013**, *175*, 125-133.
- (17) Vold, R. L.; Waugh, J. S.; Klein, M. P.; Phelps, D. E. *J. Chem. Phys.* **1968**, *48*, 3831-3832.
- (18) Meiboom, S.; Gill, D. *Rev. Sci. Instrum.* **1958**, *29*, 688-691.
- (19) Corsi, D. M.; Platas-Iglesias, C.; van Bekkum, H.; Peters, J. A. *Magn. Reson. Chem.* **2001**, *39*, 723-729.
- (20) Newell, P. A.; Rees, L. V. C. *Zeolites* **1983**, *3*, 22-27.
- (21) Meiboom, S. *J. Chem. Phys.* **1961**, *34*, 375-388.
- (22) Aime, S.; Botta, M.; Fasano, M.; Terreno, E. *Acc. Chem. Res.* **1999**, *32*, 941-949.
- (23) Aime, S.; Barge, A.; Bruce, J. I.; Botta, M.; Howard, J. A. K.; Moloney, J. M.; Parker, D.; de Sousa, A. S.; Woods, M. *J. Am. Chem. Soc.* **1999**, *121*, 5762-5772.

- (24) Barge, A.; Cravotto, G.; Gianolio, E.; Fedeli, F. *Contrast Media Mol. Imaging* **2006**, *1*, 184.
- (25) Micskei, K.; Powell, D. H.; Helm, L.; Brücher, E.; Merbach A. E. *Magn. Reson. Chem.* **1993**, *31*, 1011-1020.
- (26) Lee, Y.; Kao, C.-C.; Kim, S. J.; Lee, H.-H.; Lee, D. R.; Shin, T. J.; Choi, J.-Y. *Chem. Mater.* **2007**, *19*, 6252-6257.
- (27) Lee, Y.; Kim, S. J.; Ahn, D.-C.; Shin, N.-S. *Chem. Mater.* **2007**, *19*, 2277-2282.
- (28) Agmon, N. The Grotthuss Mechanism. *Chem. Phys. Lett.* **1995**, *244*, 456-462.
- (29) Meinhold, R. H.; Bibby, D. M. *Zeolites* **1990**, *10*, 74-84.
- (30) Ryder, J. A.; Chakraborty, A. K.; Bell, A. T. *J. Phys. Chem. B* **2000**, *104*, 6998-7011.
- (31) Franke, M. E.; Simon, U. *ChemPhysChem* **2004**, *5*, 465-472.
- (32) Kanellopoulos, J.; Gottert, C.; Schneider, D.; Knorr, B.; Prager, D.; Ernst, H.; Freude, D. *J. Catal.* **2008**, *255*, 68-78.
- (33) Han, W.; Kwan, S.; Yeung, K. *Top. Catal.* **2010**, *53*, 1394-1400.
- (34) Mirth, G.; Lercher, J. A.; Anderson, M. W.; Klinowski, J. *J. Chem. Soc. Faraday Trans.* **1990**, *86*, 3039-3044.
- (35) Baes, C. F.; Mesmer, R. E. *The hydrolysis of cations*, John Wiley, New York 1976.
- (36) Zimmerman, J. R.; Brittin, W. E. *J. Phys. Chem.* **1957**, *61*, 1328-1333.
- (37) Swift, T. J.; Connick, R. E. *J. Chem. Phys.* **1962**, *37*, 307-320.
- (38) Leigh, J. S., Jr. *J. Magn. Reson.* **1971**, *4*, 308-311.
- (39) McLaughlin, A. C.; Leigh, J. S., Jr. *J. Magn. Reson.* **1973**, *9*, 296-304.
- (40) Cossy, C.; Helm, L.; Merbach, A. E. *Inorg. Chim. Acta* **1987**, *139*, 147-149.
- (41) Reuben, J. *J. Phys. Chem.* **1971**, *75*, 3164-3167.
- (42) Powell, D. H.; NiDhubhghaill, O. M.; Pubanz, D.; Helm, L.; Lebedev, Y. S.; Schlaepfer, W.; Merbach, A. E. *J. Am. Chem. Soc.* **1996**, *118*, 9333-9346.
- (43) Peters, J. A.; van Bekkum, H.; Bovée, W. M. M. *J. Tetrahedron* **1982**, *38*, 331-335.
- (44) Gossuin, Y.; Roch, A.; Muller, R. N.; Gillis, P. *J. Magn. Reson.* **2002**, *158*, 36-42.
- (45) Fries, P. H. *J. Chem. Phys.* **2012**, *136*, 044504(01-20).
- (46) Chen, Z.; van Westrenen, J.; van Bekkum, H.; Peters, J. A. *Inorg. Chem.* **1990**, *29*, 5025-5031.
- (47) Verhoef, M. J.; Koster, R. M.; Poels, E.; Bliëk, A.; Peters, J. A.; van Bekkum, H. *Stud. Surf. Sci. Catal.* **2001**, *135*, 4590-4593.
- (48) Norek, M.; Pereira, G. A.; Geraldès, C. F. G. C.; Denkova, A.; Zhou, W.; Peters, J. A. *J. Phys. Chem. C* **2007**, *111*, 10240-10246.
- (49) Vuong, Q. L.; Berret, J.-F.; Fresnais, J.; Gossuin, Y.; Sandre, O. *Adv. Healthcare Mater.* **2012**, *1*, 502-512.

- (50) Fries, P. H.; Belorizky, E. In *The Chemistry of Contrast Agents in Medical Magnetic Resonance Imaging*; John Wiley & Sons, Ltd: 2013, pp 277-310.
- (51) Solomon, I. *Phys. Rev.* **1955**, *99*, 559-565.
- (52) Bloembergen, N.; Morgan, L. O. *J. Chem. Phys.* **1961**, *34*, 842-850.
- (53) owell, D. H.; Merbach, A. E.; González, G.; Brücher, E.; Micskei, K.; Ottaviani, M. F.; Köhler, K.; Von Zelewsky, A.; Grinberg, O. Y.; Lebedev, Y. S. *Helv. Chim. Acta* **1993**, *76*, 2129-2146.
- (54) Yazyev, O. V.; Helm, L.; Malkin, V. G.; Malkina, O. L. *J. Phys. Chem. A* **2005**, *109*, 10997-11005.
- (55) Reuben, J.; Fiat, D. *J. Chem. Phys.* **1969**, *51*, 4909-4917.
- (56) Carver, J. P.; Richards, R. E. *J. Magn. Reson.* **1972**, *6*, 89-105.
- (57) Jen, J. *J. Magn. Reson.* **1978**, *30*, 111-128.
- (58) Davis, D. G.; Perlman, M. E.; London, R. E. *J. Magn. Reson., Ser. B* **1994**, *104*, 266-275.
- (59) Peters, J. A.; Huskens, J.; Raber, D. J. *Progr. Nucl. Magn. Reson. Spectrosc.* **1996**, *28*, 283-350.
- (60) Bertini, I.; Capozzi, F.; Luchinat, C.; Nicastro, G.; Xia, Z. *J. Phys. Chem.* **1993**, *97*, 6351-6354.
- (61) Peters, J. A.; Huskens, J.; Raber, D. J. *Progr. Nucl. Magn. Reson. Spectrosc.* **1996**, *28*, 283-350.
- (62) Bonnet, C. S.; Tei, L.; Botta, M.; Tóth, É. In *The Chemistry of Contrast Agents in Medical Magnetic Resonance Imaging*; John Wiley & Sons, Ltd: 2013, pp 343-386.
- (63) Shin, T.-H.; Choi, J.-S.; Yun, S.; Kim, I.-S.; Song, H.-T.; Kim, Y.; Park, K. I.; Cheon, J. *ACS Nano* **2014**, *8*, 3393-3401.

The Effects of PEGylation on Stability and Relaxivity of Gd- Loaded Nanozeolite LTL for MR Imaging

4



The contents of this chapter are based on :
W. Zhang, J. Martinelli, J. M.A. van Hengst, J. A. Peters, C. S. Bonnet, F. Szeremeta H. Bouwmeester and K.
Djanashvili. *Manuscript in preparation.*

INTRODUCTION

A large range of nanoscale materials such as gold, fluorescent upconversion crystals, quantum dots, iron oxides, lanthanide oxides, zeolite, silica have shown to be widely applicable in biomedical imaging and therapy.¹⁻⁵ Nanoparticles (NPs) are favorable devices particularly for tumor diagnosis and therapy, as they tend to accumulate at tumor sites via the enhanced permeability and retention (EPR) effect.⁶ This effect allows NPs without targeting vectors to deliver a high payload of functional species at the site of interest for imaging and therapy. On the other hand, there has been substantial interest in creating multifunctional NPs that combine distinct specific properties (e.g. magnetic, radioactive, or optical) into one system.⁷ This can be achieved by surface engineering,⁸ which may provide the core of NPs with additional properties⁹ that enhance the specificity and improve the performance of the material. Dual radioactive and magnetic superparamagnetic iron oxides NPs,¹⁰ magnetic and optical quantum dots¹¹ as well as upconversion NPs¹² are just a few examples of nanoparticulate materials that are of great interest in this regard.

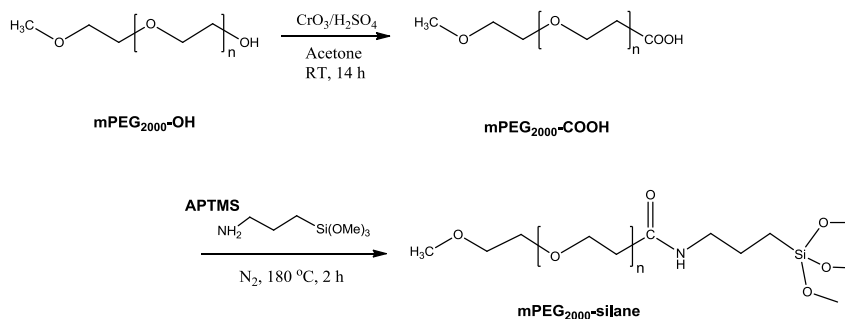
Important factors that need to be considered in design of multifunctional NPs for *in vivo* application are toxicity and biodistribution. A common approach to cope with these issues is through coating of NPs with an organic layer, such as biocompatible and hydrophilic polyethylene glycol (PEG),¹³ which may significantly reduce the cytotoxicity of NPs and leads to a longer blood circulation half-time ($t_{1/2}$).¹⁴ For example, as iron oxides¹⁰ and manganese oxides¹⁵ NPs are often originally coated with oleic acid during the synthesis, subsequent PEGylation can remove the oleic acid and therefore improve the biocompatibility and physiological stability of NPs. In addition, attachment of functional groups (e.g. $-\text{NH}_2$, $-\text{SH}$, $-\text{COOH}$) onto the terminal of PEG chains,¹⁶ may provide anchors to introduce functions such as optical tags or targeting vectors onto NPs.

Porous materials such as silica NPs and zeolites are attractive platforms to accommodate optical reporters, radiotracers and/or paramagnetic magnetic resonance imaging (MRI) contrast agents (CAs). Mesoporous silica NPs loaded with paramagnetic Gd(III)-ions and doped with Eu(III)-ions have been described as dual MRI-optical imaging agents.¹⁷ Alternatively, encapsulation of paramagnetic Gd(III)-complexes into the silica NPs results in a highly efficient MRI CA.^{18,19} Grafting of Gd(III)-complexes to silica NPs

labelled with radioisotopes leads to a promising dual agent for MRI and radionuclides-based imaging.²⁰

Zeolite LTL is a promising porous material that has been proposed as a versatile platform for accommodation of paramagnetic ions for MRI CAs.⁵ LTL has a well-defined negatively charged framework that is composed of big and small cavities, both form 1D-channels that are separated from each other and that are parallel to the *c*-axis of the crystals. An MRI-optical dual agent has been constructed by loading cationic fluorescent dyes into the interior channels of the zeolite LTL for optical imaging, while the Si-OH groups at the outside surface were conjugated with Gd(III)-DOTA chelate for MRI.²¹ Recently, we have demonstrated a different strategy to achieve MRI-optical dual functionality based on zeolite LTL.²² Both Eu(III)- and Gd(III)-ions were loaded selectively into the narrow and wide channels of the zeolite LTL, respectively. As the narrow channel is basically not accessible for the water molecules, the luminescence quenching of Eu(III) was greatly reduced, whereas fast exchange between the bulk water and water coordinated to paramagnetic Gd(III)-ions resulted in remarkable magnetic properties of the material.

The porous structures are superior to solid particles due to the large surface area of both internal (e.g. cavities, pores, or channels) and external surfaces. As a result, the porous systems can accommodate a large payload of functional species per particle, e.g. 4000 Gd(III) ions per LTL particle (20 × 40 nm).²³ This is highly beneficial for its performance as MRI CAs, since the enhancement of both longitudinal (T_1) and transverse (T_2) relaxation times is linearly proportional to the amount of paramagnetic ions per particle. Delivering a high payload of paramagnetic compound to the site of interest has become an important strategy in overcoming the intrinsic low sensitivity of MRI. The efficacy of a CA is assessed by its water proton relaxation rate ($R_n = 1/T_n$, $n = 1$ or 2) expressed as relaxivity (r_n) per amount of Gd(III)-ions ($\text{s}^{-1}\text{mM}^{-1}$). A large number of parameters governs the relaxivity, of which, water exchange and the number of water molecules bound to Gd(III) are two dominating factors.²⁴ Both can be optimal in the porous structure, thus, the MRI CAs based on zeolite and mesoporous silica NPs have much higher r_1 and/or r_2 relaxivity in comparison to paramagnetic complexes (e.g. Gd-DOTA) and solid NPs (e.g. Gd_2O_3).⁵ Recently, we demonstrated that fast prototropic exchange is the origin of exceptionally high relaxivity of Gd-loaded LTL (Gd-LTL). Moreover, Gd-LTL also exhibits high pH



Scheme 4.1. Synthesis of mPEG2000-silane for the surface functionalization of Gd-LTL.

responsiveness of both r_1 and r_2 relaxivities.²³ In the view of high potential of the porous systems for MRI application, we are interested in the effects of surface engineering on their performance as CAs. Herein, we present a systematic study on surface functionalization of zeolite LTL NPs via PEGylation. Particularly, the impact of PEGylation on the water exchange was investigated. Moreover, the cytotoxicity of Gd-LTL and PEGylated Gd-LTL were investigated. The results of the present work can be readily extrapolated to other zeolite types and silica NPs.

RESULTS AND DISCUSSIONS

PEGylation of Gd-LTL

Cylindrical nanoparticles of Gd(III)-loaded zeolite LTL with the dimensions of 20×40 nm were used to study conjugation of methoxy polyethylene glycol (mPEG) chains to its surface, and to evaluate the effects of PEGylation on the porous entrance. In order to avoid a significant increase of the hydrodynamic size of the zeolite particles, a relatively short mPEG ($M_n = 2000$) was selected. To react with the Si-OH groups on LTL surface and covalently attach PEG chains, the triethoxysilane derivative of mPEG was prepared by oxidation of mPEG₂₀₀₀-OH to mPEG₂₀₀₀-COOH, followed by amidation with (3-aminopropyl)trimethoxy silane (APTMS) giving mPEG₂₀₀₀-silane, see Scheme 4.1.

The mPEG was characterized by FT-IR and NMR spectroscopy. A characteristic carbonyl stretching vibration at 1739 cm^{-1} that was found after the oxidation step shifted to

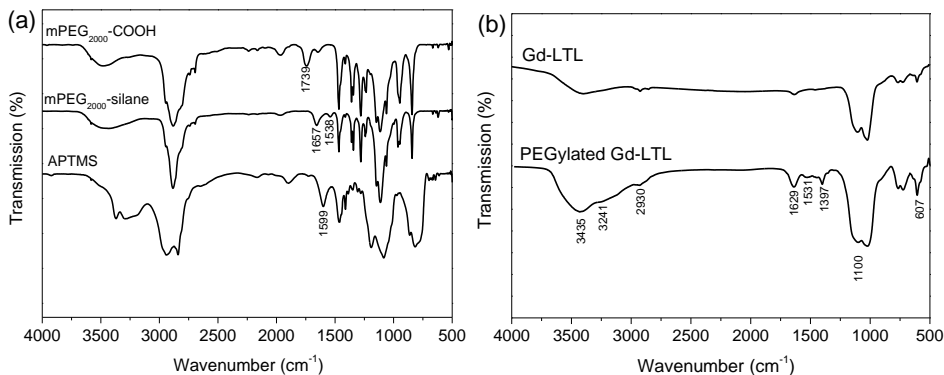


Figure 4.1. IR spectra of (a) mPEG₂₀₀₀-COOH, mPEG₂₀₀₀-silane and APTMS and (b) Gd-LTL (5.2 % Gd-loading) and PEGylated Gd-LTL (5.2 % Gd-loading) with 6.2 wt% PEG.

1657 cm⁻¹ upon reaction with APTMS (Figure 4.1a). Additionally, the -NH₂ vibration in APTMS at 1599 cm⁻¹ shifted to 1538 cm⁻¹, confirming the formation of an amide bond.

In the next step, mPEG₂₀₀₀-silane was covalently attached onto Gd-LTL surface by reaction with Si-OH groups present on the LTL surface. The IR spectra of LTL prior to PEGylation showed characteristic stretching vibrations at 3453, 1629, and bending vibrations at 1100 and 607 cm⁻¹ that can be assigned to the Si-OH groups and (Si/Al)O₄ units in zeolite (Figure 4.1b).^{25,26} After the PEGylation, additional C-H stretching bands at 2930 and 1397 cm⁻¹ and additional peaks for -NH peaks at 3241 and 1531 cm⁻¹ demonstrated the grafting.

Zeta potential (ζ) measurements of aqueous suspensions of NPs have been shown to be a good indication of successful PEGylation of the materials.¹³ Intrinsically, zeolite LTL crystals possess a negative zeta potential ($\zeta = -32.2$ mV), which is slightly compensated after the ion-exchange with lanthanide ions in Gd-loaded LTL ($\zeta = -23.8$ mV, 5.2 wt% Gd-loading). Conjugation of mPEG₂₀₀₀-silane at the surface of the zeolite further increases ζ up to -16.9 and -3.3 mV for 6.2 wt% and 9.1 wt% PEG-substitution, respectively. Comparison of ζ measured as a function of pH on aqueous suspensions of zeolite LTL after various treatments confirms the PEGylation based on electrokinetic charges. Both, the native and Gd-loaded LTL samples showed negative ζ in the whole pH range studied (Figure 4.2)

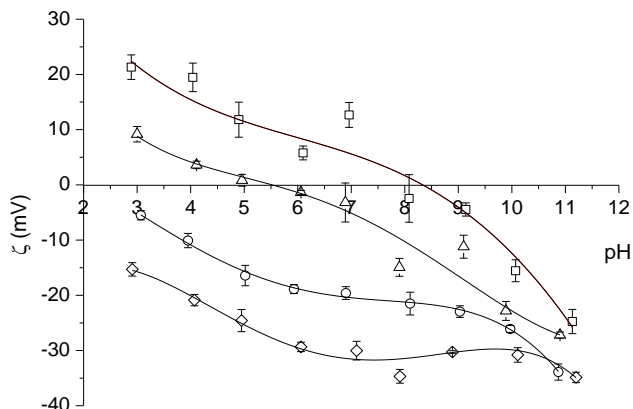


Figure 4.2. Zeta potential (ζ) of zeolite LTL suspensions as a function of pH: non-PEGylated LTL (diamond), Gd-LTL (5.2 % Gd-loading, circle), PEGylated Gd-LTL (5.2 % Gd-loading) with 6.2 wt% (triangle) and 9.1 wt% PEG (square), respectively. The curves are guides to eyes.

and hence no isoelectric point (IEP) was observed. The increase of negative charge observed ($\zeta \approx -35$ mV) can be explained by the dissociation of Si-OH groups; similar results have been observed for Si-OH rich mesoporous silica NPs.^{27,28} By contrast, Gd-LTL functionalized with mPEG₂₀₀₀-silane showed a clear IEP at pH 5.6 and 8.3 for 6.2 wt% and 9.1 wt% of PEG-loading, respectively. The presence of PEG chains is known to reduce the overall charge of the surfaces due to the effect of charge shielding.²⁹⁻³¹ In case of PEGylated Gd-LTL, the samples showed expected different ζ values compared to the non-PEGylated samples, changing from positive to negative upon increasing pH from 3 to 11. Such a changeover is less pronounced for the Gd-LTL with a lower PEG-loading. This observation is in a good agreement with the results by He *et al.* who demonstrated that PEGylated mesoporous silica NPs is less negatively charged with the increased PEG-loading.³² Interestingly, the ζ values of both PEGylated samples reached -27 mV at pH 11, which is only slightly above the ζ value of non-PEGylated samples. This suggests that only a part of the surface Si-OH groups were substituted with mPEG₂₀₀₀-silane. The residual dissociated Si-OH groups contribute to the negative charge at higher pH.^{27,28} The observed IEP of PEGylated Gd-LTL between pH 5 and 9 is due to a collective effect of protonation of PEG and dissociation of Si-OH groups.

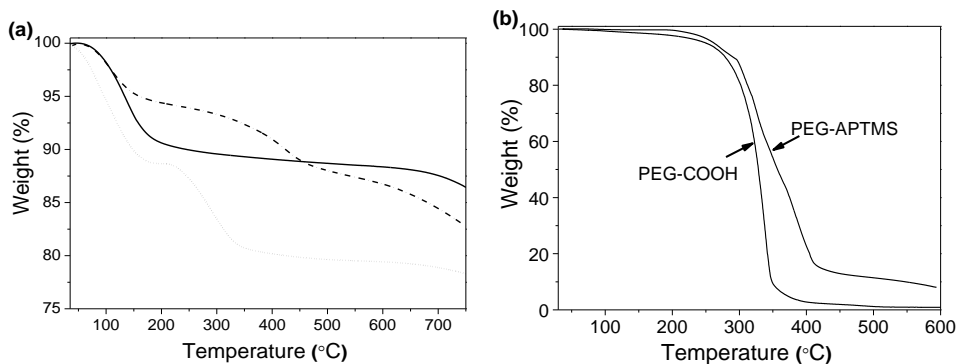


Figure 4.3. TGA profiles of (a) non-PEGylated Gd-LTL (5.2% Gd-loading, solid line), PEGylated Gd-LTL (8.7 wt% PEG, 5.2% Gd-loading, dash-dot line) and a mixture of Gd-LTL with 8.7 wt% with PEG-silane (dot line) and (b) free mPEG₂₀₀₀-COOH and mPEG₂₀₀₀-silane.

Additional information on the degree of m-PEG substitution was obtained from TGA measurements. For this purpose, dried samples were heated from 25 up to 750 °C while monitoring the weight loss (Figure 4.3). The obtained profiles can be divided into different phases of decomposition. The first stage (< 200 °C) can be assigned to the loss of water that was not removed by freeze-drying from the surface and the pores of the zeolite LTL.

During the second stage (200-600 °C), the organic content at the surface of zeolite is burnt, and finally, only the inorganic material remains. The TGA profiles of both and mPEG₂₀₀₀-silane (Figure 4.3b) show no weight decrease in the first stage indicating that there is no retained water in the samples. Between 200 and 400 °C, mPEG₂₀₀₀-COOH burns completely, whereas for mPEG₂₀₀₀-silane a residue of 10-15 wt% remains. This weight corresponds with the amount of silane after conversion to silica under the measuring conditions. The changes above 600 °C observed for the LTL-samples (Figure 4.3a) can be attributed to aging of the silica that give rise to some insignificant mass decrease of the remaining material. For the inorganic material Gd-LTL (solid line), no weight loss was observed between 200 to 600 °C, while the significant weight loss upon heating of the PEGylated Gd-LTL (dash-dot line) within the same temperature range indicates decomposition of the organic component. Quantification of this weight loss allows determination of the degree of PEGylation, which in this case corresponds to 8.7 wt% PEG substitution. To exclude the possibility of adsorption of PEG at the zeolite surface and to

prove its successful conjugation, Gd-LTL and mPEG₂₀₀₀-silane were simply mixed in the same weight ratio as in the conjugated Gd-LTL-PEG (91:9) and the TGA profile was measured for comparison (Figure 4.3a, dot line). In this case, only decomposition of PEG taking place between 150 and 400 °C with a 9.3% weight loss was observed, demonstrating a profile similar to decomposition of free PEG-derivatives.

The PEG-grafting density at the surface of particles determines the conformation of PEG-chains,³³ which is expected to influence the water exchange behavior in the case of functionalized porous materials. Therefore, investigations on the morphology of the zeolite surface, such as PEG-chain regime and thickness of PEG-layer are included in this study. Two different grafting regimes can be adopted by the PEG-chains, “mushroom” and “brush”. According to the theory based on the Flory radius (R_F),^{13,34-36} the mushroom regime is typically expected when the PEG-density is low ($D > R_F$ or $L \leq R_F$, where D is the average distance between surface grafting points and L the thickness of the grafted chains), because then the chains occupy an area that allows them not to stretch fully and thus form a thin layer at the surface. When the PEG-density is increased ($D < R_F$ or $L > 2R_F$), the PEG-chains gradually adopt a brush regime, in which they extend from the surface as long bristles, and form a thick layer at the surface. Therefore, the two regimes can be distinguished if the parameters D , R_F and L are known.³⁶ Atomic force microscopy (AFM) offers a possibility to investigate the PEG-layer thickness (L), benefiting from its atomic-scale sensitivity and resolution, as well as the ability to image the samples with non-destructive forces as small as 1 nN in a medium such as water or NaCl solution.³⁷ The fact that due to the small size and hydrodynamic movements of LTL NPs in water, it is difficult to measure directly the force between the surface of an individual LTL particle and the AFM tip. Therefore, to estimate the regime and thickness of PEG on an LTL surface, a commercially available silicon wafer was applied as model surface. The wafer has a sufficiently flat surface and its hydrophilicity is close to that of LTL (Si/Al ratio of 3.0 for LTL). Prior to the PEGylation, the flat silicon wafer was cleaned by an oxygen plasma treatment, which resulted in a suitable water contact angle of less than 10°, and increased the density of surface silanol groups.³⁷ After the plasma treatment, the silicon wafer was PEGylated by the same procedures as for were used for PEGylation of LTL. The interaction forces of this surface model recorded in MilliQ water are displayed in Figure 4.4. For the flat silicon wafer without PEG-chains, a clear attractive van der Waals force was observed

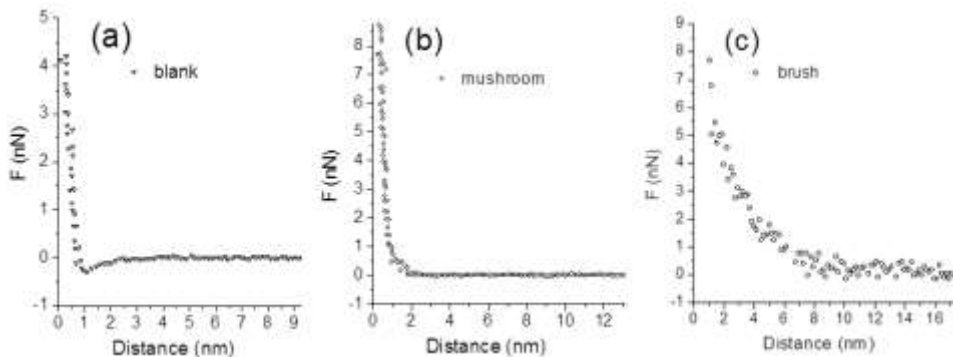


Figure 4.4. Visualization of PEG-regimes by measuring the force F (nN) as a function of the distance (nm) between the AFM tip and the surface of the silicon wafer used as the model of zeolite surface: without PEG (a), and with gradually increased PEG-density of 6.2 wt% (b) and 9.1 wt% (c).

at a distance of 1.5 nm (Figure 4.4a).^{38,39} By varying the concentration of mPEG₂₀₀₀-silane during the PEGylation, materials with various PEG-loadings were obtained. When the surface was occupied by mPEG₂₀₀₀, the force showed an exponential decay for both mushroom and brush regimes (Figure 4.4b and 4.4c), which is in good agreement with reported models.⁴⁰ When the surface is dominant with mPEG₂₀₀₀ chains in a mushroom regime ($L \leq R_F$), a mPEG₂₀₀₀ thickness of about 2 nm was directly observed (Figure 4.4b). As expected, for a higher mPEG₂₀₀₀ density, a brush regime ($L > R_F$) with a PEG thickness of 9 nm (as shown in Figure 4.4d) was observed. The R_F of mPEG₂₀₀₀ in this work is 3.5 nm, as calculated with $R_F = a n^{3/5}$, where a is the length of a monomer unit (3.5 Å for PEG), and n is the number of monomer units ($n = 45$ for mPEG₂₀₀₀). Under these conditions, the experimental value of PEG thickness on the surface model is consistent with the theoretical as well as the reported values for mPEG₂₀₀₀.^{36,41,42} Therefore, direct visualization of the PEG layer with AFM using this surface model of zeolite proves that two regimes can be adopted on the particle surface depending on the amount of PEG used in the PEGylation procedures.

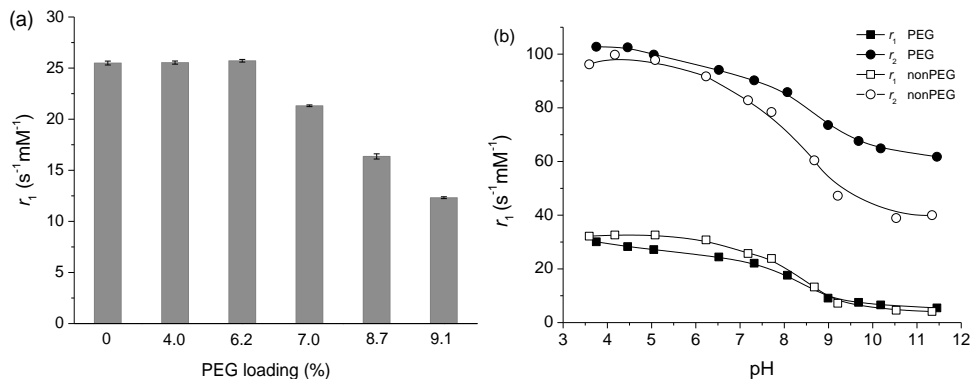


Figure 4.5. Relaxivity studies on aqueous suspension of Gd-loaded LTL stabilized with 1 % xanthan solution: (a) longitudinal relaxivity (r_1) vs PEG-loading at the surface of Gd-LTL (5.2 wt% Gd-loading, pH 5.5), (b) longitudinal (r_1) and transverse (r_2) relaxivities of non-PEGylated (3.5 wt% Gd-loading) and PEGylated Gd-LTL (3.9 wt% Gd-loading, 6.2 wt% PEG) as a function of pH. All the measurements were performed at 300 MHz and 25°C. $\tau_{\text{cp}} = 0.5$ ms was applied in all T_2 measurements.

Evaluation of the effects of PEGylation on water access to Gd(III)-ions in the LTL channels

Recently, we have reported high longitudinal (r_1) and transverse (r_2) relaxivities measured for aqueous suspensions of Gd-loaded nanozeolite LTL. For this system, six water molecules have been found in the first coordination sphere of Gd(III)-ions accommodated in the large channels of LTL.²² The relaxivities were found to be highly pH dependent, showing a steep decrease of r_1 and r_2 from 32 to 8 and from 98 to 50 $\text{s}^{-1}\text{mM}^{-1}$, respectively, when going from pH 4 to 9 (7.5 T and 25 °C).²³ This could be explained by the exchange of water protons between the interior of the zeolite, which was found to be prototropic and fast at low pH (< 6), whereas at higher pHs the exchange took place through whole water molecules with a much lower rate. The pH responsive relaxivity makes Gd-loaded LTL an interesting candidate MRI CA for example for *in vivo* pH mapping of tumors, which often have intrinsically lower pH than healthy tissues.⁴³ It may be expected that modification of the surface of porous structures might block the channel entrance by small molecules and ions. Therefore, the impact of the extension of PEGylation on relaxivity requires careful investigation to enable fine-tuning of the system.

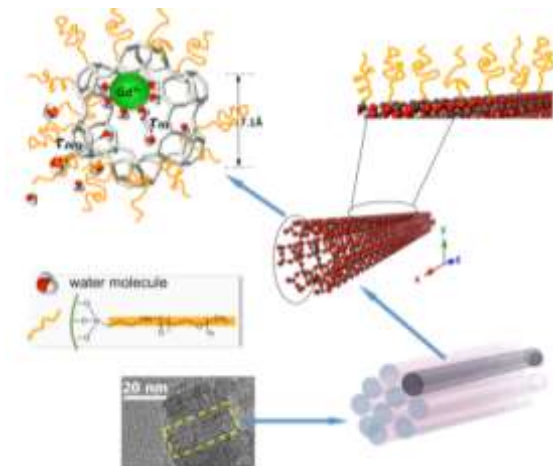
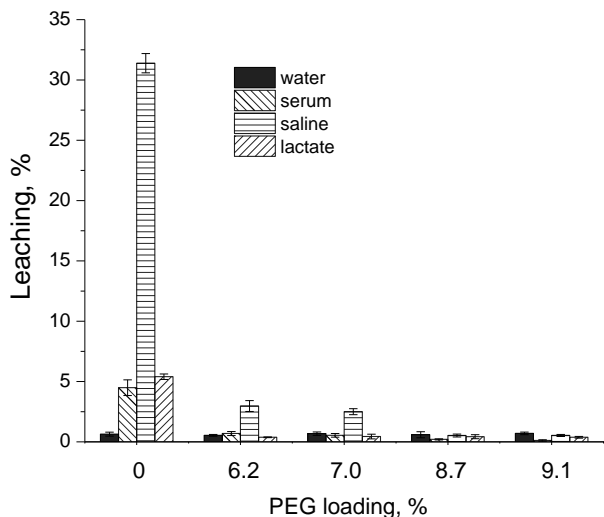


Figure 4.6. Schematic representation of PEGylated Gd(III)-loaded zeolite LTL and the water exchange parameters (τ_m is the residence time of water molecules in the first coordination sphere of Gd-ions, τ_{zeo} is the residence time of water molecules inside the zeolite). Only one cage unit is shown for convenience.

Figure 4.5a displays the r_1 values measured for aqueous suspensions of Gd-LTL with an mPEG-content varying from 0 to 9.1 wt%. The relaxivity appears to remain constant ($\sim 25 \text{ s}^{-1}\text{mM}^{-1}$) up to 6.2 wt% PEG after which it decreases to $12.3 \text{ mM}^{-1}\text{s}^{-1}$ at 9.1 wt%, which is the maximum degree of mPEG-substitution that could be reached for this zeolite. According to the evaluation based on the AFM data, the mPEG chains in the sample with 6.2 wt % of PEG ($D = 3.23 \text{ nm}$, $L = 3.57 \text{ nm}$) are in the mushroom regime. Upon increase of the mPEG densities ($D < R_F$ and $L > R_F$), a transition to the brush regime occurs in which the PEG chains stretch from the particle surface and form long bristles. Most likely, water protons (or entire water molecules at $> \text{pH } 9$) that exchange with interior water protons will then be increasingly slowed down due to interactions with the hindering PEG brushes compactly arranged at the surface (Figure 4.6), which explains the decline in relaxivity above 6.2 wt% mPEG coverage. For this mushroom regime, the pH dependence of the relaxivities was studied in some more details using a sample with 6.2 wt % mPEG coating. Figure 4.5b shows that both r_1 and r_2 relaxivities of Gd-LTL remain high after PEGylation of the surface within a mushroom regime and that the pH response is retained (Figure 4.5b).



Figures 4.7. Leaching of free Gd(III)-ions from non-PEGylated Gd-LTL (5.2 wt% Gd-loading) and Gd-LTL (5.2 wt% Gd-loading) with various PEG loadings incubated in pure water, physiological saline (0.9 w/v%), bovine serum (20 v/v%), and lactate solution (2.5 mM) at 37 °C for 24 h.

The magnitudes of r_1 are similar to those before PEGylation. As a higher density of PEG chains results in decreased relaxivity, the PEGylation degree of Gd-LTL ideally should not exceed 6.2 wt% PEG in order to preserve the high relaxivities and pH responsiveness.

Stabilizing role of PEG chains

The stability of Ln-loaded porous system is an important aspect in the design of advanced materials for imaging and therapy. Many publications report negligible leaching of Ln-ions from porous silica particles and zeolites in water.^{17,44,45} However, data for physiological media should give more relevant insights into the prospects of these materials for medical applications. PEG chains at the surface of Gd-LTL are expected to have a stabilizing effect and to provide protection against leaching of Gd(III)-ions, which are known to be highly toxic. Therefore, the leaching of free Gd(III)-ions from the non-PEGylated as well as of Gd-LTL with various degrees PEG substitution at the surface was investigated. The evaluations were conducted by using a colorimetric assay⁴⁶ in water, physiological saline, serum, and solution of lactate (Figure 4.7).

After incubation of non-PEGylated Gd-LTL at 37 °C in saline, serum and lactate solution for 24 h, about 31, 4, and 5 % of free Gd(III) was detected, respectively, compared to only 0.7 % found in water. These numbers were significantly reduced for the PEGylated analogues. For example, the leaching from PEGylated Gd-LTL decreased dramatically to 3 % (6.2 wt% PEG) and 0.5 % (9.1 wt% PEG) in saline. A similar behavior was found for PEGylated Gd-LTL samples in serum and lactate. Upon increase of PEG-density the negative surface charge gradually decreases as is reflected in ζ potential which increases from -16.9 mV to -3.3 mV for 6.2 and 9.1 wt% PEG (suspensions in Milli Q water, pH *ca.* 8.3), respectively. As a result, the ion-exchange between PEGylated Gd-LTL and electrolytic cations present in physiological media is reduced and the stability of the system is increased. To verify this, a sample of LTL particles was first PEGylated, and after that subjected to ion-exchange. In this way, only 0.42 % Gd was found to be loaded into LTL, whereas 4.5 % of Gd could be loaded into naked Gd-LTL under the same conditions. This indeed confirms the protecting effect of the PEG layer against leaching of Gd through ion exchange.

Another concern is possible blocking of the entrance of the pores due to the affinity of various molecules for the surface of porous materials. In our previous study we have found that stabilizing aqueous suspensions of Gd-LTL with 1 wt % xanthan gum, which is a common agent for the dispersion of NPs for the relaxometric studies at strong magnetic fields, results in perturbed relaxivities particularly at higher temperatures (> 25 °C).²³ At 25 °C the value of r_1 was constant over time for Gd-LTL without PEG at the surface but at 50 °C,²² a decrease of r_1 over time was observed, which appeared to be irreversible; after cooling down the sample to 25 °C the initially measured r_1 at that temperature was not reproduced.

To evaluate the role of the xanthan gum in this irreversible decrease, Gd-LTL was incubated in water at 50 °C in the absence of xanthan for 1 hour and only after cooling to 25 °C the gum was added to stabilize the suspension. The relaxivity measured on this sample was the same as that for a sample that was prepared by suspending the Gd-LTL in a solution of 1% xanthan in water at 25 °C. It may be concluded that most likely xanthan interacts with the pores of the zeolite LTL material and partially blocks them at higher temperatures. A similar study was carried out with a PEGylated Gd-LTL (6.2 wt% PEG).

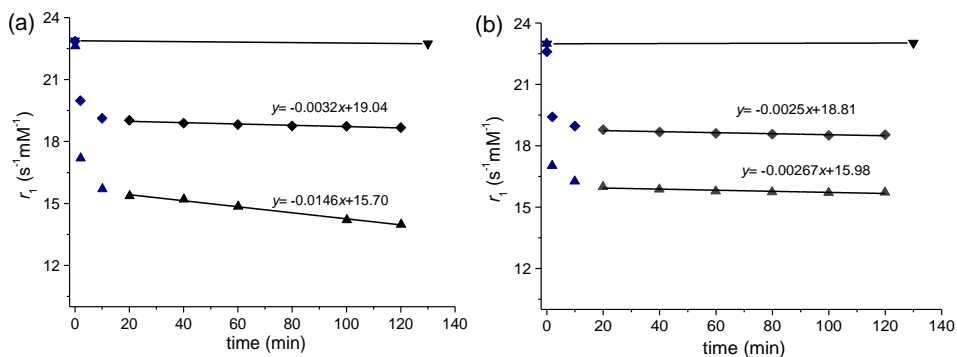


Figure 4.8. Longitudinal relaxivity of (a) non-PEGylated Gd-LTL (5.2 % Gd-loading) and (b) PEGylated Gd-LTL (5.2 % Gd-loading and 6.2 % PEG) stabilized in xanthan solution (1 wt%) at 25 (∇), 37 (\blacklozenge) and 50 °C (\blacktriangle), respectively. Linear fitting was applied to the points measured after equilibration of the sample (> 10 min) to calculate the extent of decrease in relaxivity.

The obtained relaxivities after 20 min's temperature equilibration remained constant over time at elevated temperatures (Figure 4.8b). This is a remarkable reduction of the interaction of zeolite LTL with xanthan that firstly indicates that our assumption on the origin of the r_1 effect was right, and secondly it confirms that the protecting function can be achieved by a PEG layer with a mushroom configuration without affecting the longitudinal relaxivity (with 6.2 wt% PEG).

Cytotoxicity study

The colloidal stability of both PEGylated and non-PEGylated materials in a cell medium was evaluated by DLS on suspensions of Gd-LTL (4.3% Gd-loading) at 37 °C over 24 h (Figure 4.9). The results demonstrated that no changes of hydrodynamic size occur, indicating a good colloidal stability. This allowed further *in vitro* assessment of the cytotoxicity by a viability test with macrophage cell lines using an ATP assay. As shown in Figure 4.10, no significant toxic effects were detected for the cells incubated with K-LTL (commercially available starting material), non-PEGylated Gd-LTL (4.3 wt% Gd-loading), and PEGylated Gd-LTL (4.3 wt% Gd-loading and 6.5 wt% PEG) at the doses between 10 and 250 $\mu\text{g mL}^{-1}$. Only a slight decrease of viability was observed at the highest dose of 500 $\mu\text{g mL}^{-1}$ for all the samples. The biocompatibility of PEG is already well-documented.⁴⁸

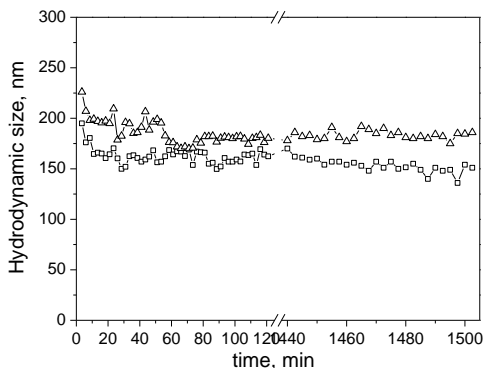


Figure 4.9. Hydrodynamic size (nm) of non-PEGylated (\square) and PEGylated (5.2 wt% PEG) (\triangle) Gd-LTL samples suspended in DMEM (with 10 % FCS) at 37 °C over 24 h. Particle concentration 750 mg/mL.

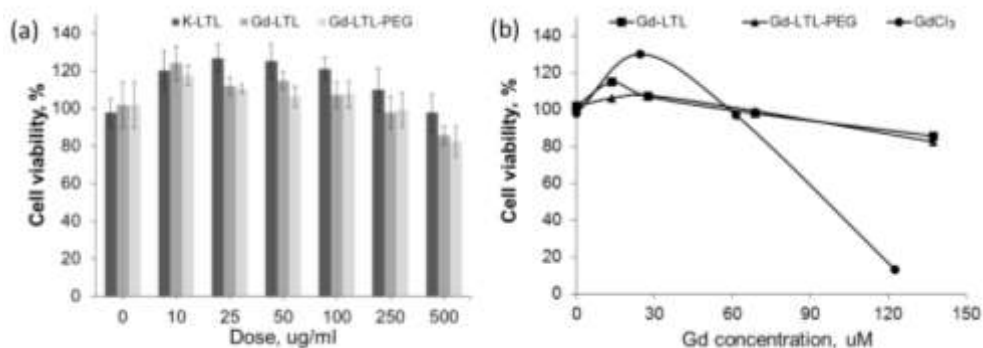


Figure 4.10. Viability of macrophage cells incubated with K-LTL, Gd-LTL (4.3% Gd-loading), and Gd-LTL-PEG (4.3% Gd-loading and 6.5 wt% PEG) at different doses (a). The comparison between Gd(III) encapsulated LTL and free Gd(III) ions (b).

Therefore, the very similar viability results obtained in this study with both PEGylated and non-PEGylated samples suggest that the cytotoxicity of LTL itself is negligible.

Kihara *et al.* reported that the cytotoxicity of zeolite particles is strongly dependent on morphology and size of the zeolites as well as the type of the cell line.⁴⁹ Interestingly, a pronounced toxicity increase was found for smaller zeolite particles (50×100 nm) compared to the bigger analogues (90×210 nm) incubated with HeLa cells most probably due to the

higher surface-to-volume ratio of the smaller particles. On the other hand, Laurent *et al.* reported non-toxicity of spherical LTL (18 nm) and other small zeolitic particles.⁵⁰

The cytotoxicity of Gd-LTL used in this study was investigated by comparing the viability of cells incubated with PEGylated/non-PEGylated Gd-LTL particles and solutions of free Gd(III)-ions with the same concentration. As clearly shown in Figure 4.10, the total cell death was caused by the free Gd(III)-ions present at the concentration of 120 μM . By contrast, the Gd-LTL particles retain excellent cell viability (90 %) at this Gd(III)-concentration, thus demonstrating the absolute necessity of the stable encapsulation of Gd(III)-ions and the nontoxicity of LTL particles, which is in a good agreement with the results from leakage study by colorimetric assay.

CONCLUSIONS

In summary, the systematic study on PEGylation of Gd-loaded LTL nanoparticles gives insights into the effects that the surface functionalization has on the channel entrance for water exchange processes and hence the relaxivity. A surface model of zeolite allowed for direct assessment of the PEG layer via AFM, confirming the different regimes that PEG can adopt at the surface of the LTL particles. Depending on the PEG-density at the LTL surface, a relatively compact PEG layer (brush regime) can limit the bulk protons/water diffusion and exchange with the water molecules in the interior of LTL. This is an important guidance for the surface engineering of porous nanoparticulate MRI CAs that take advantage of the channel entrance for water exchange. The relaxivity study of a PEGylated Gd-LTL sample with 6.2 wt% PEG showed that the high pH responsiveness of both T_1 and T_2 relaxivities is not affected compared to the non-PEGylated Gd-LTL. However, the PEG layer can effectively mediate the mutual interaction between the surroundings and Gd-LTL particles. As a result, PEGylation of the LTL NPs reduces significantly the Gd(III)-leakage under physiological conditions, due to a change of surface charge.

Furthermore, the study indicated that both Gd-LTL and PEGylated Gd-LTL particles show nontoxicity. Previously, Gd-loaded LTL has already shown great potential for MRI-optical and MRI T_1 - T_2 dual imaging,^{22,23} while the current study demonstrates the benefits from the further surface modification. Therefore, we believe that this work will steer the lanthanide-loaded zeolite LTL towards bioapplications.

EXPERIMENTAL SECTION

Materials and methods

All chemicals in this study were used as obtained (Sigma-Aldrich, Alfa-Aesar). The zeolite LTL nanoparticles (with cation K^+) were purchased from NanoScape (Planegg, GE). $GdCl_3$ obtained as hexahydrates from Strem Chemicals, Newburyport, USA. 1H and ^{13}C NMR were performed on Bruker Avance 400 NMR spectrometer. Chemical shifts in ppm are reported relative to TMS as internal standard. Thermogravimetric analyser (TGA, Perkin-Elmer) was used to evaluate the level of PEG loading of Gd-LTL samples from room temperature to 800 °C (heating rate 10 °C/min) under air atmosphere. Infrared (IR) spectra were recorded using a Thermo Nicolet 6700 FTIR spectrometer. The concentration of Gd(III)-ions was determined by using the bulk magnetic susceptibility (BMS) method with *t*-butanol as the internal reference.⁵³ The longitudinal and transverse relaxation time of all samples was measured on a Varian Unity Inova 300 NMR spectrometer. The samples were prepared by dispersing 2.5 mg of Gd-LTL or PEGylated Gd-LTL nanoparticles in 1.0 mL of MilliQ water using a sonication bath and stabilized by adding 1.0 g of 1% xanthan gum solution. The pH of the samples was adjusted by addition of either 0.1 M HCl or 0.1 M NaOH. An echo time (τ_{cp}) of 0.5 ms was applied for all the measurements of transverse relaxation times. Dynamic light scattering (DLS) and zeta potential experiments were performed on a Malvern Zetasizer NanoZS at 25 °C. The average diameter and values of zeta potential were based on three individual measurements, 15 scans of each measurement. For the AFM measurement of the model surface of zeolite, a (100) silicon wafer (1 cm x 1 cm) with a natural oxidized layer (about 2 nm) was purchased from Sil'Tronix Silicon Technologies. The wafer was rinsed with MilliQ-water and ethanol several times, and sonicated in ethanol and acetone for 5 min, respectively. After drying under N_2 flow, the wafer was subjected to plasma treatment with oxygen plasma for 1 min under the pressure of 1600 mTorr using a Harrick plasma cleaner (Anadis Instruments). The wafer was then stored in MilliQ-water for 24 h. After the above treatments, the silicon wafer was PEGylated using the procedures for PEGylation of LTL. The AFM and the tip used in the force measurement were fabricated by NT-MDT (Russia). The height of the silicon tip was 14-16 μm with a curvature radius of 10 nm. The length, width and thickness of the cantilever were $135\pm 5 \mu m$, $30\pm 5 \mu m$ and 1.5 μm , respectively. The resonant frequency of

the cantilever was 57 kHz and the force constant of the tip was 0.7 N/m. The landing speed of the tip was 350 nm/s.

Synthesis of mPEG₂₀₀₀-COOH and mPEG₂₀₀₀-silane

PEG-COOH was synthesized according to the published procedure.⁵¹ Then, 5.0 g of mPEG₂₀₀₀-COOH (2.5 mmol) was mixed with 450 μ l of APTMS (2.5 mmol) under nitrogen atmosphere and reacted at 180 °C for 2h to yield the mPEG₂₀₀₀-silane conjugate.⁵² After that, the reaction mixture was cooled down to room temperature and stored in a desiccator. ¹H-NMR of mPEG₂₀₀₀-silane (400 MHz, CDCl₃): δ = 0.59 (CH₂CH₂Si), 1.56 (CH₂CH₂CH₂Si), 2.63 (-NCH₂CH₂CH₂), 3.35 (Si-O-CH₃), 3.1-4.5 (mPEG-signals), 8.11 (NH). For the PEGylated zeolite particles used in cytotoxicity study, the PEG-silane was synthesized following a different protocol: tosylated PEG (mPEG₂₀₀₀OTs) was first synthesized according to the published procedures.⁵³ The resultant mPEG₂₀₀₀OTs (5.0 mmol) was reacted with APTMS (10.0 mmol) in 25mL chloroform refluxed at 70 °C for 8 h, in order to bind the silane group to the end of PEG chains through the amino functionality. After filtration over Celite, the solution was concentrated and dried under vacuum. ¹H-NMR (400 MHz, CDCl₃): δ = 0.59 (CH₂CH₂Si), 1.51 (CH₂CH₂CH₂Si), 2.64 (-NCH₂CH₂CH₂), 3.32 (Si-O-CH₃), 3.2-3.9 (mPEG-signals).

Procedures for PEGylation

Ln³⁺-loaded zeolite L (50 mg) was dispersed in a mixture of EtOH and water (25 mL, 3:2, v/v), sonicated and vigorously stirred, followed by the addition of 0.5 mL of NH₄OH (25%). To obtain different PEG-loading levels, different amounts of a 0.23 M mPEG₂₀₀₀-silane stock solution in water were added to the particle suspension (25 μ l for 6.2% PEG-loading). The mixture was gently stirred for 24 h and then centrifuged, washed with water (3x) and freeze-dried.

Stability assessment

The assessment of leaching of Gd(III)-ions from the obtained samples was performed with 1.5 mg/mL zeolite dispersions in water, physiological saline (0.9 w/v%) and serum (20 v/v%), respectively. After being incubated in a shaker at 37 °C for 24h, the supernatant was

collected and determined by the xylenol orange complexation method using UV-Vis spectroscopy, as has been previously reported.⁴⁶

Cytotoxicity test

LTL samples. 15 mg of lyophilized pure-zeolite LTL, Gd-LTL, and Gd-LTL-PEG NPs were suspended in 1 ml of filter sterile water with 0.05% BSA. These stock suspensions were sonicated for 10 min at 20 °C in a Branson 5510 water bath sonicator (Emerson, USA) at 100% output (4W specific ultrasound energy (240 J/m³)). The suspensions were transferred to glass vials, after which the total volume was set to 3 ml with 0.05% BSA (final concentration stock solutions 5000 µg/ml).

Cell culture. Mouse macrophage cells, RAW 264.7 (ATCC TIB-71) were obtained from the American Type Culture Collection, Manassas, VA (ATCC). Cells were used at passages 8 and 10. RAW264.7 cells were cultured in Dulbecco Modified Eagle's Minimal Essential medium (DMEM; 4.5 g/L glucose, w/o L-glutamine, w/o phenol red, Lonza, Verviers, Belgium) supplemented with glutamax (Gibco). Also, penicillin-streptomycin (PEST; 1% v/v; Sigma, St. Louis, MO), and heat-inactivated fetal bovine serum (FBS; 10% v/v; Gibco) were added to the medium. Cells were incubated at 37°C in a humidified environment (95% relative humidity; RH) and 5% carbon dioxide (Thermo Scientific HERAcCell 240). Cells were passed at 80% confluency by sub-cultivation at a ratio 1:6 twice a week until use. All media and solutions were pre-warmed to 37 °C before use.

ATPlite assay. 100 µl cells with a concentration of 2×10^4 cells/ml were seeded in 96 wells white plates with clear bottom (Costar) (6250 cells/well). After 48 hours these cells reached a confluency of 30%. To assess the possible cytotoxic effect of the NPs on RAW264.7 cells, a dilution range of 10, 25, 50, 100, 250, and 500 µg/ml nanoparticles (corresponding to 2.87, 7.17, 14.3, 28.7, 71.7, and 143.4 µM GdCl₃) was added to the cells for 24h. The viability was assessed using the ATPlite assay (Perkin Elmer). Briefly, 50 µL mammalian cell lysis solutions was added to 100 µl of cell suspension, and incubated for 5 minutes in an orbital shaker at 700 rpm. Subsequently 50 µL substrate solution was added, followed by another 5 minutes at 700 rpm, and a final incubation in the dark for 10 minutes. Chemoluminescence was measured at 590 nm with the appropriate. A control of NPs without cells, showed no interference of the NPs with the ATPlite assay.

Acknowledgements

Thanks are due to Dr. Hans Bouwmeester (Wageningen UR) for the cytotoxicity tests, Kai Zhang (TU Delft) for the TEM measurements and Liangyong Chu for AFM measurements.

References

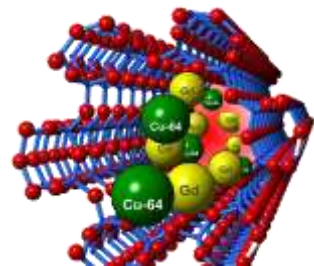
- (1) Howes, P. D.; Chandrawati, R.; Stevens, M. M.; *Science* **2014**, *346*, 1247390-1247400.
- (2) Chen, G.; Qiu, H.; Prasad, P. N.; Chen, X.; *Chem. Rev.* **2014**, *114*, 5161-5214.
- (3) Gallo, J.; Long, N. J.; Aboagye, E. O.; *Chem. Soc. Rev.* **2013**, *42*, 7816-7833.
- (4) Kim, T. J.; Chae, K. S.; Chang, Y.; Lee, G. H.; *Curr. Top. Med. Chem.* **2013**, *13*, 422-433.
- (5) Peters, J. A.; Djanashvili, K.; *Eur. J. Inorg. Chem.* **2012**, *2012*, 1961-1974.
- (6) Cheng, Z.; Al Zaki, A.; Hui, J. Z.; Muzykantov, V. R.; Tsourkas, A.; *Science* **2012**, *338*, 903-910.
- (7) Huang, W.-Y.; Davis, J. J.; *Dalton Trans.* **2011**, *40*, 6087-6103.
- (8) Erathodiyil, N.; Ying, J. Y.; *Acc. Chem. Res.* **2011**, *44*, 925-935.
- (9) Groult, H.; Ruiz-Cabello, J.; Pellico, J.; Lechuga-Vieco, A. V.; Bhavesh, R.; Zamai, M.; Almarza, E.; Martin-Padura, I.; Cantelar, E.; Martinez-Alcazar, M. P.; Herranz, F.; *Bioconjugate Chem.* **2015**, *26*, 153-160.
- (10) Torres Martin de Rosales, R.; Tavaré, R.; Paul, R. L.; Jauregui-Osoro, M.; Protti, A.; Glaria, A.; Varma, G.; Szanda, I.; Blower, P. J.; *Angew. Chem. Int. Ed.* **2011**, *50*, 5509-5513.
- (11) Jing, L. H.; Ding, K.; Kershaw, S. V.; Kempson, I. M.; Rogach, A. L.; Gao, M. Y.; *Adv. Mater.* **2014**, *26*, 6367-6386.
- (12) Cheng, L.; Yang, K.; Li, Y.; Chen, J.; Wang, C.; Shao, M.; Lee, S.-T.; Liu, Z.; *Angew. Chem. Int. Ed.* **2011**, *50*, 7385-7390.
- (13) Jokerst, J. V.; Lobovkina, T.; Zare, R. N.; Gambhir, S. S.; *Nanomedicine* **2011**, *6*, 715-728.
- (14) Pernia Leal, M.; Rivera-Fernandez, S.; Franco, J. M.; Pozo, D.; de la Fuente, J. M.; Garcia-Martin, M. L.; *Nanoscale* **2015**, *7*, 2050-2059.
- (15) Huang, H.; Yue, T.; Xu, Y.; Xu, K.; Xu, H.; Liu, S.; Yu, J.; Huang, J.; *J. Appl. Polym. Sci.* **2015**, *132*, 42360-42367.
- (16) Zalipsky, S.; *Bioconjugate Chem.* **1995**, *6*, 150-165.
- (17) Tse, N. M. K.; Kennedy, D. F.; Kirby, N.; Moffat, B. A.; Muir, B. W.; Caruso, R. A.; Drummond, C. J.; *Adv. Healthcare Mater.* **2013**, *2*, 836-845.
- (18) Wartenberg, N.; Fries, P.; Raccurt, O.; Guillermo, A.; Imbert, D.; Mazzanti, M.; *Chem. Eur. J.* **2013**, *19*, 6980-6983.
- (19) Taylor, K. M. L.; Kim, J. S.; Rieter, W. J.; An, H.; Lin, W.; Lin, W.; *J. Am. Chem. Soc.* **2008**, *130*, 2154-2155.
- (20) Laprise-Pelletier, M.; Bouchoucha, M.; Lagueux, J.; Chevallier, P.; Lecomte, R.; Gossuin, Y.; Kleitz, F.; Fortin, M.-A.; *J. Mater. Chem. B* **2015**, *3*, 748-758.

- (21) Tsotsalas, M.; Busby, M.; Gianolio, E.; Aime, S.; De Cola, L.; *Chem. Mater.* **2008**, *20*, 5888-5893.
- (22) Mayer, F.; Zhang, W.; Brichtart, T.; Tillement, O.; Bonnet, C. S.; Tóth, É.; Peters, J. A.; Djanashvili, K.; *Chem. Eur. J.* **2014**, *20*, 3358-3364.
- (23) Zhang, W.; Peters, J. A.; Mayer, F.; Helm, L.; Djanashvili, K.; *J. Phys. Chem. C* **2015**, *119*, 5080-5089.
- (24) Tóth, é.; Helm, L.; Merbach, A. In *The Chemistry of Contrast Agents in Medical Magnetic Resonance Imaging*; John Wiley & Sons, Ltd: 2013, p 25-81.
- (25) Zecchina, A.; Arean, C. O.; *Chem. Soc. Rev.* **1996**, *25*, 187-197.
- (26) Das, S. K.; Mahanta, S. P.; Bania, K. K.; *RSC Adv.* **2014**, *4*, 51496-51509.
- (27) Colilla, M.; Izquierdo-Barba, I.; Sánchez-Salcedo, S.; Fierro, J. L. G.; Hueso, J. L.; Vallet-Regí, M.; *Chem. Mater.* **2010**, *22*, 6459-6466.
- (28) Musso, G. E.; Bottinelli, E.; Celi, L.; Magnacca, G.; Berlier, G.; *Phys. Chem. Chem. Phys.* **2015**, *17*, 13882-13894.
- (29) Ogris, M.; Brunner, S.; Schuller, S.; Kircheis, R.; Wagner, E.; *Gene Ther.* **1999**, *6*, 595-605.
- (30) Mannisto, M.; Vanderkerken, S.; Toncheva, V.; Elomaa, M.; Ruponen, M.; Schacht, E.; Urtti, A.; *J. Controlled Release* **2002**, *83*, 169-182.
- (31) Petersen, H.; Fechner, P. M.; Martin, A. L.; Kunath, K.; Stolnik, S.; Roberts, C. J.; Fischer, D.; Davies, M. C.; Kissel, T.; *Bioconjugate Chem.* **2002**, *13*, 845-854.
- (32) He, Q.; Zhang, J.; Shi, J.; Zhu, Z.; Zhang, L.; Bu, W.; Guo, L.; Chen, Y.; *Biomaterials* **2010**, *31*, 1085-1092.
- (33) Perry, J. L.; Reuter, K. G.; Kai, M. P.; Herlihy, K. P.; Jones, S. W.; Luft, J. C.; Napier, M.; Bear, J. E.; DeSimone, J. M.; *Nano Lett.* **2012**, *12*, 5304-5310.
- (34) Marsh, D.; Bartucci, R.; Sportelli, L.; *Biochimica et Biophysica Acta (BBA) - Biomembranes* **2003**, *1615*, 33-59.
- (35) de Gennes, P. G.; *Adv. Colloid Interface Sci.* **1987**, *27*, 189-209.
- (36) Damodaran, V. B.; Fee, C. J.; Ruckh, T.; Papat, K. C.; *Langmuir* **2010**, *26*, 7299-7306.
- (37) Ducker, W. A.; Senden, T. J.; Pashley, R. M.; *Nature* **1991**, *353*, 239-241.
- (38) Verwey, E. J. W.; Overbeek, J. T. G. *Theory of the Stability of Lyophobic Colloids*; Elsevier Pub. Co., 1948.
- (39) Derjaguin, B. V.; Landau, L.; *Acta physicochimica* **1941**, *14*, 633-662.
- (40) Al-Hashmi, A. R.; Luckham, P. F.; *Colloids Surf. Physicochem. Eng. Aspects* **2012**, *393*, 66-72.
- (41) Xu, Z.; Marchant, R. E.; *Biomaterials* **2000**, *21*, 1075-1083.
- (42) Heuberger, M.; Drobek, T.; Spencer, N. D.; *Biophys. J.* **2005**, *88*, 495-504.

- (43) Tannock, I. F.; Rotin, D.; *Cancer Res.* **1989**, *49*, 4373-4384.
- (44) Peters, J. A.; Djanashvili, K.; Geraldes, C. F. G. C.; Platas-iglesias, C. In *The Chemistry of Contrast Agents in Medical Magnetic Resonance Imaging*; John Wiley & Sons, Ltd: 2013, p 209-276.
- (45) Yan, Y.; Shao, E.; Deng, X.; Liu, J.; Zhang, Y.; Tang, Y.; *J. Mater. Chem. B* **2014**, *2*, 3041-3049.
- (46) Barge, A.; Cravotto, G.; Gianolio, E.; Fedeli, F.; *Contrast Media & Molecular Imaging* **2006**, *1*, 184-188.
- (47) Knop, K.; Hoogenboom, R.; Fischer, D.; Schubert, U. S.; *Angew. Chem. Int. Ed.* **2010**, *49*, 6288-6308.
- (48) Kihara, T.; Zhang, Y.; Hu, Y.; Mao, Q.; Tang, Y.; Miyake, J.; *J. Biosci. Bioeng.* **2011**, *111*, 725-730.
- (49) Laurent, S.; Ng, E. P.; Thirifays, C.; Lakiss, L.; Goupil, G. M.; Mintova, S.; Burtea, C.; Oveisi, E.; Hebert, C.; de Vries, M.; Motazacker, M. M.; Rezaee, F.; Mahmoudi, M.; *Toxicol. Res.* **2013**, *2*, 270-279.
- (50) Corsi, D. M.; Platas-Iglesias, C.; Bekkum, H. v.; Peters, J. A.; *Magn. Reson. Chem.* **2001**, *39*, 723-726.
- (51) Lele, B. S.; Kulkarni, M. G.; *J. Appl. Polym. Sci.* **1998**, *70*, 883-890.
- (52) Barrera, C.; Herrera, A. P.; Rinaldi, C.; *J. Colloid Interface Sci.* **2009**, *329*, 107-113.
- (53) Köllhofer, A.; Plenio, H.; *Chem. Eur. J.* **2003**, *9*, 1416-1425.

**Rapid Radiolabeling of Gd-
Loaded Zeolite LTL for
Application in MR-PET Dual
Imaging**

5



INTRODUCTION

Combination of contrast agents (CAs) for several imaging modalities (e.g. optical, magnetic, and radioactive) in single nanoparticulate platform is a promising strategy in biomedicine.¹ For example, MRI has as advantages that it has excellent soft-tissue and temporal resolution (10-100 μm) without the use of harmful ionizing radiation.² However, the low sensitivity and the difficult quantifiability of MRI CAs are inherent limitations.

Clinically applied MRI CAs, mainly paramagnetic Gd-chelates or superparamagnetic iron oxide nanoparticles improve the contrast of images by altering respectively either longitudinal (T_1) or transverse (T_2) relaxation times of water protons in their proximity.³ Due to the low sensitivity, large amounts of MRI CAs (e.g. 4×10^7 Gd ions per cell) need to be delivered locally for molecular imaging purposes. The emergence of multimodal imaging that combines highly sensitive reporters such as tracers for positron emission tomography (PET) or single photon computed tomography (SPECT) with MRI CAs opens possibilities to assess physiological parameters, such as pH, metabolic rates, and receptor densities with a single probe.^{4,5} Furthermore, such a combination can also be used to introduce a therapeutic component into a probe, which is then known as theranostics.

Combination of MRI with radionuclide-based PET/SPECT is highly synergistic: it provides both high resolution images of the morphology and highly sensitive and quantifiable information on the location of the CA.⁶ Usually, labeling of MRI CAs with a tiny concentration of radionuclides (10^{-13} - 10^{-11} M) is sufficient for easy localization and quantification of the CAs. Metal-based radionuclides that exhibit relatively long half-life times (e.g. $^{64/67}\text{Cu}$ ($t_{1/2} = 12.7$ or 62.0 h), ^{89}Zr ($t_{1/2} = 78.5$ h), $^{66/67/68}\text{Ga}$ ($t_{1/2} = 9.5, 78.3,$ or 1.1 h) and ^{86}Y ($t_{1/2} = 14.7$ h)) are of great interest as they can be handled without loss of a substantial amount of activity in chemical procedures (synthesis, purification, characterization) and in shipment.⁷ Efficient methodologies for radio-chemical synthesis are very important.⁷⁻⁹ Rosales *et al.* reported a novel chelate bis(dithiocarbamatebisphosphonate), which has the ability to bind PET tracers (^{64}Cu and $^{99\text{m}}\text{Tc}$) after their conjugation at the surface of the superparamagnetic iron oxide nanoparticles.^{10,11} On the other hand, chelate-free radiolabeling has become a promising alternative to label nanoparticles in a facile and rapid manner without laborious synthetic procedures. Such an approach also minimizes the effect of the labeling on the pharmacodynamics of the applied probes.¹² Recently, Liu *et al.* demonstrated this for a

MRI-PET dual probe, which was prepared in a chelate-free approach.¹³ Iron oxides nanoparticles modified with meso-2,3-dimercaptosuccinic acid were self-assembled on the surface of atomically thin MoS₂ nanosheets by forming sulfur bridges with defected sites of MoS₂. Then, ⁶⁴Cu²⁺-ions could, thanks to their high affinity to sulfur atoms, also anchor the MoS₂ defect sites in the nanosheets, resulting in a MRI-PET nanoprobe.

Zeolite Linde Type L (LTL) has been proved to be a versatile carrier in potential biosensors^{14,15} and MRI CAs.^{16,17} LTL has a negatively charged framework with well-defined big and small cavities that can accommodate a large amount of positively charged ions. Previously, we have shown that a dual MRI-optical probe can be prepared by loading the large and small cavities selectively with Gd³⁺ and Eu³⁺, respectively.¹⁷ The Gd-loaded LTL provides very high T_1 (bright contrast) and T_2 (dark contrast) relaxation enhancement. Both relaxation enhancements show high pH responsiveness due to a changeover of fast prototropic exchange to relatively slow full water exchange between the interior of the zeolite and the exterior at above pH 7.¹⁸

Herein, we report a chelate-free radiolabeling of Gd³⁺-loaded LTL nanoparticles with ⁶⁴Cu and ⁸⁹Zr and demonstrate the potential of the resulting materials as MRI-PET dual agents with both T_1 and T_2 MRI contrast enhancing abilities. ⁶⁴Cu and ⁸⁹Zr are two isotopes that are important in PET imaging due to their favorable properties.¹⁹ ⁶⁴Cu has a half-life time 12.7 h, and its decay has 18% β^+ (0.653 MeV), 39 % β^- (0.579 MeV) and 43% electron capture. Moreover, the relatively high decay energies of ⁶⁴Cu make this isotope also suitable for radiotherapy.²⁰ ⁸⁹Zr exhibits a longer half-life time (78.4 h) and decay of 22.7 % β^+ (0.897 MeV) and 77 % electron capture (0.909 MeV). ⁸⁹Zr is an upcoming isotope that is not widely used yet in PET imaging. Up to now its application is mainly focused in immuno-PET (⁸⁹Zr-labeled proteins and antibodies).^{21,22} In order to prepare PET agents using ⁶⁴Cu or ⁸⁹Zr, a large variety of chelates have been designed to form stable complexes with radiometals,^{7,19} but application of zeolites for the design of MRI/PET probe has not been reported so far.

RESULTS AND DISCUSSION

Ion-exchange efficiency

Previously we prepared Gd^{3+} -loaded LTL by incubating nanozeolite LTL with an aqueous solution of GdCl_3 at room temperature during 24 h, a time usually used for the loading of zeolites.^{23,24} In this way, a quantitative loading of Gd^{3+} -ions into the big channels of LTL was achieved. For the preparation of the MRI-PET dual probe based on the zeolite LTL in the current study, the time needed for the exchange between Na^+ and Gd^{3+} or Cu^{2+} ions were minimized to avoid too much loss of radioactivity of ^{64}Cu during the preparation. There are 3.6 Na^+ ions coordinated per unit cell in the large channels of LTL,²⁵ which can be substituted with Gd^{3+} ions. As a result, the theoretical maximum loading of Gd is 6.4 wt % after the exchange with 3 Na^+ ions, whereas the maximum experimental Gd^{3+} -loading at room temperature is 5.2 wt %.¹⁷ After stirring of Na-LTL nanoparticles in an aqueous solution with 2.7 wt % Gd^{3+} (with respect to LTL) for 0.5 h, the Gd^{3+} -loading as determined by the bulk magnetic susceptibility (BMS) method²⁶ was quantitative (2.7 wt %). Upon longer incubation times (up to 24 h) the Gd^{3+} -loading remained constant.

The ion-exchange between cold Cu^{2+} and Na^+ was investigated at room temperature by means of colorimetric assay using xylenol orange.²⁷ Therefore, a suspension of LTL was stirred at room temperature in the presence of Cu^{2+} (1.5 wt % with respect to LTL). The concentration of Cu^{2+} -ions in water before and after the exchange was determined from the

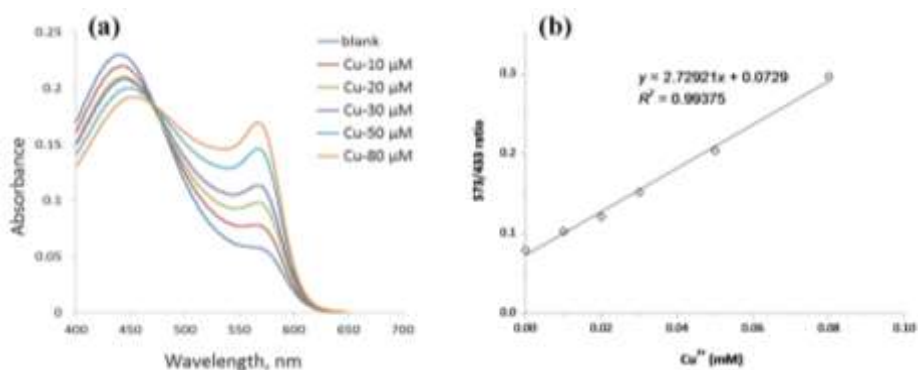


Figure 5.1. Colorimetric assay for determination of the concentration of Cu^{2+} -ions: (a) UV-Vis spectra of solutions of xylenol orange (blank, 16 μM) and the products of its complexation with Cu^{2+} -ions at various concentrations (μM), (b) the calibration curve.

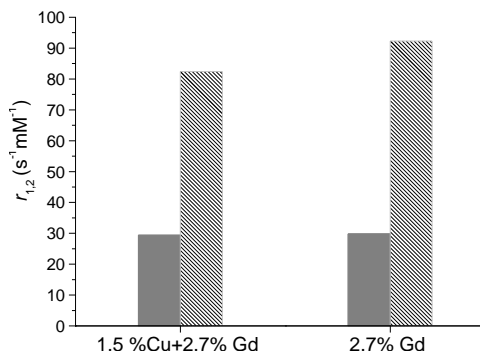


Figure 5.2. Comparison of r_1 (solid) and r_2 (dashed) of LTL co-loaded with Cu^{2+} and Gd^{3+} -ions (1.5 % Cu + 2.7 % Gd) and LTL loaded with Gd^{3+} -ions exclusively (2.7 % Gd), measured at 25°C and 7 T.

ratio of the UV-Vis absorbances at 573 and 433 nm (see Figure 5.1). After the exchange between Cu^{2+} and Na^+ during 0.5 h, the obtained Cu-LTL solid appeared to be complete (1.5 wt% loading). The resulting Cu^{2+} -loaded zeolite showed a slightly blue color. This indicates that co-loading of zeolite LTL with Gd^{3+} and radioactive $^{64}Cu^{2+}$ is possible in a very short time, and hence this leaves plenty of time for any post-loading surface functionalization.

Co-loading of Cu^{2+} and Gd^{3+} into LTL, relaxivity study and surface functionalization

A mixture of 2.7 wt % Gd^{3+} and 1.5 wt % Cu^{2+} -ions were loaded into LTL to assess the suitability of the resulting particles for MR imaging. The relaxivity expressed in $s^{-1}mM^{-1}$ of Gd (r_i ($i = 1,2$)) was measured at 25 °C and 7 T. As shown in Figure 5.2, the relaxivities ($r_1 = 29.4 s^{-1}mM^{-1}$ and $r_2 = 82.4 s^{-1}mM^{-1}$) are compared with the relaxivities measured for a sample that was loaded exclusively with 2.7 % Gd^{3+} ($r_1 = 29.8 s^{-1}mM^{-1}$ and $r_2 = 92.3 s^{-1}mM^{-1}$). It may be concluded that the effect of Cu^{2+} on the relaxivities in the zeolite with both Gd^{3+} and Cu^{2+} is negligible. This result is in a good agreement with our previous study, in which it was shown that the presence of diamagnetic La^{3+} has no effect on the relaxivity of Gd^{3+} -loaded LTL.¹⁸ By virtue of the high r_1 value, the Gd-loaded LTL nanoparticles are promising for T_1 -weighted MRI. Moreover, the very high r_2 value and low r_2/r_1 ratio (< 5.0) make this material interesting as a T_1 - T_2 dual agent.

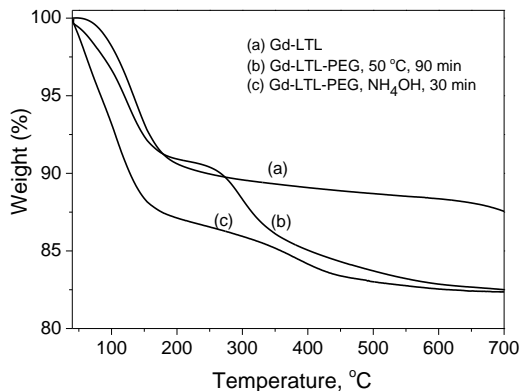


Figure 5.3. TGA curves of Gd-LTL and PEGylated Gd-LTL samples. The PEGylation was carried out either under heating (50 °C) or catalytic conditions (the use of NH₄OH).

As we have shown in our previous studies (Chapter 4), PEGylation of the surface of LTL significantly prevents leakage of loaded ions from the inner cavities. Therefore in the current case, loading with a ⁶⁴Cu radiotracer is expected to demand for a prompt surface functionalization, and the PEGylation step requires optimization. Here, for this purpose methoxypolyethylene glycol (mPEG) ($M_n = 2000$) conjugated with (3-aminopropyl) trimethoxysilane (mPEG₂₀₀₀-silane) was attached to the silanol-rich surface of zeolite. Two methods were investigated to reduce the PEGylation time. In the first method, a mixture of LTL and an excess of mPEG₂₀₀₀-silane (ratio of 1 : 5, w / w) was incubated at 50 °C for 90 min, followed by triple washing with PBS and freeze drying. Thermogravimetric analysis (TGA) showed successful 8.1 wt % PEGylation. The TGA curve of the PEGylated sample (Figure 5.3) showed a typical decomposition range of 200 to 600 °C that can be assigned to mPEG₂₀₀₀-silane. The second method involved PEGylation at room temperature using NH₄OH as a catalyst. As shown in Figure 5.3, successful PEGylation with 5.0 % PEG can be achieved within 30 min under these conditions. The TGA curve of this sample showed quite similar PEG decomposition with that of samples using NH₄OH, which is in agreement with our previous results (Chapter 4). Extraction of significant amounts of Cu²⁺ from the zeolite interior by application of NH₄OH due to formation of [Cu(NH₃)₄]²⁺·nH₂O could be excluded by a quantitative gamma counting study on the leaching using ⁶⁴Cu-loaded LTL (20 MBq, 1.2×10⁻⁵ wt % of ⁶⁴Cu) during PEGylation: the leaching with and without using

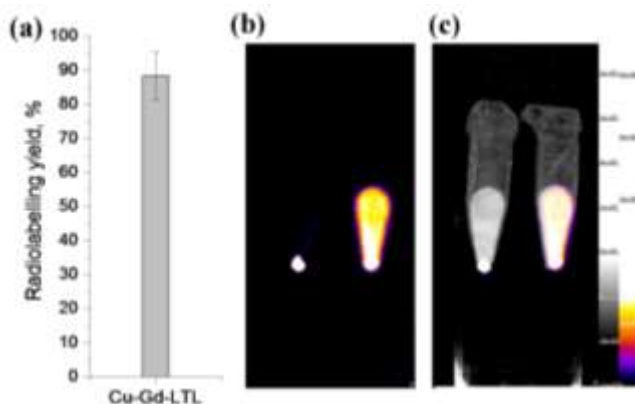


Figure 5.4. Radiolabeling of Gd-LTL with ^{64}Cu . (a) The average activity measured by gamma counting after loading of Gd^{3+} and $^{64}\text{Cu}^{2+}$, (b) PET and (c) PET-CT phantom images. In both images, the centrifuged sample is on the left while the non-centrifuged is on the right.

NH_4OH for PEGylation was very small, 7.3 % and 7.6% of the loaded amount, respectively. Therefore, both PEGylation methods described above can be used for the post-loading PEGylation of LTL particles.

Radiolabeling of Gd-LTL using ^{64}Cu

The radiolabeling of LTL with ^{64}Cu was performed following the procedures described above. The obtained labeled LTL was PEGylated under heating conditions. After ion-exchange between Na^+ and the mixture of Gd^{3+} (4.3 wt % loading) and $^{64}\text{Cu}^{2+}$ (20 MBq) for 30 min and PEGylation at 50 °C for 90 min, the reaction mixture was centrifuged and washed thoroughly with PBS. The resulting sample showed a radiolabeling yield as high as 88.4 ± 7.2 % (Figure 5.4a).

To confirm the successful loading of ^{64}Cu into LTL, gamma counting measurement and acquisition of PET phantoms were used. After the radiolabeling, PEGylation and purification, the obtained sample was first split into two Eppendorf vials, one was centrifuged while the other one was not. Clearly, the centrifuged sample showed centered radioactivity in the pellet while the non-centrifuged sample exhibited distributed radioactivity throughout the suspension (Figure 5.4b and 5.4c). Therefore, the PET and PET-CT phantom images indicate the successful loading of $^{64}\text{Cu}^{2+}$ into LTL. Noteworthy,

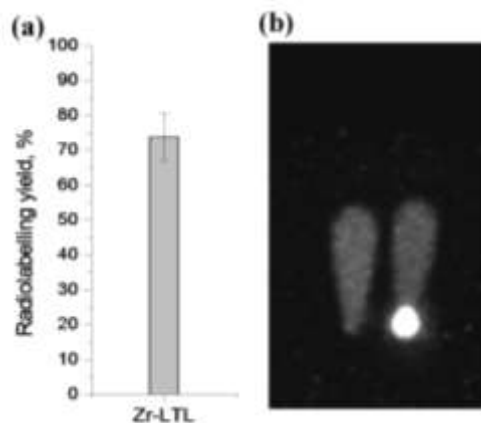


Figure 5.5. Radiolabeling of Gd-LTL with ^{89}Zr . (a) The average activity measured by gamma counting after labeling using $^{89}\text{Zr}^{4+}$. (b) PET images of the non-centrifuged (left) and centrifuged (right) samples.

when the CT images are included (Figure 5.4c), we observed a background of the supernatant, which should result from the tiny amount of remaining zeolite particles after centrifugation. This, however, was not observed in PET images due to the very low ^{64}Cu concentration remaining in this supernatant (e.g. only 1.2×10^{-5} wt % of ^{64}Cu loaded into zeolite in the radiolabeling experiment).

Radiolabeling of Gd-LTL using ^{89}Zr

Labeling of Gd^{3+} -loaded LTL with ^{89}Zr was performed at pH 3.0-4.0 for 1.5 h by adding 1.0 MBq of ^{89}Zr (in oxalic acid) into LTL suspension. After the reaction and purification, this sample showed an average radiolabeling yield of 74 % (Figure 5.5a). In contrast to the fast labeling with ^{64}Cu (0.5 h), increasing the incubation time of ^{89}Zr from 0.5 to 1.5 h resulted in an increase of loading from 46.7 to 80.3 ± 6.7 %. This suggests a labeling mechanism that differs from that for the fast ion-exchange between Cu^{2+} and Na^{+} is operative here. ^{89}Zr is typically produced in oxalic acid and exists as ^{89}Zr oxalate $[\text{Zr}(\text{C}_2\text{O}_4)_4]^{4-}$, with a Zr-coordination number of 8 under acidic conditions (pH 3.0-4.0). The oxalate dissociates to give 6-coordinated $[\text{Zr}(\text{C}_2\text{O}_4)_3]^{2-}$,²⁸ which provides space on Zr^{4+} to coordinate with silanol oxygen atoms at the surface of LTL. As the calculated diagonal dimension of $[\text{Zr}(\text{C}_2\text{O}_4)_3]^{2-}$ is 7.3 Å and thus larger than the pore opening of LTL (7.1 Å), it

can be assumed that ^{89}Zr strongly coordinates to the oxygens at the surface of LTL rather than those of the interior. Furthermore, all Zr^{4+} -complexes present in solution are negatively charged, which prevents entering the negatively charged framework of zeolite LTL. It may be concluded that the ^{89}Zr label is present on the surface of the LTL nanoparticles.

The successful labeling was confirmed by PET phantoms (Figure 5.5b). The background in images of both centrifuged and non-centrifuged samples appears similar caused by the necessary software manipulation during image construction due to the low activity used.

Stability of ^{64}Cu -LTL and ^{89}Zr -LTL under physiological conditions

The stability of the radiolabeled LTL was evaluated by incubating the samples in PBS (pH = 7.4) and human serum at 37 °C for 24 h, respectively. As shown in Table 5.1, the leakage of ^{64}Cu is 11.1% in PBS and 89.7% in serum despite 5 % PEG coating on the surface PEG. On the contrary, the leakage of ^{89}Zr from the unPEGyalted Zr-LTL is significantly lower in both media (1.6 and 7.1 %, respectively). The difference in stability of the two radiolabeled LTL samples can be most probably explained by the different location of the radioactive label as discussed above.

Table 5.1. Stability of ^{64}Cu -LTL and ^{89}Zr -LTL in PBS and Serum at 37 °C for 24 h.

	Leakage of ^{64}Cu , %		Leakage of ^{89}Zr , %	
	In PBS	In Serum	In PBS	In Serum
PEGylated	11.1	89.7	1.6	7.1
Calcined and Extracted	n.d. ^a	8.0	/	/

^a n.d. = not determined.

Next, two methods were investigated to increase the stability of ^{64}Cu -LTL: 1) increasing the PEG-loading and 2) locking the $^{64}\text{Cu}^{2+}$ -ions in the small cavities of LTL. Upon increasing the PEG-density on ^{64}Cu -LTL from 5.0 to 7.0 %, the leaching of $^{64}\text{Cu}^{2+}$ -ions indeed decreased by 23.2 % to 66.5 % in serum. However, further increase of the PEG-density is not preferred as it will eventually result in restriction of water exchange processes and hence decrease of relaxivity (see Chapter 4). Locking of the Cu^{2+} ions was achieved by a procedure analogous to that used previously to selectively load Eu^{3+} ions into

the locked small cavities of LTL.¹⁷ The $^{64}\text{Cu}^{2+}$ ions were first loaded into the big channels of LTL by ion-exchange. After calcination at 600 °C for 2 h and extraction with EDTA (0.05M) (three times), $^{64}\text{Cu}^{2+}$ ions remaining at the surface of LTL (55 wt %) were extracted, suggesting that 45 wt % of $^{64}\text{Cu}^{2+}$ ions were effectively retained in the big and small cavities of LTL. The resultant sample was then incubated in serum at 37 °C for 24 h. It turned out that after the calcination and extraction only 8.0 % $^{64}\text{Cu}^{2+}$ leached out. Therefore, it can be concluded that calcination is an effective method to stabilize the $^{64}\text{Cu}^{2+}$ in LTL. The total time needed for the preparation of ^{64}Cu -LTL in this way is less than 7 h, including ion-exchange, calcination and extraction, which is still shorter than one half-life time of ^{64}Cu and thus is favorable to prepare the final MRI-PET dual agent. In the following work, both calcination and PEGylation will be used to stabilize the ^{64}Cu -Gd-LTL, which is expected to prevent the leaching completely.

CONCLUSIONS

The chelate-free radiolabeling of zeolite LTL can be achieved by using ^{64}Cu and ^{89}Zr through ion-exchange with Na^+ in the zeolite cavities and coordination with silanol oxygen on the surface of LTL, respectively. Both labelings have very high efficiency and labeling yield. Incubation of ^{64}Cu -LTL under physiological conditions, particularly in serum, showed significant leaching of ^{64}Cu . The leakage can be circumvented by the relocation of ^{64}Cu -ions to the small cavities of LTL upon calcination where they can be locked due to the restrict dimension of the cavities. PEGylation can be further applied to improve the stability of the ^{64}Cu -LTL. By contrast, ^{89}Zr -LTL shows very high stability (7.1% in serum), which can be explained by a stronger binding of $[\text{Zr}(\text{C}_2\text{O}_4)_3]^{2-}$ species with the surface oxygen.

In conclusion, this preliminary study demonstrates the versatility of LTL nanozeolite for the application in bioimaging and provides useful insights into the radiolabeling strategies with ^{64}Cu and ^{89}Zr . After the following careful optimizations it may lead to a highly stable MRI-PET dual imaging probe.

EXPERIMENTAL SECTION

Production of ^{64}Cu and radiolabeling of zeolite LTL

^{64}Cu was produced by a cyclotron at the PET Imaging Centre, St. Thomas' Hospital, London, UK. The ^{64}Cu solution obtained (20 MBq) was transferred into a small glass vial, dried at 90 °C under N_2 gas flow, and then re-dissolved by adding 286.4 μL of aqueous solution of GdCl_3 (1mM, pH = 5.5). The resulting solution was added to a suspension of 1.0 mg of LTL particles in 1.0 mL of MilliQ H_2O prepared by sonication. The radioactivity of the final mixture was 18.0 MBq. The solution was then kept at 45 °C for 0.5 h and shaken manually every 5 min. After that 10 μL of mPEG₂₀₀₀-silane solution (10 mM) was added and incubated for another 1.5 h. Finally, the mixture was centrifuged (10,000 rpm) and washed three times with PBS. The radioactivity was measured by a gamma counter.

The leakage study of ^{64}Cu was carried out at the Reactor Institute Delft. ^{64}Cu was produced in the SmallBeBe facility in the reactor. 40 mg of ^{64}Zn (pure Zn, 99.97%) was irradiated with a thermal neutron flux of $3.71 \times 10^{17} \text{ n m}^{-2} \text{ s}^{-1}$, epithermal flux of $3.59 \times 10^{16} \text{ n m}^{-2} \text{ s}^{-1}$ and fast flux of $2.05 \times 10^{17} \text{ n m}^{-2} \text{ s}^{-1}$ for 12 h. After decaying for 3 h, the product was dissolved in a small amount of HCl (8 M). This solution was purified through a 2x8 Dowex resin column, and the ^{64}Cu was extracted by a second wash with 1 M HCl. The radiolabeling following the procedures as those at King's College London (see above) by first transferring the ^{64}Cu solution into a small glass vial and drying it at 90 °C under N_2 gas flow. After the labeling, the suspension of LTL particles was transferred into a porcelain crucible and carefully dried under N_2 gas flow. The calcination was then performed at 600 °C for 2h. To extract the ^{64}Cu ions from the big cavities, the calcined ^{64}Cu -LTL particles were suspended in 1.5 mL of EDTA (0.05 M), incubated for 10 min, centrifuged (3,500 rpm) and washed twice with EDTA. The extracted particles were finally suspended in 1.5 ml of pure serum and incubated at 37 °C for 24. The leakage was determined by counting the radioactivity of the supernatant and pellet after centrifugation.

Radiolabeling of zeolite LTL using ^{89}Zr

The radionuclide ^{89}Zr was produced by BV Cyclotron VU, The Netherlands. The labeling was performed by addition of 1.0 MBq ^{89}Zr (30 μL in oxalic acid) into 1.0 mL of Na-LTL suspension (1.0 mg/mL) followed by incubation at 55 °C for 1.5 h. The pH value of the

suspension was determined to be between 3.0-4.0. After incubation the mixture was centrifuged at 10.000 rpm for 5 min, the radioactivity of both supernatant and precipitate were measured, and the labeling yield was calculated.

PET/CT phantoms and radioactivity measurements

PET phantom images were acquired with a NanoPET-CT TM preclinical animal scanner (Mediso Ltd., Bioscan Inc.). The image acquisition was set in list mode format.¹⁰ Acquisition time was 15 min. OSEM was used as the reconstruction method (6 subset s, 8 iterations, 0.29 mm pixel size, 0.585 mm axial thickness) based on SSRB 2D LOR rebinning (linear interpolation, 16 span-size). The CT images were acquired with 55 kVp tube voltage, 1.2 s exposure time in 360 projections. The images of two modalities (PET-CT) were fused using InVivoScope (Bioscan) software. The radioactivity of the obtained samples was measured with a dose calibrator (CRC-25R, Capintec, USA) or a gamma-counter (1282 CompuGamma, LKB Wallac, Finland).²⁹

Relaxation time measurements

The longitudinal and transverse relaxation times of all samples were measured on a Varian Unity Inova 300 NMR spectrometer, as described in Chapter 3. In typical procedures, 2.5 mg of LTL samples were stabilized in 2.0 mL of 0.5 % xanthan gum solution. Longitudinal relaxation times were measured with the inversion recovery method. Transverse relaxation times were measured with the CPMG pulse sequence in which the length of the spin echo train was varied. An echo time of 0.5 ms was applied for all measurements. The concentration of Gd³⁺-ions was determined using the bulk magnetic susceptibility (BMS) method.²⁶

Acknowledgements

This chapter was possible thanks to collaboration with Dr. Rafael T. M. de Rosales from the King's College London, under the financial support from COST Action (STSM-TD1007-17171), and the collaboration with Robin de Kruijff and Dr Antonia G. Denkova from the Reactor Institute Delft.

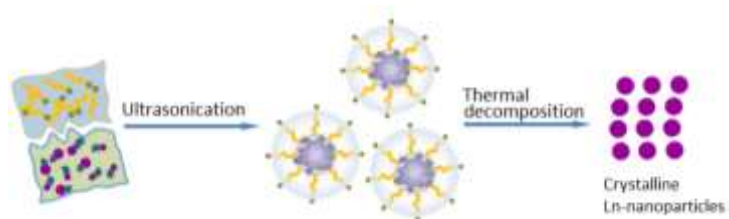
References

- (1) Frullano, L.; Meade, T.; *J. Biol. Inorg. Chem.* **2007**, *12*, 939-949.
- (2) Weissleder, R.; Pittet, M. J.; *Nature* **2008**, *452*, 580-589.
- (3) Doan, B.-T.; Meme, S.; Beloeil, J.-C. In *The Chemistry of Contrast Agents in Medical Magnetic Resonance Imaging*; John Wiley & Sons, Ltd: 2013, p 1-23.
- (4) Bonnet, C. S.; Tei, L.; Botta, M.; Tóth, É. In *The Chemistry of Contrast Agents in Medical Magnetic Resonance Imaging*; John Wiley & Sons, Ltd: 2013, p 343-385.
- (5) Caravan, P.; Zhang, Z. In *The Chemistry of Contrast Agents in Medical Magnetic Resonance Imaging*; John Wiley & Sons, Ltd: 2013, p 311-342.
- (6) de Rosales, R. T. M.; *J. Labelled Compd. Radiopharm.* **2014**, *57*, 298-303.
- (7) Price, E. W.; Orvig, C.; *Chem. Soc. Rev.* **2014**, *43*, 260-290.
- (8) Wong, R. M.; Gilbert, D. A.; Liu, K.; Louie, A. Y.; *ACS Nano* **2012**, *6*, 3461-3467.
- (9) Suchy, M.; Bartha, R.; Hudson, R. H. E.; *RSC Adv.* **2013**, *3*, 3249-3259.
- (10) de Rosales, R. T. M.; Tavaré, R.; Paul, R. L.; Jauregui-Osoro, M.; Protti, A.; Glaria, A.; Varma, G.; Szanda, I.; Blower, P. J.; *Angew. Chem. Int. Ed.* **2011**, *50*, 5509-5513.
- (11) de Rosales, R. T. M.; Tavaré, R.; Glaria, A.; Varma, G.; Protti, A.; Blower, P. J.; *Bioconjugate Chem.* **2011**, *22*, 455-465.
- (12) Zhou, M.; Zhang, R.; Huang, M.; Lu, W.; Song, S.; Melancon, M. P.; Tian, M.; Liang, D.; Li, C.; *J. Am. Chem. Soc.* **2010**, *132*, 15351-15358.
- (13) Liu, T.; Shi, S.; Liang, C.; Shen, S.; Cheng, L.; Wang, C.; Song, X.; Goel, S.; Barnhart, T. E.; Cai, W.; Liu, Z.; *ACS Nano* **2015**, *9*, 950-960.
- (14) Popović, Z.; Otter, M.; Calzaferri, G.; De Cola, L.; *Angew. Chem. Int. Ed.* **2007**, *46*, 6188-6191.
- (15) Popović, Z.; Busby, M.; Huber, S.; Calzaferri, G.; De Cola, L.; *Angew. Chem. Int. Ed.* **2007**, *46*, 8898-8902.
- (16) Peters, J. A.; Djanashvili, K.; *Eur. J. Inorg. Chem.* **2012**, *2012*, 1961-1974.
- (17) Mayer, F.; Zhang, W.; Brichart, T.; Tillement, O.; Bonnet, C. S.; Tóth, É.; Peters, J. A.; Djanashvili, K.; *Chem. Eur. J.* **2014**, *20*, 3358-3364.
- (18) Zhang, W.; Peters, J. A.; Mayer, F.; Helm, L.; Djanashvili, K.; *J. Phys. Chem. C* **2015**, *119*, 5080-5089.
- (19) Wadas, T. J.; Wong, E. H.; Weisman, G. R.; Anderson, C. J.; *Chem. Rev.* **2010**, *110*, 2858-2902.
- (20) Anderson, C. J.; Ferdani, R.; *Cancer Biother. Radiopharm.* **2009**, *24*, 379-393.

- (21) Perk, L.; Visser, O.; Stigter-van Walsum, M.; Vosjan, M. W. D.; Visser, G. M.; Zijlstra, J.; Huijgens, P.; van Dongen, G. M. S.; *Eur. J. Nucl. Med. Mol. Imag.* **2006**, *33*, 1337-1345.
- (22) Börjesson, P. K. E.; Jauw, Y. W. S.; Boellaard, R.; de Bree, R.; Comans, E. F. I.; Roos, J. C.; Castelijns, J. A.; Vosjan, M. J. W. D.; Kummer, J. A.; Leemans, C. R.; Lammertsma, A. A.; van Dongen, G. A. M. S.; *Clin. Cancer. Res.* **2006**, *12*, 2133-2140.
- (23) Csajbók, É.; Bányai, I.; Vander Elst, L.; Muller, R. N.; Zhou, W.; Peters, J. A.; *Chem. Eur. J.* **2005**, *11*, 4799-4807.
- (24) Platas-Iglesias, C.; Vander Elst, L.; Zhou, W.; Muller, R. N.; Geraldes, C. F. G. C.; Maschmeyer, T.; Peters, J. A.; *Chem. Eur. J.* **2002**, *8*, 5121-5131.
- (25) Newell, P. A.; Rees, L. V. C.; *Zeolites* **1983**, *3*, 22-27.
- (26) Corsi, D. M.; Platas-Iglesias, C.; Bekkum, H. v.; Peters, J. A.; *Magn. Reson. Chem.* **2001**, *39*, 723-726.
- (27) Barge, A.; Cravotto, G.; Gianolio, E.; Fedeli, F.; *Contrast Media Mol. Imaging* **2006**, *1*, 184-188.
- (28) Holland, J. P.; Vasdev, N.; *Dalton Trans.* **2014**, *43*, 9872-9884.
- (29) Sandiford, L.; Phinikaridou, A.; Protti, A.; Meszaros, L. K.; Cui, X.; Yan, Y.; Frodsham, G.; Williamson, P. A.; Gaddum, N.; Botnar, R. M.; Blower, P. J.; Green, M. A.; de Rosales, R. T. M.; *ACS Nano* **2013**, *7*, 500-512.

Molecular Architecture Control in Synthesis of Spherical Ln- Containing Nanoparticles

6



INTRODUCTION

Lanthanide-containing nanoparticles (Ln-NPs) have attracted considerable interest in recent years, and their properties have been thoroughly investigated in relation to the various applications such as optics,¹ catalysis² or biomedicine,³⁻⁶ including cell labelling, diagnostics, therapy and combinations thereof. For instance, due to their high Ln³⁺-loading, targeting Ln-NPs can deliver high payloads of Ln-ions to the site of interest,⁷ which allows the detection of biomarkers expressed at low levels on a cell surface.⁸ Size and morphology control plays an essential role in application of NPs. For example, it has been demonstrated that non-spherical shapes translate into cytotoxicity due to a higher chance to damage the cell membranes.⁹ Furthermore, the cellular as well as tissue and organ distribution of NPs is highly dependent on the particle size.^{10,11} Particles less than 100 nm in diameter can easily pass through the vasculature, and the smallest ones can even spread into organs.^{12,13} In case of application of NPs as contrast agents (CAs) for magnetic resonance imaging (MRI), the size becomes particularly essential as it determines their usefulness for either T_1 - or T_2 -weighted imaging. Since the efficacy of positive (T_1) nanoparticulate CAs depends on the interaction of water molecules with paramagnetic ions at the surface of NPs, a high surface-to-volume ratio is required and thus NPs with a diameter smaller than 10 nm are preferred. On the other hand, negative (T_2) contrast depends on magnetic susceptibility and the magnitude of magnetic moment, which are in direct relation with the number of paramagnetic ions per particle and hence the size, shape and surface-to-volume of the applied NPs.

A large number of publications reports on Ln-based NPs such as oxides,^{14,15} carbonates,¹⁶ oxysulfides,¹⁷ polysiloxane networks,¹⁸ hybrids,¹⁹ zeolites, and porous silica supporters.⁶ The size of these particles varies widely in the range of 1-200 nm depending on the preparation methodologies applied. The polyol method is particularly useful to prepare ultrasmall Gd-oxide NPs (1-3 nm).²⁰ However, for larger particles this procedure is time-consuming due to slow nucleation and the need for repetition of seed growth, and poorly reproducible as there is no control over the yield and uniformity of the resultant NPs. The polyol method has also raised concerns about inhibitory effects on neutrophil oxidative burst that might be caused by the presence of diethylene glycol on the surface of particles prepared in

such solvent.²¹ We have previously reported that Ln carbonate NPs (turning into oxides upon calcination) can be readily prepared *via* controlled microwave-assisted seed growth.¹⁶ The smallest size achievable with reasonable yield and good homogeneity by this method is 40 nm, as demonstrated by dynamic light scattering. Finally, the solvothermal method is dominating in the synthesis of upconversion NPs with highly controlled size and morphological uniformity. The resulting particles have promising applicability in optical imaging, but their usefulness with respect to MRI is limited.²² Recently, Eu-doped Gd₂O₃ particles in a 5-200 nm range for multimodal/sequential CAs prepared by chemical vapor synthesis at high temperature have been reported.²³ Alternatively, a laser ablation method performed by focusing the laser beam onto a Gd target has been described,²⁴ resulting in spherical Gd₂O₃ particles with an average diameter of 7 nm.

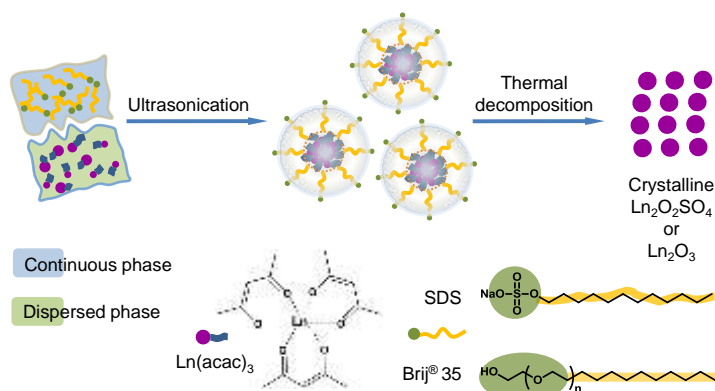
The miniemulsion (or nanoemulsion) technique, widely applied in polymer chemistry,^{25,26} is however uncommon for the preparation of inorganic NPs. Considering the great interest towards NPs with defined size, we describe herein a novel miniemulsion method for the facile size-controlled preparation of spherical Ln-based NPs in the otherwise not readily accessible range of 5-40 nm. A miniemulsion consists of dispersed nanosized droplets formed from two phases of different polarity upon exposure to high power ultrasound. The resulting nanodroplets usually have a narrow size distribution and can be well stabilized in emulsion by an appropriate surfactant. The formation of the droplets highly depends on tunable factors such as composition, phase or surfactant,²⁵ and the miniemulsion technique can be extended to the generation of composite materials, in which different metals as well as surface coatings can be incorporated.²⁷⁻²⁹

The method reported herein involves two steps: an easy and efficient preparation of miniemulsions consisting of Ln nanodroplets, and a subsequent thermal decomposition to obtain Ln-containing solid particles. It is noteworthy that the nature of the product obtained through thermal decomposition is highly dependent on the surfactant in the continuous phase: for example Ln₂O₃ is obtained using Brij® 35, while Ln₂O₂SO₄ is produced in the presence of sodium dodecyl sulfate (SDS). This simple miniemulsion method opens new and interesting alternatives to prepare NPs for a variety of applications, including imaging and therapy.

RESULTS AND DISCUSSION

Formation of the nanodroplets

In order to obtain a miniemulsion containing homogeneous and stable nanodroplets, a hydrophobic dispersed phase and a hydrophilic continuous phase need to be mixed and sonicated. In general, once homogeneously distributed nanodroplets are obtained, no decomposition or aggregation takes place and the nanodroplets can be converted into a solid material by removal of the solvents. This strategy was successfully exploited for the synthesis of lanthanide-containing NPs (Scheme 6.1).



Scheme 6.1. Two-step preparation of Ln-NPs. Small and homogeneous nanodroplets in miniemulsion were first achieved by powerful sonication followed by evaporation of the hydrophobic solvent; freeze-drying and subsequent calcination led to the aimed systems.

Homogeneous nanodroplets in miniemulsion were prepared by powerful sonication of a mixture of $\text{Ln}(\text{acac})_3$ in the dispersed phase and surfactant in the continuous phase. The conditions of sonication in terms of mechanical energy and duration were chosen to allow the nanodroplets in emulsion to reach a steady state.³⁰ The presence of a surfactant facilitates the nucleation by forming a region of hydrophobic tails where nanosized chloroform or dichloromethane cores containing $\text{Ln}(\text{acac})_3$ are trapped and act as nanoreactors; the hydrophilic moieties extend into a polar continuous phase of water. Such configuration provides discrete particle formation. The resulting nanodroplets were then isolated and thermally decomposed into solid nanoparticles.

Table 6.1. Experimental data for the preparation of Ln-containing nanodroplets and NPs under different conditions

Entry	Metal ^a	Dispersed phase ^b	Octadecane (mg)	Continuous phase	Surfactant (mM) ^c	DLS size ^d (nm)	PDI	Product after calcination ^e	TEM size (nm)
1	Ho	CHCl ₃	30	H ₂ O	SDS (10)	37 ± 6	0.25	Ho ₂ O ₂ SO ₄	15 ± 3.1
2	Ho	CHCl ₃	5	H ₂ O	SDS (10)	43 ± 4	0.34	Ho ₂ O ₂ SO ₄	18 ± 3.8
3	Ho	CHCl ₃	0	H ₂ O	SDS (10)	45 ± 4	0.37	Ho ₂ O ₂ SO ₄	24 ± 5.7
4	Ho	CHCl ₃	0	H ₂ O	SDS (30)	51 ± 7	0.44	Ho ₂ O ₂ SO ₄	^{-f}
5	Ho	DCM	0	H ₂ O	SDS (10)	26 ± 3	0.39	Ho ₂ O ₂ SO ₄	8 ± 1.8
6	Ho	DCM	0	H ₂ O /EtOH	SDS (10)	37 ± 9	0.31	Ho ₂ O ₂ SO ₄	18 ± 2.0
7	Ho	DCM	0	H ₂ O /EtOH	SDS (20)	57 ± 6	0.39	Ho ₂ O ₂ SO ₄	^{-f}
8	Ho	DCM	0	H ₂ O	Brij® 35 (5.2)	109 ± 9	0.087	Ho ₂ O ₃	12 ± 2.0
9	Gd	DCM	0	H ₂ O	SDS (10)	33 ± 7	0.40	Gd ₂ O ₂ SO ₄	^{-f}
10	Gd	DCM	0	H ₂ O	Brij® 35 (5.2)	98 ± 11	0.10	Gd ₂ O ₃	7 ± 2.1

^a 50 mg of Ln(acac)₃ for each batch. ^b 2.5 ml for each batch. ^c With respect to the continuous phase. ^d Average diameter. ^e As determined by XRD. ^f not measured.

Different synthetic conditions, such as combinations and amounts of solvents and surfactants, were investigated (Table 6.1). The various products obtained were preliminary characterized *via* DLS size measurements. At first, preparations were carried out with Ho(acac)₃ in chloroform as dispersed phase, while SDS was used as surfactant in the aqueous phase. It is a common strategy in miniemulsion techniques to add a hydrophobic co-stabilizing agent to stabilize the droplets against Ostwald ripening.³¹ Here, we selected octadecane to adjust the osmotic pressure of the miniemulsion. It appeared that the presence of octadecane in the dispersed phase had a positive effect on reducing the size of the Ho-containing droplets, but decreasing its concentration led to higher polydispersity index (PDI) values (Table 6.1, entries 1-3). TEM images of the particles obtained after thermal decomposition of these droplets showed that the presence of octadecane leads to less homogenous solid particles. Therefore, a hydrophobic agent was omitted in the next preparations in order to achieve a better homogeneity of the resultant solid particles.

Although it has been demonstrated that in general the concentration of surfactant plays a crucial role in controlling the size of the droplets,³² this effect was observed only to a limited extent in the present case: varying the concentration of SDS in the

continuous phase from 10 to 30 mM (Table 6.1, entries 3 and 4) did not change the droplet size significantly (as measured by DLS, 45 vs. 51 nm). Furthermore, increasing the SDS concentration over 30 mM resulted in unstable nanodroplets precipitating within 3 days.

The diffusion of the dispersed phase through the water phase has been shown to limit the growth of nanodroplets.²⁵ With this in mind, we investigated the use of more polar DCM as the solvent of the dispersed phase. When keeping the other conditions unmodified (Table 6.1, entries 3 and 5) the diameter of the droplets in the miniemulsion was only 26 nm as compared to 45 nm in CHCl_3 . This can be explained in terms of a different interface activity, where the interfacial tension is 32.80 mN m^{-1} for $\text{H}_2\text{O}/\text{CHCl}_3$ and 28.31 mN m^{-1} for $\text{H}_2\text{O}/\text{DCM}$.³³ Thus, a relatively minor change in the polarity of the dispersed phase has a strong impact on the formation of the droplets in the miniemulsion. To further investigate this effect, 12.5 wt% of ethanol was added to the continuous phase to improve the diffusion at the interface between H_2O and DCM:³⁴ this led to an increase in the size of the nanodroplets from 26 to 37 nm (Table 6.1, entries 5 and 6), in accordance with the improved solubility of $\text{Ln}(\text{acac})_3$ and the higher miscibility of DCM towards the continuous phase. Doubling the concentration of SDS for the $\text{H}_2\text{O}+\text{EtOH}/\text{DCM}$ resulted in notably bigger nanodroplets (from 37 to 57 nm; Table 6.1, entries 6 and 7). It was also noticed that with anionic SDS as surfactant, the PDIs of the obtained nanodroplets were relatively high (generally between 0.3 and 0.4). This may be explained by the effect of collisions between nanodroplets: the smaller the droplets, the shorter the distance and the higher their number, thus the collision rate increases; eventually, this leads to destabilization and a broader PDI.³⁵

However, when SDS was replaced with Brij® 35, a purely organic and non-ionic surfactant, the PDI dropped dramatically (*e.g.* 0.09 vs. 0.39; Table 6.1, entries 5 and 8). At the same time the size of the nanodroplets increased significantly (109 vs. 26 nm). The latter phenomenon is the consequence of the good affinity between water and the long hydrophilic polyethylene glycol chain of Brij® 35.

Once the factors influencing the preparation of Ho-nanodroplets were assessed, the applicability and reproducibility were checked by preparing analogous Gd-based systems. With $\text{Gd}(\text{acac})_3$ under the same conditions (Table 6.1, entries 5 and 9) the

obtained Gd-nanodroplets had a size of 33 nm, consistent with the value previously measured for the corresponding Ho-based products (26 nm). Also the replacement of SDS with Brij® 35 as surfactant had similar effects (Table 6.1, entries 9 and 10); a remarkable increase in size (98 vs. 33 nm) and a significant lowering of the PDI (from 0.40 to 0.10). These results show that the formation of nanodroplets in a miniemulsion process can be reliably tuned not only by adjusting the polarity of the two phases, but also by playing with the other components in general and the surfactant in particular.

Formation of the nanoparticles

The second step in the preparation of Ln-NPs consists of the transformation of the nanodroplets from the miniemulsion into solid particles through calcination (Scheme 6.1). Both the Ho- and Gd-containing nanodroplets were dried and then decomposed under aerobic conditions at 800 °C for 1 h. The nature of the product after thermal decomposition turned out to depend on the surfactant added during the synthesis. When SDS was used, the calcination yielded oxysulfates ($\text{Ln}_2\text{O}_2\text{SO}_4$) nanocrystals, the surfactant being the source of sulphur. The XRD pattern of the dried Ho-nanodroplets is mainly featureless, indicating a basically amorphous nature (Figure 6.1). The evolution in the crystal structure can be observed by X-ray powder diffraction measurements. After calcination, $\text{Ho}_2\text{O}_2\text{SO}_4$ is obtained instead in a crystalline form (Figure 6.1a). All the XRD reflections revealed a crystal structure of $\text{Ho}_2\text{O}_2\text{SO}_4$ with calculated lattice constants $a = 4.045 \text{ \AA}$, $b = 4.185 \text{ \AA}$ and $c = 12.963 \text{ \AA}$. In addition, a diffraction peak of Ho_2O_3 was observed (Figure 6.1a), the intensity of which was mainly dependent on the applied $\text{Ho}(\text{acac})_3$:SDS ratio.

The thermal decomposition of Gd-containing nanodroplets showed analogous effects (Figure 5.1b). Noteworthy, it is possible to obtain $\text{Ln}_2\text{O}_2\text{SO}_4$ NPs with higher purity by adjusting the molar ratio of starting materials, as shown for $\text{Gd}(\text{acac})_3$ and SDS during the preparation of the corresponding nanodroplets. The XRD pattern of the obtained crystalline $\text{Gd}_2\text{O}_2\text{SO}_4$ reveals calculated lattice constants $a = 4.051 \text{ \AA}$, $b = 4.174 \text{ \AA}$ and $c = 12.973 \text{ \AA}$.

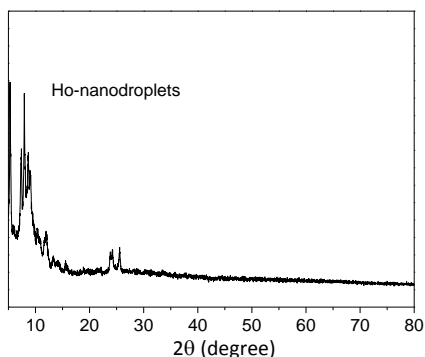


Figure 6.1. XRD pattern of dried Ho-nanodroplets before calcination.

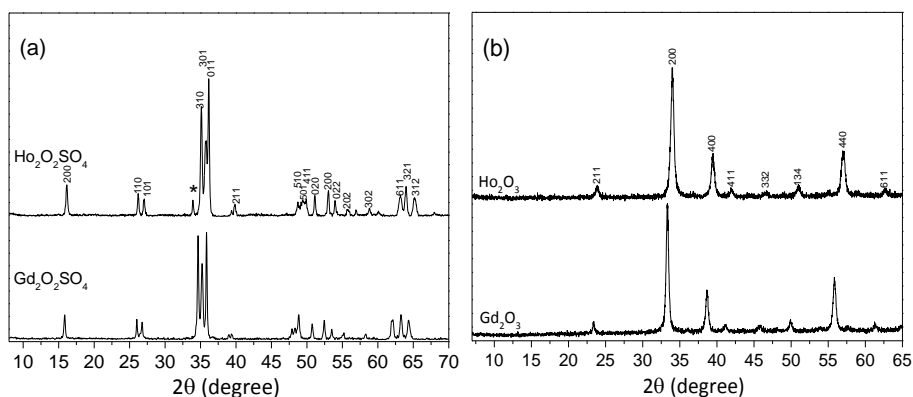


Figure 6.2. XRD patterns of the solid Ln-containing NPs obtained by miniemulsion and subsequent open-air thermal decomposition at 800 °C for 1 h. (a) $\text{Ln}_2\text{O}_2\text{SO}_4$ NPs, SDS was used as surfactant; the peak marked with an asterisk is due to Ho_2O_3 . (b) Ln_2O_3 NPs, Brij® 35 was used as surfactant.

When non-ionic surfactant Brij® 35 was used in the miniemulsion, the subsequent thermal decomposition yielded crystalline oxide (Ln_2O_3) nanocrystals (Figure 6.1b). All reflections in the XRD spectra can be indexed to the cubic structure of Ln_2O_3 (space group: $Ia-3$ (No. 206)) with calculated lattice constants $a = 10.606 \text{ \AA}$ for Ho_2O_3 and $a = 10.812 \text{ \AA}$ for Gd_2O_3 , in perfect agreement with those reported (JCPDS 44-1268, $a = 10.610 \text{ \AA}$ and JCPDS 65-3181, $a = 10.818 \text{ \AA}$ respectively). The observed red shift of the patterns is attributed to the use of Co $K\alpha$ radiation (1.789 \AA) instead of usual Cu (1.541 \AA).

TGA profiles of the thermal decompositions were recorded (Figure 6.3). The starting material $\text{Ho}(\text{acac})_3$ has a major multistep weight loss in the temperature range 30 - 550 °C that includes the dehydration of structurally bound water between

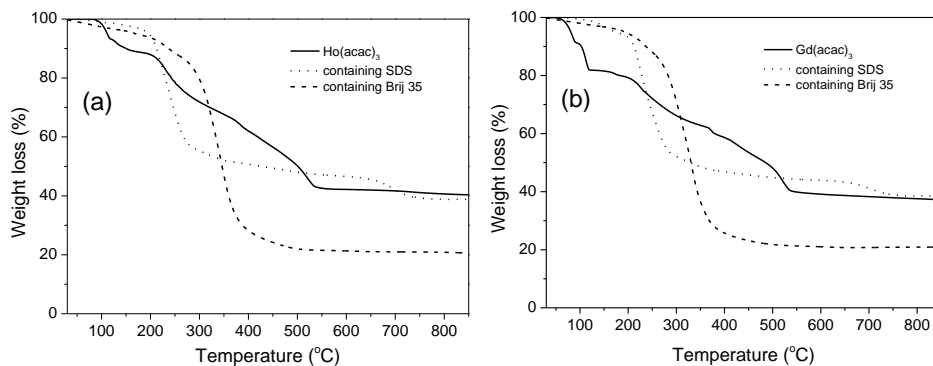


Figure 6.3. TGA profiles of Ln(acac)₃ and the corresponding Ln-containing nanodroplets prepared by using SDS or Brij® 35 as surfactants. Ln = Ho (a) or Gd (b).

30 and 200 °C and decomposition of the organic chelate acetylacetonate up to 550 °C; holmium oxide is finally obtained. The thermogravigram between 30 and 850 °C of a sample of Ho-containing nanodroplets obtained from Ho(acac)₃ in the presence of SDS as surfactant shows a dominant loss (45%) between 170 and 350 °C, that can be attributed to the major decomposition of SDS and acetylacetonate. A total 62% loss was measured until 760 °C, in agreement with the value calculated when considering the reaction scheme (1) with 35 wt% retained taking S, Ho and O into account.



It has been reported that an alternative stacking of $\text{La}_2\text{O}_2^{2+}$ and SO_4^{2-} layers takes place under treatment at high temperature of hydrous nitrates ($\text{Ln}(\text{NO}_3)_3 \cdot n\text{H}_2\text{O}$) intercalated with dodecyl sulphate ions.^{36,37} The gradual decomposition observed in the range 300 - 700 °C can thus be ascribed to the stacking mechanism leading to the formation of $\text{Ln}_2\text{O}_2\text{SO}_4$. Such gradual process proceeds until 760 °C to yield Ln-oxy sulfates, in agreement with the XRD evolution (Figure 6.4). The formation of $\text{Gd}_2\text{O}_2\text{SO}_4$ follows a totally analogous pathway (Figure 6.3b).

Different TGA profiles were recorded for dried nanodroplets obtained in the presence of Brij® 35 as surfactant (Figure 6.3). The dominant weight loss (~78%) between 200 and 500 °C corresponds to the decomposition of organic Brij® 35 and

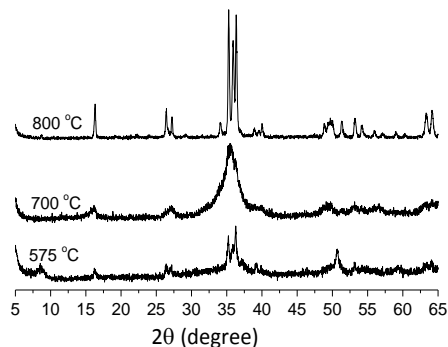


Figure 6.4. XRD patterns of Ho-containing species obtained upon calcination of nanodroplets at different temperatures. The evolution indicates the formation of solid $\text{Ho}_2\text{O}_2\text{SO}_4$ nanoparticles.

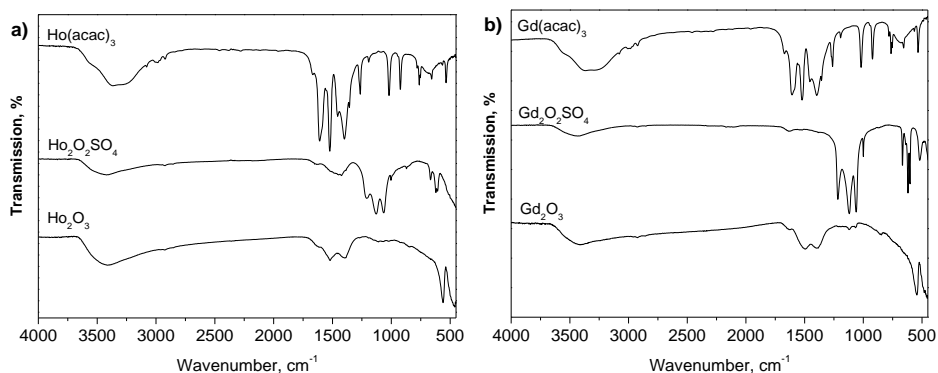


Figure 6.5. FTIR spectra of the starting material $\text{Ln}(\text{acac})_3$ and obtained products $\text{Ln}_2\text{O}_2\text{SO}_4$ and Ln_2O_3 NPs. Ln = Ho (a) or Gd (b).

acetylacetonate. Above 500 °C, the thermogravigram reaches a plateau, indicating that Ho_2O_3 or Gd_2O_3 NPs are obtained.

The surface chemical structure of the obtained various NPs were characterized by Fourier transform infrared spectroscopy (Figure 6.5). The main starting material $\text{Ln}(\text{acac})_3$ (Ln = Ho or Gd) shows the characteristic bands of enolized β -diketones at about 1610, 1520 and 1400 cm^{-1} . After thermal decomposition, the resulting $\text{Ln}_2\text{O}_2\text{SO}_4$ exhibited characteristic bands of SO_4^{2-} ion coordinated to Ln^{3+} ion at 1210, 1130, 997, 664 and 619 cm^{-1} , with an indication of low site symmetry in the oxysulfate.³⁸ In contrast, the spectra of materials prepared by using Brij® 35, exhibited a strong peak at 550 cm^{-1} , typical for cubic-type Ln_2O_3 NPs.³⁹

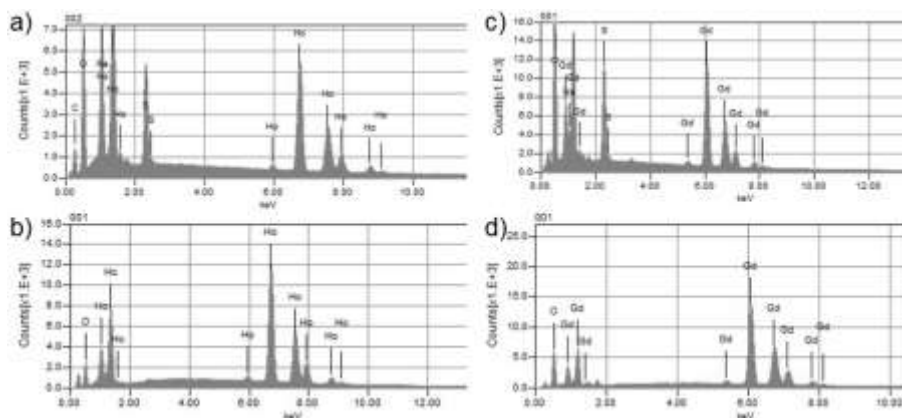


Figure 6.6. EDS spectrum of (a) $\text{Ho}_2\text{O}_2\text{SO}_4$, (b) Ho_2O_3 (c) $\text{Gd}_2\text{O}_2\text{SO}_4$ and (d) $\text{Gd}_2\text{O}_3\text{NPs}$ obtained after calcination, respectively.

Energy dispersive X-ray spectroscopy (EDS) was further applied to determine the compositions of various Ln-based NPs, as shown in Figure 6.6. It is clear that the obtained NPs are composed of $\text{Ln}_2\text{O}_2\text{SO}_4$ and Ln_2O_3 when SDS and Brij® 35 were used, respectively. The solids obtained after thermal decomposition consisted of fairly uniform spherical particles, as determined by TEM images (Figure 6.7).

As mentioned above, with this technique it was also possible to observe how the use of octadecane as a co-stabilizing agent in miniemulsions affects the final size of the particles: under the same reaction conditions (Table 6.1, entries 2 and 3) the addition of octadecane (10 wt% with respect to Ln-acetylacetonate) led to particles (Figure 6.7a) with a diameter (18 nm) smaller than that (24 nm) obtained in its absence (Figure 6.7b). This effect is consistent with the reported claim that increasing the osmotic pressure leads to a decrease in the particles size.³⁰ However, one of the advantages of the method discussed herein is that a hydrophobic co-reagent is not decisive in the preparation of nanodroplets.

As described above, changing the solvent in dispersed phase from CHCl_3 to DCM (Table 6.1, entries 3 and 5) resulted in Ho-nanodroplets with a significantly reduced diameter (from 45 to 26 nm). This is confirmed by the TEM images of the corresponding final $\text{Ho}_2\text{O}_2\text{SO}_4$ NPs (Figure 6.7b and 5.7c) with diameters 24 and 8 nm, respectively. This further highlights the importance of the interfacial activity on the formation of the nanodroplets and, consequently, of the solid particles.

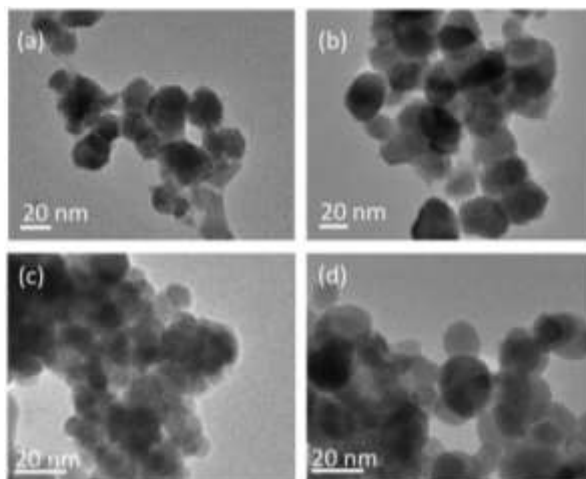


Figure 6.7. TEM images of solid $\text{Ho}_2\text{O}_2\text{SO}_4$ NPs prepared using SDS: (a) and (b) correspond to entries 2 and 3 in Table 5.1 with 10 and 0 wt% of octadecane in dispersed phase, respectively; (c) and (d) correspond to entry 5 and 6 with 0 and 12.5 wt% of ethanol in continuous phase, respectively.

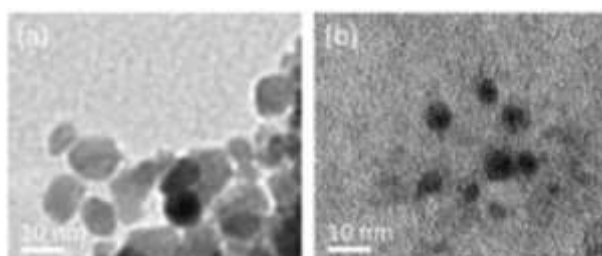


Figure 6.8. TEM images of (a) Ho_2O_3 and (b) Gd_2O_3 nanoparticles, corresponding to entries 9 and 10 in Table 5.1, respectively. Brij® 35 was used in the continuous phase.

The increase in size of the nanodroplets prepared with the addition of ethanol (Table 6.1, entry 6) is reflected in the TEM images of the corresponding final NPs (Figure 6.7d), for which an average diameter of 8 nm was measured. Upon replacement of SDS with Brij® 35 as surfactant in the miniemulsion, the TEM images of Ho_2O_3 and Gd_2O_3 obtained upon calcination showed spherical particles with a diameter of 12 and 7 nm, respectively (Figure 6.8). Although the hydrodynamic diameters of the corresponding nanodroplets were by far larger (109 and 98 nm, respectively) due to the long polymer chain of Brij® 35 (Table 6.1, entries 9 and 10), the solid Ln_2O_3 particles showed the expected small sizes.

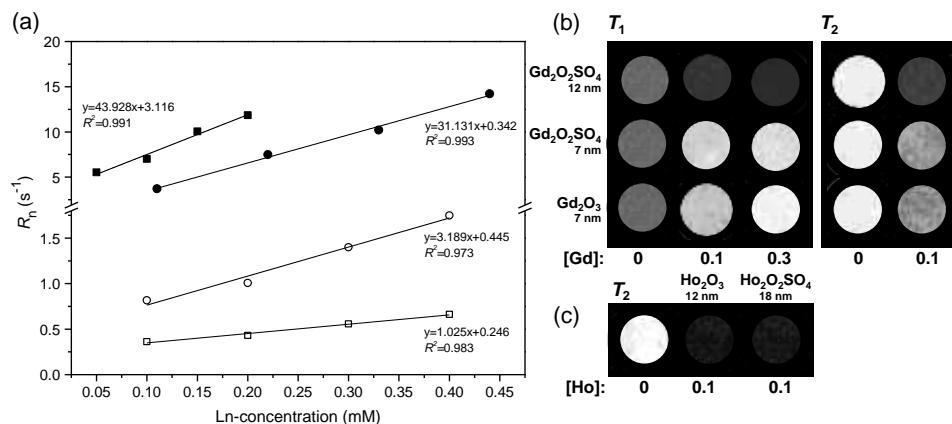


Figure 6.9. MR relaxation rates and MR images of Gd- and Ho-based NPs dispersed in 0.5 % solution of xanthan: (a) Transversal (Ho, solid symbols) and longitudinal (Gd, open symbols) relaxivities of oxysulfates (squares) and oxides (circles) NPs (7 T and 25 °C). (b) MR phantoms containing 0.1 and 0.3 mM Gd₂O₃ and Gd₂O₂SO₄ NPs (7 T and 25 °C), left: T_1 -weighted spin-echo MR images, TE = 10.6 ms and TR = 250 ms; right: T_2 -weighted MR images, TE = 90 ms and TR = 3s. (c) T_2 -weighted images of xanthan phantoms containing 0.1 mM Ho₂O₃ and Ho₂O₂SO₄.

Relaxivity measurements of Ln₂O₂SO₄ and Ln₂O₃ NPs

As an example of their applicability, the Ln-NPs prepared as described above were evaluated in terms of their performance as magnetic resonance imaging contrast agents. Because of its seven unpaired 4f-electrons Gd is the most paramagnetic stable metal ion, and therefore Gd³⁺-complexes are nowadays the most common longitudinal- or T_1 -CAs in medical MRI.^{40,41} On the other hand, Ho (together with dysprosium) is the most efficient transversal- or T_2 -CA for its highest magnetic moment.⁴² In view of their possible application as MRI CAs, the final Ho- or Gd-based NPs were evaluated for transverse (r_2) and longitudinal (r_1) proton relaxivities. The water proton relaxation rates ($R_n = 1/T_n$, n = 1 or 2) of four samples of each Ln were measured at 25 °C and 7 T, and then plotted against the related concentration of paramagnetic Ln³⁺ ion in order to attain the corresponding relaxivity value as the slope of the obtained straight line (Figure 6.9a). For Gd₂O₂SO₄ (12 nm) and Gd₂O₃ (7 nm) particles r_1 is 1.0 and 3.1 s⁻¹mM⁻¹, respectively and is expected to be more impressive at the clinically used magnetic fields (1.5 - 3 T), according to the typical

Table 6.2. Longitudinal and transversal relaxivities of Gd- and Ho-containing NPs as function of their size at 7 T and 25 °C.

Material	Diameter (nm)	r_1 ($s^{-1}mM^{-1}$)	r_2 ($s^{-1}mM^{-1}$)	Preparation method ^a	r_2/r_1	Ref.
Gd ₂ O ₃	2.2	8.8	11.4	PL	1.3	²⁰
Gd ₂ O ₃	3.8	8.8	28.8	PL	3.3	²⁰
Gd ₂ O ₃	4.6	4.4	28.9	PL	6.6	²⁰
Gd ₂ O ₃	7.0	3.1	30.0	ME	9.7	This work
Gd ₂ O ₂ SO ₄	12.0	1.0	35.7	ME	35.7	This work
Gd ₂ O ₂ S	25.0	0.2	55.0	ST	275.0	¹⁷
Ho ₂ O ₃	12.0	0.2	31.1	ME	155.5	This work
Ho ₂ O ₂ SO ₄	18.0	0.4	43.9	ME	109.8	This work
Ho ₂ (CO ₃) ₃	40.0	-	105.0	MW	-	¹⁶

^a PL=polyol; ME=miniemulsion; ST=solvothermal; MW=microwave.

¹H nuclear magnetic relaxation dispersion profiles of solid NPs.^{20,41} The effect of particle size on the MRI contrast enhancement is demonstrated by the acquisition of T_1 - and T_2 -weighted images of phantoms containing various concentrations of the particles at 25 °C and 7 T. The brightness of T_1 -weighted images acquired with Gd₂O₃ or Gd₂O₂SO₄ particles of 7 nm is increasing with increasing concentrations between 0.1 and 0.3 mM (Figure 6.9b). This effect is in agreement with the obtained r_2/r_1 ratio of 10, which is known to be favorable for the T_1 contrast.⁶ Increasing the particle size to 12 nm has a clear negative (dark) effect on the T_1 -weighted intensity, due to higher r_2/r_1 ratio (up to 36, Table 6.2) and a consequent dominance of T_2 - on the intensity (Figure 5b).

The r_2 values obtained for Ho₂O₂SO₄ and Ho₂O₃ are 43.9 and 31.1 mM⁻¹ s⁻¹, respectively. The difference in diameter between the two systems (18 and 12 nm, respectively) must be taken into account, due to the strong linear dependence of r_2 on the particle size.⁴³ Based on the low r_1 values, and consequently, high r_2/r_1 ratio, these particles are suitable for T_2 -weighted imaging, as demonstrated in Figure 6.9c.

Besides the size and chemical composition, several experimental parameters, such as temperature, pH, the strength of the applied magnetic field *etc.* determine the r_1 and r_2 of NPs. Therefore, the relaxivities of even similar types of NPs reported in the literature often cannot be compared directly. Taking this into account, in Table

6.2 a small selection of literature data is compiled to demonstrate the consistency of the relaxivities of Gd- and Ho-NPs obtained by different preparation methods, and measured under the same conditions (7 T, 25 °C). The data clearly show a decrease of r_1 for Gd-NPs upon increase of their particle size as the consequence of the decreasing in the surface-to-volume ratio for oxides as well as for oxysulfates and oxysulfides.

Ho-containing NPs show a strong size-dependence of r_2 . The chemical composition of NPs seems to be of minor importance, as the values for oxide, oxysulfate and carbonate follow the same linear increase of r_2 upon increase in the size. Finally, the relaxivities of Gd- and Ho-NPs obtained from the miniemulsion method fit perfectly in the r_n vs diameter trend and are in agreement with those previously reported for analogous Ln-containing NPs.⁴⁰

CONCLUSIONS

We have demonstrated a facile miniemulsion technique and subsequent thermal decomposition that can be advantageously applied for the preparation of Ln-containing NPs. Such methodology is particularly useful for the preparation of NPs in the size range of 5 to 40 nm as it is far less time-consuming, more reproducible and results in a higher productivity than the polyol strategies suitable for ultrasmall NPs. Therefore, the present miniemulsion method is a valid and convenient alternative strategy with attractive advantages for the synthesis of Ln-NPs.

The formation of nanodroplets under emulsion conditions is highly influenced by the selection of the surfactant and the nature of the dispersed and continuous phases. In the present study, the interfacial activity and the type of surfactant revealed to be the key parameters determining not only the size of the nanodroplets and hence the final solid particles, but also their chemical composition. In particular, depending on the surfactant used, the main products are either lanthanide oxysulfates or oxides. By adjusting these parameters, spherical NPs with a defined diameter can be readily obtained through further thermal decomposition. Both types of particles exhibited the relaxivities that are in accordance to the size and the values reported in the literature. The r_2 relaxivities measured on smaller Ho-NPs (< 20 nm) confirm the linear size-dependence reported previously for larger Ho-NPs (> 40 nm).¹⁶ The MR

images indicate a good T_2 -weighted contrast, and hence, suitability of these NPs prepared by the miniemulsion method as T_2 CAs after a proper surface functionalization. On the contrary, the r_1 relaxivities of Gd-containing NPs decrease with the particle size, and as the result of T_2 -effect becoming dominant, the brightness of the T_1 -weighted MR images acquired with bigger Gd-NPs (> 7 nm) is less. These observations demonstrate the importance of size-control for the applications of Ln-based nanoparticles as MRI CAs.

Considering the similarity of chemical properties of the f -elements, the present technique can be predictably expanded for the preparation of NPs of the whole series of lanthanides to be exploited in a variety of fields such as catalysis (oxysulfates for oxygen storage/release),² optics (oxides with luminescence properties),¹ and diagnostics (paramagnetic nanoparticles).⁴²

EXPERIMENTAL SECTION

Materials and methods

All chemicals were used as supplied from commercial sources: analytical grade solvents, sodium dodecyl sulfate, octadecane (Sigma-Aldrich), polyethylene glycol dodecyl ether (Brij® 35, $M_n \sim 1198$), acetylacetone (acac) (Fluka). “H₂O” refers to high purity water with conductivity of $0.04 \mu\text{S cm}^{-1}$, obtained from a Milli-Q purification system. Lanthanide chlorides ($\text{LnCl}_3 \cdot 6\text{H}_2\text{O}$, Strem Chemicals) were dissolved in 10 mL water, the obtained solutions were filtered over a $200 \mu\text{m}$ Nylon syringe filter and evaporated to dryness under high vacuum before use. $\text{Ln}(\text{acac})_3$ were synthesized according to published procedures:³⁰ typically, acetylacetone (0.220 mol) was dissolved in H₂O (135 ml) and the pH of this solution was adjusted to 8.5 by portion-wise addition of 25% ammonium hydroxide; LnCl_3 (10 mmol; Ln = Gd, Ho) was dissolved in H₂O (5 ml) and slowly added to the above-mentioned solution under stirring. The mixture was stirred overnight and the pink ($\text{Ho}(\text{acac})_3$) or white ($\text{Gd}(\text{acac})_3$) crystals were filtered, washed three times with water and air-dried.

Preparation of Ln-containing nanodroplets by miniemulsion

In a typical procedure to prepare the miniemulsion, the dispersed hydrophobic phase was obtained by mixing Ln(acac)₃ (50 mg) in CHCl₃ or dichloromethane (DCM) (2.5 ml). This suspension was then added dropwise to a continuous phase consisting of SDS or Brij® 35 dissolved in H₂O (8 ml). The mixture was vigorously stirred at room temperature for 1 h (pre-emulsion) and then ultrasonicated (Qsonica Sonicator, 500 W, 1/2 inch tip, 80% amplitude, time interval 0.5 s) for 5 min under ice cooling, yielding milky miniemulsions (pink for Ho and white for Gd). The hydrophobic solvents were removed by careful rotary evaporation at 30 °C to avoid aggregation, until a turbid dispersion appeared. These dispersions were used to measure the hydrodynamic radius of the nanodroplets, and they were then freeze-dried yielding Ln-containing powders.

Phase transformation

Thermal decomposition of the previously obtained powders was performed by calcination at 800 °C under air atmosphere for 1 h applying a heating rate of 2.5 °C min⁻¹. The average yield of this procedure was 82% with respect to Ln(acac)₃.

Characterization

The size of the nanodroplets in the miniemulsion was measured by dynamic light scattering (DLS). The experiments were carried out by using a Malvern Zetasizer NanoZS operating in a particle size range from 0.6 nm to 6 μm and equipped by a He-Ne laser with λ=633 nm. The measurements were performed at 25 °C, and the average diameter was based on three individual measurements, 20 scans for each measurement. To evaluate the process of conversion of the freeze-dried Ln-containing nanodroplets into solid particles, thermogravimetric analysis (TGA) was conducted by using a Perkin-Elmer Thermogravimetric Analyzer TGA7 equipped with a Thermal Analysis Controller TAC 7/DX, from 25 to 900 °C (10 °C min⁻¹) under air atmosphere. X-ray diffractometry (XRD) measurements were performed on a Bruker D8 Advance X-ray diffractometer using Co Kα radiation (1.789 Å) at 35 kV and 40 mA. The data were collected from 5° to 80° 2θ with a step size of 0.020° 2θ and a counting time of 0.5 s per step. Lattice constants were calculated and corrected using MDI JADE software. Transmission electron microscopy (TEM)

analyses were performed on a JOEL JEM-2100 transmission electron microscope. Samples of nanoparticles from dilute aqueous dispersions were evaporated over a 400-mesh copper measurement grid. The instrument operated at an accelerating voltage of 200 kV for the acquisition of section images. The surface composition of formed NPs was characterized by Infrared (IR) spectroscopy performed on a Perkin Elmer Spectrum One FT-IR spectrometer using KBr tablet. The chemical composition of NPs was analyzed by Energy dispersive X-ray spectroscopy (EDS) on a JEOL-JMS 6010 scanning electron microscope with an acceleration voltage of 20kV. The longitudinal (T_1) and transversal (T_2) water proton relaxation times were measured on a Varian-INOVA 300 NMR spectrometer applying inversion recovery and CPMG sequences, respectively. For the latter sequence the half interval time (τ_{cp}) between the successive 180° pulses was fixed at 1.0 ms. The samples for these measurements were prepared by suspending defined amounts of particles in 0.5% xanthan gum solution. The same equipment was exploited to determine the concentrations of Ln^{3+} ($\text{Ln} = \text{Ho}$ and Gd) ions in the aqueous solutions *via* bulk magnetic susceptibility (BMS) method.⁴⁴ MRI experiment were conducted on a PharmaScan 7 T horizontal magnet (B-C 70/16 US, Bruker BioSpin, Wissembourg, France) equipped with B-GA09 gradient system (120 mT/m maximal strength and 90 mm inner diameter) and Paravision 4.0 software (Bruker BioSpin). T_1 -weighted and T_2 - weighted MR images were acquired with spin-echo sequence (RARE sequence with one echo to get a small echo time (TE) equal to the effective-TE) at 25 °C. T_1 -weighted images were acquired with 10.6 ms TE and 250 ms TR (Repetition Time) and $200 \times 200 \mu\text{m}^2$ resolution with a matrix 128×128 in 32 s. T_2 -weighted images were acquired with 90 ms TE and 3000 ms TR and $400 \times 400 \mu\text{m}^2$ resolution with a matrix 64×64 in 3min. All images have 2.0 mm thickness.

Acknowledgements

Thanks are due to Ms. Wan Gengping (Hainan University, China) for TEM, Mr. Ben Norder (TU Delft) for the XRD and Duco Bosma (TU Delft) for the EDX measurements.

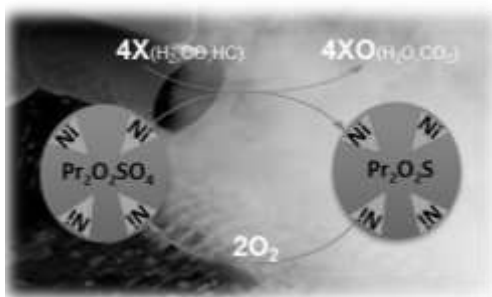
References

- (1) Eliseeva, S. V.; Bunzli, J.-C. G.; *Chem. Soc. Rev.* **2010**, *39*, 189-227.
- (2) Machida, M.; Kawamura, K.; Ito, K.; Ikeue, K.; *Chem. Mater.* **2005**, *17*, 1487-1492.
- (3) Comby, S.; Surender, E. M.; Kotova, O.; Truman, L. K.; Molloy, J. K.; Gunnlaugsson, T.; *Inorg. Chem.* **2013**, *53*, 1867-1879.
- (4) Liu, Y.; Zhang, N.; *Biomaterials* **2012**, *33*, 5363-5375.
- (5) Nicolay, K.; Strijkers, G.; Gröll, H. In *The Chemistry of Contrast Agents in Medical Magnetic Resonance Imaging*; John Wiley & Sons, Ltd: 2013, p 449-487.
- (6) Peters, J. A.; Djanashvili, K.; *Eur. J. Inorg. Chem.* **2012**, *2012*, 1961-1974.
- (7) Bruckman, M. A.; Yu, X.; Steinmetz, N. F.; *Nanotechnology* **2013**, *24*, 20.
- (8) Lin, W.; Hou, Y.; Lu, Y.; Abdelrahman, A. I.; Cao, P.; Zhao, G.; Tong, L.; Qian, J.; Baranov, V.; Nitz, M.; Winnik, M. A.; *Langmuir* **2014**, *30*, 3142-3153.
- (9) Kihara, T.; Zhang, Y.; Hu, Y.; Mao, Q.; Tang, Y.; Miyake, J.; *J. Biosci. Bioeng.* **2011**, *111*, 725-730.
- (10) Li, S.-D.; Huang, L.; *Mol. Pharm.* **2008**, *5*, 496-504.
- (11) Lu, F.; Wu, S.-H.; Hung, Y.; Mou, C.-Y.; *Small* **2009**, *5*, 1408-1413.
- (12) He, C.; Hu, Y.; Yin, L.; Tang, C.; Yin, C.; *Biomaterials* **2010**, *31*, 3657-3666.
- (13) Sonavane, G.; Tomoda, K.; Makino, K.; *Colloids Surf. B. Biointerfaces* **2008**, *66*, 274-280.
- (14) Lu, N.; Song, X.; Zhang, J.; *Mater. Lett.* **2009**, *63*, 1089-1092.
- (15) Nelson, J. A.; Bennett, L. H.; Wagner, M. J.; *J. Am. Chem. Soc.* **2002**, *124*, 2979-2983.
- (16) Mayer, F.; Peters, J. A.; Djanashvili, K.; *Chem. Eur. J.* **2012**, *18*, 8004-8007.
- (17) Osseni, S. A.; Lechevallier, S.; Verelst, M.; Perriat, P.; Dexpert-Ghys, J.; Neumeyer, D.; Garcia, R.; Mayer, F.; Djanashvili, K.; Peters, J. A.; Magdeleine, E.; Gros-Dagnac, H.; Celsis, P.; Mauricot, R.; *Nanoscale* **2014**, *6*, 555-564.
- (18) Truillet, C.; Lux, F.; Moreau, J.; Four, M.; Sancey, L.; Chevreux, S.; Boeuf, G.; Perriat, P.; Frochot, C.; Antoine, R.; Dugourd, P.; Portefaix, C.; Hoeffel, C.; Barberi-Heyob, M.; Terryn, C.; van Gulick, L.; Lemercier, G.; Tillement, O.; *Dalton Trans.* **2013**, *42*, 12410-12420.
- (19) Zhang, B.; Jin, H.; Li, Y.; Chen, B.; Liu, S.; Shi, D.; *J. Mater. Chem.* **2012**, *22*, 14494-14501.
- (20) Bridot, J.-L.; Faure, A.-C.; Laurent, S.; Rivière, C.; Billotey, C.; Hiba, B.; Janier, M.; Jossereand, V.; Coll, J.-L.; Vander Elst, L.; Muller, R.; Roux, S.; Perriat, P.; Tillement, O.; *J. Am. Chem. Soc.* **2007**, *129*, 5076-5084.
- (21) Abrikosova, N.; Skoglund, C.; Ahrén, M.; Bengtsson, T.; Uvdal, K.; *Nanotechnology* **2012**, *23*, 275101.

- (22) Chen, G.; Qiu, H.; Prasad, P. N.; Chen, X.; *Chem. Rev.* **2014**, *114*, 5161-5214.
- (23) Assouline, J. G.; Sweeney, S. K.; Contrast imaging applications for lanthanide nanoparticles, WO2014035620A1, 2014
- (24) Luo, N.; Tian, X.; Yang, C.; Xiao, J.; Hu, W.; Chen, D.; Li, L.; *Phys. Chem. Chem. Phys.* **2013**, *15*, 12235-12240.
- (25) Landfester, K. In *Colloid Chemistry II*; Antonietti, M., Ed.; Springer Berlin Heidelberg: 2003; Vol. 227, p 75-123.
- (26) Mason, T. G.; Wilking, J. N.; Meleson, K.; Chang, C. B.; Graves, S. M.; *J. Phys.: Condens. Matter* **2006**, *18*, R635.
- (27) Barrios, S. B.; Petry, J. F.; Weiss, C. K.; Petzhold, C. L.; Landfester, K.; *J. Appl. Polym. Sci.* **2014**, *131*, 40569.
- (28) Schreiber, E.; Ziener, U.; Manzke, A.; Plettl, A.; Ziemann, P.; Landfester, K.; *Chem. Mater.* **2009**, *21*, 1750-1760.
- (29) Yang, Y.; Daniels, E. S.; Klein, A.; *J. Appl. Polym. Sci.* **2015**, DOI: 10.1002/app.41933.
- (30) Landfester, K.; Bechthold, N.; Tiarks, F.; Antonietti, M.; *Macromolecules* **1999**, *32*, 5222-5228.
- (31) Antonietti, M.; Landfester, K.; *Prog. Polym. Sci.* **2002**, *27*, 689-757.
- (32) Hecht, L. L.; Wagner, C.; Landfester, K.; Schuchmann, H. P.; *Langmuir* **2011**, *27*, 2279-2285.
- (33) Demond, A. H.; Lindner, A. S.; *Environ. Sci. Technol.* **1993**, *27*, 2318-2331.
- (34) Zhang, J.; Chen, Z.; Wang, Z.; Zhang, W.; Ming, N.; *Mater. Lett.* **2003**, *57*, 4466-4470.
- (35) Chesters, A. K.; *Chem. Eng. Res. Des.* **1991**, *69*, 259-270.
- (36) Machida, M.; Kawamura, K.; Kawano, T.; Zhang, D.; Ikeue, K.; *J. Mater. Chem.* **2006**, *16*, 3084-3090.
- (37) Zhang, D.; Yoshioka, F.; Ikeue, K.; Machida, M.; *Chem. Mater.* **2008**, *20*, 6697-6703.
- (38) Machida, M.; Kawano, T.; Eto, M.; Zhang, D.; Ikeue, K.; *Chem. Mater.* **2007**, *19*, 954-960.
- (39) McDevitt, N. T.; Baun, W. L.; *Spectrochim. Acta* **1964**, *20*, 799-808.
- (40) Kim, T. J.; Chae, K. S.; Chang, Y.; Lee, G. H.; *Curr. Top. Med. Chem.* **2013**, *13*, 422-433.
- (41) Tóth, É.; Helm, L.; Merbach, A. In *The Chemistry of Contrast Agents in Medical Magnetic Resonance Imaging*; John Wiley & Sons, Ltd: 2013, p 25-81.
- (42) Norek, M.; Peters, J. A.; *Prog. Nucl. Magn. Reson. Spectrosc.* **2011**, *59*, 64-82.
- (43) Norek, M.; Kampert, E.; Zeitler, U.; Peters, J. A.; *J. Am. Chem. Soc.* **2008**, *130*, 5335-5340.
- (44) Corsi, D. M.; Platas-Iglesias, C.; Bekkum, H. v.; Peters, J. A.; *Magn. Reson. Chem.* **2001**, *39*, 723-726.

Nanoparticles of Lanthanide Oxysulfate/Oxysulfide for Improved Capabilities in O₂ Storage/Release

7

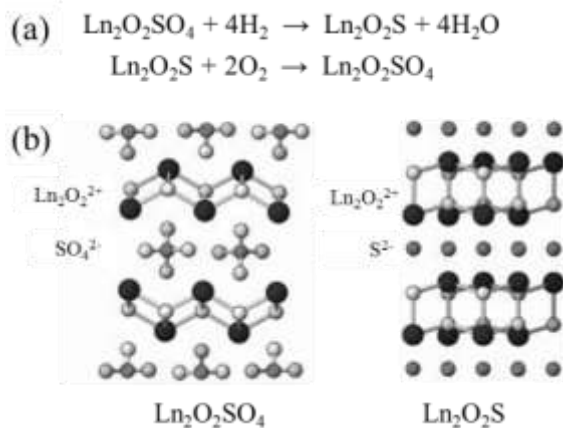


INTRODUCTION

Materials with a capacity for cyclic oxygen storage and release are important oxygen carriers (OCs) in automotive catalytic combustion. Under oxidative conditions metal oxides are formed, which can in turn be reduced by fuel components such as CO, hydrocarbons and NO_x. These metal oxides thus act as combustion catalysts and their advantage is that they can act as buffer for oxygen under oxygen lean conditions, thus regulating the oxygen concentration.¹⁻³

The redox reactions of the OCs must be fully reversible and quantitative. Commonly, transition metal oxides on various supports, e.g. dendrimers, TiO₂, Al₂O₃, zeolites, SiO₂, etc., have been studied for this purpose.⁴ However, metal oxides are generally susceptible to sulfur poisoning, which is a true disadvantage when using common carbon fuels.^{5,6} In addition, CeO₂ is an attractive OC material because of the reversible and fast redox reactions between Ce⁴⁺ and Ce³⁺ at relatively mild temperatures (< 400 °C). However the maximum capacity of oxygen storage per mole of CeO₂ is limited to 0.25 mol of O₂ and its stability is not sufficient under operating conditions.^{7,8} An attractive material that does not depend on metal, and which is sulfur tolerant is CaSO₄.^{9,10} Sulfate compounds can have an oxygen storage capacity of 2 mol of O₂ per mol of CaSO₄ due to the redox number of sulfur from +6 (in SO₄²⁻) to -2 in sulfide (S²⁻). Therefore CaSO₄ has been extensively studied as oxygen carrier.^{9,10} However CaSO₄ exhibits only high rates for reduction above 1000 °C, and at these temperatures SO₂ is also produced.¹¹

In 2004, Machida and coworkers reported lanthanide oxysulfates (Ln₂O₂SO₄) as OCs, which have much larger capacities for oxygen storage (2 mole of O₂ per mole of S).¹² These OCs do not depend on metal ions, but, as in the case of CaSO₄, are based on the reversible redox of sulfur (S⁶⁺/S²⁻, Scheme 7.1a).¹ The structures for Ln₂O₂SO₄ and Ln₂O₂S are depicted in Scheme 7.1b. Ln₂O₂SO₄ is stable at very high temperatures (> 1000 °C) and no release of H₂S or SO₂ occurs. Moreover, a wide range of lanthanides can be applied for this purpose.^{1,13} Despite the above-mentioned advantages, the practical application of Ln₂O₂SO₄ is limited due to the still high reaction temperatures (600-800 °C) required. By the impregnation of the Ln₂O₂SO₄ materials with noble metals (Pt or Pd), a significant reduction of the operative temperature by 100-200 °C for both oxygen release and storage processes could be achieved due to the activation of hydrogen and oxygen.¹²



Scheme 7.1. Redox reactions of (a) $\text{Ln}_2\text{O}_2\text{SO}_4$ and $\text{Ln}_2\text{O}_2\text{S}$, and (b) the corresponding crystal structures (adapted from Ref. 1).

The reaction rates could also be accelerated by increasing the surface area of the $\text{Ln}_2\text{O}_2\text{SO}_4$ materials.¹⁴ Doping by Ce is another effective way of improving the activity of $\text{Ln}_2\text{O}_2\text{SO}_4$. It causes structural distortion of tetrahedral SO_4 units (thus promoting the rates of both oxygen release and storage),¹⁵ while the presence of $\text{Ce}^{3+}/\text{Ce}^{4+}$ on the surface of $\text{Ln}_2\text{O}_2\text{SO}_4$ further accelerates the redox of sulfur. The detailed X-ray structural study revealed that the oxygen release and storage behavior is accompanied by noticeable differences in S–O distances and O–S–O angles of the SO_4 units, as well as differences in the crystal structure of the $\text{Ln}_2\text{O}_2^{2+}$ unit, as shown in Scheme 7.1b.^{13,16} In a very recent report, Lisi *et al* demonstrated that Cu-doping can also enhance the oxygen mobility in the $\text{La}_2\text{O}_2\text{SO}_4$ structure, leading to a decreased reaction temperature for both reduction and oxidation.¹¹

The $\text{Ln}_2\text{O}_2\text{SO}_4$ materials for OC purposes reported so far, have been prepared by different methods, such as calcination of $\text{Ln}_2(\text{SO}_4)_3 \cdot n\text{H}_2\text{O}$,¹ utilization of precursors of layered Ln-dodecyl sulfate mesophases,^{14,17} or Ln-precipitation.¹⁸ All these procedures lead to bulk materials with an irregular morphology. It has been demonstrated that the size and shape of OC particles (e.g. CeO_2) have a strong influence on their catalytic performance, due to the increased surface-to-volume ratio, and the exposure of reactive metal ions at the surface.¹⁹⁻²¹ However, the effects on oxygen storage/release performance of $\text{Ln}_2\text{O}_2\text{SO}_4$

materials as a function of size and shape have not yet been investigated. Herein, we report on a remarkable enhancement of the catalytic activity of $\text{LnPr}_2\text{O}_2\text{SO}_4$ (with $\text{Ln} = \text{Pr}$) by (i) using nanoparticles rather than bulk material and (ii) by doping the $\text{Pr}_2\text{O}_2\text{SO}_4$ with cost-effective Ni(II) . $\text{Pr}_2\text{O}_2\text{SO}_4$ was selected, because among the lanthanides it can act as oxidation catalyst with high rates at relatively low temperatures ($< 600\text{ }^\circ\text{C}$).¹

RESULTS AND DISCUSSION

Recently, we have developed a facile method for the preparation of nanosized $\text{Ln}_2\text{O}_2\text{SO}_4$ ($\text{Ln} = \text{Gd}$ and Ho) based on thermal decomposition of nanodroplets (NDs) formed by Ln-acetylacetonates ($\text{Ln}(\text{acac})_3$) under emulsifying conditions.²² The choice of the surfactant during the formation of NDs was found to determine the elemental composition of the nanoparticles (NPs) obtained after calcination of the dried NDs. Therefore, in the present study we prepared $\text{Pr}_2\text{O}_2\text{SO}_4$ NPs by using sodium dodecyl sulfate and $\text{Pr}(\text{acac})_3$ and subsequent calcination of the lyophilized NDs. The thermogravimetric analysis (TGA) profile of the lyophilized NDs visualizes the formation of $\text{Pr}_2\text{O}_2\text{SO}_4$ particles (Figure 7.1). Dehydration and combustion of organic moieties were observed below $300\text{ }^\circ\text{C}$. The formation of $\text{Pr}_2\text{O}_2\text{SO}_4$ NPs is expected to occur between 300 and $800\text{ }^\circ\text{C}$ by the alternative staging between SO_4^{2-} and $\text{Pr}_2\text{O}_2^{2+}$ (Scheme 7.1b).^{14,15} Above $800\text{ }^\circ\text{C}$ a stabilized curve was observed, indicating the full formation of inorganic NPs. Therefore, in order to obtain the solid NPs, the calcination was carried out at $800\text{ }^\circ\text{C}$ for 1 h to give $\text{Pr}_2\text{O}_2\text{SO}_4$ NPs in 82 % yield with respect to $\text{Pr}(\text{acac})_3$.

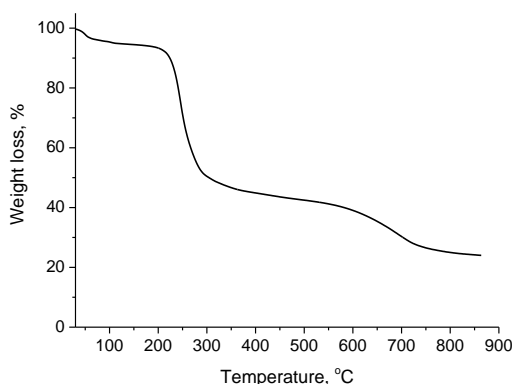


Figure 7.1. TGA profile of nanodroplets containing sodium dodecyl sulfate and $\text{Pr}(\text{acac})_3$ prepared by miniemulsion method.

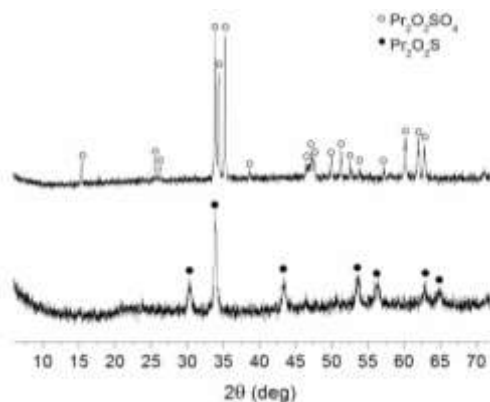


Figure 7.2. Powder XRD patterns of nanoparticulate Pr₂O₂SO₄ obtained by miniemulsion method, and Pr₂O₂S resulted from the subsequent reduction by 10 % H₂/Ar.

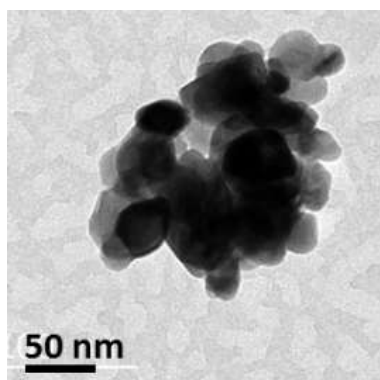


Figure 7.3. TEM images of the solid Pr₂O₂SO₄ NPs.

Figure 7.2 demonstrates the X-Ray Diffraction (XRD) patterns of the crystalline Pr₂O₂SO₄ as well as the oxysulfide Pr₂O₂S, which was obtained after reduction of the oxysulfate by H₂ (10 %) in Ar. The XRD pattern reveals an orthorhombic structure of Pr₂O₂SO₄ with calculated lattice constants $a = 4.240 \text{ \AA}$, $b = 4.138 \text{ \AA}$, and $c = 13.422 \text{ \AA}$, which are in a relatively good agreement with the reported values (PDF#41-0679). Additionally, the XRD pattern of Pr₂O₂S shows lattice dimensions of $a = 3.574 \text{ \AA}$, $b = 3.974 \text{ \AA}$ and $c = 6.798 \text{ \AA}$, corresponding to a hexagonal cell (p3ml-164, PDF#65-3453). TEM images show that fairly spherical particles were obtained with a diameter of $28 \pm 5.1 \text{ nm}$ (Figure 7.3).

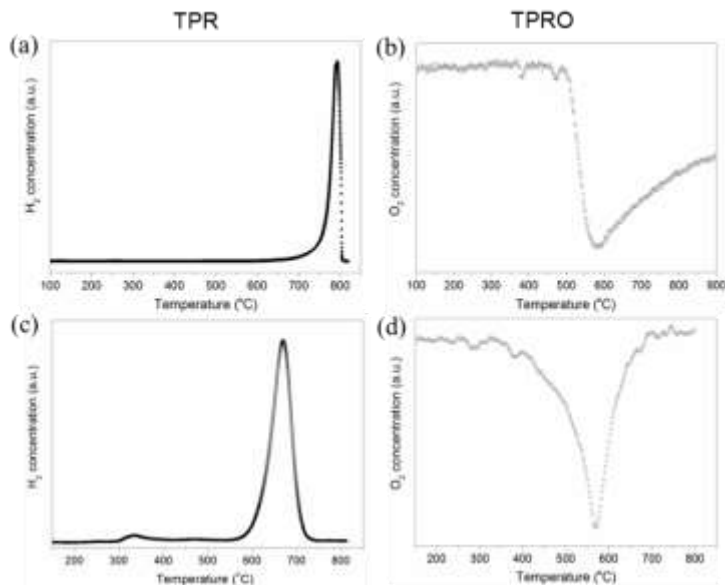


Figure 7.4. Temperature programmed profiles of redox reactions catalyzed by nanoparticulate $\text{Pr}_2\text{O}_2\text{SO}_4$: on the left are TPR profiles of non-doped (a) and 1.9 % Ni-doped (c) $\text{Pr}_2\text{O}_2\text{SO}_4$ in a flow of 10 % H_2/Ar and on the right are TPRO profiles of non-doped (b) and 1.9 % Ni-doped (d) $\text{Pr}_2\text{O}_2\text{SO}_4$ in a flow of 20 % O_2/He . Heating rate $10\text{ }^\circ\text{C min}^{-1}$.

Following the successful preparation of $\text{Pr}_2\text{O}_2\text{SO}_4$ NPs, their thermo-chemical behaviour as oxygen carriers was investigated by carrying out TPR/TPRO cycles using H_2 and O_2 (Figure 7.4 a,b). Temperature programmed reduction (TPR) was carried out in a conventional flow system by heating the sample at $10\text{ }^\circ\text{C min}^{-1}$ in a stream of 10 % H_2 in Ar as shown in Figure 7.4 a. The reduction started at about $700\text{ }^\circ\text{C}$ and gave a peak in H_2 -uptake at $790\text{ }^\circ\text{C}$, whereas the reaction was completed at around $800\text{ }^\circ\text{C}$. The asymmetric peak in the narrow temperature range indicated a very fast reduction of $\text{Pr}_2\text{O}_2\text{SO}_4$. The oxysulfate was reduced into oxysulfide ($\text{Pr}_2\text{O}_2\text{S}$), as proven by its XRD pattern shown in Figure 7.2. The obtained oxysulfide was then subjected to temperature programmed reoxidation (TPRO) in a stream of 20 % O_2 in He (Figure 7.4 b). The oxygen consumption started at about $480\text{ }^\circ\text{C}$ and exhibited a maximum at $580\text{ }^\circ\text{C}$. Above this temperature, the reoxidation rate became slower and was not even completed until $900\text{ }^\circ\text{C}$. Based on the integration from TPR and TPRO, the amount of consumed O_2 and H_2 was 1.34 and 3.97 mol $^{-1}$ for $\text{Pr}_2\text{O}_2\text{SO}_4$ and $\text{Pr}_2\text{O}_2\text{S}$, respectively. The O_2 consumption (per mol of $\text{Pr}_2\text{O}_2\text{SO}_4$)

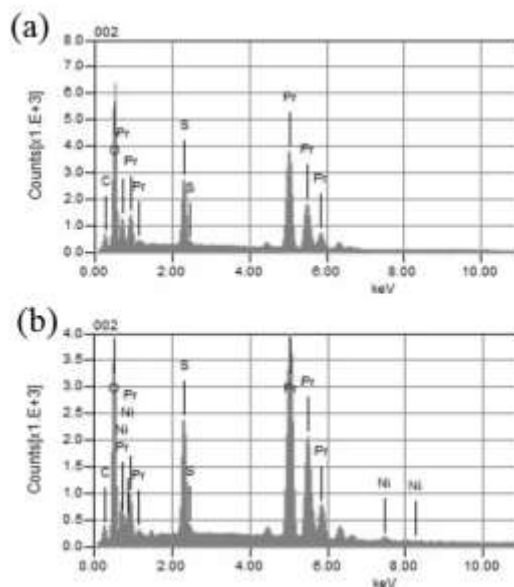


Figure 7.5. EDS spectrum of (a) Pr₂O₂SO₄ and (b) Ni-doped Pr₂O₂SO₄ NPs. The amount of Ni is 1.9 wt% from three separate spot analyses.

is significantly lower than 2, thus indicating that the re-oxidation was not completed under the conditions applied.

These results can be compared with those for the bulk material as reported in literature: the nanosized Pr₂O₂SO₄ displays a fast reduction in TPR between 700 - 800 °C, and a low temperature for the maximum uptake of oxygen in TPRO (580 °C). In contrast, the previously reported bulk Pr₂O₂SO₄ exhibited lesser performance: the reduction took place in the range of 700 to > 900 °C and maximum oxygen uptake was observed only at 700 °C.¹

In a next step, motivated by the redox behavior of nanosized Pr₂O₂SO₄, we doped the Pr₂O₂SO₄ with Ni(II) aiming at a further enhancement of the redox properties. Ni(II) is a cost-effective alternative for Pt and Pd for both the activation of both hydrogen and oxygen.^{2,23} The Pr₂O₂SO₄ NPs described above were impregnated with an aqueous solution of NiCl₂ and then calcined at 450 °C for 90 min to give Pr₂O₂SO₄ doped with 1.9 wt% Ni. The extent of Ni-doping was calculated from the Energy Dispersive Spectrum (EDS) of the

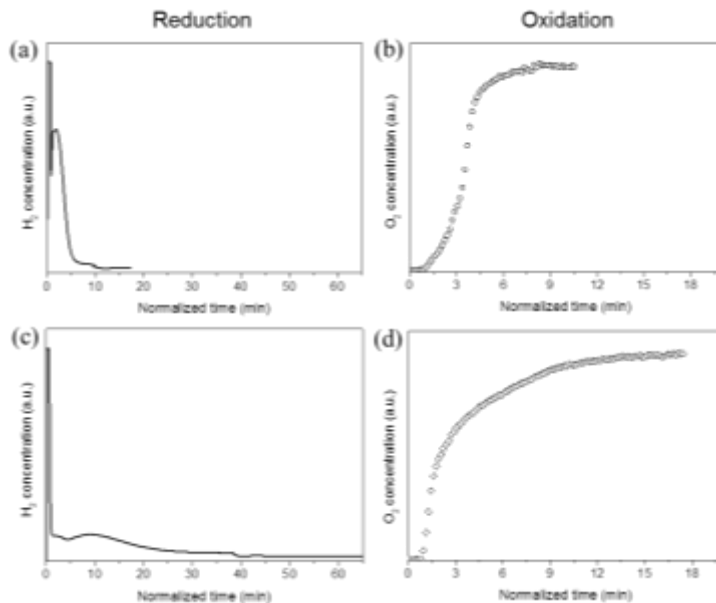


Figure 7.6. H₂ and O₂ consumption profiles of 1.9 wt% Ni-doped Pr₂O₂SO₄ at 700 °C (a,b) and 600 °C (c,d) under a feed stream of 10 % H₂/Ar or 5 % O₂/He.

prepared materials (Figure 7.5). The TPR/TPRO profiles of these Ni-doped NPs (Figure 7.4 c,d) show that the reduction took place in the temperature range of 570 to 730 °C with consumption of 3.89 mol of H₂ per mol of Pr₂O₂SO₄. The reoxidation started at about 400 °C, reached a maximum at 580 °C, and was completed at about 700 °C with 1.93 mol of O₂ uptake per mol of Pr₂O₂S. The ratio H₂/O₂ uptake is 2, which is in perfect agreement with fully reversible redox reactions.

The rate of reduction with H₂, and oxidation with O₂, is an important property that characterizes the performance of the Ln₂O₂SO₄ as a storage material. We performed the redox reactions at both 700 and 600 °C, as shown in Figure 7.6. For the 1.9 wt% Ni-doped Pr₂O₂SO₄ sample, surprisingly, both reduction and reoxidation were completed within 10 min at 700 °C. The reaction rates calculated from the redox profiles are 0.51 mmol·g⁻¹·min⁻¹ for the reduction, and 0.66 mmol·g⁻¹·min⁻¹ for the reoxidation. We thus observe that nanoparticulate Pr₂O₂SO₄ doped with Ni, displays two times higher oxidation rates

Table 7.1. Oxygen Release and Storage Properties of Pr₂O₂SO₄.

Catalyst	Reaction Temp.	reduction with H ₂	oxidation with O ₂	Ref.
	°C	mmol·g ⁻¹ min ⁻¹	mmol·g ⁻¹ min ⁻¹	
Pr ₂ O ₂ SO ₄ NPs, 1.5wt% Ni	700	0.51	0.66	This work
Pr ₂ O ₂ SO ₄ NPs, 1.5wt% Ni	600	0.13	0.36	This work
Bulk Pr ₂ O ₂ SO ₄ , 1wt% Pd	700	0.11	0.325	13
Bulk Pr ₂ O ₂ SO ₄ , 1wt% Pd	600	0.01-0.11	N.A.	17

compared to that of the best bulk Pr₂O₂SO₄ materials doped with 1 wt% Pd reported in the literature (see Table 7.1). At 600 °C, the storage rate of Ni-doped Pr₂O₂SO₄ is still faster than that of the bulk material measured at 700 °C. Admittedly these data need further confirmation by studies for both materials under identical conditions, but the first indication is that 1) NPs of Pr₂O₂SO₄ compared to bulk material exhibit higher activity in both reduction and oxidation, and 2) Ni is a suitable alternative to doping by Pd. The nanoparticulate nature of nanosized Pr₂O₂SO₄ particles, is expected to be beneficial for higher oxidation and reduction activities. The smaller NPs lead to rapid gas diffusion and solid-gas reactions that facilitate oxygen storage and release.^{14,17} Additionally, as discussed above, the obtained Pr₂O₂SO₄ NPs exhibit an orthorhombic structure with shortened *a* (4.240 Å) but extended *c* (13.422 Å) of the lattice parameters, compared to those of the bulk material with a monoclinic structure (*a* = 14.047 Å, and *c* = 8.281 Å).¹³ Stacking of SO₄²⁻ and Pr₂O₂²⁺ layers along the *a*-axis changes the crystal structure of Pr₂O₂SO₄ NPs by distortion of the SO₄ tetrahedral units in which each oxygen atom is coordinated to a Pr atom.¹⁶ This is, therefore, probably advantageous for the faster redox reactions observed in the present study. As for the observed rates for oxidation being faster than those for reduction, this is in agreement with the data for the bulk material: Machida and co-workers postulated that the coexistence of Pr⁴⁺ with Pr³⁺ ions on the particle surface is one of the factors responsible for this and it seems to be specific for Pr-based oxysulfates.^{13,17}

CONCLUSIONS

In summary, the nanoparticulate (around 30 nm in diameter) $\text{Pr}_2\text{O}_2\text{SO}_4$ was synthesized by the miniemulsion method. Properties for oxygen storage (oxidation with oxygen leading to oxysulfates) and release (reduction of oxysulfates by hydrogen leading to sulfides) were evaluated by temperature programmed reduction/reoxidation (TPR/TPRO). The samples were doped with 1.9 wt% Ni in order to further promote the redox behavior due to increased oxygen mobility known to occur at the surface of Ni(II) with available d-orbitals. The Ni-doping represents a cost-effective alternative to the more expensive Pt and Pd. The results of TPR/TPRO for the Ni-doped $\text{Pr}_2\text{O}_2\text{SO}_4$ showed that at 700 °C, the rates for oxygen storage and release are respectively 2 and 4.6 times higher than these of the best bulk 1 wt% Pd-doped $\text{Pr}_2\text{O}_2\text{SO}_4$ reported. In addition, the $\text{Pr}_2\text{O}_2\text{SO}_4$ is already very active at 600 °C. The overall improved performance is proposed to be caused by a collective effect of a higher surface-to-volume ratio, the copresence of Pr^{4+} and Pr^{3+} ions at the particle surface, the distorted crystal structure leading to more reactive SO_4 units, and Ni doping of the obtained $\text{Pr}_2\text{O}_2\text{SO}_4$ nanoparticles. Further studies will be directed to the exact structure of the Ni-doped material, and towards determining its reactivity versus real reductants (CO, hydrocarbons, NO_x) as a function of Ni-content.

EXPERIMENTAL

Materials and methods

All chemicals were used as purchased without further purification: analytical grade solvents (Sigma-Aldrich), sodium dodecyl sulfate (99%, Sigma-Aldrich), octadecane (99%, Sigma-Aldrich), acetylacetone (acac, 98%, Fluka) and lanthanide chlorides ($\text{LnCl}_3 \cdot 6\text{H}_2\text{O}$, Stem Chemicals).

Preparation of nanosized $\text{Pr}_2\text{O}_2\text{SO}_4$ and characterization

The NPs of $\text{Pr}_2\text{O}_2\text{SO}_4$ were prepared by a previously reported miniemulsion method²⁴ starting from $\text{Pr}(\text{acac})_3$, which was synthesized according to published procedures.²⁷ To prepare nanodroplets in a miniemulsion containing Pr^{3+} , the dispersed hydrophobic phase was obtained by dissolving 100 mg of $\text{Pr}(\text{acac})_3$ and 20 mg of octadecane in 5 mL of dichloromethane. The dispersed phase was then added dropwise to a continuous phase

consisting of 50 mg of SDS in 16 mL of water. The mixture was vigorously stirred at room temperature for 1 h (pre-emulsion) and then ultrasonicated for 5 min under ice cooling at 62% amplitude with time intervals at 1 s (Qsonica Sonicator, 500 W, 1/2 inch tip) yielding a greenish milky miniemulsion. The hydrophobic phase was then removed by careful evaporation at slightly reduced pressure and room temperature (to avoid aggregation), until an opaque dispersion appeared. The obtained dispersion was freeze-dried, yielding Pr-containing fluffy powders. To obtain solid Pr₂O₂SO₄, thermal decomposition was performed by calcination at 850 °C in an air atmosphere for 1 h with a heating rate of 10 °C min⁻¹. TGA was used to evaluate conversion of the freeze-dried Ln-containing nanodroplets into the solid particles. The structure of the Pr₂O₂SO₄ was identified by a Bruker D8 Advance X-ray diffractometer using Co K α radiation (1.789 Å) at 35 kV and 40 mA. The data were collected from 5.0° to 80° 2 θ with a step size of 0.020° 2 θ and a counting time of 0.5 s per step. Lattice constants of Ln-oxysulfates and Ln-oxides were calculated and corrected using MDI JADE software. The particle size and morphology were analyzed by TEM (JOEL JEM-2100) with 200 kV acceleration voltages.

The reduction/reoxidation profiles of Pr₂O₂SO₄ NPs were measured by temperature-programmed reduction and reoxidation (TPR/TPRO) in a conventional flow-reactor. A tubular quartz reactor with 6 mm inner diameter was firstly filled with a layer of quartz wool, followed by a layer of 200 mg of SiC and 15-20 mg of Pr₂O₂SO₄ sample, followed by another 200 mg of SiC. The reactor was connected to an inert system and to a differential evacuation system. After careful flushing by He, the reactor was heated in a flowing gas mixture of 10 % H₂ in Ar (20 mL min⁻¹) with a constant rate 10 °C min⁻¹ until 900 °C. The effluent gas was analyzed by a residual gas analyzer mass spectrometer. After the completion of the TPR measurement, the sample was cooled down in a N₂ flow. This was followed by evacuation and a second heating in a flow of 20 % O₂ in He (20 mL min⁻¹) at a heating rate 10 °C min⁻¹ up to 900 °C to measure the TPRO profile. The overall H₂ and O₂ consumptions in TPR and TPRO are calibrated by the redox of a known amount of CuO. To calculate the redox rate of the Ni-doped Pr₂O₂SO₄ sample, 15-20 mg of Pr₂O₂SO₄ was kept at 600/700 °C, 10 % H₂ in Ar and 5 % O₂ in He were applied in the reduction and oxidation, respectively.

Acknowledgements

Bart van der Linden (Catalysis Engineering, TU Delft) is acknowledged for the help with TPR/TPRO measurements.

References

- (1) Machida, M.; Kawamura, K.; Ito, K.; Ikeue, K.; *Chem. Mater.* **2005**, *17*, 1487-1492.
- (2) Wang, J.; Chen, H.; Hu, Z.; Yao, M.; Li, Y.; *Catal. Rev.: Sci. Eng.* **2015**, *57*, 79-144.
- (3) Motohashi, T.; Ueda, T.; Masubuchi, Y.; Takiguchi, M.; Setoyama, T.; Oshima, K.; Kikkawa, S.; *Chem. Mater.* **2010**, *22*, 3192-3196.
- (4) Yu, W.; Porosoff, M. D.; Chen, J. G.; *Chem. Rev.* **2012**, *112*, 5780-5817., and references therein.
- (5) Nasri, N. S.; Jones, J. M.; Dupont, V. A.; Williams, A.; *Energy & Fuels* **1998**, *12*, 1130-1134.
- (6) Carvalho, L. S.; Pieck, C. L.; do Carmo Rangel, M.; Fígoli, N. S.; Parera, J. M.; *Industrial & Engineering Chemistry Research* **2004**, *43*, 1222-1226.
- (7) Kašpar, J.; Fornasiero, P.; *J. Solid State Chem.* **2003**, *171*, 19-29.
- (8) Matsumoto, S. i.; *Catal. Today* **2004**, *90*, 183-190.
- (9) Tian, H.; Guo, Q.; *Ind. Eng. Chem. Res.* **2009**, *48*, 5624-5632.
- (10) Song, Q.; Xiao, R.; Deng, Z.; Zhang, H.; Shen, L.; Xiao, J.; Zhang, M.; *Energy Convers. Manage.* **2008**, *49*, 3178-3187.
- (11) Lisi, L.; Mancino, G.; Cimino, S.; *Int. J. Hydrogen Energy* **2015**, *40*, 2047-2054.
- (12) Machida, M.; Kawamura, K.; Ito, K.; *Chem. Commun.* **2004**, 662-663.
- (13) Machida, M.; Kawano, T.; Eto, M.; Zhang, D.; Ikeue, K.; *Chem. Mater.* **2007**, *19*, 954-960.
- (14) Machida, M.; Kawamura, K.; Kawano, T.; Zhang, D.; Ikeue, K.; *J. Mater. Chem.* **2006**, *16*, 3084-3090.
- (15) Zhang, D.; Yoshioka, F.; Ikeue, K.; Machida, M.; *Chem. Mater.* **2008**, *20*, 6697-6703.
- (16) Ikeue, K.; Kawano, T.; Eto, M.; Zhang, D.; Machida, M.; *J. Alloys Compd.* **2008**, *451*, 338-340.
- (17) Zhang, D.-J.; Eto, M.; Ikeue, K.; Machida, M.; *J. Ceram. Soc. Jpn.* **2007**, *115*, 597-601.
- (18) Shen, W.; Naito, S.; *Adv. Mater. Res. (Durnten-Zurich, Switz.)* **2014**, *886*, 196-199.
- (19) Aneggi, E.; Wiater, D.; de Leitenburg, C.; Llorca, J.; Trovarelli, A.; *ACS Catal.* **2014**, *4*, 172-181.
- (20) Sun, C.; Xue, D.; *Phys. Chem. Chem. Phys.* **2013**, *15*, 14414-14419.
- (21) Imagawa, H.; Suda, A.; Yamamura, K.; Sun, S.; *J. Phys. Chem. C* **2011**, *115*, 1740-1745.
- (22) Zhang, W.; Martinelli, J.; Mayer, F.; Bonnet, C. S.; Szeremeta, F.; Djanashvili, K.; *RSC Adv.* **2015**, *5*, 69861-69869.
- (23) Ran, R.; Wu, X.; Weng, D.; Fan, J.; *J. Alloys Compd.* **2013**, *577*, 288-294.

(24) Nijsen, J. F. W.; Zonnenberg, B. A.; Woittiez, J. R. W.; Rook, D. W.; Swildens-van Woudenberg, I. A.; van Rijk, P. P.; van het Schip, A. D.; *Eur. J. Nucl. Med.* **1999**, *26*, 699-704.

Summary

Multimodal imaging techniques are emerging in medical diagnosis. The synergistic combination of imaging techniques, such as MRI and PET/SPECT, is highly useful to strengthen each of the individual imaging modalities while reducing any of their disadvantages. In recent years, the progress of technical integration of imaging scanners has led to a clear motivation to design multimodal agents that can be used simultaneously and hence profit optimally of the new hybrid imaging scanners. Nanoscaffolds combining discrete functions (e.g. magnetic, radioactive, optical or therapeutic) are particularly interesting in this regard. There has been an increasing endeavour to design and synthesize multifunctional nanocomposites for practical applications in dual imaging modalities such as MRI-optical, MRI-PET, PET-optical, PET-CT, MRI-SPECT. Chapter 1 of this thesis summarizes the state-of-the-art in the development of multimodal probes for medical imaging and therapy.

The immense structural diversity of more than 200 known zeolites is the basis for the wide variety of applications of these fascinating materials ranging from catalysis and molecular filtration to agricultural uses. Despite this versatility, the potential of zeolites in medical imaging has not yet been much exploited. The well-defined pore and/or channel systems of the zeolite crystals allows specific chemical multifunctionalization with functional moieties. In Chapter 2, a novel strategy is presented to selectively deposit different ions into distinct framework locations of zeolite-LTL (Linde type L). It is demonstrated that carefully ion-exchanged Gd/Eu-containing nanocrystals acquire exceptional magnetic properties in combination with enhanced luminescence. This smart exploitation of the framework structure results in the highest relaxivity density ($13.7 \text{ s}^{-1} \text{ Lg}^{-1}$ at 60 MHz and 25 °C) reported so far for aluminosilicates, rendering these materials promising candidates for the design of dual magnetic resonance/optical imaging probes, as demonstrated in preliminary phantom studies.

Chapter 3 reports on thorough investigations of relaxometric properties of Gd-loaded nanozeolite LTL by ^1H , ^{17}O NMR, and EPR relaxation studies. Both the longitudinal and the transverse relaxivity of these Gd^{3+} loaded materials are strongly pH dependent and therefore, they have great potential as pH responsive contrast agents. For example, LTL-nanocrystals loaded with 3.5 wt% Gd show a dramatic decrease in the longitudinal relaxivity from 32 to $7 \text{ s}^{-1} \text{ mM}^{-1}$ (7.5 T and 25 °C) when going from pH 4 to 9. ^1H and ^{17}O

NMR show that this phenomenon can be rationalized by a decrease in proton mobility between the zeolite interior and the exterior due to a change from a fast prototropic exchange to a three orders of magnitude slower water exchange mechanism. The same material also has a high transverse relaxivity ($98 \text{ s}^{-1} \text{ mM}^{-1}$ at 7.5 T, 25 °C, and pH 5 as measured with the CPMG pulse sequence), which is governed by proton exchange too, while water diffusion plays a minor role. The high relaxivities and pH dependence render Gd-loaded LTL materials promising pH responsive contrast agents. Since the r_2/r_1 ratio of the designed probe strongly increases with the magnetic field strength, these materials are expected to be applicable for both T_1 and T_2 weighted MRI at low and high fields, respectively.

Chapter 4 describes the effects of surface functionalization on the relaxivities of Gd-loaded LTL nanoparticles by conjugation with long PEG-chains. The methoxy PEG was modified to yield PEG-silane, which was then successfully attached onto the surface of LTL, and the PEG-density could be controlled by adjusting the amount of reacting materials. It appeared that the longitudinal relaxivity decreased with increasing PEG loading. When the PEG loading increased from 6.2 to 9.1 %, the longitudinal relaxivities decreased from 25.7 to $12.3 \text{ mM}^{-1} \text{ s}^{-1}$ for 5.2 % Gd-loaded sample. This can be rationalized by PEG chains blocking the channel entrance of LTL to such an extent that the exchange between the interior water and bulk water becomes limited. The presence of PEG layer on LTL surface, however, did not change the high pH responsiveness of Gd-loaded LTL. Benefiting from the neutralization of surface charge after PEGylation, the leakage of Gd-ions under physiological conditions was significantly reduced. A stronger interaction between PEGylated LTL and cells was also observed. A cytotoxicity study showed that both PEGylated and non-PEGylated Gd-LTL are not toxic up to the dose $500 \text{ } \mu\text{g mL}^{-1}$. Additionally, the PEG layer effectively protects the pore entrances of Gd-LTL against blocking by compounds in the medium in which it is dispersed (e.g. xanthan).

Chapter 5 presents the radiolabeling of the Gd-loaded LTL nanoparticles with two potential PET-tracers ^{64}Cu and ^{89}Zr , aiming at the design of MRI-PET dual agents. A very high labeling yield, 88.4 % for ^{64}Cu and 74.0 % for ^{89}Zr , was reached in 60 min. Importantly, the T_1 and T_2 relaxivities are not affected by the coexistence of the radionuclides. The successful radiolabeling of LTL with ^{64}Cu is based on a simple ion-exchange with Na^+ , whereas radiolabeling with ^{89}Zr is due to coordination of ^{89}Zr -ions by

oxygens of LTL framework. These two different mechanisms determine the radionuclide leakage of the obtained LTL samples. The former exhibited very high leakage of ^{64}Cu , up to 11.1 % in PBS and 89.7 % in serum at 37°C for 24 h. On the contrary, the leakage of ^{89}Zr -ions from the latter sample was determined to be 1.6 % in PBS and 2.3 % in serum. A significant reduction of ^{64}Cu leakage (8.0 %) was achieved by calcination of ^{64}Cu -loaded LTL at 600 °C for 2 h. It may be expected that a further improvement may be realized by surface coating of LTL particles with PEG.

Chapter 6 reports a facile method to synthesize Ln-containing NPs. Among the procedures to prepare Ln-containing nanoparticles a gap exists in the range between 5 and 40 nm. The miniemulsion technique presented here is intended to fill this discontinuity and offers a facile method that can be applied for the preparation of nanoparticles for various applications, e.g. medical imaging, optics and catalysis. We demonstrate that formation of nanodroplets under emulsion conditions is the key step in the size control of the nanoparticles. The type of surfactant and the nature of the dispersed and continuous phases strongly influence the interfacial activity and consequently, the size of the solid particles that finally result from the subsequent thermal decomposition. Moreover, the choice of the surfactant determines the final elemental composition of the particles, leading to either lanthanide oxides or oxysulfates when using Brij® 35 or sodium dodecyl sulphate, respectively. Nanoparticles of holmium and gadolinium were prepared and their applicability as magnetic resonance imaging contrast agents was proved.

In Chapter 7 the versatility of lanthanide-based nanoparticles is demonstrated by the application of lanthanide oxysulfate for oxygen storage/release purposes in catalytic oxidation. Nanosized $\text{Pr}_2\text{O}_2\text{SO}_4$ particles (around 30 nm in diameter) were synthesised via the miniemulsion method, followed by Ni-doping (1.9 wt%) which is a cost-effective alternative to Pd- or Pt-doping. The temperature programmed reduction/reoxidation (TPR/TPRO) profiles show that this material has an excellent performance in both oxygen release and storage in terms of reaction rate and temperature. The rate of oxygen storage is more than 2 times higher than that of the best bulk 1 wt% Pd-doped $\text{Pr}_2\text{O}_2\text{SO}_4$ at 700 °C reported so far. The 1.9 wt% Ni-doped nanosized $\text{Pr}_2\text{O}_2\text{SO}_4$ is already very active at 600 °C. The improved performance is attributed to a collective effect of higher surface-to-volume ratio, copresence of Pr^{4+} and Pr^{3+} ions at the surface, and crystal deformation of the obtained $\text{Pr}_2\text{O}_2\text{SO}_4$ nanoparticles.

Samenvatting

Multimodale imagingtechnieken zijn sterk in opkomst in de medische diagnostiek. Synergetische combinatie van imaging technieken zoals MRI en PET/SPECT is erg nuttig ter versterking van elk van de individuele imaging modaliteiten, terwijl het ook eventuele nadelen kan verminderen. De vooruitgang in de technische integratie van imaging scanners stimuleert het ontwikkelen van multimodale contrast reagentia die simultaan gebruikt kunnen worden, zodat optimaal geprofiteerd kan worden van de nieuwe hybride scanners. In dit verband zijn vooral nanodeeltjes interessante platformen waarop afzonderlijke functies (magnetische, radioactieve, optische, of therapeutische) kunnen worden gecombineerd. De aandacht voor het ontwerp en de synthese van multifunctionele nanocomposieten met potentiële praktische toepassingen als MRI-optisch, MRI-PET, PET-optisch, PET-CT, MRI-SPECT neemt toe. Hoofdstuk 1 van dit proefschrift is een samenvatting van de ontwikkeling van multimodale “probes” voor medische imaging en therapie.

De enorme structurele diversiteit in de meer dan 200 bekende zeolieten, vormt de basis voor een breed scala aan toepassingen van deze fascinerende materialen in gebieden variërend van katalyse en moleculaire filtratie tot landbouw. Ondanks deze veelzijdigheid zijn de mogelijkheden van zeolieten in medische imaging nog nauwelijks onderzocht. Het structureel goed gedefinieerde porie- en/of kanalsysteem van zeolieten maakt het mogelijk om, door middel van specifieke chemische modificaties, functionele groepen aan te brengen. In Hoofdstuk 2 wordt een nieuwe strategie gepresenteerd om selectief verschillende ionen op bepaalde posities in het zeoliet-L (Linde type L) rooster aan te brengen. Aangetoond wordt dat zorgvuldig uitgewisselde Gd-Eu houdende nanokristallen zowel bijzondere magnetische eigenschappen, als versterkte luminescentie hebben. Deze slimme benutting van de structuur van het rooster leidt tot de hoogste relaxatiedichtheid ooit voor aluminosilicaten gerapporteerd ($13.7 \text{ s}^{-1} \text{ L g}^{-1}$ at 60 MHz en 25 °C). Dit maakt deze materialen veelbelovende kandidaten voor het ontwerp van duale magnetische resonantie-optische imaging “probes”. Deze veelbelovende toepassing wordt geïllustreerd aan de hand van resultaten van verkennende fantoomstudies.

Hoofdstuk 3 rapporteert een grondig onderzoek naar de relaxatie eigenschappen van Gd-geladen zeoliet LTL met behulp van ^1H , ^{17}O NMR, en EPR relaxatie studies. Zowel de

longitudinale als de transversale relaxivity van deze Gd^{3+} -geladen materialen zijn sterk pH afhankelijk en daarom zijn ze veelbelovend als potentiële pH-gevoelige contrastmiddelen. Bijvoorbeeld LTL-nanokristallen geladen met 3.5 gew.% Gd vertonen gaande van pH 4 naar 9 een dramatische afname van de longitudinale relaxatie van 32 tot $7 \text{ s}^{-1} \text{ mM}^{-1}$ (bij 7.5 T en $25 \text{ }^\circ\text{C}$). ^1H en ^{17}O NMR tonen aan dat dit fenomeen verklaard kan worden door een afname van de protonmobiliteit tussen de binnen- en de buitenkant van de zeoliet ten gevolge van een overgang van de snelle prototropische uitwisseling naar een orde drie langzamere uitwisseling van ongedissocieerd water. Hetzelfde materiaal heeft ook een hoge transversale relaxatie ($98 \text{ s}^{-1} \text{ mM}^{-1}$ bij 7.5 T , $25 \text{ }^\circ\text{C}$, en pH 5 gemeten met de CPMG pulssequentie), wat eveneens bepaald wordt door de protonuitwisseling, terwijl de waterdiffusie van minder belang is. De hoge relaxaties en de pH-afhankelijkheid maken dat Gd-LTL materialen veelbelovende pH contrastmiddelen zijn. Omdat de r_2/r_1 verhouding van de ontworpen “probe” sterk toeneemt bij toenemende magnetische veldsterkte, wordt er verwacht dat deze materialen toepasbaar zijn voor zowel T_1 als T_2 gewogen MRI, bij respectievelijk laag en hoog veld.

Hoofdstuk 4 beschrijft de effecten van het aanbrengen van lange PEG ketens op het oppervlak van Gd-geladen LTL. Methoxy-PEG werd omgezet in PEG-silaan, dat vervolgens met succes bevestigd werd aan het oppervlak van LTL. De dichtheid van de PEG ketens op het oppervlak kon gecontroleerd worden door aanpassing van de hoeveelheid reactant. De longitudinale relaxatie bleek af te nemen met toenemende PEG-belading. Een PEG-beladingstoename van 6.2 tot 9.1 % resulteerde in een longitudinale relaxatie-afname van 25.7 tot $12.3 \text{ mM}^{-1} \text{ s}^{-1}$ voor een 5.2 % Gd-geladen monster. Dit kan verklaard worden doordat de PEG ketens de ingang van de LTL kanalen in een zodanige mate blokkeren, dat de uitwisseling van water tussen het interieur van de zeoliet en de bulk geremd wordt. De aanwezigheid van een PEG-laag op het oppervlak had echter geen invloed op de hoge pH-respons van Gd-geladen LTL. Dankzij de neutralisatie van de oppervlaktelading door PEGylering, verminderde de lekkage van Gd-ionen onder fysiologische omstandigheden aanzienlijk. Er werd een sterkere interactie tussen gePEGyleerd LTL en cellen waargenomen. Cytotoxiciteitsonderzoek toonde aan dat, tot een dosis van $500 \text{ } \mu\text{g mL}^{-1}$, zowel gePEGyleerd als niet-gePEGyleerd Gd-LTL niet giftig zijn. Bovendien beschermt de PEG-laag de porie-openingen van Gd-LTL tegen blokkering door stoffen uit het medium waarin het zich bevindt.

Hoofdstuk 5 handelt over de radiolabeling van Gd-geladen LTL nanodeeltjes met twee potentiële PET-tracers, ^{64}Cu en ^{89}Zr , met als uiteindelijk doel het ontwerp van MRI-PET duale contrastmiddelen. In 30 min tijd werd een zeer hoge labeling opbrengst gehaald (88.4% voor ^{64}Cu en 74.0% voor ^{89}Zr). Hierbij is belangrijk dat de relaxaties niet beïnvloed bleken te worden door de aanwezigheid van de radionucliden. De succesvolle radiolabeling van LTL met ^{64}Cu is gebaseerd op een eenvoudige ionenwisseling met Na^+ , terwijl de radiolabeling met ^{89}Zr berust op coördinatie van ^{89}Zr door de zuurstofatomen van het LTL rooster. Deze twee verschillende mechanismes bepalen de lekkage van radionucliden uit het verkregen LTL monster. Het eerste vertoonde een zeer hoge lekkage van ^{64}Cu : tot 11.1% in PBS en 89.7% in serum bij 37 °C gedurende 24 u. Daarentegen was de lekkage van ^{89}Zr ionen uit het laatste monster slechts 1.6 % in PBS en 2.3 % in serum. Een aanzienlijke vermindering van de ^{64}Cu lekkage werd verkregen door het ^{64}Cu geladen LTL gedurende 2 u bij 600 °C te calcineren. Het valt te verwachten dat een verdere verbetering gerealiseerd kan worden door het oppervlak van de LTL deeltjes te coaten met PEG.

Hoofdstuk 6 rapporteert een eenvoudige methode om Ln-bevattende nanodeeltjes te synthetiseren. Tot op heden bestond er nog geen procedure om nanodeeltjes in het bereik van 5-40 nm te synthetiseren. De hier gerapporteerde mini-emulsietechniek vult dit gat op en het is een eenvoudige methode voor de bereiding van nanodeeltjes voor verschillende toepassingsgebieden, zoals bijvoorbeeld in medische beeldvorming, optica, en katalyse. We tonen aan dat de vorming van nanodruppels onder emulsiecondities de sleutel is tot het beheersen van de afmetingen van de gevormde nanodeeltjes. Hierbij zijn het type oppervlakte-actieve stof en de aard van de disperse en de continue fases van grote invloed op de activiteit van het grensvlak en daarom ook op de thermische ontleding in de volgende stap. Bovendien bepaalt de keuze van de oppervlakte-actieve stof de uiteindelijke elementaire samenstelling van de deeltjes: gebruik van Brij@35 geeft lanthanide oxides en natrium dodecylsulfaat lanthanide oxysulfaten. Holmium en gadolinium nanodeeltjes werden bereid en hun toepasbaarheid als MRI contrastmiddelen werd aangetoond.

In hoofdstuk 7 wordt de veelzijdigheid van op lanthaniden gebaseerde nanodeeltjes gedemonstreerd met de toepassing van lanthanide oxysulfaat als katalysator voor zuurstof-opslag en afgifte. Met behulp van de mini-emulsiemethode werden nanodeeltjes van $\text{Pr}_2\text{O}_2\text{SO}_4$ gesynthetiseerd van ongeveer 30 nm, die vervolgens beladen werden met 1.9 gew.% Ni. Dit is een kostenefficiënt alternatief is voor het gebruik van Pd of Pt..

Temperatuur-geprogrammeerde reductie/re-oxidatie (TPR/TPRO) toonde aan dat dit materiaal, wat betreft reactiesnelheid en temperatuur, uitstekend presteert in zowel zuurstofopslag als -afgifte. De begin- en eindtemperatuur hierbij waren lager en de opnamesnelheid van zuurstof was twee keer hoger dan het tot op heden gepubliceerde best presterende bulk $\text{Pr}_2\text{O}_2\text{SO}_4$ met 1 gew-% Pd. Deze prestatieverbetering kan worden toegeschreven aan de gezamenlijke effecten van een hogere oppervlakte/volume verhouding, een aanwezigheid van zowel Pr^{4+} als Pr^{3+} ionen aan de oppervlakte, en kristalvormingen in de verkregen $\text{Pr}_2\text{O}_2\text{SO}_4$ nanodeeltjes.

LIST OF PUBLICATIONS

Publications

1. J. Martinelli, A. Denkova, A. Arranja, W. Zhang and K. Djanashvili, Fate of Organic Functionalities Conjugated to Theranostic Nanoparticles upon Their Activation. *Bioconjugate Chemistry*, **2016**, *27*, 446–456.
2. W. Zhang, J. A. Peters, F. Mayer, L. Helm and K. Djanashvili, Prototropic Exchange Governs T1 and T2 Relaxivities of a Potential MRI Contrast Agent Nanozeolite Gd–LTL with a High pH Responsiveness, *The Journal of Physical Chemistry C*, **2015**, *119*, 5080-5089.
3. W. Zhang, J. Martinelli, F. Mayer, C. S. Bonnet, F. Szeremeta and K. Djanashvili, Molecular Architecture Control in Synthesis of Spherical Ln-Containing Nanoparticles, *RSC advances*, **2015**, *5*, 69861-69869.
4. X. Cui, M. A. Green, P. J. Blower, D. Zhou, Y. Yan, W. Zhang, K. Djanashvili, D. Mathe, D. S. Veres and K. Szigeti, Al(OH)₃ Facilitated Synthesis of Water-Soluble, Magnetic, Radiolabelled and Fluorescent Hydroxyapatite Nanoparticles, *Chemical Communications*, **2015**, *51*, 9332-9335.
5. F. Mayer, W. Zhang, T. Brichart, O. Tillement, C. S. Bonnet, É. Tóth, J. A. Peters and K. Djanashvili, Nanozeolite-LTL with Gd(III) Deposited in the Large and Eu(III) in the Small Cavities as a Magnetic Resonance Optical Imaging Probe. *Chemistry – A European Journal*, **2014**, *20*, 3358-3364.
6. W. Zhang, I. Arends and K. Djanashvili, Nanoparticles of Lanthanide oxysulfate/oxysulfide for improved capabilities in oxygen storage/release. *Manuscript submitted*.
7. W. Zhang, J. Martinelli, J. M.A. van Hengst, J. A. Peters, C. S. Bonnet, F. Szeremeta, H. Bouwmeester and K. Djanashvili, Surface Engineering of Gd-loaded Zeolite LTL for pH Responsive Dual-Functional MRI Agents. *Manuscript in preparation*.

Oral presentations

1. Wuyuan Zhang, Joop A Peters and Kristina Djanashvili. Nanoparticles of Gd^{3+} exchanged zeolite LTL as multimodal imaging probes. Forth International Conference on Multifunctional, Hybrid and Nanomaterials, Sitges, Spain. 10 March, 2015.
2. Wuyuan Zhang and Kristina Djanashvili. Accurate positioning of Ln^{3+} ions in zeolite LTL for bimodal imaging. Symposium for the department of biotechnology, Biezenmortel, the Netherlands. 2-4 July 2013.

Posters

1. W. Zhang, J. A Peters, K. Djanashvili. Nanoparticles of Gd^{3+} exchanged zeolite LTL as multimodal imaging probes. CHAINS 2014, Dutch Chemistry Conference, 17-18 November, 2014.
2. W. Zhang, F. Mayer, J. A. Peters, K. Kristina, Ln(III)-loaded zeolites for multimodal imaging, Lunteren, the Netherlands, 22-24 October, 2012.
3. W. Zhang, F. Mayer, J. A. Peters, K. Kristina, Nanozeolite-LTL with Gd^{3+} deposited in the large and Eu^{3+} in the small cavities as an MR-Optical imaging probe, Lunteren, the Netherlands, 11-13 November, 2013.

ACKNOWLEDGEMENTS

How time flies! I could still remember clearly the first days I just arrived in the Netherlands, a wonderful place where is famous for the fantastic tulips, windmills, rivers and cheese. At that moment I could hardly imagine the right moment to put a dot on my PhD life. Doing a PhD is not just the attempt to be a master of scientific work, but also be myself in personal growth. Passing the ups and downs, it is time to wrap the research project up in a thesis, and I can finally acknowledge people who have contributed in ways they probably do not realize, for the kind help, support, friendship, fun or just being around making my life more colorful.

I am indebted to Kristina Djanashvili, without whose daily guidance, faith, advice and gentle prodding, I would never be able to get through the PhD with both fruitful scientific achievements and pleasant feelings. Kristina, you've been a charming and special teacher. You motivated me in a natural and friendly way, so that I could constantly keep my enthusiasm in the work. I was shy, or more precisely, unconfident at the beginning of starting a new life in an exotic environment. You showed me great tolerance while I made many mistakes, and respected my choices in research. When I was down, you shared your own experience, your own views with me so that I know there is a way to cheer up. I am especially honored and lucky to meet you in Delft. I appreciated the easiness of reaching you and the efficient and kind way that you would address any problems. I had a wonderful period of time working with you, thank you for all fun in the work, and sharing your sense of humor. The enthusiasm, knowledge and skills in the professions, as well as the understandings in life I picked up from you, wherever I will be, they will certainly stay with me in future.

This all could not be true without my promotor Isabel Arends. Thank you for giving me the valuable chance to join the biocatalysis group. When I was standing in the crossing road after just finished the master's study, you and Kristina gave me an opportunity to pursue a doctorate in the group. This for sure has changed the footprint in my whole life. I could still remember one sentence from a text book in school when I was brought into contact with English language: "Never underestimate the impression you may make on others". I believe that this can truly express my appreciation to you since the first interview.

A special acknowledgement goes to Joop Peters. I am truly honored to get advice and guidance from you. Thank you very much for sharing your sense of humor. Your enthusiasm and dedication to science have greatly influenced me during the past three years; the inexpressible motivations will always accompany me in the future career.

Rogelio, sincere thanks to you for the interesting talks and short but unforgettable time we have had together. Thank you for sharing with me your understanding and fun of life. And thanks for the special kindness and affection from you and your wife on my little daughter. It was such great pleasure and big honor to meet you in Delft.

I would also like to convey my appreciation to Frank Hollmann. Frank, thanks for your kindness, and showing how to solve problems with possibilities in all directions. We only had several short talks during my PhD period; however, I got inspired a lot each time. Moreover, thank you for the chance to work with you in the near future. I am pretty sure I will be infected by your passion in science.

Doing a PhD with culture and language challenges is not an easy task. Therefore, I would like to thank all the colleagues and friends for their everyday support and company. First of all, I thank Mieke van de Kooij for her willingness to help. There was always a fast solution from you whenever I had difficulties in settling down in BOC. Franca Post, many thanks for your thorough guidance in, basically, everything after I just arrived in the Netherlands, which made my life abroad much easier at the very beginning. Florian Mayer, great thanks for your support and patience in the entire period of time we have worked together. You introduced me to NMR, freeze drier, TGA, ultrasonication probe, etc., actually everything needed in the research, to guarantee the efficiency in writing my thesis. It was a great and indelible pleasure to work with you, and talk to you. Jonathan Martinelli, thanks a lot for sharing with me your passion in science, sense of humor and constant edification to become a confident and green chemist. It has been an unforgettable time to work with you. Florian and Jonathan, thank you for the involvement in the project, very helpful discussions and solutions. Bishuang Chen and Yan Ni, thanks for many talks and fun, as well as huge dinners with you. It was such a wonderful and unforgettable time with you. Wherever I will be, it is always a nice memory.

I would also like to acknowledge Rafael T. M. de Rosales for the supervision and support in the radioactive laboratory at King's College London, Lydia Sandiford and Xianjin Cui for the kind help with radioactive work and TEM measurements. Special

thanks also go to Robin de Kruijff, Antonia Denkova and Baukje Terpstra at the Reactor Institute at TU Delft, for the great support in the practical work with Cu-64 and Ho-166. Formulation of Chapter 5 is possible because of all your support and guidance.

Thanks are due to the nice colleagues Kathrin Müller, Maarten Gorseling, Remco van Oosten, Caroline Paul, Stephen Eustace, Guzman Torrelo, Giang-Son Nguyen, Katya Churakova, Selin Kara, Adeline Ranoux, Laura Leemans Martin, Verena Resch, Serena Gargiulo, Tobias Müller, Jacob van Hengst, Kai Liu, Mauro Di Matteo, Elena Fernandez Fueyo, Alvaro Baraibar, Serge Endenburg, Marc Strampraad, Duco Bosma, Ben Norder, and many others, for the fun or technical support we had during and outside of work. Kathrin, Caroline and Maarten, thanks for many interesting discussions we ever had.

Thanks are also extended to the large group of Chinese mafia. Yong Zhang, Yifan Pan, Huayang Cai, Ping Liu, Tao Zou, Tiantian Yao, Linfeng Chen, Tay Wee Beng, Jianbing Fang, Jialun Liu, Jia Xu, Bo Qu, Feifei Wang, Weiwei Wang, Wenhao Yuan, Kai Li, ShuLan Shu, Yu Sun, Zilong Wei, Xiaowei Ouyang, and so many others abroad and also in China, for the friendship, great food and fun we had together. Yong, you are such a nice roommate and friend with great reliability, thanks for sharing with me your experience and fun in life, and endless help at the moment I just arrived in Delft. The Chinese friends in ChemE, Zhen Liu, Anping Cao, Kai Zhang, Liangyong Chu, Li Zhu, Jicheng Feng, Xiaohui Sun, Yu Bi, Zheng Cao, Yunlong Yu and Guanglin Wang, thank you for the friendship, I really enjoyed the great time with you, wonderful food, wonderful games and wonderful discussions. Anping, Kai, and Zhen, special thanks due to the great time we spent together, the fun and cheers. I am truly lucky and happy to meet you in Delft. The fantastic memory with you will accompany me forever.

The Chinese neighbors, Likun Ma, Qi Wang, and your better half Lin Liu, Hong Pan, sincere thanks for the friendship, sharing, unconditional help and support. I am especially touched by you. I had a wonderful time, excellent homemade food, great fun with you as well as with the little ones.

I would like to deeply thank my parents, for their endless and unconditional love and faith when I studied abroad. And my sister Xin, who fully supports and believes in me with everything. Deep thanks also go to my parents-in-law, for their unconditional support and thorough taking care of my little daughter, which was an invaluable help when we ever had a tough time.

I have been fortunate throughout my life to start a family that I can always rely on for praise, reassurance, and acceptance. For this reason, I would like to convey my special appreciation to Yi Cheng, my beloved wife. Thank you for your unconditional love, company and support. You devote your thorough attention and love to the family while you suffer from a chronic disease, you truly touched me. Whenever and wherever we are, I know you are an absolutely reliable person in my life. And moreover, thank you for bringing me such a cute daughter. Yuran, a special thanks to you, my little roommate and daughter, for choosing me as your parent and bringing us so much fun and happiness, which would be never possible to experience in life without you.



Delft, 3-9-2015

Curriculum Vitae

Wuyuan Zhang was born on March 22, 1987 in Gansu province, China. He obtained his secondary school diploma in 2005 at the 1st High School Huachi and was admitted in the same year to Hainan University (China). After four years study of chemistry he received his Bachelor degree in September 2009. Afterwards, he continued Master study at the same university under the supervision of Dr. Lingbin Lu and Prof. Dr. Qiang Lin. He obtained his Master degree in June 2012, with the thesis entitled “*Mechanochemical-synthesis and performance of double metal cyanide catalysts for copolymerization of carbon dioxide and epoxides*”, which was distinguished as the best Master thesis in 2012-13 in Hainan University. In September 2012, he started his PhD project under the daily supervision of Dr. Kristina Djanashvili in the group of Biocatalysis and Organic Chemistry at Delft University of Technology, the Netherlands. The project has been focusing on development of nanoscaffolds for the design of multimodal imaging agents. After graduation he continues his research career as a postdoctoral researcher in the same group under the supervision of Dr. Frank Hollmann, working on the use of water as a cosubstrate (electron donor) in enzymatic reactions.

